Control and operation of MMC-HVDC system for connecting offshore wind farm

A THESIS SUBMITTED FOR THE DEGREE OF

Doctor of Philosophy

Yiran Jing

Power Electronics, Drives and Energy Conversion (PEDEC) Group

Department of Electronic and Electrical Engineering

University of Strathclyde

August 2019

This thesis is the result of the author's original research. It has been composed by the author and has not been previously submitted for examination which has led to the award of a degree.

Signed:

Date:

Dedicated to my family

Acknowledgements

First and foremost, I would like to express my sincerest gratitude to my supervisor Prof. Lie Xu. He provides me technical guidance, valuable suggestions and timely comments on my work with full of patience throughout my Ph.D. research. His encyclopedic knowledge on power electronics, rigorous working manner and serious researching attitude will always inspire me to be more fearless facing the academic challenges. It is my pleasure and fortunate to have Lie as my supervisor.

I greatly appreciate Dr. Rui Li who helps me a lot with my research and patient in reviewing my papers. He always answers my questions with his strong fundamental in power electronics when I am stuck. And thanks to all my colleagues in PEDEC group, especially Lujie Yu, Yin Chen and Gabriele Amico. Thank you all for helping dispel my doubts and encourage me when I am confused. Thanks to Shuren Wang who helped with my thesis.

Yinyong Zhang and Chunpeng Li are my true friends without whom my life will be tedious. Yinyong is considerate and she helped me a lot with my daily life. We share all the joys and griefs. Chunpeng whom I often talked with gives me many strengths and advice with his optimistic attitude. And also, thanks to Jieyun with her support during my writing up stage.

Finally, I would like to thank my parents for their encouragement and endless love throughout my life. I cannot finish my Ph.D. study without their support.

Abstract

For connection of large offshore wind farms over distances 80-100 km, modular multi-level converter (MMC) based high voltage DC (HVDC) system emerges as a more suitable solution than HVAC due to its flexible control and transmission distance not affected by the cable charging current. For HVDC connected wind farms, the offshore wind farm AC networks are established by the offshore MMC stations which exhibit significant difference compared to conventional onshore networks. Consequently, this thesis focuses on the offshore AC voltage control, system stability, and fault analysis of the offshore wind farm system connected with MMC-HVDC transmission.

To control the offshore AC voltage and frequency using the offshore MMC, fixed frequency control is the most common approach. However, offshore system with fixed frequency control presents a slow response, especially during large transients. Thus, in order to improve the voltage controllability and system performances, a PLL based enhanced voltage and frequency control is proposed for the offshore MMC station. The performance of the proposed control is validated through time-domain simulations. The stability of the offshore system with the proposed control is further analysed using a developed small-signal offshore system model, including the offshore MMC and lumped wind turbine grid side converters. Bode plots and pole/zero maps are utilized to investigate suitable control parameter ranges and interactions between the power and AC voltage.

For the offshore AC network, system control and response during offshore AC faults need to be carefully considered. During an offshore fault, both the offshore MMC and WT converters have to ensure their safe operation by limiting the currents to be within their maximum ranges, and in the meantime, enable satisfactory operation of the overcurrent protection relays. Considering the requirements of overcurrent relay, a fault current providing control for the offshore MMC is proposed which ramps up current during faults over a predefined profile. This ensures adequate fault current for the relays while avoids excessive overcurrent during WT string faults. The proposed fault current providing

control is validated with offshore AC faults at different locations in a wind farm (e.g. clusters and strings).

Onshore faults which lead to the rapid reduction of power transition capability of the onshore MMC is another challenge to MMC-HVDC connected offshore wind farm system. A DC voltage dependent AC voltage control is thus applied at offshore MMC station which reduces the offshore AC voltage once DC overvoltage is detected. The reduced offshore AC voltage results in the automatic reduction of power generated by the wind farm such that the power imported to and exported from the HVDC link can be rebalanced. Therefore, DC overvoltage is alleviated and when the onshore fault is cleared, the offshore AC voltage returns to the nominal value, and normal power generation and transmission can be quickly restored. Different onshore fault conditions with voltage drops of 100%, 50% and 20% are tested to show the satisfactory onshore fault ride-through control of the system.

Contents

Acknowledgements iii

Abstract iv

Contents vi

List of Figures ix

Abbreviations xv

Symbols xvii

1. Introduction 1

1.1. Growth of renewable energy 1

1.2. Comparison of HVDC and HVAC power transmission systems 3

1.3. HVDC transmission systems 5

1.3.1. LCC-HVDC 5

1.3.2. VSC-HVDC 6

1.4. Challenges of MMC-HVDC system for connecting offshore wind farm 7

1.5. Motivation and contributions 8

1.6. Organization of thesis 9

2. Review on HVDC transmission system connecting offshore wind farms 11

2.1. Introduction 11

2.2. Offshore transmission system configuration 11

2.2.1. Point-to-point HVDC transmission system 12

2.2.2. Parallel HVDC transmission system 13

2.2.3. Multi-terminal HVDC transmission system 13

2.3. Control of HVDC systems connected with offshore wind farm 14

2.3.1. Control of offshore wind farm side converter 14

2.3.2. Control of onshore grid side converter 16

2.4. Review on fault ride-through of offshore wind farms 17

2.4.1. Offshore AC fault ride-through operation 17

2.4.2. Onshore AC fault ride-through operation 19

2.4.3. DC fault right-through operation 22

2.5. Summary 23

3. Fundamentals of converter modelling and control 24
3.1. Introduction 24
3.2. WT grid side VSC 24
3.2.1. VSC principles 25
3.2.2. VSC control 26
3.3. Modular multilevel converter 30
3.3.1. MMC principles 30
3.3.2. MMC control 35
3.4. Summary 40
4. Control of the offshore wind farm system 41
4.1. Introduction 41
4.2. System structure 42
4.2.1. Wind turbine modelling 43
4.2.2. Control of wind turbine converters 44
4.3. Basic control on offshore MMC station 45
4.3.1. Inner current loop 46
4.3.2. Outer voltage loop for AC voltage control 47
4.3.3. Offshore frequency control 48
4.4. Enhanced AC voltage and frequency control 49
4.5. Simulation results on normal operation of offshore wind farm 51
4.5.1. Start-up duration 53
4.5.2. Wind turbine connection and power ramping up 56
4.5.3. System response during large power step 60
4.6. Summary 64
5. Small-signal modelling and analysis of offshore AC system 65
5.1. Introduction 65
5.2. Offshore wind farm small-signal modelling 65
5.2.1. Offshore MMC small-signal modelling 66
5.2.2. Offshore wind farm small-signal modelling 74
5.2.3. Small-signal modelling of the complete offshore system 80
5.2.4. Offshore wind farm small-signal model validation 82
5.3. Stability analysis with small-signal model of offshore wind farm 86

5.3.1. Stability analysis of PLL based frequency loop 87
5.3.2. Stability analysis of PCC voltage 89
5.3.3. Wind power interaction with PCC voltage 98
5.4. Summary 100

6. Fault analysis of MMC-HVDC system connecting offshore wind farm 101
6.1. Introduction 101
6.2. Control and operation during offshore AC faults 102
6.2.1. Fault current providing control 102
6.2.2. Wind farm relay design 105
6.2.3. Overcurrent detection of offshore AC faults 111
6.2.4. SM capacitance requirements 115
6.3. Control and operation during onshore AC Faults 116
6.4. Simulation results 118
6.4.1. Offshore AC faults on WT cluster cable 120
6.4.2. Offshore AC faults on WT string 125
6.4.3. Onshore AC faults 128
6.5. Summary 139

7. Conclusion and Future Work 140
7.1. General conclusion 140
7.2. Author's contribution 143
7.3. Further work 144

References **145**

Author's Publications **155**

List of Figures

Figure 1.1 Continental shares in new capacity (%). 2
Figure 1.2 Global cumulative offshore wind capacity in 2017 and 2018. 3
Figure 1.3 Cost comparison of HVDC and HVAC transmission systems [7]. 4
Figure 1.4 LCC-HVDC connecting two AC grids. 6
Figure 1.5 VSC-HVDC connecting two AC grids. 7
Figure 2.1 OWPP connected through offshore HVDC links. 12
Figure 2.2 General control scheme of VSC-HVDC connected offshore wind farm. 14
Figure 2.3 Amplitude-angle voltage control scheme [38]. 14
Figure 2.4 Nested vector control scheme. 15
Figure 2.5 GSC control scheme. 16
Figure 2.6 Current limitation control at WFC. 18
Figure 2.7 AC voltage control with reactive current providing on WFC. 18
Figure 2.8 Power-synchronization control of VSC [53]. 19
Figure 2.9 VSC-HVDC system with DBR [57]. 20
Figure 2.10 Communication layout of VSC-HVDC connecting offshore wind farm [59]. 21
Figure 2.11 Offshore AC voltage limiting control for FRT at WFC. 21
Figure 3.1 Two level VSC structure. 25
Figure 3.2 Sinusoidal pulse width modulation. 25
Figure 3.3 Grid connected VSC structure. 27
Figure 3.4 Simplified current control loop. 28
Figure 3.5 Synchronous frame and source vector. 29
Figure 3.6 PLL control diagram. 29
Figure 3.7 MMC topology structures. 30
Figure 3.8 Simplified MMC model. 34
Figure 3.9 Nearest level modulation diagram. 36
Figure 3.10 Voltage balancing control [95]. 38
Figure 3.11 Common mode current controller [96]. 40
Figure 3.12 Compete control diagram for average MMC model. 40

Figure 4.1 Structure of MMC-HVDC connected offshore wind farm system. 42
Figure 4.2 Offshore wind farm system structure with lumped WT clusters. 44
Figure 4.3 Structure of single simplified WT cluster. 44
Figure 4.4 Control structure on WT side VSC. 45
Figure 4.5 Current control loop structure. 47
Figure 4.6 Voltage control loop structure. 48
Figure 4.7 Offshore MMC station AC voltage control strategy with fixed frequency. 49
Figure 4.8 PLL based frequency control strategy. 49
Figure 4.9 PLL synchronization control. 50
Figure 4.10 Offshore MMC station AC voltage control strategy with PLL-based frequency loop. 51
Figure 4.11 Simulation waveforms of offshore station MMC_1 during start-up. 54
Figure 4.12 Offshore system frequency during start-up. 55
Figure 4.13 Simulation waveforms comparison of AC voltage amplitude on PCC during start-up. 55
Figure 4.14 Simulation waveforms of offshore station MMC_1 during enable of WTs and power increasing. 57
Figure 4.15 Offshore frequency during enable of WTs and power up. 58
Figure 4.16 Current and power flows at onshore MMC_2 station during connecting of WTs and power ramp up. 58
Figure 4.17 AC current and output power on each WT cluster during enable of WTs and power increasing. 59
Figure 4.18 Simulation waveforms of offshore station MMC_1 during power step. 61
Figure 4.19 AC current and output power on each WT cluster during power step. 62
Figure 4.20 Voltage and current comparison during the WT disconnection. 63
Figure 5.1 Offshore wind farm equivalent circuit. 66
Figure 5.2 The circuit diagram of the PCC side grid connected with equivalent MMC. 67
Figure 5.3 State space model of PCC side grid. 69
Figure 5.4 Linearized MMC control block diagram. 71
Figure 5.5 Control structure of offshore MMC with PLL angle shift. 71

Figure 5.6 Frequency responses comparisons on SS model and TD model at PCC side. 73
Figure 5.7 Linearized control diagram on WT VSC. 76
Figure 5.8 The entire control structure of WT with PLL angle shift. 77
Figure 5.9 Frequency response comparisons between the SS model and TD model at WT side. 79
Figure 5.10 Reference frame transformation 80
Figure 5.11 SS model of the offshore wind farm system. 81
Figure 5.12 Comparisons of PCC voltage and frequency from TD and SS model during the power disturbance. 83
Figure 5.13 VSC_1 current and power responses comparisons during the power disturbance. 84
Figure 5.14 PCC voltage and frequency responses comparisons during voltage oscillation. 85
Figure 5.15 VSC_1 current and power responses comparisons during the voltage disturbance. 86
Figure 5.16 Bode plot of the frequency control loop. 87
Figure 5.17 The p/z map of PCC voltage with variable K_f. 88
Figure 5.18 Simulation waveforms of PCC frequency and voltage with variable K_f. 89
Figure 5.19 The p/z map of PCC voltage with variable f_v. 90
Figure 5.20 Simulation waveforms of PCC frequency and voltage when f_v increase from 15 Hz to 20 Hz 91
Figure 5.21 Zoomed-in p/z map of PCC voltage when f_v increases from 15 to 20. ... 92
Figure 5.22 Simulation waveforms of PCC frequency and voltage when f_v increase from 17 Hz to 18 Hz 93
Figure 5.23 The p/z map of PCC voltage with variable ζ_v. 94
Figure 5.24 The zoomed-in p/z map of voltage on PCC bus with variable ζ_v. 95
Figure 5.25 Simulation results on PCC frequency and voltage with ζ_v =0.8 and 0.9. 96
Figure 5.26 P/z map when voltage control parameter ζ_{vs} increases from 0.4 to 5. 97
Figure 5.27 The zoomed-in p/z map of voltage on PCC bus with variable ζ_{vs}. 98
Figure 5.28 Bode plots comparison from power to PCC voltage response in two systems. 99

Figure 6.1 Fault current injection control of offshore MMC station. 103
Figure 6.2 Fault current supply by WTs. 105
Figure 6.3 Mixed curves IDMT characteristic [121]. 106
Figure 6.4 Offshore wind farm structure with defined current and relays. 108
Figure 6.5 System relay characteristics. 110
Figure 6.6 Arm voltage of MMC, where the offshore station provides q-axis current to enable fault detection after an offshore AC fault at t=0.1 s. 116
Figure 6.7 Characteristics of the HVDC voltage dependent offshore AC voltage. . 117
Figure 6.8 Offshore wind farm connected with MMC-HVDC model. 118
Figure 6.9 Simulation waveforms of offshore MMC_1 during WT cluster fault. 121
Figure 6.10 Simulation waveforms of offshore WT cluster and string during WT cluster fault. 123
Figure 6.11 Simulation waveforms of HVDC link during WT cluster fault. 124
Figure 6.12 Simulation waveforms of offshore MMC_1 during WT string fault. 126
Figure 6.13 Simulation waveforms of offshore WT cluster and string during the fault occurs on the string cable. 127
Figure 6.14 Current through CB_{21} while WTs without fault current control. 128
Figure 6.15 Simulation waveforms of onshore MMC_2 during 100% voltage drop at onshore site. 130
Figure 6.16 Simulation waveforms of offshore MMC_1 during 100% voltage drop at onshore site. 131
Figure 6.17 Simulation waveforms of WT side during 100% voltage drop at onshore site. 132
Figure 6.18 Simulation waveforms of onshore MMC_2 during 50% voltage drop at onshore site. 134
Figure 6.19 Simulation waveforms of offshore MMC_1 during 50% voltage drop at onshore site. 135
Figure 6.20 Simulation waveforms of WT side during 50% voltage drop at onshore site. 136
Figure 6.21 Simulation waveforms of onshore MMC_2 during 20% voltage drop at onshore site. 137

Figure 6.22 Simulation waveforms of offshore MMC_1 during 20% voltage drop at onshore site. 138

List of Tables

Table 1.1 Global Renewable Energy Capacity [1]..... 1
Table 1.2 Comparative study between HVAC and HVDC transmission systems [9]. 5
Table 3.1 Switching status and output voltage of HBSM. 31
Table 3.2 Switching status of FBSM. 32
Table 3.3 Inserted SMs and the output voltage. 33
Table 4.1 Parameters of the MMC-HVDC system. 52
Table 4.2 Parameters of the lumped wind turbine models. 52
Table 5.1 Parameters on offshore wind farm PCC side. 72
Table 5.2 Parameters at offshore wind farm WT side. 78
Table 6.1 Offshore wind farm system parameters and relay setting. 109
Table 6.2 Relay tripping time with the WT cluster fault. 113
Table 6.3 Relay tripping time with the WT string fault. 114
Table 6.4 Parameters of the MMC-HVDC system. 118

Abbreviations

AC	Alternative Current
CB	Circuit breaker
CDSM	Clamp double half-bridge based sub-module
DBR	Dynamic braking resistors
DC	Direct Current
ECS	Energy capacitor system
FBSM	Full-bridge based sub-module
FRT	Fault ride-through
GSC	Grid side converter
HBSM	Half-bridge based sub-module
HVAC	High Voltage Alternative Current
HVDC	High Voltage Direct Current
IDMT	Inverse definite with minimum time lag relay
IGBT	Insulated Gate Bipolar Transistor
KCL	Kirchhoff's current law
KVL	Kirchhoff's voltage law
LCC	Line commuted converter
LPF	Low pass filter
MMC	Modular Multilevel Converter
NLM	Nearest level modulation
OWPP	Offshore wind power plant

P/z map	Pole/zero map
PCC	Point of common coupling
PI	Proportional–integral
PLL	Phase lock loop
PR	Proportional-resonant
PWM	Pulse Width Modulation
RMS	Root mean square
SM	Sub-module
SS	Small-signal
STATCOM	Static Synchronous Compensator
SVC	Static var compensator
TD	Time-domain
VSC	Voltage source converter
WFC	Wind farm side converter
WT	Wind turbine

Symbols

VSC and MMC modelling symbols

i_{comm}	MMC common mode current
i_j	Three-phase current
i_{SM}	MMC SM current
i_{ua}, i_{la}	MMC upper, lower arm current
K_p, K_i	Proportional and integral gain of PI controller
L	VSC converter reactor
L_{arm}	MMC arm inductance
L_{mmc}	MMC equivalent inductance
M	Modulation index
N	SM number at each arm
P, P^{-1}	*dq* transform parameter matrix
V_c	SM capacitor voltage
V_{dc}	DC voltage
v_g	Grid side AC voltage
v_j	Three-phase voltage
v_{mmc}	MMC equivalent vantage
v_s	Converter AC voltage
v_{SM}	MMC SM voltage
v_{uj}, v_{lj}	MMC upper, lower arm voltage
ζ	Damping value of PI parameter

θ	Phase angle
ω	System frequency (rotating speed)
ω_i	Natural frequency of current PI controller

Offshore wind farm symbols

C, C_c	Equivalent capacitance at PCC bus
C_{wt}	WT VSC capacitance
f	System frequency
f_c	Nature frequency of MMC current controller
f_{PLL}	Nature frequency of WT PLL controller
f_v	Nature frequency of MMC voltage controller
f_{wt}	Nature frequency of WT VSC current controller
i_1	Offshore MMC station AC current
i_2	WT collector bus current
i_{CB}	Circuit breaker current
i_{fs}	Fault current supplied my offshore MMC
i_{wt}	WT VSC current
i_{wtc}	WT cluster current
K	Droop control gain of MMC frequency control
K_{fp}, K_{fi}	Proportional and integral gain of MMC frequency PI controller
K_{ip}, K_{ii}	Proportional and integral gain of MMC current PI controller
K_{PLLp}, K_{PLLi}	Proportional and integral gain of WT PLL controller
K_{vp}, K_{vi}	Proportional and integral gain of MMC voltage PI controller
K_{wtp}, K_{wti}	Proportional and integral gain of WT current PI controller

L_{trans}, R_{trans}	Inductance and resistance of offshore MMC transformer
L_{wt}	WT VSC inductance
n_1	Offshore MMC transformer ratio
n_2	WT cluster transformer ratio
P_{MMC1}, Q_{MMC1}	Real and reactive power at offshore MMC station
P_{VSC}, Q_{VSC}	Real and reactive power of offshore VSC
t_{CB}	Operation time of relay
t_s	Safety margin duration
t_{trip}	Tripping time of relay
v_c	Offshore MMC generating AC voltage
v_{pcc}	Voltage at PCC bus
V_{thu}, V_{thl}	DC voltage upper and lower threshold
v_{wt}	WTs connection point voltage
v_{wtc}	WT collector bus voltage

Onshore grid symbols

i_{MMC2}	Onshore MMC AC current
P_{MMC2}, Q_{MMC2}	Real and reactive power at onshore MMC station
v_{grid}	Onshore grid voltage

Chapter 1

Introduction

1.1. Growth of renewable energy

The high carbon emission caused by large fossil energy consumption has resulted in significant environmental problems such as climate change, air pollution, etc. The increased focus is now moving to the use of renewable energy and from the Renewables 2019 Global Status Report [1], renewable energy has seen huge growth with the advancement in enabling technologies, reduced costs, and increased investment. The total installed renewable power capacity (including hydropower) was around 2378 Gigawatts (GW) worldwide and the added capacity was around 8% during 2018. Wind power occupies the most among the existing non-hydropower renewables as listed in Table 1.1.

Table 1.1 Global Renewable Energy Capacity [1].

Power Capacity (GW)	**Added during 2018**	**Total at End-2018**
Bio-Power	8.8	130
Geothermal power	0.5	13.3
Hydropower	20	1,132
Ocean power	0	0.5
Solar PV	100	505
Concentrating solar thermal power (CSP)	0.6	5.5
Wind power	51	591

The huge growth of renewable power generation is driven by the increased power demand for clean energy and continuous cost reduction especially for wind power [2]. By the end of 2018, wind turbines installed worldwide were able to supply more than 5% of the global electricity demand. Denmark leads the way, and its wind power shares 43% of the total power supply, which is then followed by Germany, Ireland, Portugal, Spain [3]. With the data published by the World Wind Energy Association [4], the global wind energy installed capacity can be described as shown in Figure 1.1. By the end of 2018, China and US had the largest installation shares of 36% and 16%, respectively. 100% of the electricity generated by renewable sources is being considered by the European Union and its member states [3].

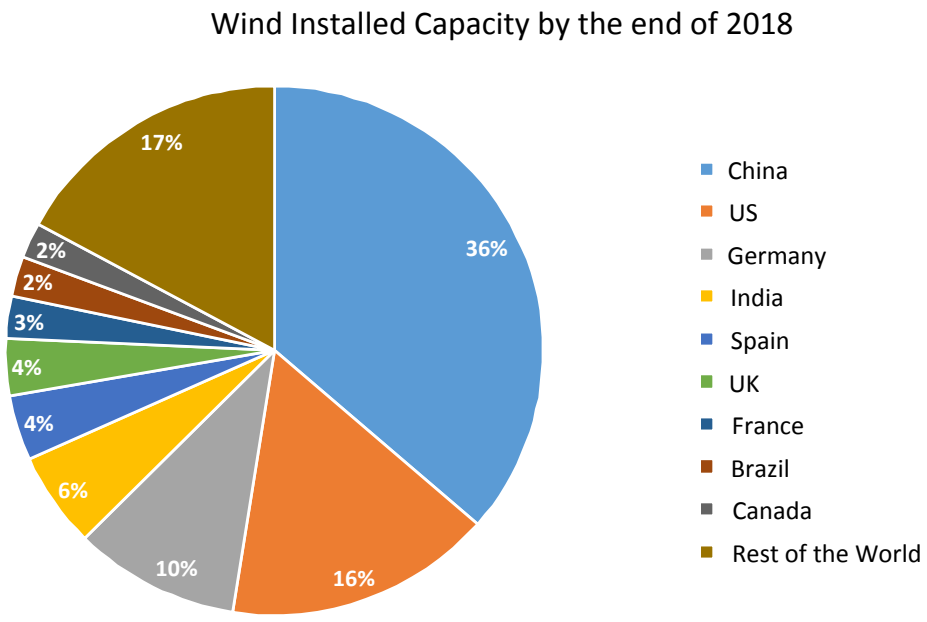

Figure 1.1 Continental shares in new capacity (%).

Due to various limitations related to onshore wind farm development, moving wind farms offshore provides significant benefits and offshore wind power technologies have been evolving with many innovations. Although the capital cost of offshore wind farms is still higher than that of onshore wind farms, the gap is reducing and can also be offset by higher capacity factors due to better wind resource and less turbulence.

Offshore wind energy has been identified as a key power generation technology for renewable energy in the future. Currently, Europe leads the world in the development of offshore wind power. According to the reports from Global Wind Energy Council (GWEC) and International Renewable Energy Agency [5, 6], the global cumulative offshore wind power installed capacity has reached 23 GW with an addition of 4.43 GW in 2018, as shown in Figure 1.2. As seen, UK led the offshore wind farm development with an accumulated capacity of more than 8 GW by the end of 2018.

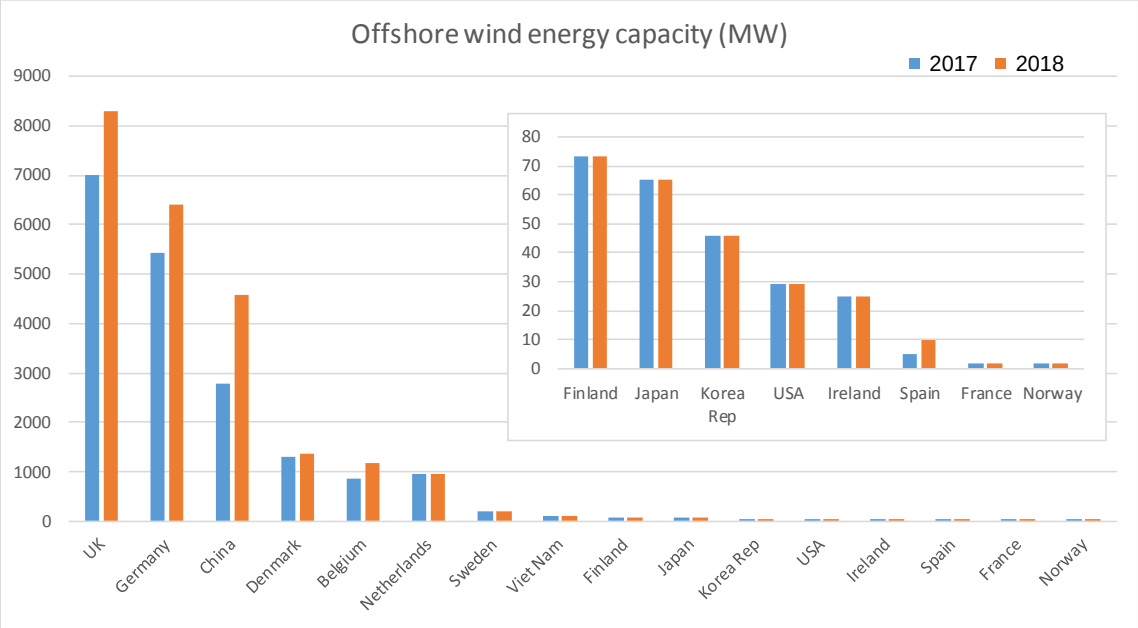

Figure 1.2 Global cumulative offshore wind capacity in 2017 and 2018.

Although the potential of offshore wind energy is vast, many key techniques still need further research and development, such as system optimization, resource estimation, electric transmission and grid connection.

1.2. Comparison of HVDC and HVAC power transmission systems

Due to the rapid expansion of offshore wind farms, the electrical connection system between wind farm and onshore power grid becomes one of the main challenges. When

connecting an offshore wind farm, the traditional AC transmission system may not meet the requirements if the connection distance is long, due to the high cable capacitive charging current resulting in high power loss and need for reactive power compensation. Thus, high voltage DC (HVDC) transmission might become the only viable option for long-distance offshore wind farm integration.

References [7] and [8] compare the costs on high voltage AC (HVAC) and HVDC transmission system for offshore wind farm connecting. As shown in Figure 1.3, the total cost for the HVDC transmission system is lower than the HVAC system when the distance is over the breakeven distance.

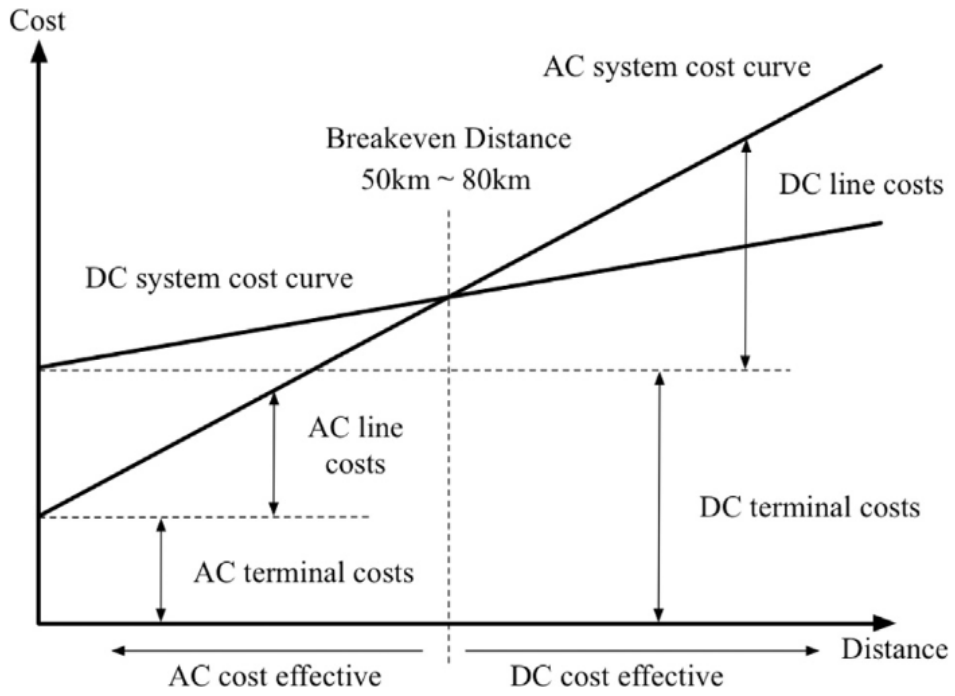

Figure 1.3 Cost comparison of HVDC and HVAC transmission systems [7].

In addition, HVDC system enables full control of power flow which makes this technique more attractive. The overall comparison of the characteristics of the HVAC and HVDC systems for offshore wind farm integration are summarized in Table 1.2 [9].

Table 1.2 Comparative study between HVAC and HVDC transmission systems [9].

	HVAC	**HVDC**
Overall Losses	High losses • skin effect • dielectric loss • line charging current	Low losses • No reactive loss • less I^2R loss
Cost of transmission	Economical for short distance but high cost for long distance	High cost for short distance but low cost for long distance
Cost of Equipment	Low	High (due to high converters cost)
Power flow Control	Power flow cannot be controlled	Full control of power flow
Maximum transmitted power and distance	Distance dependent	Largely independent on distance

1.3. HVDC transmission systems

As described, compared to HVAC system, HVDC is more attractive when long-distance and complex interconnections are required. There are two main HVDC technologies, i.e. line commuted converter based HVDC (LCC-HVDC) using thyristors and voltage source converter based HVDC (VSC-HVDC) using IGBTs (Insulated Gate Bipolar Transistor). LCC-HVDC requires external circuits for commutation whereas VSC-HVDC uses self-commutated converters [10].

1.3.1. LCC-HVDC

LCC-HVDC is a mature technology commonly used for large power transmission over a long distance. Compared to VSC-HVDC, LCC-HVDC is suitable for transmitting very large power using ultra-high voltage transmission due to its relatively lower losses,

lower cost, higher reliability and overload capability, and minimal maintenance [11]. The configuration of LCC-HVDC connecting two AC grids is shown in Figure 1.4.

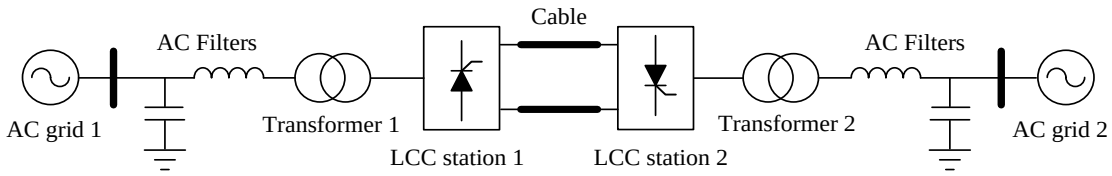

Figure 1.4 LCC-HVDC connecting two AC grids.

However, LCC requires an external commutation voltage supplied by, e.g., synchronous compensator [12] or STATCOM (Static Synchronous Compensator) [13]. It should be noticed that the current direction at DC side of LCC cannot be changed. Consequently, the change of power direction needs to be realized by changing the polarity of the DC voltage which can be cumbersome in practical systems.

The critical disadvantages related to LCC-HVDC are listed below:

- Lack of independent control on real and reactive power.
- A strong AC network is required for normal operation and the risk of commutation failure exists during network disturbances.
- Large site area required due to the need for large AC filters.

1.3.2. VSC-HVDC

VSC-HVDC overcomes many limitations of LCC-HVDC system. Compared with LCC-HVDC, no external AC source for commutation is required by VSC-HVDC systems, and it can create its own voltage in case of black-start [14]. These features make VSC-HVDC more attractive when used for connecting offshore wind farms. The recently developed modular multilevel converter (MMC), a converter topology used for VSC based HVDC systems, has solved many challenges associated with VSC-HVDC systems. The distinctive characteristics of VSC-HVDC are listed as follows [15] whereas Figure 1.5 shows a simplified VSC-HVDC configuration when connecting two AC grids.

- Full control of real and reactive power can be achieved without external voltage source.
- No requirement of reactive power compensations and reduced filter (or no filter) requirement, leading to a compact design and installation (especially important for offshore installation).
- Can restore an offshore wind farm without relying on the external electric power transmission network (black start capability) [16].

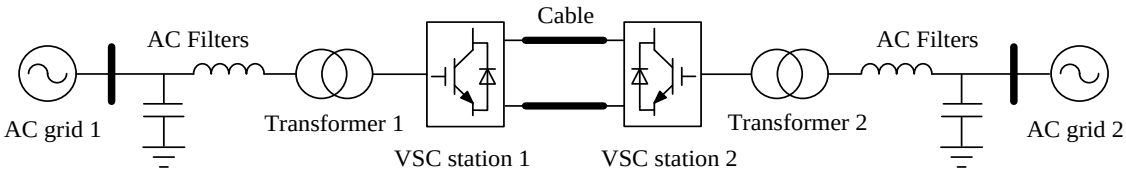

Figure 1.5 VSC-HVDC connecting two AC grids.

1.4. Challenges of MMC-HVDC system for connecting offshore wind farm

The connection systems for offshore wind farm must have very high reliability due to the long repair time and high maintenance cost. To ensure safe operation and power transmission, adequate system control during normal operation and fault conditions is necessary.

For HVDC connected offshore wind farms, the offshore network is formed by the HVDC converter and wind turbine converters. Such offshore AC grid with no rotating machine shows a different characteristic compared with onshore grids. Consequently, distinctive controls of the HVDC converters have to be adopted, e.g. frequency control, DC voltage control, offshore AC voltage control and power control. The control schemes for converters which apply at island network has been introduced in [17]. For offshore AC grid, the varying wind power and high cable capacitance may cause voltage instability and

harmonic resonance. Thus, a stable AC voltage and frequency control at the offshore system is required [18].

System behavior and response during fault conditions need to be addressed. During various faults, e.g. onshore AC fault, DC fault, offshore AC fault, the offshore system needs to be properly protected and remains optional if possible.

For offshore AC fault, large fault currents could potentially cause damage to the offshore systems and thus, the offshore converter must ensure fast response in manipulating the fault current of offshore system. Consequently, the main requirements for the offshore converters are controlling and limiting the fault current within the safety range, whilst contribute to a more rapid system recovery [19] and facilitate the operation of protecting devices.

The behaviour of an offshore wind farm system during an onshore AC voltage drop is another important aspect which needs to be researched. To ensure onshore grid stability, the large wind farm usually is not allowed to be disconnected during such onshore voltage dip and meanwhile the transmitted power is limited. Therefore, a well-coordinated control on the HVDC converter and offshore wind farm needs to be considered, and the wind farm system stays connected during onshore AC faults whilst any overvoltage on HVDC link is avoided.

1.5. Motivation and contributions

The research work will focus on the use of MMC-based VSC-HVDC systems for connecting large offshore wind farms. Coordinated control of the wind farms and HVDC converters to ensure adequate system stability and dynamic response are investigated. Transient behavior during offshore and onshore AC network faults are studied and the corresponding control during fault conditions is proposed to ensure fast system recovery.

The main contributions of this thesis are:

- Proposing an enhanced AC voltage and frequency control of offshore MMC station for wind farm connection. The proposed control improves the voltage performance of the offshore network and enables better dynamic response of the offshore wind farm system. The stability of the proposed scheme and selection of control parameters are investigated using developed small-signal models.
- A fault current injection control is proposed to ride-through offshore AC faults and to provide adequate fault current for protection equipment.
- To ride-through onshore AC faults, a DC voltage dependent offshore AC voltage control method is proposed to ensure that the wind power is automatically reduced when the onshore AC voltage drops to enable power balance and reduce DC overvoltage.

1.6. Organization of thesis

The thesis is organized into seven chapters as follow:

Chapter 2: Review of HVDC transmission system connected with offshore wind farms.

The research on HVDC connected offshore wind farm system is reviewed, including HVDC transmission system configurations, control of VSC-HVDC transmission system and system fault-ride-through (FRT).

Chapter 3: Fundamentals of converter modelling and control.

In Chapter 3, the principle of VSC-HVDC system is studied and the basic controls are overviewed. The structure, modelling and basic control of MMC including voltage balancing and circulating current control are introduced.

Chapter 4: Control of the offshore wind farm system.

An enhanced AC voltage and frequency control of offshore MMC station for wind farm connection is proposed in this chapter. An additional frequency control loop is added

to the offshore MMC control to improve the dynamic response of the offshore wind farm system. Comparisons between the proposed control and conventional control are presented during start-up and power step changes.

Chapter 5: Small-signal modelling and analysis of offshore AC system.

To investigate system stability with the proposed enhanced AC voltage and frequency control, a small-signal model of offshore wind farm system is developed. With the small-signal state space model, the stabilities of offshore wind farm voltage and frequency are analysed. Furthermore, by using the pole/zero map, the ranges of parameters are investigated.

Chapter 6: Fault analyses of MMC-HVDC system connecting offshore wind farm.

In the event of offshore AC faults, offshore MMC and wind turbines should remain connected with the controlled current. In the meantime, adequate fault currents should be provided to the offshore network to enable fault detection and isolation. A fault current injection control is proposed in this chapter to facilitate offshore AC fault over-current protection and fast system recovery. During onshore grid fault, a DC voltage dependent offshore AC voltage control is introduced to ensure balanced transmission power of the HVDC line. Simulation results are presented to demonstrate the performance of the wind farm system with the proposed control methods.

Chapter 7: Conclusions

Chapter 7 draws the conclusions of the researches and outlines the contributions of this thesis. Further work is also recommended.

Chapter 2

Review on HVDC transmission system connecting offshore wind farms

2.1. Introduction

As discussed in Chapter 1, VSC-HVDC transmission system is the most suitable technology to connect large-scale offshore wind farms over long-distance. Many researches have been carried out on the control and operation of the HVDC system and offshore wind turbines. This chapter focuses on the VSC-HVDC system connected with offshore wind farms and reviews the general configurations of the transmission system, control of the HVDC converters and the fault ride-through (FRT) capability of the offshore wind farm systems.

2.2. Offshore transmission system configuration

For a large offshore wind farm, VSC-HVDC transmission system structures can be designed as a point-to-point HVDC transmission system, parallel HVDC links connected to the offshore wind farm AC system and multi-terminal HVDC (MTDC) transmission system depending on different situations [20]. Compared to the simplest and the most commonly used point-to-point links, the parallel and MTDC configurations increase power transmission capability and system availability but have more complex configurations and high requirements on control. In addition, the selection of offshore HVDC configurations should consider the economic assessment, and regulatory and geographical limitations [21]. Figure 2.1 shows the three mentioned configurations of HVDC system connected offshore wind power plants (OWPP).

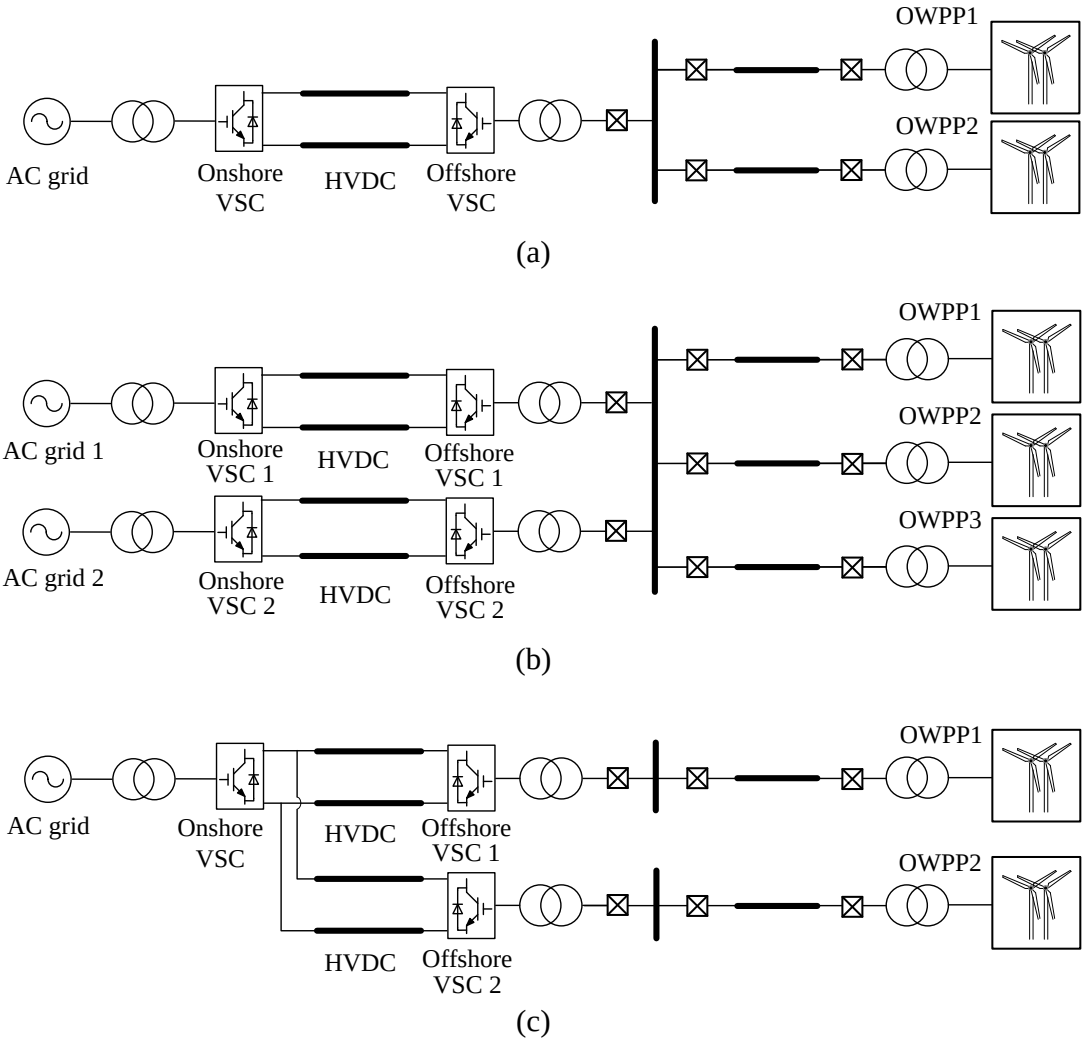

Figure 2.1 OWPP connected through offshore HVDC links.
(a) Point-to-point HVDC connection, (b) parallel HVDC connection, (c) multi-terminal HVDC connection.

2.2.1. Point-to-point HVDC transmission system

The point-to-point HVDC system has the simplest structure, and the VSC-HVDC system can well control the offshore network during AC system disturbances and variation of wind power. Moreover, the VSC-HVDC has black start capability which is a critical requirement at offshore WPP sites. In the case of DC faults, converters at both terminals of the HVDC link can isolate the DC link through AC side breakers to help the fault

clearance, and thus, no DC breakers are necessary [7, 22]. However, the most serious challenge of point-to-point HVDC system is that the entire offshore power would be lost during the outage of the HVDC link.

2.2.2. Parallel HVDC transmission system

As shown in Figure 2.1 (b), all the OWPP are connected to the offshore AC collector and then deliver their power to the onshore site through two parallel HVDC links. With such configuration, the availability of the HVDC system can be improved significantly, as the wind power can be exported through the other route during faults on one HVDC link (converters or cables) [23]. Active power flow through the two parallel links need to be controlled to allow certain power sharing. Similar to the point-to-point configuration, it also allows the breakers at AC sides to isolate DC faults.

2.2.3. Multi-terminal HVDC transmission system

Considering system reliability, power supply security, operational flexibility and maintenance strategies, multi-terminal HVDC configurations were introduced [24-27]. With the increasing number of operating point-to-point HVDC links in close range, the availability could be enhanced, and the total costs decreased by interconnecting them together to form MTDC systems [28]. Studies have shown that multi-terminal HVDC links improve power exchange flexibility between multiple areas and provide better system redundancy [29, 30]. Also, coordinated converter controls such as voltage droop control which is able to provide robust performances with power-sharing, improves system transient stability and ensures safe operation of the system [31, 32].

However, the feasibility of the multi-terminal VSC-HVDC link is limited by the lack of mature HVDC breakers and associated DC protection systems [22, 33], and the total cost may even higher than equivalent AC systems due to the DC breakers [34]. To overcome the DC fault issues, the protection of large HVDC systems is under extensive research [33]. Converters with fault blocking capability have also been considered, though the main drawback of these converters is their relatively higher cost and power loss [35].

2.3. Control of HVDC systems connected with offshore wind farm

VSC-HVDC connected to an offshore wind farm system transmits wind power to the onshore grid and provide AC voltage control to the offshore AC grid. Usually, the onshore grid side converter of the HVDC system controls the DC voltage of the HVDC link and transfers the received active power to the onshore grid. For the offshore wind farm side converter, it forms the voltage and frequency of the offshore AC grid, as shown in Figure 2.2.

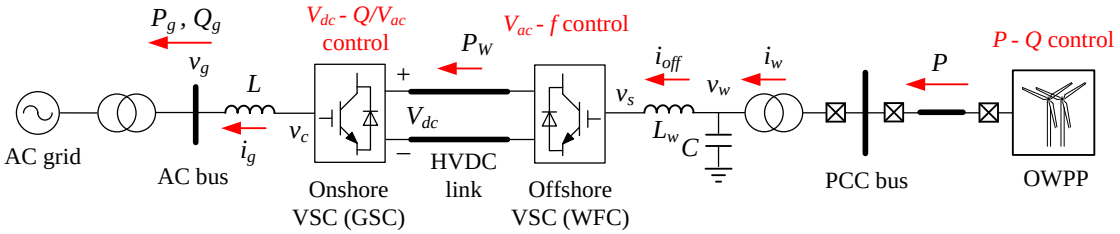

Figure 2.2 General control scheme of VSC-HVDC connected offshore wind farm.

2.3.1. Control of offshore wind farm side converter

The offshore wind farm side HVDC converter (WFC) is required to build up the offshore AC grid and controls the AC voltage and frequency. The frequency can be directly fixed and the phase angle θ is derived using the fixed frequency. Thus, PLL is not required for the WFC. Two main control designs have been proposed for the WFC:

- Voltage amplitude-angle control generates the AC voltage by simply using the AC reference amplitude V^*_w and fixed frequency ω_w without *dq* transform [36], as schematically shown in Figure 2.3. This control does not include current loops and thus, the converter may experience overcurrent during large transients [37].

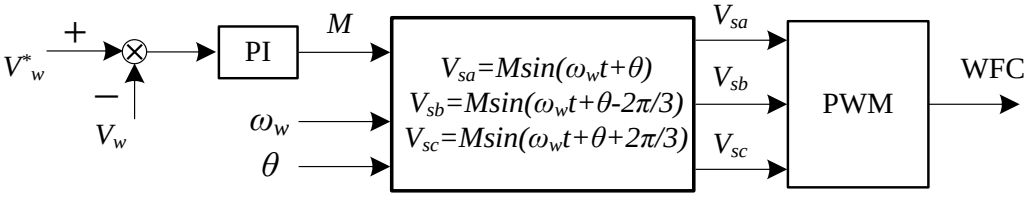

Figure 2.3 Amplitude-angle voltage control scheme [38].

- Nested vector control with fast inner current loop and outer voltage loop is able to limit the overcurrent during large transients [39, 40]. This control is the most common approach where *d*-axis PCC (point of common coupling) voltage reference is set at the desired voltage value and the *q*-axis voltage reference is always set at 0, as shown in Figure 2.4. The current and voltage symbols are defined in Figure 2.2.

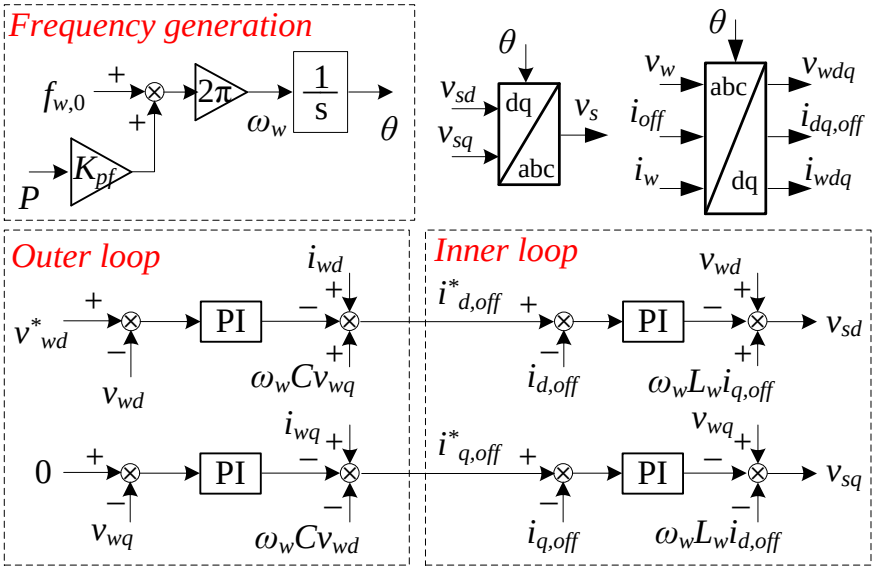

Figure 2.4 Nested vector control scheme.

Although the nested vector control has a more complex design than the other one, it provides current control capability [41, 42]. Due to high wind generation variation, HVDC connected offshore wind farm network may pose difficulties such as harmonic resonance and voltage instability [43]. Various control strategies have been proposed to enhance the offshore AC network stability and improve power transmission efficiency. Reference [44] and [45] study the power-synchronization control, in which the offshore grid frequency is dependent on the active power, as shown in Figure 2.4, where K_{pf} is a non-zero droop gain. However, for the offshore network, system instabilities and grid resonances have not been well understood, especially the interactions among the HVDC and WT converters are requiring further investigation.

2.3.2. Control of onshore grid side converter

As described, for MMC-HVDC system connected with an offshore wind farm, the onshore MMC station usually controls the DC link voltage to ensure balancing of the imported and exported power of the HVDC link. The most common control strategy applied at the grid side converter (GSC) is vector control where the *d*-axis current regulates the DC voltage or active power and the *q*-axis current is used to control the AC voltage or reactive power, as shown in Figure 2.5. The PLL is used to track the AC voltage phase angle and frequency of the onshore grid.

For point-to-point HVDC configuration, as long as the injected power of the GSC is within its power limit, the GSC normally operates in V_{dc}-Q (AC voltage, shown in Figure 2.5) control mode. In the event when the GSC reaches its power/current limits, GSC might transfer to power limit or current limit mode. For a MTDC configuration in which several GSCs are connected to the DC link, the GSCs need to be coordinated to prevent conflict in DC voltage control [46]. In normal practice, one GSC controls the DC voltage while the others either directly regulate active power injected to the AC grid or utilize DC voltage-power droop control [47, 48], shown in Figure 2.5.

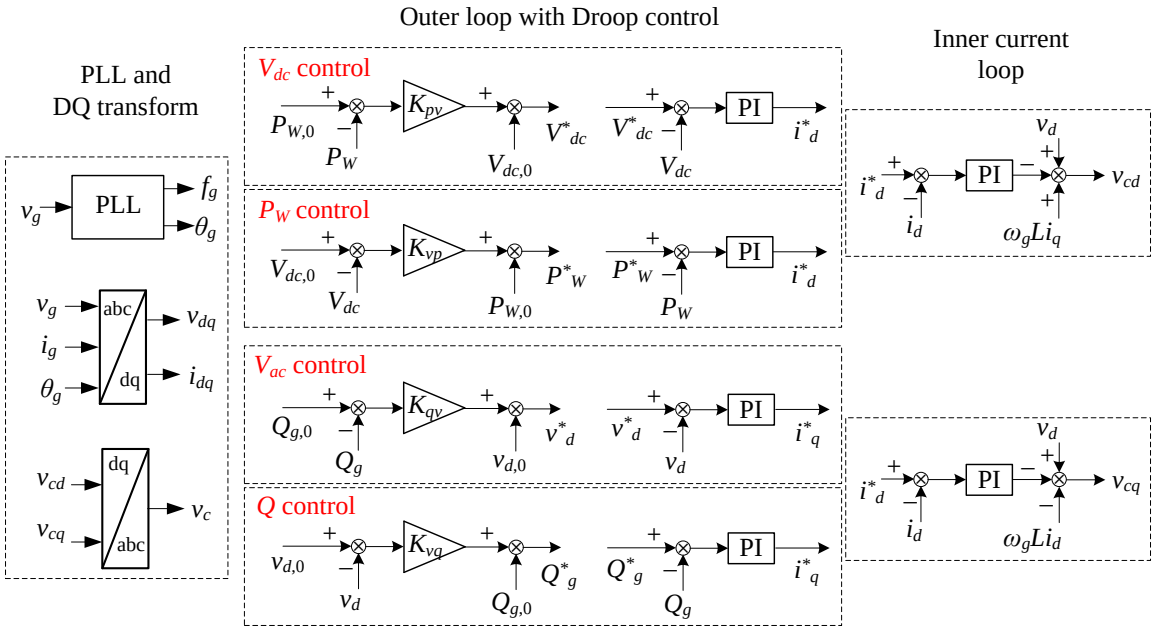

Figure 2.5 GSC control scheme.

2.4. Review on fault ride-through of offshore wind farms

To ensure the safety of the equipment, the operation, also protection of the HVDC at offshore and onshore AC networks in the event of a network fault, the system must be designed and controlled to cope with such fast transients. Various faults including offshore and onshore AC faults, DC fault need to be considered.

During an offshore AC fault, both the offshore wind turbines and offshore MMC must be able to ride-through fault and ensure fast post-fault recovery. Minimizing the overcurrent, overvoltage and thermal stress which could happen to WTs and MMC should all be considered.

In the event of an onshore AC grid fault, the onshore voltage dip during the fault can impact on the DC link voltage and thus the operation of the HVDC link. In particular, the power transmission capability of the onshore MMC is reduced and the imbalanced power transmission between the onshore and offshore sites could lead to rapid rise of the DC voltage at the HVDC link. This must be dealt with otherwise the entire system may have to be disconnected [49].

This section reviews the control and operation of WTs and MMC-HVDC system during faults. DC fault at HVDC link which is another serious system condition is also briefly reviewed although it is not studied in this thesis.

2.4.1. Offshore AC fault ride-through operation

The rapid drop of AC voltage on the PCC bus during an offshore fault could potentially lead to overcurrent in the offshore MMC [50] . Therefore, current limitation control is required on offshore MMC. To limit the fault currents and avoid damage of offshore MMC station, three-phase currents are measured in [51] to adjust the voltage control loop reference as illustrated in Figure 2.6, where f_0 is the fixed frequency (usually 50 Hz). If the currents are out of the predefined range, the offshore voltage is reduced accordingly in order to decrease the MMC output currents.

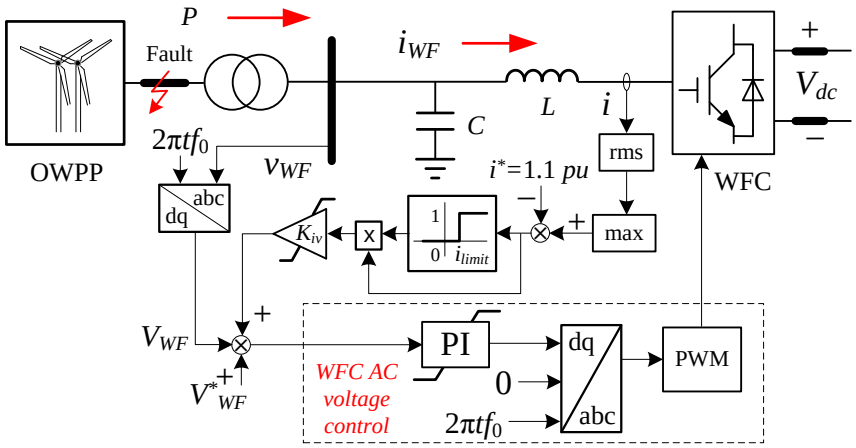

Figure 2.6 Current limitation control at WFC.

Reference [51] also introduces a short-circuit protection scheme for offshore AC grid during offshore AC faults. However, it does not consider the requirements for the operation of the protection relays, and it takes a long time to recover power transmission after fault clearance. Reference [52] proposes a coordinated voltage control scheme which enables the offshore VSCs to provide fault currents after offshore AC fault to support the offshore grid, shown in Figure 2.7. However, the fault current is large during the fault condition (due to the exist of i_d and i_q) which indicates large capacity overcurrent relay is necessary and fast communication is also required between the offshore MMC stations and WT converters.

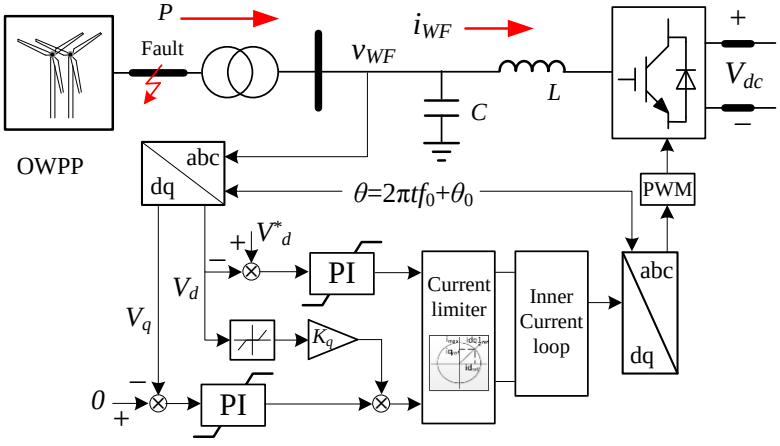

Figure 2.7 AC voltage control with reactive current providing on WFC.

To provide fast current limiting during offshore AC faults, the inner current loop is applied [53] and a decoupled current controller which is bypassed during normal operation is further introduced in [18, 53-56]. Once the currents are out of the predefined threshold, the current controllers are trigged to limit the output currents and the offshore MMC is switched to current control mode as shown in Figure 2.8. After fault clearance, MMC is switched back to voltage control mode. However, the switching between voltage and current control modes can potentially lead to transient overcurrent.

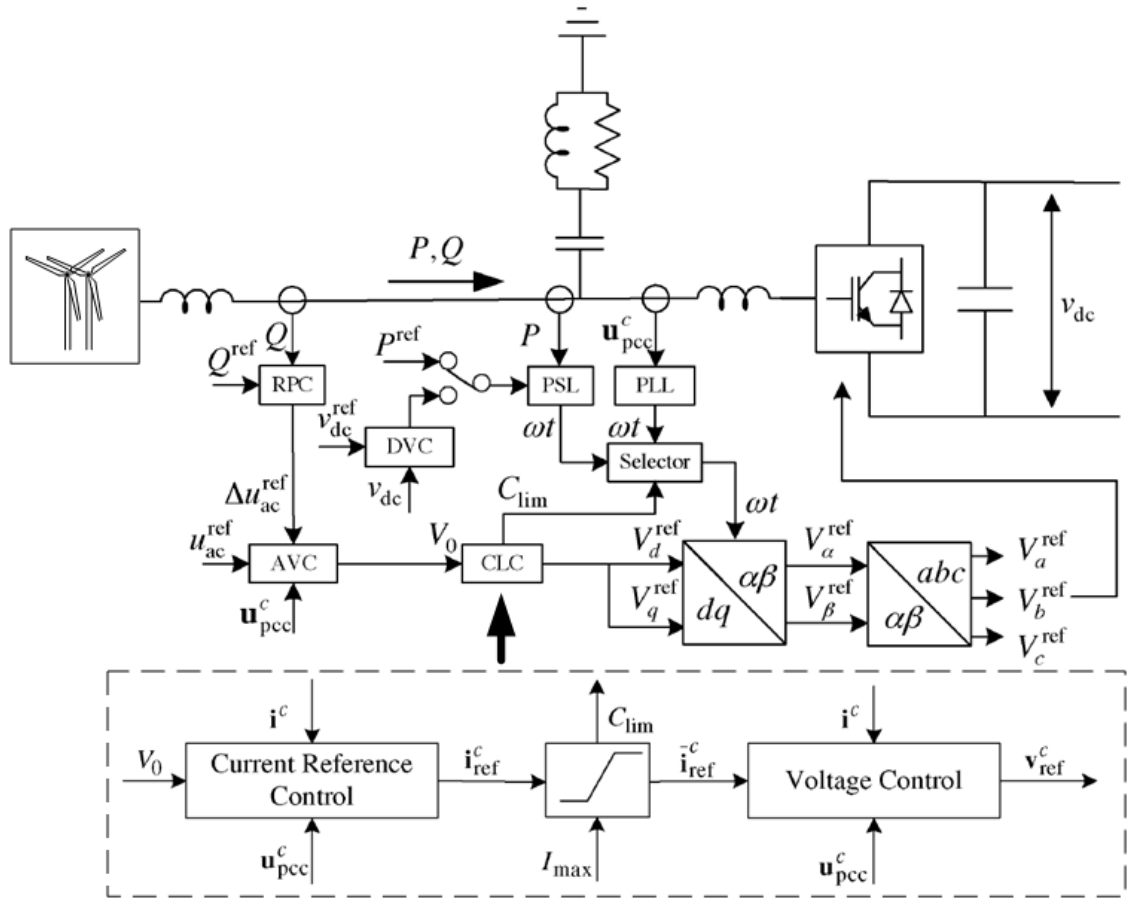

Figure 2.8 Power-synchronization control of VSC [53].

2.4.2. Onshore AC fault ride-through operation

During onshore AC network faults, the power transmission capability of the GSC is likely to be severely reduced. The continuous power output from the wind farms (WF) to the HVDC link leads to power imbalance in the DC link and rapid DC voltage increase of

the HVDC transmission system. To avoid damage to the HVDC link, the excess power has to be dissipated or the power transmitted from WF needs to be reduced.

The simplest way to de-load the excess power during onshore faults to avoid DC overvoltage is using DC choppers or dynamic braking resistors (DBR) at HVDC link [42, 57, 58] as shown in Figure 2.9 (a). The DBR can be configured in different ways as shown in Figure 2.9 (b), and with PWM control of the switches, the power dissipated can be regulated. DBR circuit is reliable which can ensure the safe operation of the system and the offshore wind farm is not disturbed during the onshore AC faults. However, they increase investment costs.

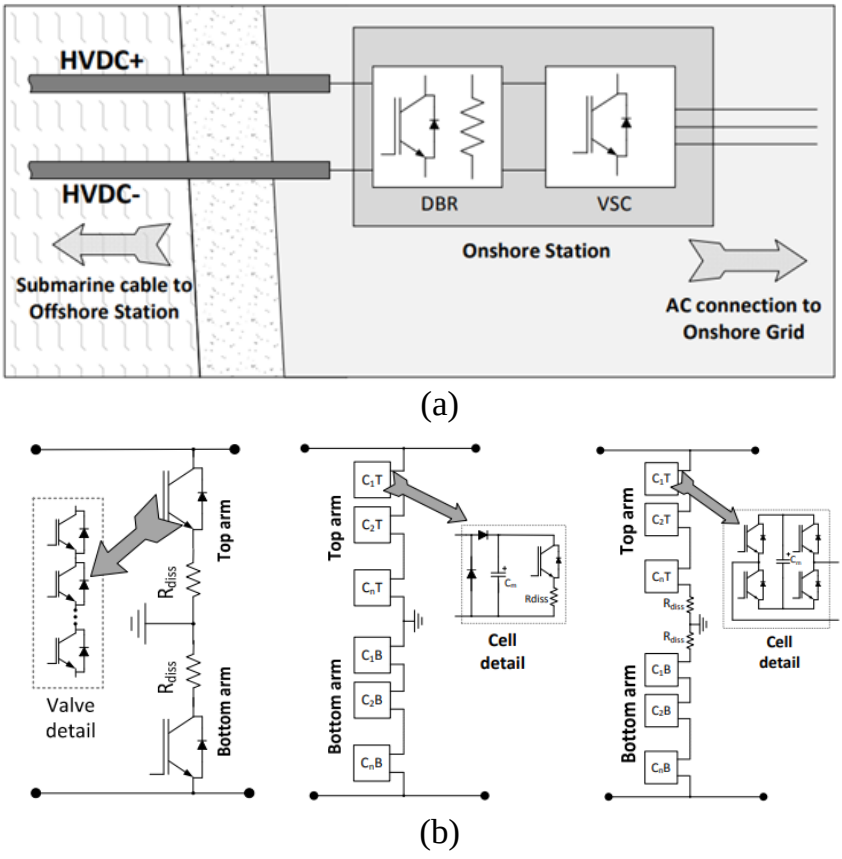

Figure 2.9 VSC-HVDC system with DBR [57].

System control based on communication is employed in [59-61] and the layout is shown in Figure 2.10. Wind turbines reduce their output power after receiving the signals

from the offshore MMC through fast speed communication. The main drawback thus is the need of communication, and with this method, communication delays and reliability directly influence the system performance.

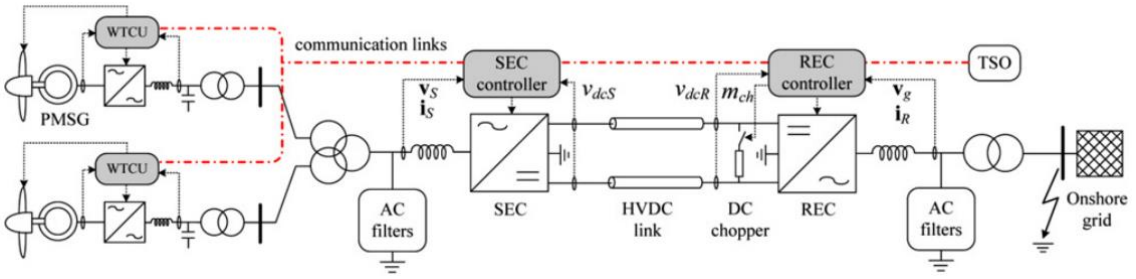

Figure 2.10 Communication layout of VSC-HVDC connecting offshore wind farm [59].

Reference [62] proposes an offshore AC voltage limiting method. The offshore AC voltage limit is reduced linearly according to the exceeded DC voltage, and then a method of de-loading which rapidly reduces the generator torque is used at every WT. The control diagram is shown in Figure 2.11. However, with this method the current is uncontrollable, and simply setting on the upper limit of the PI controller may influence the system dynamic response and cause oscillations in the system.

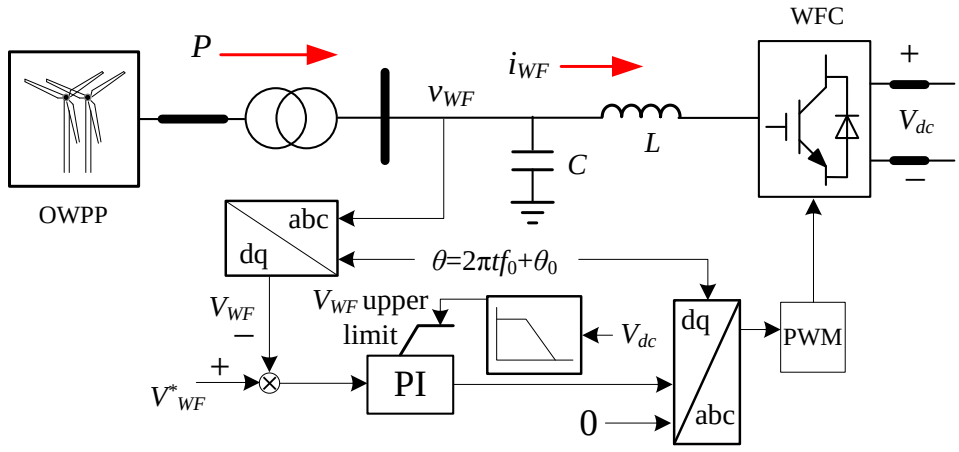

Figure 2.11 Offshore AC voltage limiting control for FRT at WFC.

In [38], once the fault occurs at the onshore AC system and the increase of the DC voltage is detected by the WFC, the WFC regulates the frequency rise of the offshore AC

system. When the wind turbines detect the increased frequency, the output power is reduced accordingly. However, the frequency response is slow, and the wind turbines have to adopt special designs.

2.4.3. DC fault right-through operation

MMC based on half-bridge (HB) sub-module (SM) is the most commonly used in HVDC system. When a fault occurs on the DC side, all the submodules are blocked, and the SM capacitances are bypassed. However, the freewheeling diodes are still connected in the circuit, and the blocked MMC acts as an uncontrolled rectifier feeding fault current from AC to the DC fault points [63].

Using MMCs with SMs which are able to block DC faults, e.g. full-bridge (FB) SMs, is a potential method to tackle DC faults. Reference [64] investigates the DC FRT capability of a hybrid MMC combining HB and FB SMs, which can also block the DC fault while reducing cost and power loss compared to FB MMC. However, FB SMs result in higher power loss and higher cost compared to HB SMs.

The method to isolate the DC fault in [65] is to disconnect the entire wind farm network when a fault occurs on the DC link to de-energize the DC link and then uses DC disconnectors to clear the DC fault. The drawback of this approach is slow recovery and long-time loss of large power generation. The slow recovery could also lead to the disconnection of offshore WTs due to the blocked offshore MMC station and lost control of offshore AC voltage and frequency.

The most direct way to isolate the DC fault is to use DC circuit breakers (DCCB) though they are not yet commercially available [65]. Because of the challenge on the high requirements on operation speed, size and cost, further research and development on HVDC circuit breakers are required. In [66], a solid-state DC breaker is investigated for HVDC system though the high power loss during normal operation prohibits it from practical use. With further development in DC breakers technology such as hybrid DCCB [67, 68], fast fault isolation in HVDC systems can be achieved, and leading to reduced disturbance to the connected offshore wind farm and onshore networks.

2.5. Summary

This chapter mainly reviews HVDC connected offshore wind farm configurations, control of HVDC transmission system and FRT requirement of offshore wind farms. To ensure stable offshore AC voltage and frequency, various offshore HVDC converter controls have been developed. The existing control methods use open-loop fixed frequency for generating offshore AC voltage which can lead to slow system response and recovery after large transients, and thus further investigation is required. To ensure safe operation of the HVDC scheme and offshore wind farm, adequate protection and operation during various faults, e.g. onshore and offshore AC faults must be incorporated. The existing work related to offshore AC faults largely concentrates on providing certain fault current without considering the needs and characteristics for protection relays. Significant further investigations are required to tackle the control and operation of such systems during various faults conditions.

Chapter 3

Fundamentals of converter modelling and control

3.1. Introduction

As mentioned in the previous chapters, HVDC connection is an economical solution for integrating long distance offshore wind farms when compared with AC transmission. Modular multilevel converter (MMC) has been developed recently and is now the converter topology used for VSC based HVDC systems due to its advantages of modular design, flexible control and configuration, low power loss and good waveform quality [69-72]. Therefore, MMC based HVDC system is considered in the work of this thesis.

For the offshore wind farm studied in this thesis, variable speed WTs with full sized back-to-back converters are considered. As the focus of the study is on the offshore AC network, only the grid side WT characteristics are included and thus all the WTs are presented as simplified VSCs with the DC side voltage fixed.

In this chapter, the modelling of WT VSC and the MMC used in HVDC system is introduced in detail, and their basic controls are discussed.

3.2. WT grid side VSC

VSC can synthesize an AC voltage from a DC supply voltage by controlling the duty cycle of the power devices, and in this study, the WTs grid side VSCs are aggregated into different sizes to presents the different capacities of WTs.

3.2.1. VSC principles

The basic structure of a two-level VSC is shown in Figure 3.1. As illustrated, by switching the IGBTs on and off in each phase of the VSC, the voltage on each phase can present positive or negative value, and thus, the output voltage of VSC can be controlled. To avoid the short circuit at each phase, the IGBTs of the upper and lower arm at each phase must not be turned on simultaneously.

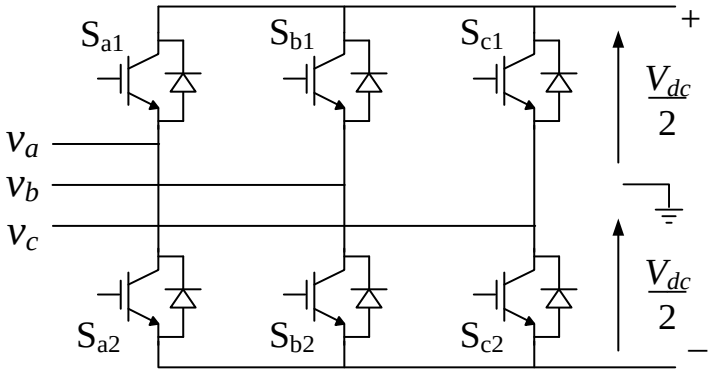

Figure 3.1 Two level VSC structure.

To synthesize a smooth output AC waveform and reduce the harmonic contents, the sinusoidal Pulse Width Modulation (PWM) strategy is applied to control the converter states as schematically shown in Figure 3.2.

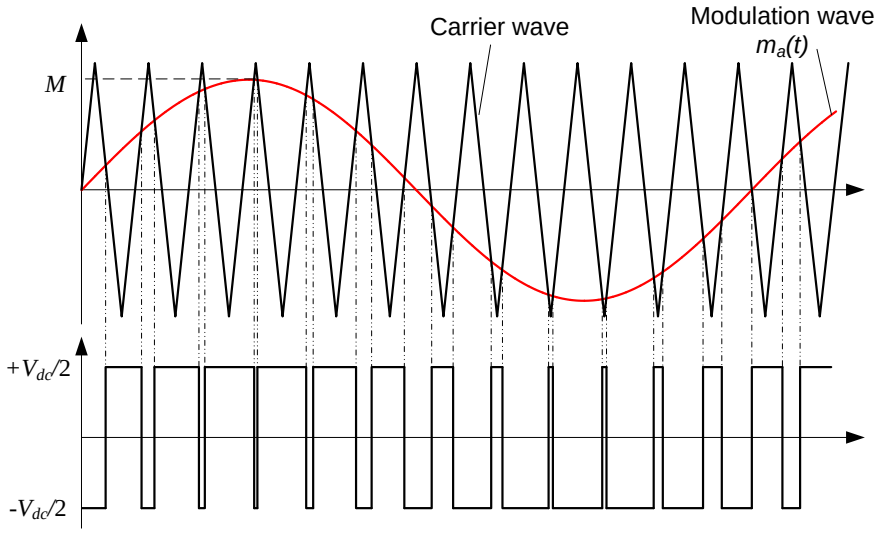

Figure 3.2 Sinusoidal pulse width modulation.

During the process, the reference sinusoidal signal (modulation waveform) is compared with a periodical triangular waveform (carrier wave) at the required IGBT switching frequency. In regular operation, the IGBT at the upper arm switches on when the reference exceeds the carrier and vice versa.

As seen in Figure 3.2, the modulation function m_a is applied in the PWM method to control the output fundamental frequency voltage v_a of the VSC with the following relationship:

$$v_a(t) = \frac{V_{dc}}{2} m_a(t) = \frac{V_{dc}}{2} M \sin(\omega t + \theta) \tag{3.1}$$

where M is the modulation index which can adjust the voltage magnitude, ω is the frequency, and θ is the phase angle.

To avoid distortion and additional harmonics, the maximum output voltage v_a is limited to $V_{dc}/2$ with the maximum modulation index M limited to 1. To improve the DC voltage utilization and achieve a higher AC output from the same DC supply, the third harmonic can be injected to the modulation waveform to increase the output voltage [73].

3.2.2. VSC control

For the WT VSCs, by adjusting their modulation index M and phase angle θ, the output voltage can be controlled to regulate the power output to the grid [54]. In this section, the basic VSC control is discussed.

a) *dq* transform

Direct-quadrature transformation (*dq* transform or Clark transformation) is a mathematical transformation which transforms three-phase quantities to *dq* quantities to simplify the circuit analysis as:

$$\begin{aligned} x_{dq} &= P x_{abc} \\ x_{abc} &= P^{-1} x_{dq} \end{aligned} \tag{3.2}$$

where x_{abc} can be voltage or current in the three-phase frame, and x_{dq} is the corresponding quantities in the *dq* frame. The *dq* transform parameter matrix $\boldsymbol{P}$ and $\boldsymbol{P^{-1}}$ with the system phase angle θ are described as:

$$P = \frac{2}{3}\begin{bmatrix} \cos\theta & \cos(\theta - 2\pi/3) & \cos(\theta + 2\pi/3) \\ -\sin\theta & -\sin(\theta - 2\pi/3) & -\sin(\theta + 2\pi/3) \\ 1/2 & 1/2 & 1/2 \end{bmatrix} \tag{3.3}$$

$$P^{-1} = \begin{bmatrix} \cos\theta & -\sin\theta & 1 \\ \cos(\theta - 2\pi/3) & -\sin(\theta - 2\pi/3) & 1 \\ \cos(\theta + 2\pi/3) & -\sin(\theta + 2\pi/3) & 1 \end{bmatrix}. \tag{3.4}$$

By applying the transformation matrix $\boldsymbol{P}$, three separate sinusoidal phase quantities can be transformed into two axes frame using the displacement angle between the three-phase and *dq* frames.

b) Vector current control

Figure 3.3 illustrates a simple structure when a VSC is connected to a grid through a reactor *L*.

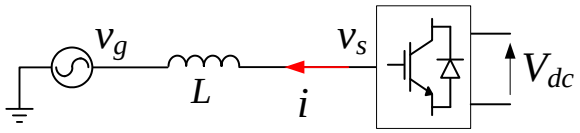

Figure 3.3 Grid connected VSC structure.

By applying Kirchhoff's voltage law (KVL) and considering the fundamental frequency voltage produced by the VSC, the relationship between the grid voltage v_g, the output voltage of converter v_s, and the line current *i* can be described as:

$$v_g = v_s - L\frac{di}{dt}. \tag{3.5}$$

Taking the transformation parameter matrix $\boldsymbol{P}$ and $\boldsymbol{P^{-1}}$ into (3.5) , the system dynamics can be transformed into *dq* frame as:

$$\begin{bmatrix} v_{gd} \\ v_{gq} \end{bmatrix} = \begin{bmatrix} v_{sd} \\ v_{sq} \end{bmatrix} + \begin{bmatrix} 0 & \omega L \\ -\omega L & 0 \end{bmatrix} \begin{bmatrix} i_d \\ i_q \end{bmatrix} - \begin{bmatrix} L & 0 \\ 0 & L \end{bmatrix} \frac{d}{dt} \begin{bmatrix} i_d \\ i_q \end{bmatrix} \tag{3.6}$$

where v_{gd} and v_{gq} are the *d*- and *q*-axis components of the grid voltage v_g, v_{sd} and v_{sq} are the *d*- and *q*-axis components of the converter voltage v_s, i_d and i_q are the *d*- and *q*-axis components of the three-phase current *i*, and ω is the rotating speed of the *dq* frame and is given as $\omega = d\theta/dt$.

From (3.6), current i_{dq} in the system can be adjusted by regulating the converter output voltages v_{sd} and v_{sq}. Based on this equation, the fast dynamic inner current control loop can be designed with proportional-integral (PI) regulators as:

$$\begin{cases} v_{sd}^* = v_{gd} + \omega L i_q - \left[k_p (i_d^* - i_d) + k_i \int (i_d^* - i_d) dt \right] \\ v_{sq}^* = v_{gq} - \omega L i_d - \left[k_p (i_q^* - i_q) + k_i \int (i_q^* - i_q) dt \right] \end{cases} \tag{3.7}$$

With the PI controller, the vector current control loop can be simplified as a second-order close loop system as shown in Figure 3.4 and the transfer function can be written as:

$$\frac{i}{i_{ref}} = \frac{k_p s + k_i}{L s^2 + k_p s + k_i}. \tag{3.8}$$

Thus, the PI parameters k_p and k_i can be presented as:

$$\begin{cases} k_p = L \times 2\zeta\omega_i \\ k_i = L \times \omega_i^2 \end{cases}. \tag{3.9}$$

where ζ is the controller damping ratio, ω_i is the natural frequency of the control loop, i_d^* and i_q^* are the references of the *d*- and *q*-axis currents [74]. Later in this thesis, the parameter *L* is designed as a gain of PI controller and the parameters k_p and k_i is defined without the *L*.

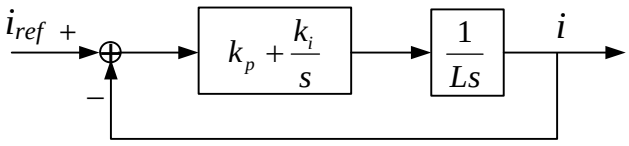

Figure 3.4 Simplified current control loop.

c) Phase lock loop

The phase lock loop (PLL) is used to ensure the *d*-axis of the synchronous *dq* frame is aligned with the grid source voltage vector. As illustrated in Figure 3.5, the grid voltage v_g is rotating at frequency ω_s whilst the *d*-axis alignment of the converter which rotating with frequency ω has an angle displacement with the grid voltage vector.

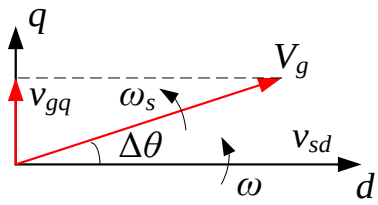

Figure 3.5 Synchronous frame and source vector.

Considering that the angle difference $\Delta\theta$ is small and V_g is the voltage magnitude of v_g, the *q*-axis voltage can be described as:

$$v_{gq} = V_g \sin\Delta\theta \approx V_g \Delta\theta \ . \tag{3.10}$$

Equation (3.10) stipulates that v_{gq} reflects the angle difference between the *d*-axis of the *dq* frame and the grid voltage vector, which is zero under ideal alignment. On the other hand, the angle difference can be described as:

$$\begin{aligned} \Delta\theta &= \int (\omega_s - \omega) dt \\ \frac{d\Delta\theta}{dt} &= \omega_s - \omega = \Delta\omega \end{aligned} \tag{3.11}$$

where ω_n is the rated grid frequency and $\Delta\omega$ is the small diversion which actual frequency deviates away from the rated value. To design a PLL, a PI controller which takes v_{gq} as the input can be applied as demonstrated in Figure 3.6.

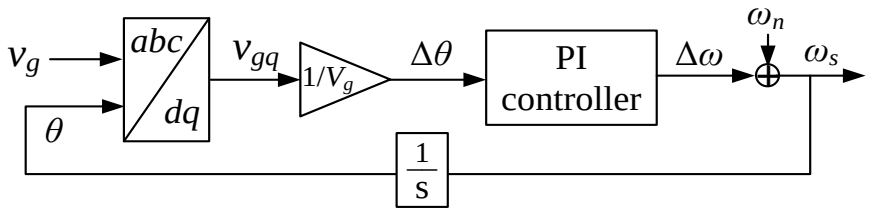

Figure 3.6 PLL control diagram.

3.3. Modular multilevel converter

Due to many restrictions of 2-level VSCs for HVDC application, such as high uniformity requirements on series connection of switching devices to withstand high voltage, poor AC waveform quality and substantial AC filter requirement, high power losses etc. [75], the MMC was first proposed in 2003 and has been further developed. It has become the most commonly used VSC topology for HVDC transmission applications. The modularity characteristic of MMC brings many benefits, such as better scalability and flexibility when adapting to any voltage level [76, 77], high efficiency, better power quality with reduced (or even without) filters [78], and possible fault-blocking capacity when applying in HVDC systems [76]. In this section, the fundamentals of MMC, including the structure and basic control strategies, are discussed.

3.3.1. MMC principles

a) MMC structure

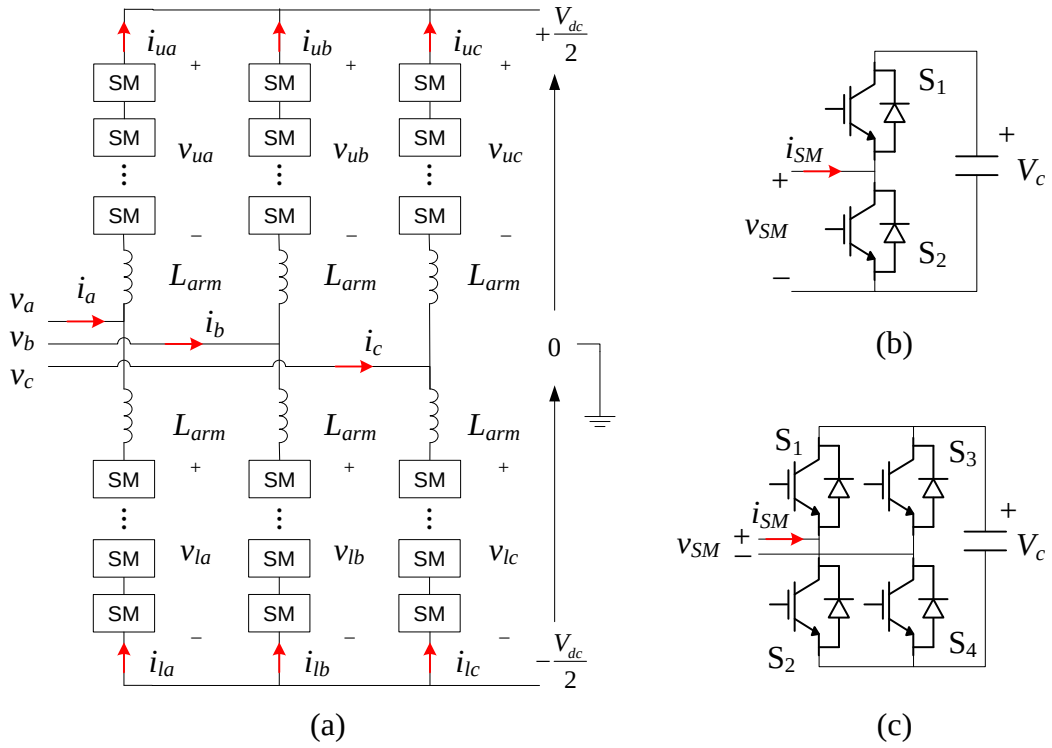

Figure 3.7 MMC topology structures.

The three-phase MMC circuit diagram is shown in Figure 3.7 (a). As illustrated, each phase consists of an upper arm and a lower arm, and each arm is formed by N cascaded SMs and an arm inductor. By controlling the states of the SMs at each arm, the output AC voltage can be adjusted. Figure 3.7 (b) and (c) illustrate two different circuit structures of SMs. With different SM structures, the MMCs presents different characteristics.

The half-bridge based SM (HBSM) as shown in Figure 3.7 (b) is the most commonly used topology for MMC. Because of the simple topology, it has the lowest loss and cost comparing to other MMC topologies [77]. The SM capacitor voltage V_c equals to V_{dc}/N, and the switching status of HBSM is shown in Table 3.1. The output voltage of each HBSM is 0 or V_c. In the event of a fault on the DC side, the collapse of the DC voltage could potentially lead to the discharge of the SM capacitors and high fault current. The IGBTs in all the SMs can be blocked to prevent SM capacitors from discharging though the MMC will behave like an uncontrolled rectifier and AC side fault current can continue feeding through the diodes to the DC fault [79, 80].

Table 3.1 Switching status and output voltage of HBSM.

States	**S_1**	**S_2**	**v_{SM}**	**i_{SM}**	**Capacitor status**
1	On	Off	V_c	>0	Charging
	On	Off	V_c	<0	Discharging
2	Off	On	0	-	Bypassed
3	Off	Off	-	-	Blocked

Figure 3.7 (c) illustrates the full-bridge based SM (FBSM) circuit structure. With FBSM, the voltage of each SM can be positive or negative. The switching status of FBSM are described in Table 3.2.

In contrast to HBSM, in the event of a fault on the DC side, and negative voltage from the SMs can prevent AC side fault current from feeding to the DC fault and thus MMC with FBSM has DC fault blocking capability. However, the doubled numbers of

IGBT and diode used in FBSM lead to the lower efficiency and higher cost when compared to the HBSM based MMC topology [81].

Table 3.2 Switching status of FBSM.

States	**S_1**	**S_2**	**S_3**	**S_4**	**v_{SM}**	**i_{SM}**	**Capacitor status**
1	On	Off	On	Off	0	-	Bypassed
2	On	Off	Off	On	V_c	>0	Charging
	On	Off	Off	On	V_c	<0	Discharging
3	Off	On	On	Off	$-V_c$	>0	Discharging
	Off	On	On	Off	$-V_c$	<0	Charging
4	Off	On	Off	On	0	-	Bypassed
5	Off	Off	Off	Off	-	-	Blocked

A variety of SM topologies have been studied to provide improved MMC characteristics, e.g. fault blocking, reduced losses etc. For example, the clamp double half-bridge based SM (CDSM) [82] has lower power loss than the FBSM whilst retaining fault blocking capacity, and the flying capacitor SM presents less circulating current and voltage ripple, higher efficiency but with increased challenge on voltage balancing [83]. The development of power semiconductor devices, new demands and regulations will continue driving and shaping future MMC technologies [82, 84].

b) MMC operations

For a three-phase MMC with N numbers of SMs at each arm (2N each phase), each arm can generate voltage waveform with N+1 levels. To ensure stable voltage at DC side, the sum voltage of the upper arm and lower arm at each phase should be Vdc, and the inserted SM number at each phase should be equal to N (considering SM capacitor voltage Vc=Vdc/N). By controlling the inserted SMs at the upper and lower arms, the output

voltage can be adjusted. The relationship between the output voltage at the AC side (taken Vdc/2 as the reference) and the inserted SMs number is shown in Table 3.3.

Table 3.3 Inserted SMs and the output voltage.

Upper arm Inserted SMs	**Lower arm Inserted SMs**	**Phase inserted SMs**	v_j
0	N	N	(N/2) V_{dc}/N
1	N-1	N	(N/2-1) V_{dc}/N
2	N-2	N	(N/2-2) V_{dc}/N
…	…	N	…
N/2	N/2	N	0
N/2+1	N/2-1	N	-V_{dc}/N
N/2+2	N/2-2	N	-2V_{dc}/N
…	…	N	…
N	0	N	-(N/2) V_{dc}/N

c) MMC equivalent model

The SMs at each arm of MMC can be represented by arm voltage sources as shown in Figure 3.8. According to Figure 3.8, by applying KVL, the equations at MMC AC side can be derived as:

$$\begin{cases} v_{uj} = -v_j + \dfrac{V_{dc}}{2} + L_{arm}\dfrac{di_{uj}}{dt} \\ v_{lj} = v_j + \dfrac{V_{dc}}{2} + L_{arm}\dfrac{di_{lj}}{dt} \end{cases} \tag{3.12}$$

where v_j (phase j=a, b, c) denotes the three-phase MMC voltage, v_{uj} and v_{lj} are the sum voltage of SMs in the upper and lower arm at each phase respectively; V_{dc} is the DC

voltage of the MMC station, i_{uj} and i_{lj} are the MMC upper and lower arm currents respectively at each phase, L_{arm} is the arm inductance.

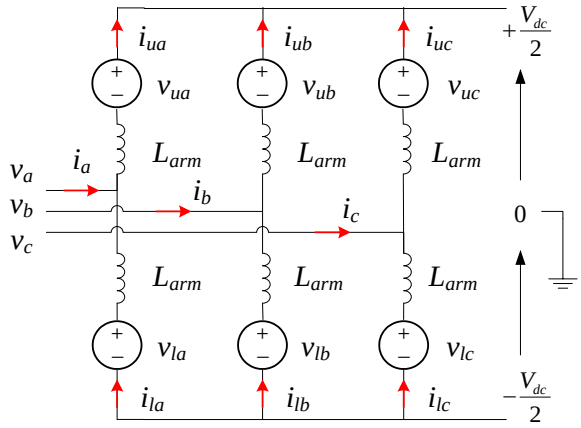

Figure 3.8 Simplified MMC model.

Arm currents i_{uj} (upper arm) and i_{lj} (lower arm) at each phase comprise half of the phase current i_j, one-third of the DC current and any circulating currents that may present among the three-phase legs. Considering the circuiting currents of MMCs are well suppressed by the controller, they are assumed at zero during the analysis. By applying KCL, the arm currents can be represented as:

$$\begin{cases} i_{uj} = \dfrac{i_j}{2} + i_c \\ i_{lj} = -\dfrac{i_j}{2} + i_c \end{cases} \tag{3.13}$$

where i_j is three-phase current, i_c is the DC component in the arm.

By substituting (3.13) into (3.12), the three-phase voltages can be described as:

$$\begin{aligned} v_{lj} - v_{uj} &= 2v_j + L_{arm}\left(\frac{di_{lj}}{dt} - \frac{di_{uj}}{dt}\right) \\ v_j &= \frac{L_{arm}}{2}\frac{di_j}{dt} + \frac{v_{lj} - v_{uj}}{2} \end{aligned} \tag{3.14}$$

Defining:

$$v_{mmcj} = \frac{v_{lj} - v_{uj}}{2}$$
$$L_{mmc} = \frac{L_{arm}}{2} \tag{3.15}$$

equation (3.14) which describes the MMC voltage can be rewritten as:

$$v_j = L_{mmc} \frac{di_j}{dt} + v_{mmcj}. \tag{3.16}$$

Thus, the MMC acts as a controlled voltage source on its AC side as described in (3.16), and the AC side current can be controlled accordingly.

3.3.2. MMC control

The operation process of MMC controls the switching status of the SMs to select the total inserted SM capacitors to resemble the required arm voltage. However, this configuration and working mode leads to complex interactions on the SM voltage and phase current, such as:

1. the charging and discharging of the connected SM capacitor which causes voltage variation;
2. existing circulating current among the arms leading to increased power loss.

The large numbers of SMs in each arm also means the conventional PWM is not suitable for MMC and new modulation methods are required.

a) Modulation methods

For controlling multilevel converters, the phase-shift PWM and level-shift PWM are commonly used. Using the phase-shift PWM method at MMC, many carrier waves are required and the small phase displacement (phase shift) requires an accurate carrier wave generation when the number of SMs is large [85]. Level-shift PWM introduced in [86] also employs *N* carrier waves which are vertically located within different bands for *N*+1 level MMC. Both these two modulation methods become impractical when the number of SMs (i.e. *N*) is high due to the potential high switching frequency and complexity of the

switching decisions [87]. The nearest level modulation (NLM) introduced in [88] reduces the switching frequency, and is the simplest modulation method for MMC.

NLM without carrier signals selects the number of SMs which allows the converter to generate the nearest output voltage level to the modulation wave. For N+1 level MMC, each phase (including the upper and low arms) has N SMs switched on at any time, as described in Table 3.3. Assuming that the voltage is balanced, the average SM capacity voltage is V_c that can be described as:

$$V_c = V_{dc} / N \,. \tag{3.17}$$

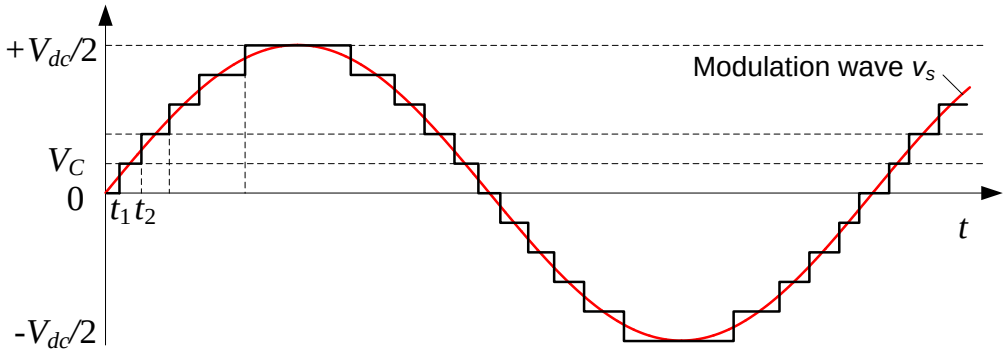

Figure 3.9 Nearest level modulation diagram.

As illustrated in Figure 3.9, the red wave v_s is the desired voltage, and the inserted SM numbers at upper arm N_{upper} and lower arm N_{lower} can be described as (3.18) while *round* means the closest integer.

$$\begin{cases} N_{upper} = \dfrac{N}{2} - round(\dfrac{v_s}{V_c}) \\ N_{lower} = \dfrac{N}{2} + round(\dfrac{v_s}{V_c}) \end{cases} . \tag{3.18}$$

b) Voltage balancing

During operation, the on-state of SM leads to the charging or discharging of its DC capacitor. To ensure safe operation, the capacitor voltages of all the SMs must be monitored and kept balanced [89]. In general, the most common voltage balancing method

is based on the sorting and selecting method [86, 90], which involves the following procedures:

1. Monitoring and sorting the SMs according to their capacitor voltages.
2. Measuring the direction of arm current and determining the charging and discharging status.
3. Selecting the SM with the lowest capacitor voltage at charging status and selecting the SM with the highest capacitor voltage at discharging status.

One of the drawbacks for the sorting method is the high computation requirement as all the SMs have to be sorted based on their capacitor voltages during each sampling period. To address this problem, a slow-rate sorting strategy based on a closed-loop modified method is studied in [91]. This method only sorts a limited number of SMs during a period rather than all the SMs. With this method, if additional SMs are required to be turned on at the next control period, only the off-state SMs are sorted and vice versa. Reference [92] proposes and investigates a fundamental-frequency sorting method. With this method, all the SMs are only sorted when the AC output voltage is at the two peak AC voltage levels ($V_{dc}/2$ and $-V_{dc}/2$ when M=1). Based on this updated index list and the direction of arm current, the required number of SMs are selected. A hybrid balancing strategy which combines a predictive method is also studied in [92]. This strategy combines the traditional sorting method and predictive sorting method by comparing the predicted capacitor voltage error in the one-step forward control cycle with their average values to select the SMs to be inserted.

In this thesis, average MMC model is used where each arm voltage is represented by a controlled voltage source and one lumped DC capacitor [93, 94]. This effectively assumes all the SM capacitors are perfectly balanced.

Another important aspect of MMC operation is to ensure the stored energies in all the 6 arms are equal. This means the voltages across the 6 lumped arm capacitors in the average MMC model should be balanced. Voltage balancing between the upper and lower arms of the same phase is usually called vertical balancing and voltage balancing between

the upper (or lower) arms of the three phases is usually called horizontal balancing. The sum and difference voltages of the upper and lower arm at each phase are defined as:

$$\begin{aligned} \sum V_{cj} &= V_{cuj} + V_{clj} \\ \Delta V_{cj} &= V_{cuj} - V_{clj} \end{aligned} \tag{3.19}$$

where V_{cuj} and V_{clj} are the upper and lower SM capacitors voltages for phase j.

According to [95, 96], injecting a small fundamental current into the common-mode current as defined in (3.20) can eliminate the DC voltage error between the upper and lower SM capacitor voltages.

$$i_{comm} = \frac{i_{uj} + i_{lj}}{2}. \tag{3.20}$$

Therefore, three PI controllers (one for each phase) for vertical voltage balancing control can be designed as shown in Figure 3.10 and the ΔV_{cj} is the difference in capacitor voltages in phase j (j=a,b,c). A band pass filter tuned at fundamental frequency ω is used to remove the fundamental frequency oscillation in the voltage difference so as to extract the DC error component.

A DC offset injecting to the common-mode current can eliminate the DC voltage error between the three phases [95, 96]. As illustrated in Figure 3.10, a PI controller is applied at each phase for the horizontal voltage balancing control. The $\sum V^*_{cj}$ is the sum voltage reference of SM capacitor ($2NV^*_c$) at each phase. A band pass filter tuned at 2ω is used for removing the second-order behavior in the sum of the capacitor voltage [97].

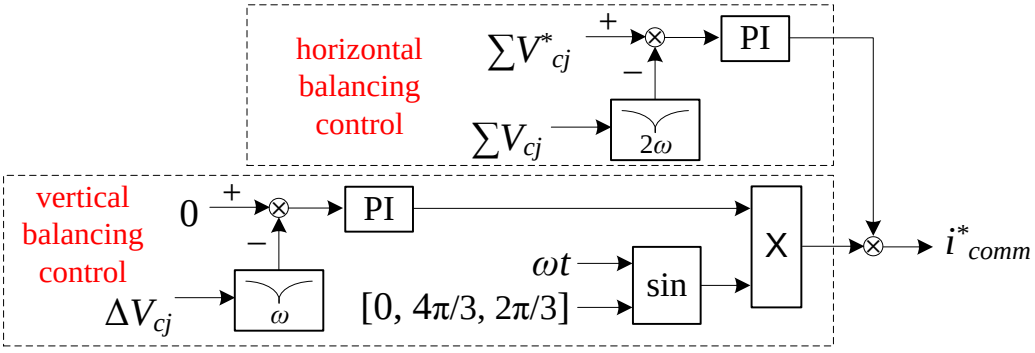

Figure 3.10 Voltage balancing control [95].

By regulating the common-mode current which does not affect the MMC AC output voltage and current, the horizontal voltage balancing, and vertical voltage balancing can be achieved. The common-mode current control will be introduced in the next section.

c) Circulating current and common mode current control

The current circulating between the three phases is a distinctive characteristic of MMC. The circulating current mainly includes the DC component which is used for converting real power and the second-order harmonic component [98]. Reference [99] investigates the relationship between circulating current and MMC performances, and proves that the second-order circulating current affects power loss and capacitor voltage ripples. Therefore, control of circulating current in MMC is necessary and the main target is to eliminate the second order harmonic circulating current and minimize the voltage ripple of SM capacitors.

Reference [100] applies a circulating current suppressing strategy based on the inner current control loop with a proportional-resonant (PR) controller. However, the method only targets at arm current reduction without considering the capacitor voltage ripple. The control methods proposed in [101, 102] reduce the capacitor voltage ripple, but the extensive output current measurements complicate the control structure and the increased arm current leads to more substantial power loss.

In this study, two PR controllers resonating at ω (fundamental frequency) and 2ω are adopted to control the circuiting current as described in (3.21).

$$G_{(s)} = K_p + \frac{2K_{r1}s}{s^2+\omega^2} + \frac{2K_{r2}s}{s^2+(2\omega)^2}. \tag{3.21}$$

The PR controller at resonant frequency ω is adopted to control the fundamental frequency current as required by the vertical capacitor voltage balancing shown in Figure 3.10, whereas the other one at resonant frequency 2ω is used for suppressing the second-order circulating current. The control structure for the common mode current control is schematically shown in Figure 3.11 where the i^*_{comm} is feed from voltage balancing control and i_{comm} is calculated by (3.20). The $v^{*'}_{uj}$ and $v^{*'}_{lj}$ in Figure 3.11 come from the inner

current loop of the MMC as demonstrated in Figure 3.12, which shows the complete control diagram of the MMC based on average model (the simplified MMC model as shown in Figure 3.8).

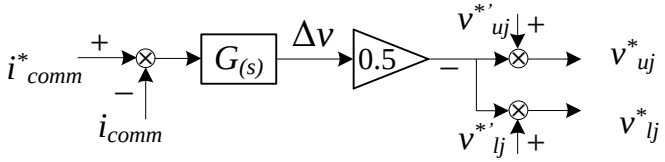

Figure 3.11 Common mode current controller [96].

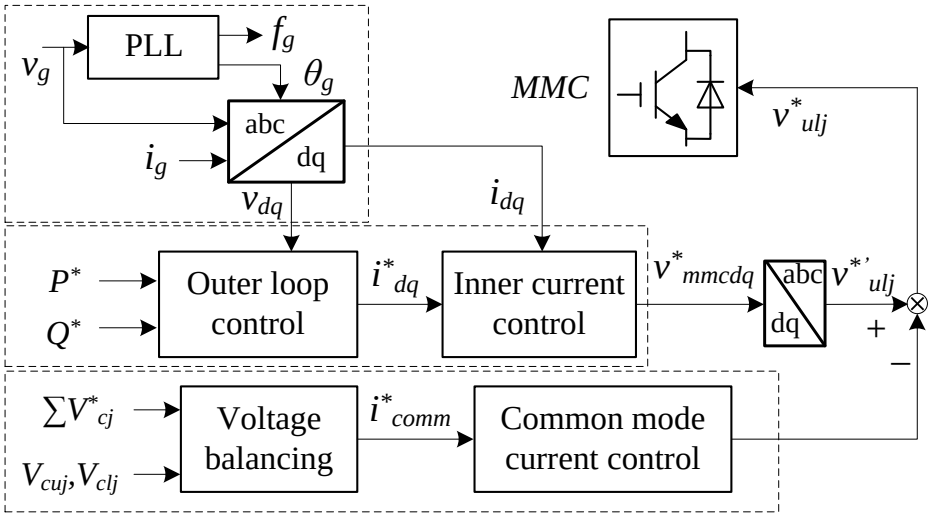

Figure 3.12 Compete control diagram for average MMC model.

3.4. Summary

In this chapter, WT VSC structure and operating principles are introduced. The inner current control loop applied at VSC based on *dq* frame is discussed. The operating principles of MMC are also introduced. The inherent characteristics of MMC, such as circulating current and capacity voltage variation are studied. Typical system configurations and control strategies for MMC are discussed, and various modulation strategies for ensuring capacitor voltage balancing are illustrated.

Chapter 4

Control of the offshore wind farm system

4.1. Introduction

For offshore wind farms connected using HVDC, the offshore VSC (i.e. MMC) station has to form the AC power systems in offshore wind farms, which exhibit different characteristics compared to conventional onshore power systems, and potential voltage oscillation or harmonic resonance in the event of faults can be induced [103-108]. Stable AC voltage and frequency control is thus a prerequisite for the transmission of offshore wind energy.

Fixed frequency control by the offshore MMC station as discussed in Chapter 2 is the most common approach to regulate the AC voltage of offshore networks. With fixed offshore frequency, the phase angle is generated using the fixed frequency, and a PI controller is used to regulate the *d*-axis voltage, thereby the offshore voltage magnitude [109]. Besides the control methods reviewed in Chapter 2, in [110], offshore grid three-phase voltages are added to the output of the PR controllers as feedforwards to improve the dynamics of offshore voltage controller. However, as these control schemes only contain voltage control loop and do not have current control, the system performance of the offshore MMC stations, especially during large transients, cannot be guaranteed.

In this chapter, the basic MMC control method is described first, and an enhanced AC voltage and frequency control of the offshore MMC station connected with wind farms is then proposed. Considering the operating principle of the PLL, the offshore frequency flexibility is utilized to improve the offshore voltage control leading to faster dynamic response and better performance of offshore AC voltage.

4.2. System structure

When using MMC-HVDC systems for connecting offshore wind farms, MMC station located onshore usually regulates the DC voltage of the HVDC link to ensure stable power transmission from offshore wind farms to onshore grids. The DC voltage control method on the onshore MMC has been introduced in the previous chapter. With the stable DC voltage, offshore MMC controls the offshore AC voltage at the PCC bus and ensures the offshore wind turbines have a stable AC network voltage for controlling their active and reactive power generation.

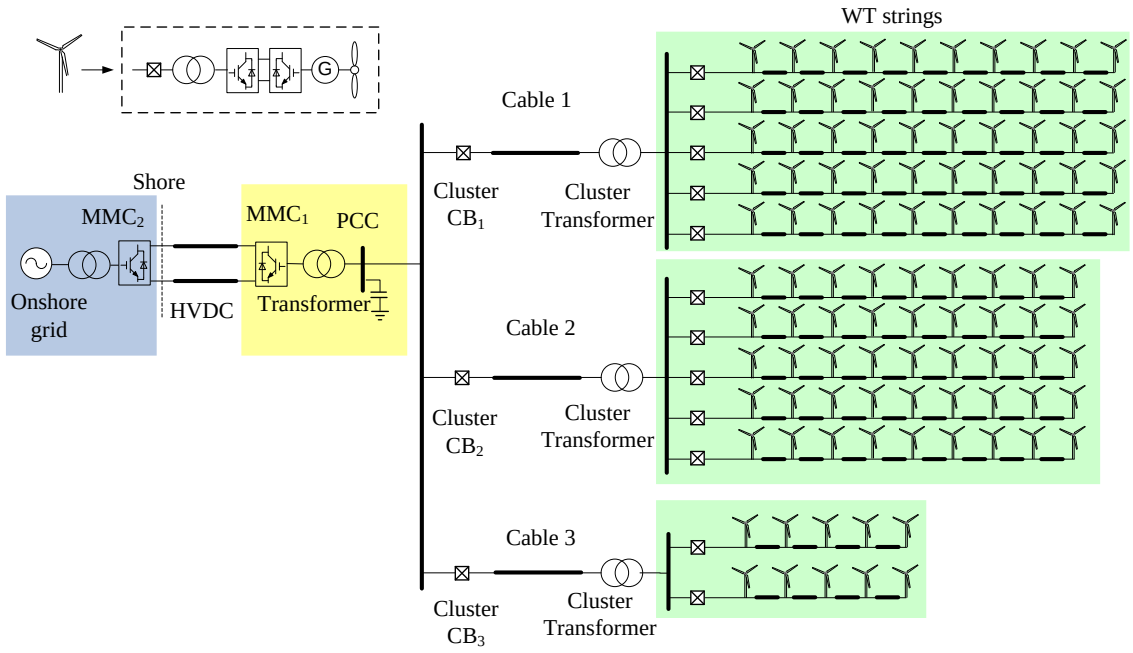

Figure 4.1 Structure of MMC-HVDC connected offshore wind farm system.

The considered offshore wind farm connected with an MMC-HVDC is schematically shown in Figure 4.1. A symmetrical monopole HVDC system with the rated DC voltage of ±400 kV and two submarine cables are considered in this study. At the onshore side, a single AC source with certain impedance is used to represent the onshore electrical power grid. The onshore station MMC_2 which connected to the onshore power grid regulates the DC voltage of the HVDC link. At the offshore side, the offshore station MMC_1 controls the AC voltage and frequency of the offshore network. The offshore wind farm is

represented by three 33kV wind turbine cluster models which are connected to the offshore 200 kV HVAC network through 33kV/200kV transformers. The three wind turbine cluster models are rated at 500MW, 450MW, and 50 MW respectively, so events with different power scales can be simulated in the late studies. The three wind turbine clusters are connected at different locations with different distances to the PCC bus. At the end of each cluster cable, AC circuit breakers are equipped to isolate the fault branch and enable continuous operation of the healthy wind turbines in the event of a fault in the offshore AC network.

4.2.1. Wind turbine modelling

With the increasing scale on wind farms, simulating an offshore wind farm system becomes computationally intensive when modelling each wind turbine (WT) in detail [111]. As this thesis mainly investigates offshore AC voltage and frequency control and the WTs mostly follow the network established by the offshore MMC, aggregated and simplified WT systems are used. Thus, the detail influence factors of each WT can be neglected, such as wake effect or different power output due to the variable wind speed and direction, and only the total output power and current need to be focused.

To aggregate WTs, there are two types of methods that can be used: Single-Machine Representation Method (SRM) and Multi-Machines Representation Method (MRM) [112]. SRM represents the whole WF into one equivalent WT whereas MRM clusters the WF in different WT groups according to the operation characteristics and then uses parameter estimation to model each group of WTs as one equivalent WT [113]. Because the dynamics of the WT mechanical system and wind generator are not the focus of this thesis and for simplification of analysis, the WTs are classified and represented by three lumped different capacity WT converters. In the WT converter models, only the grid side converter is modelled, and the DC side is considered as a simple DC source. Different power orders are applied to simulate the variation of wind power generation.

With the aggregation of WTs, offshore wind farm structure in Figure 4.1 can be simplified to the circuit as shown in Figure 4.2. All the wind turbines are classified and

combined to the equivalent three different wind turbine clusters which are represented by the three lumped WT models. These three WT models demonstrate wind turbine clusters with different capacity according to the numbers of WTs connected to each cluster. The aggregated wind turbines and their filters are connected to the terminals through a transformer at each wind turbine cluster.

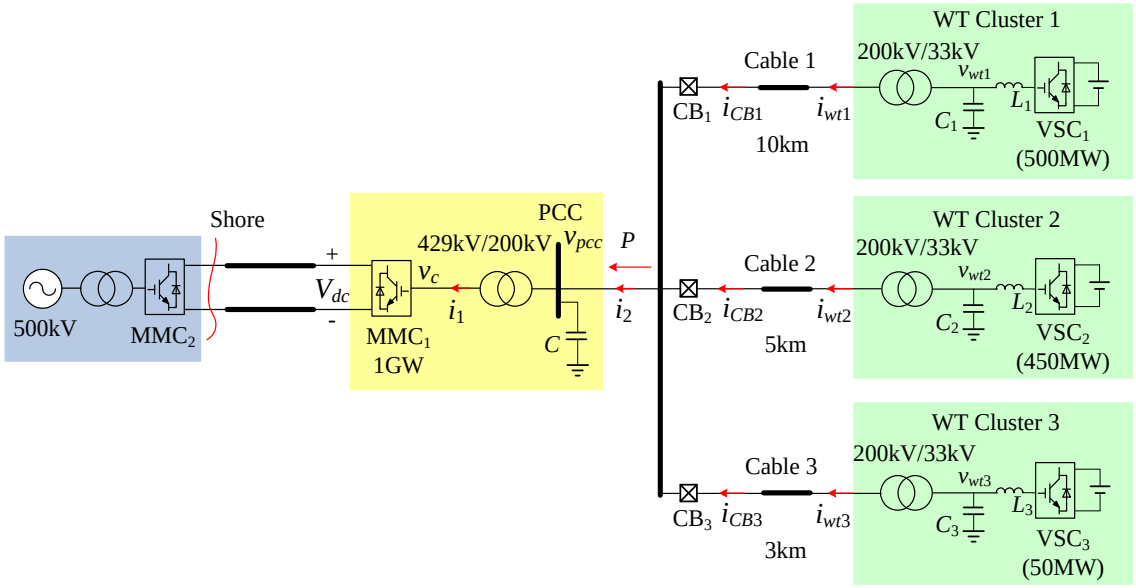

Figure 4.2 Offshore wind farm system structure with lumped WT clusters.

4.2.2. Control of wind turbine converters

As shown in Figure 4.2, the system is represented by three lumped WTs, which are modeled as three two-level VSCs connected to constant DC sources. Figure 4.3 shows the connection of one WT converter. The lumped VSC model generates a voltage v_{vsc} through an inner vector control loop which has been introduced in Chapter 3. The PWM modulation described in previous chapter is applied to generate the switching pulses as demonstrated in Figure 4.4.

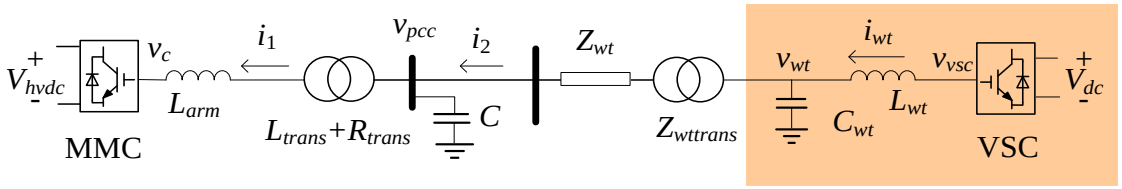

Figure 4.3 Structure of single simplified WT cluster.

The control diagram of lumped WT VSC based on decoupled *dq* frame with fault current limitation is given in Figure 4.4. In this VSC control structure, the three-phase voltage v_{wt} on the WT connection point is measured first and a PLL is used to obtain the phase angle and frequency. The voltage and current are then transformed from three-phase to those in the *dq* reference frames. The PLL control principle has been introduced in the previous chapter so no further discussion is given here.

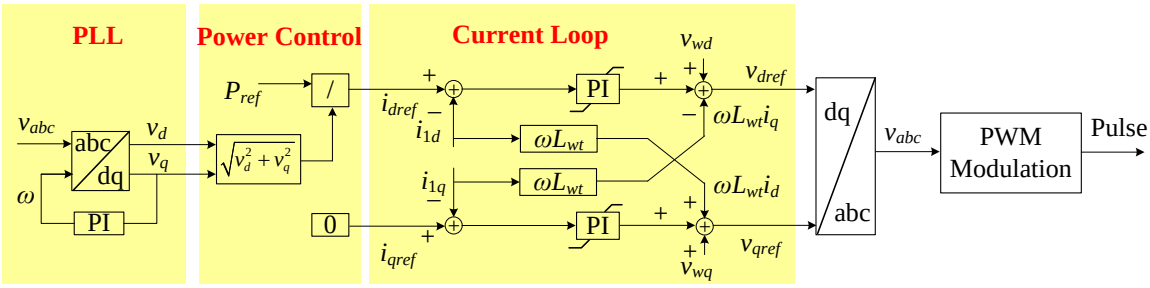

Figure 4.4 Control structure on WT side VSC.

In the power control loop, reference current on *d*-axis i_{dref} can be calculated as:

$$i_{dref} = \frac{2}{3} \times \frac{P_{ref}}{v_{wtd}} \tag{4.1}$$

where the P_{ref} is the output wind power of VSC, v_{wtd} is the *d*-axis voltage of v_{wt}. The reference current on *q*-axis is set as 0 in the illustration but can be set to different values as required.

4.3. Basic control on offshore MMC station

The offshore MMC station works as a grid-forming converter to establish the offshore AC network frequency and voltage, as well as balancing the transmitted active power between WTs and the offshore network. The offshore MMC typically contains an outer AC voltage control loop and an inner current loop to provide fast system dynamics and to enable MMC fault current limiting capability during offshore AC faults.

4.3.1. Inner current loop

For the offshore MMC_1 shown in Figure 4.2, by applying Kirchhoff's voltage law (KVL) at the PCC bus and equivalent the voltage to transformer's primary side (MMC side), the relationship between current and voltage on the PCC bus in three-phase static coordinate frame can be described as shown in the dynamic differential equation (4.2). In this equation, v_c is the three-phase voltage generated by the MMC_1 station, i_1 describe the three-phase AC current while v_{pcc} is the three-phase voltage on PCC bus. R_{trans} is the transformer resistance; L is the total inductance including the transformer leakage inductance L_{trans} and MMC arm inductance L_{mmc} as (4.3), and n is the transformer ratio.

$$nv_{pcc} = v_c + L\frac{di_1}{dt} + R_{trans}i_1 \tag{4.2}$$

$$L = L_{trans} + L_{mmc}\,. \tag{4.3}$$

The resistor on the transform is relatively small and thus is neglected in the control part. Therefore, the three-phase dynamic differential equations on AC side can be described into matrix form as:

$$\begin{bmatrix} v_{ca} \\ v_{cb} \\ v_{cc} \end{bmatrix} = n\begin{bmatrix} v_{pcca} \\ v_{pccb} \\ v_{pccc} \end{bmatrix} - L\frac{d}{dt}\begin{bmatrix} i_{1a} \\ i_{1b} \\ i_{1c} \end{bmatrix}. \tag{4.4}$$

Applying dq transform with parameter matrixes which have been described in Chapter 3, the three-phase system (4.4) can be transformed into dq quantities. The current loop dynamics in the dq reference frame where the d-axis is fixed to the PCC voltage v_{pcc} can be expressed as:

$$\begin{bmatrix} v_{cd} \\ v_{cq} \end{bmatrix} = n\begin{bmatrix} v_{pccd} \\ v_{pccq} \end{bmatrix} + \begin{bmatrix} 0 & \omega L \\ -\omega L & 0 \end{bmatrix}\begin{bmatrix} i_{1d} \\ i_{1q} \end{bmatrix} - \begin{bmatrix} L & 0 \\ 0 & L \end{bmatrix}\frac{d}{dt}\begin{bmatrix} i_{1d} \\ i_{1q} \end{bmatrix} \tag{4.5}$$

where ω is the angular frequency of the offshore network; i_{1d} and i_{1q} are the MMC dq currents; v_{cd} and v_{cq} are the MMC output dq voltages; v_{pccd} and v_{pccq} are the PCC voltages in the dq frame.

From (4.5), by adjusting the offshore MMC station output voltages, the *dq* currents can be regulated. Thus, the current controllers in the *dq* axes including the proportional-integral (PI) regulators can be designed as illustrated in Figure 4.5 and described as (4.6).

$$\begin{cases} v_{cd}^{*} = nv_{pccd} + \omega L i_{1q} - \left[k_{ip}(i_{1d}^{*} - i_{1d}) + k_{ii}\int (i_{1d}^{*} - i_{1d})dt \right] \\ v_{cq}^{*} = nv_{pccq} - \omega L i_{1d} - \left[k_{ip}(i_{1q}^{*} - i_{1q}) + k_{ii}\int (i_{1q}^{*} - i_{1q})dt \right] \end{cases}. \tag{4.6}$$

In (4.6) and Figure 4.5, the signals with superscript * indicate reference values, k_{ip} and k_{ii} are the parameters of the PI regulators in the current control loop.

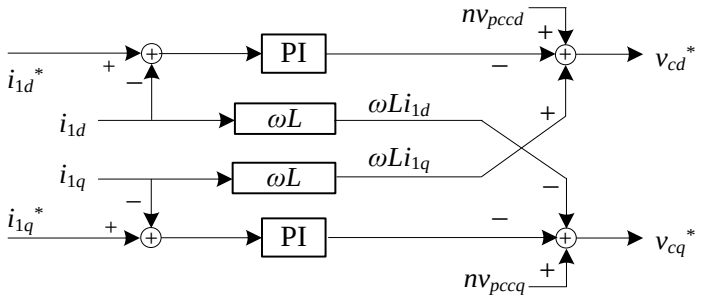

Figure 4.5 Current control loop structure.

4.3.2. Outer voltage loop for AC voltage control

Transform the MMC current i_1 to the secondary side of transformer (PCC side), the relationship between current and voltage at the PCC is shown as:

$$n\begin{bmatrix} i_{1a} \\ i_{1b} \\ i_{1c} \end{bmatrix} = \begin{bmatrix} i_{2a} \\ i_{2b} \\ i_{2c} \end{bmatrix} - C\frac{d}{dt}\begin{bmatrix} v_{pcca} \\ v_{pccb} \\ v_{pccc} \end{bmatrix}. \tag{4.7}$$

As shown in Figure 4.2, i_1 is the current flowing into the offshore MMC station and i_2 is the current flowing from the WT collector network to the PCC bus. *C* represents the equivalent AC capacitance seen at the PCC point. Transforming (4.7) into *dq* frame yields:

$$\begin{bmatrix} i_{1d} \\ i_{1q} \end{bmatrix} = \frac{1}{n}\begin{bmatrix} i_{2d} \\ i_{2q} \end{bmatrix} + \begin{bmatrix} 0 & \frac{\omega C}{n} \\ \frac{-\omega C}{n} & 0 \end{bmatrix}\begin{bmatrix} v_{pccd} \\ v_{pccq} \end{bmatrix} - \begin{bmatrix} \frac{C}{n} & 0 \\ 0 & \frac{C}{n} \end{bmatrix}\frac{d}{dt}\begin{bmatrix} v_{pccd} \\ v_{pccq} \end{bmatrix}. \tag{4.8}$$

From (4.8), it can be concluded that the outer AC voltage loop can set the current references to control the PCC voltages. Thus, the outer voltage loop can be designed in a similar way as for the current loop as:

$$\begin{cases} i_{1d}^{*} = \dfrac{i_{2d}}{n} + \dfrac{\omega C}{n} v_{pccq} - \left[k_{vp}(v_{pccd}^{*} - v_{pccd}) + k_{vi} \int (v_{pccd}^{*} - v_{pccd}) dt \right] \\ i_{1q}^{*} = \dfrac{i_{2q}}{n} - \dfrac{\omega C}{n} v_{pccd} - \left[k_{vp}(v_{pccq}^{*} - v_{pccq}) + k_{vi} \int (v_{pccq}^{*} - v_{pccq}) dt \right] \end{cases}. \tag{4.9}$$

In (4.9), signals with superscript * indicate reference values, k_{vp} and k_{vi} are the parameters of the PI regulators in the voltage control loop. Figure 4.6 illustrates the control diagram based on (4.9).

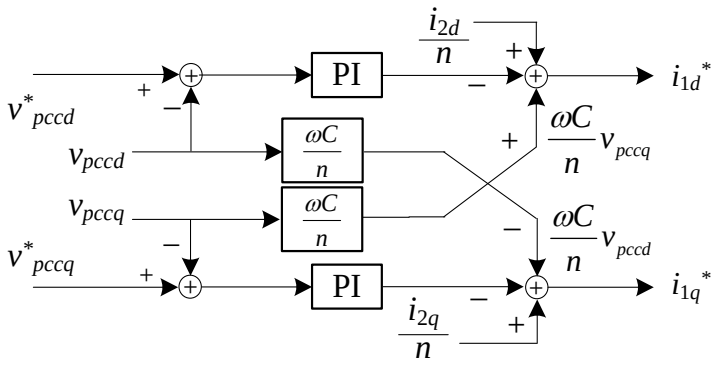

Figure 4.6 Voltage control loop structure.

4.3.3. Offshore frequency control

In the existing methods, no PLL is used and the offshore frequency f is typically fixed (e.g. 50 Hz). The phase angle θ is simply derived using the fixed frequency as:

$$\theta = 2\pi ft = 100\pi t . \tag{4.10}$$

The MMC station then forms the offshore network according to the phase information obtained by (4.10) [114]. This approach is easy to implement. The overall control structure is shown in Figure 4.7 in which the *d*-axis PCC voltage reference is set at the desired value while the q-axis voltage reference is always 0. However, with fixed frequency, the offshore frequency flexibility is not utilized, which reduces the offshore voltage performance especially under transient conditions as will be demonstrated later.

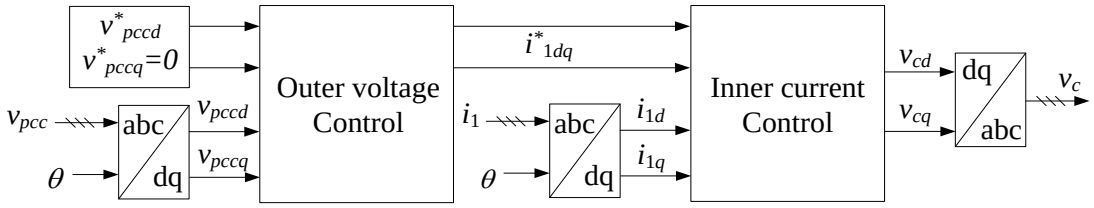

Figure 4.7 Offshore MMC station AC voltage control strategy with fixed frequency.

4.4. Enhanced AC voltage and frequency control

To improve the dynamic response of the offshore system and provide a better control on offshore AC voltage, a PLL based frequency control is proposed in this section. This control method is able to improve the AC voltage control by utilizing the offshore frequency flexibility of the MMC station.

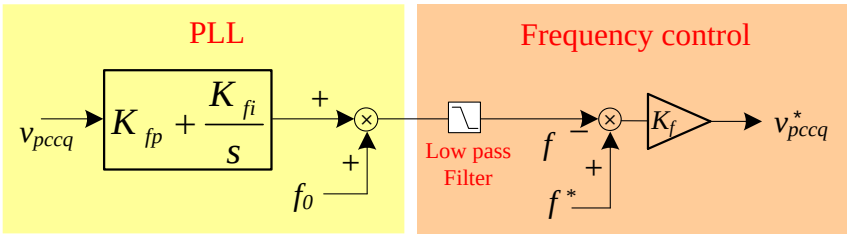

Figure 4.8 PLL based frequency control strategy.

Due to the robustness and ease of implementation, PLL is widely used in tracking AC voltage angle and frequency [55, 104]. It usually measures the q-axis voltage v_{pccq} and a PI regulator drives the frequency in order to obtain zero v_{pccq}, as illustrated in Figure 4.8 where the PLL part can be described as:

$$f = \frac{1}{1+T_s \cdot s}\left(k_{fp} v_{pccq} + k_{fi} \int v_{pccq} dt + f_0\right) \tag{4.11}$$

where T_s is the time constant of the low pass filter (LPF) and f_0 is the desired frequency, e.g. 50Hz.

Since the output frequency and the phase angle of the offshore MMC derived by the PLL, form the offshore AC network, an additional PLL-based frequency loop is proposed

to generate the desired v^*_{pccq}. The proposed offshore MMC frequency control considers the operating principle of the PLL, and sets the q-axis voltage reference v^*_{pccq} by the reference frequency and the q-axis voltage droop control as:

$$v^*_{pccq} = K_f (f^* - f) \tag{4.12}$$

where K_f is the droop control gain and f^* is the frequency reference. The PLL acquires the frequency f and the deviation of actual frequency and reference frequency acts on the q-axis voltage value on the PCC as shown in Figure 4.8.

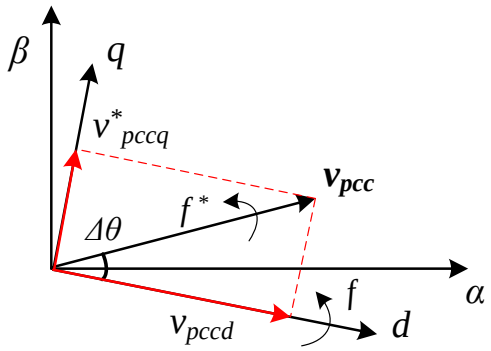

Figure 4.9 PLL synchronization control.

The operation principle can be further explained in detail by considering Figure 4.9. The d-axis v_{pccd} is the initial position measured by the PLL. If the MMC instantly generates an AC voltage v_{pcc} which leads the d-axis by a certain angle $\Delta\theta$, the PLL will detect a positive v_{pccq} in the next sampling step as can be seen in Figure 4.9. Consequently the new measured frequency f increases, as depicted by (4.11) and Figure 4.8. This in deed will increase the MMC output voltage frequency since the measured frequency is used for generating the output voltage. Thus, if the real offshore frequency obtained by PLL is less than the reference value, i.e. $f < f^*$, the frequency loop outputs a positive v^*_{pccq} with (4.12) which is then fed to the MMC AC voltage loop to generate the corresponding positive v_{pccq}. In the next measurement step on PLL, the positive v_{pccq} is detected by the PLL and the offshore AC frequency controlled by the MMC increases accordingly. Similarly, if the measured frequency is higher than the reference, i.e. $f > f^*$, a negative voltage reference v^*_{pccq} is generated by the frequency loop and the MMC generates a negative v_{pccq}. Under

such a condition, the frequency detected by the PLL reduces due to the negative *q*-axis voltage ($v_{pccq} < 0$) and so as the new frequency of the MMC AC output. Therefore, with the proposed frequency control, the offshore frequency *f* can be tightly controlled at the reference value. The overall control strategy is shown in Figure 4.10.

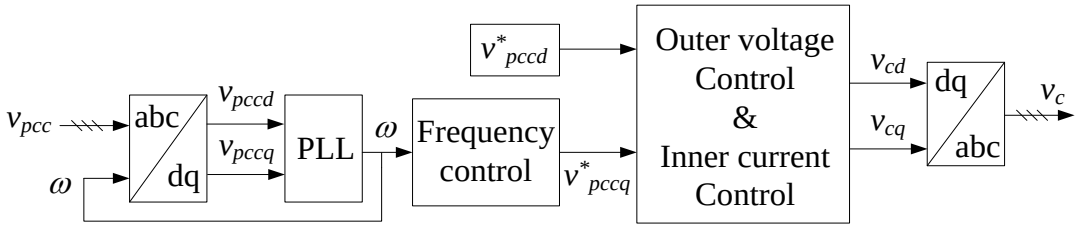

Figure 4.10 Offshore MMC station AC voltage control strategy with PLL-based frequency loop.

Compared with the traditional method shown in Figure 4.7, a PLL-based frequency control is added to MMC to provide dynamic *q*-axis voltage reference. By utilizing the offshore frequency flexibility, the proposed strategy tightly controls the AC voltage and frequency of the offshore network and ensures a stable transmission of the offshore wind energy, as will be demonstrated in the following section.

4.5. Simulation results on normal operation of offshore wind farm

The proposed control strategy is tested in Matlab/Simulink environment using the model shown in Figure 4.2, where the generator-side WT converters are represented by DC voltage sources for simplicity. Average models (as reviewed in Chapter 3) are used for the MMC stations [115], and detailed 2-level VSC switch models are adopted for the grid-side WT converters. As previously described, the offshore wind farm has three lumped wind turbine models rated at 500 MW, 450 MW, and 50 MW respectively, and connected to the collector buses through 10 km, 5 km and 3 km cables respectively. The detailed parameters of the offshore MMC-HVDC system and the WT converters are listed in Table 4.1 and Table 4.2 respectively.

Table 4.1 Parameters of the MMC-HVDC system.

AC grid voltage		429 kV
HVDC voltage		800 kV
MMC power rating		1000 MW
MMC side transformer	Reactance	0.2 pu
	Resistance	0.004452 pu
MMC side AC capacitance		0.01 pu
PCC voltage		200 kV
***R, L,* and *C* of Cable**		15 mΩ/km, 0.3 mH/km, 0.12 μF/km

Table 4.2 Parameters of the lumped wind turbine models.

DC voltage of WT converter		65 kV
WT side transformer	Reactance	0.1 pu
	Resistance	0.004 pu
WT side capacitor		0.15 pu
WT side inductor		0.2 pu
***R, L,* and *C* of Cable 1 (10km)**		15 mΩ/km, 0.3 mH/km, 0.12 μF/km
***R, L,* and *C* of Cable 2 (5km)**		16.5 mΩ/km, 0.33 mH/km, 0.11 μF/km
***R, L,* and *C* of Cable 3 (3km)**		150 mΩ/km, 3 mH/km, 0.012 μF/km

4.5.1. Start-up duration

a) Start-up process

After the stabilization of the HVDC-link voltage regulated by the onshore station MMC_2, the offshore station MMC_1 is enabled at 0.05 s and the waveforms associated with the start-up process are shown in Figure 4.11. All three WT converters are not enabled (i.e. the IGBTs are blocked) initially, but their AC filters are connected to the offshore AC network. At 0.1 s, the offshore MMC station starts to build up the offshore AC voltage and the AC voltage reaches the rated value at around 0.2 s and remains stable. The three-phase AC voltage and current of the offshore grid during start-up with the proposed frequency control methods are displayed in Figure 4.11 (b) and (c), respectively, whereas Figure 4.11 (e) and (f) illustrate the PCC voltage in *dq* frame. When the proposed control started at 0.1 s, the *d*-axis voltage v_{d_pcc} follows the reference tightly and the *q*-axis voltage v_{q_pcc} is also regulated to around zero. The frequency dynamic response with the proposed control is illustrated in Figure 4.12, where it can be seen that the offshore AC frequency is controlled around the desired value of 50 Hz by the proposed frequency control. Due to the considerable capacitive reactive power produced by the WT converter filters, inductive reactive power is needed from the offshore MMC station as can be seen in Figure 4.11 (d). As all the WTs are blocked, no active power generation by the WTs in the offshore system, seen Figure 4.11 (d).

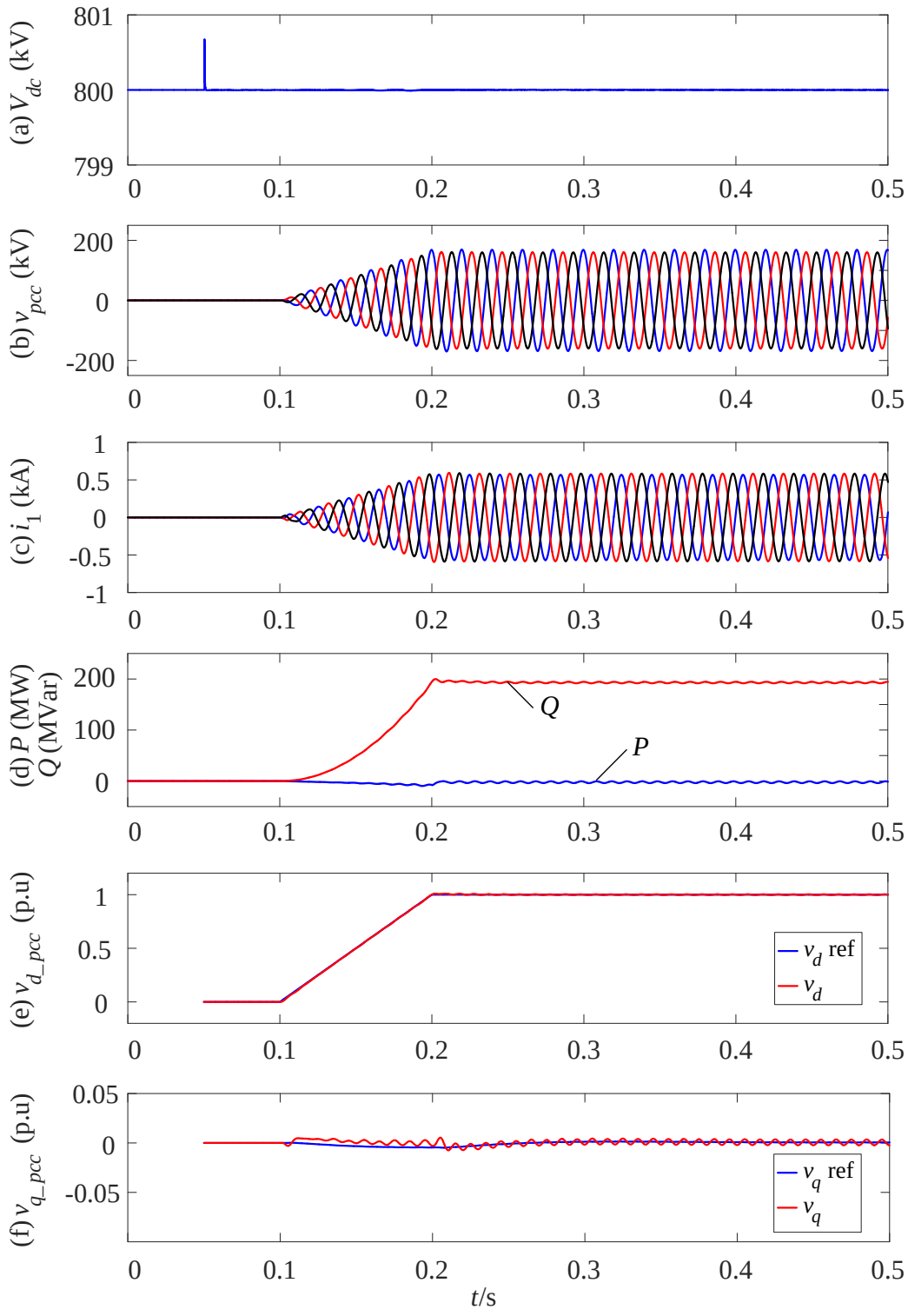

Figure 4.11 Simulation waveforms of offshore station MMC_1 during start-up.

(a) DC voltage on HVDC link, (b) three-phase voltage on PCC, (c) three-phase currents i_1, (d) MMC_1 active and reactive power, (e) PCC d-axis voltage, (f) PCC q-axis voltage.

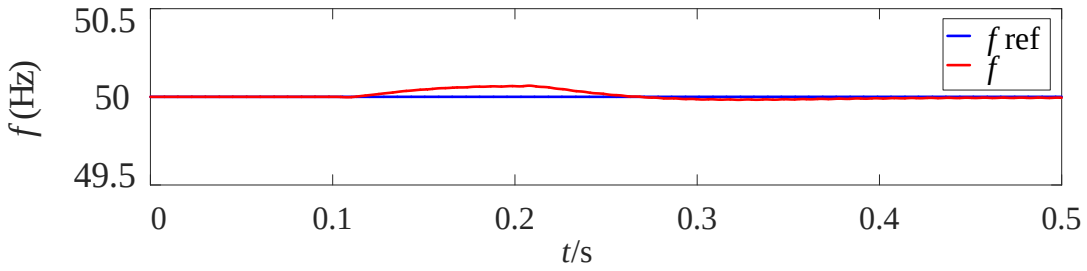

Figure 4.12 Offshore system frequency during start-up.

b) Comparison between the proposed and conventional controls during start-up

The AC voltage amplitude at the PCC bus of the offshore grid during start-up with the conventional and proposed frequency control methods are compared in Figure 4.13. The detailed waveforms compared in Figure 4.13 (b) and (c) shows that the voltage v_{d_pcc1} with proposed control has a better reference tracking than v_{d_pcc2} with conventional control method with the fixed frequency.

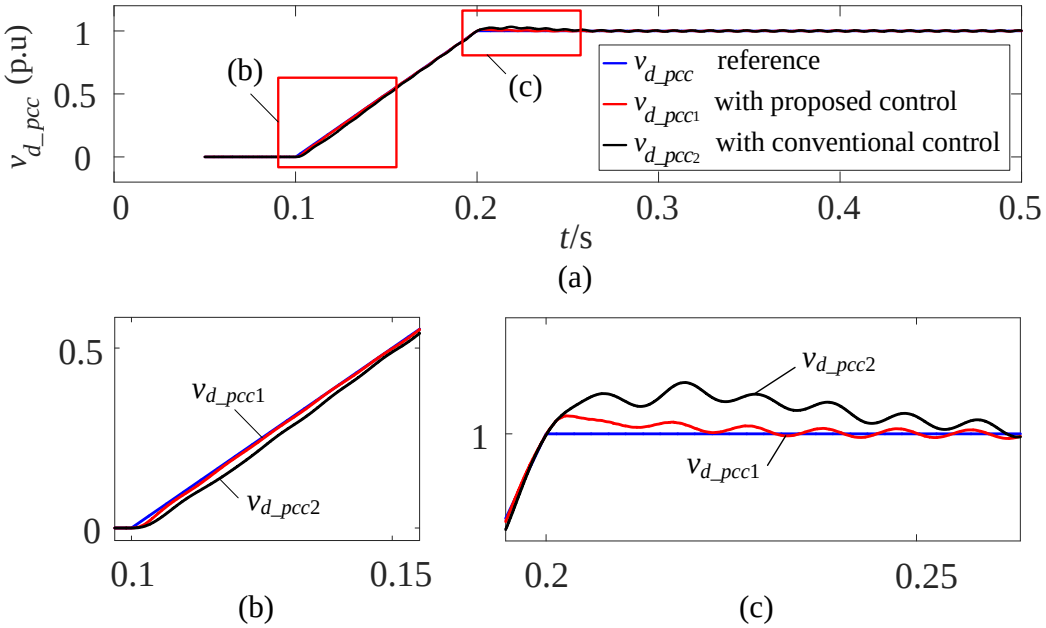

Figure 4.13 Simulation waveforms comparison of AC voltage amplitude on PCC during start-up.

(a) Comparison of *d*-axis PCC voltage with different control strategies, (b) detailed waveforms around 0.1 s, (c) detailed waveforms around 0.2 s.

Figure 4.13 demonstrates that by utilizing the offshore frequency flexibility, the proposed strategy controls the AC voltage of the offshore network more tightly than the conventional approach with fixed offshore frequency. Further studies on the stability of the offshore system with proposed control will be reported in the small-signal analysis in the following chapters.

4.5.2. Wind turbine connection and power ramping up

The three lumped wind turbines are all enabled at 0.5 s and start generating power from 0.7 s. Throughout the process, the DC voltage of the HVDC link is well controlled by the onshore MMC as shown in Figure 4.14 (a). The AC voltage amplitude at the PCC slightly deviates from the reference but is restored quickly during wind power ramp up, demonstrated in Figure 4.14 (b) and (e). As shown in Figure 4.14 (c), (d), the AC currents of the offshore station MMC_1 increases with the increase of the received wind power after 0.7 s. The offshore frequency is also tightly regulated around the reference during wind power increase, benefitting from the proposed frequency control, as shown in Figure 4.15. After t=1.05 s, the power generated by the three wind turbines reaches the rated values, and the offshore MMC operates in steady-state condition and transmits rated power to the onshore side.

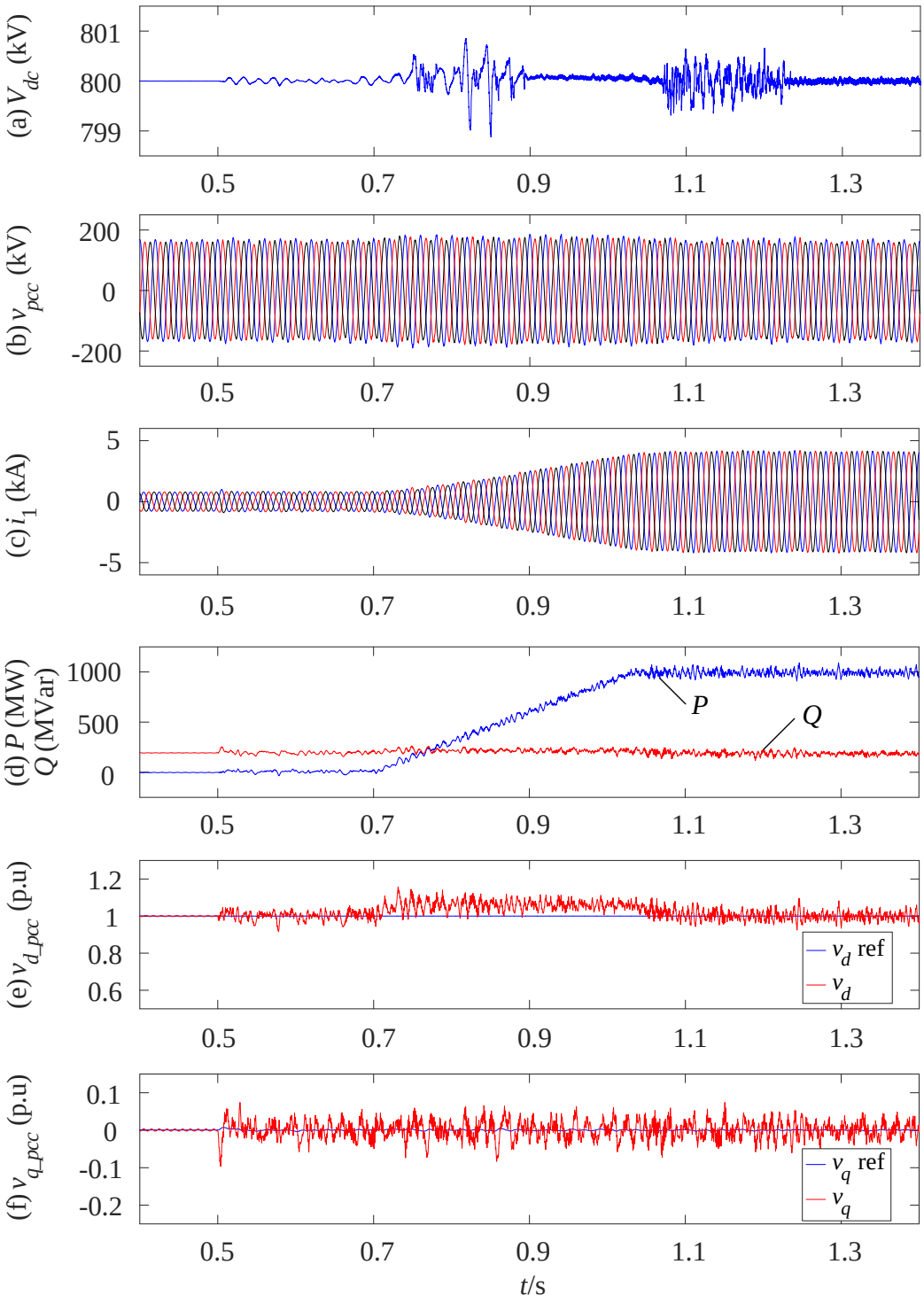

Figure 4.14 Simulation waveforms of offshore station MMC_1 during enable of WTs and power increasing.

(a) DC voltage on HVDC link, (b) three-phase voltage on PCC, (c) three-phase currents i_1, (d). MMC_1 active and reactive power, (e) PCC d-axis voltage, (f) PCC q-axis voltage.

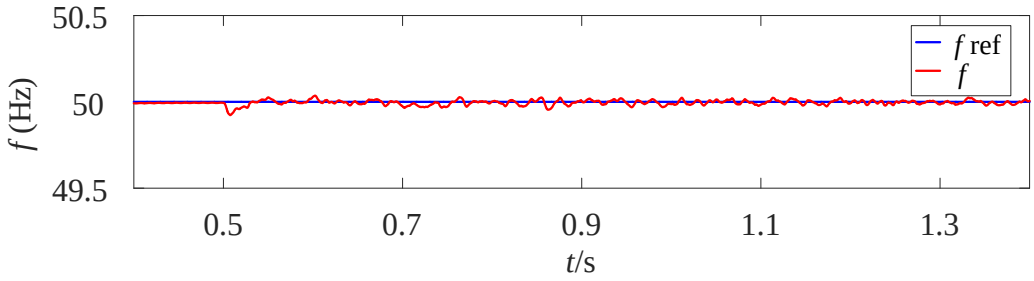

Figure 4.15 Offshore frequency during enable of WTs and power up.

For onshore site, Figure 4.16 shows the onshore AC current and power flow. At t=0.7s, the AC current of onshore MMC_2 begins to increase and MMC_2 starts to receive the active power. In the simulation, the reactive power reference for MMC_2 is set at zero and so as the measured reactive power is always zero as illustrated in Figure 4.16 (b).

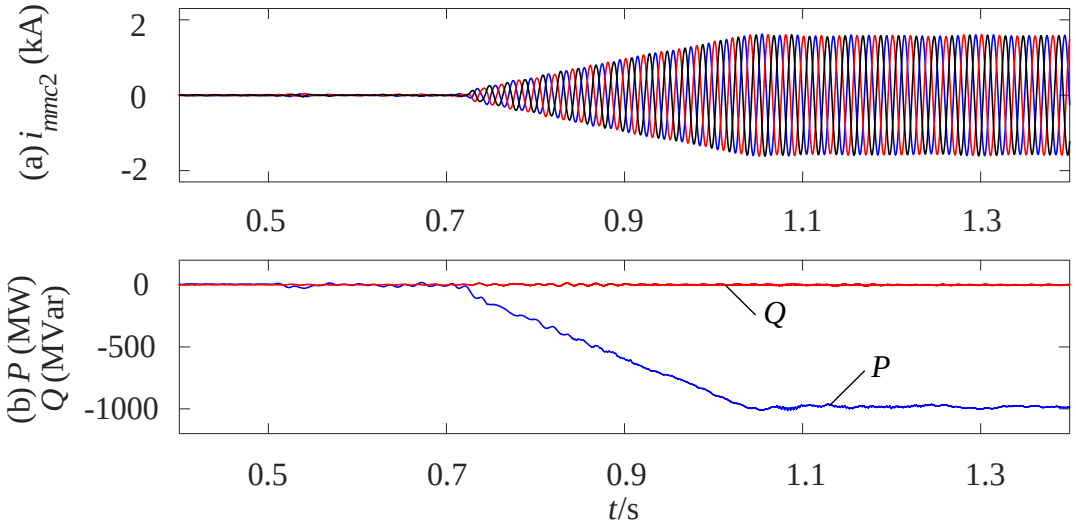

Figure 4.16 Current and power flows at onshore MMC_2 station during connecting of WTs and power ramp up.

(a) Three-phase current at onshore MMC_2 station, (b) active and reactive power received by onshore MMC_2 station.

The current and active and reactive power waveforms of the three WTs are shown in Figure 4.17. As stated, the three WT clusters with respective capacities of 500 MW, 450MW and 50MW are enabled at 0.5 s and ramp up power generation from 0.7 s at a rate of 3 pu/s. At around 1.05 s, the three wind turbine clusters all reach their rated values and operate in stable conditions.

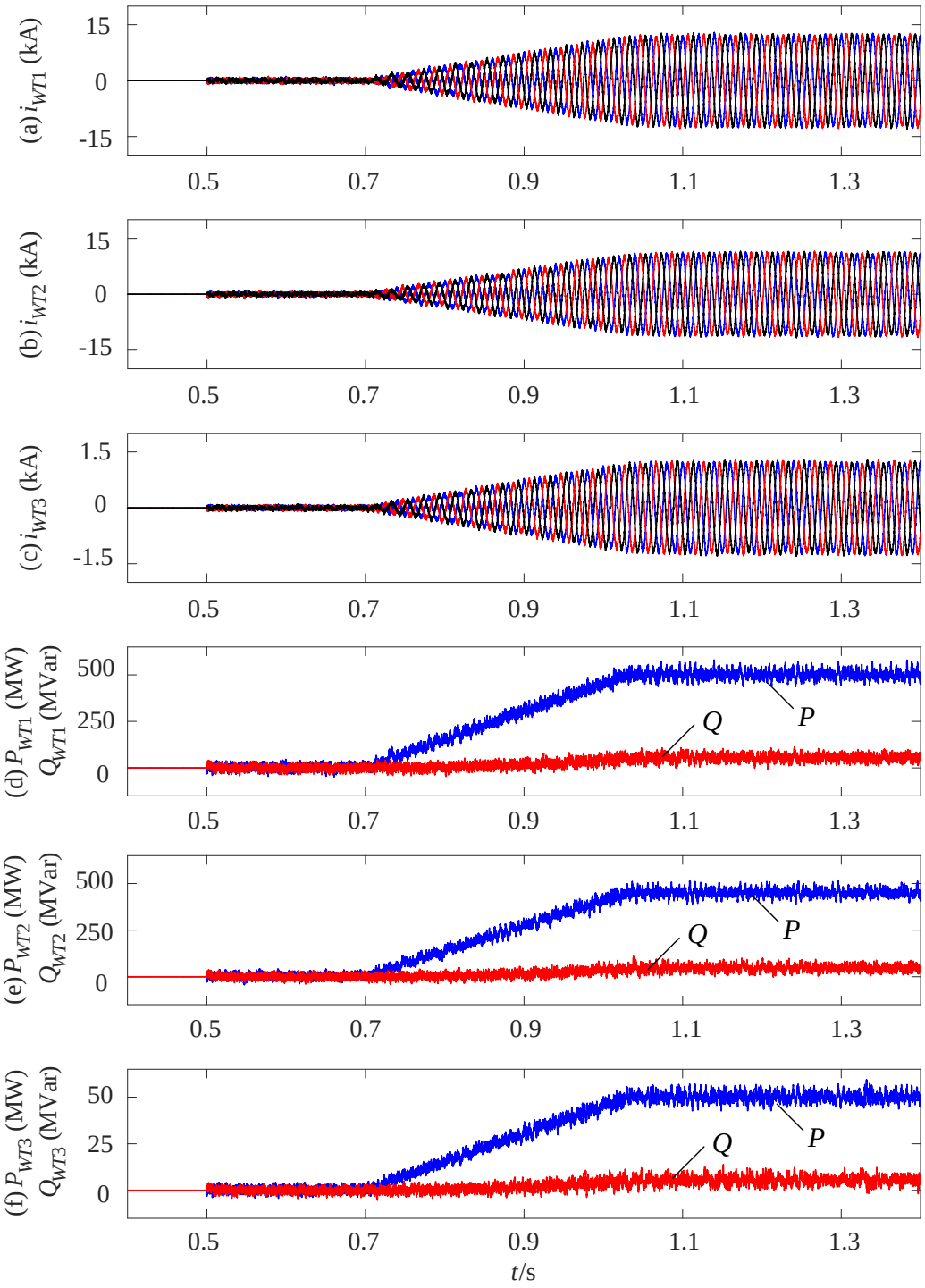

Figure 4.17 AC current and output power on each WT cluster during enable of WTs and power increasing.

(a) Three-phase current of VSC_1, (b) Three-phase current of VSC_2, (c) Three-phase current of VSC_3, (d) active and reactive power generated by VSC_1, (e) active and reactive power generated by VSC_2, (f) active and reactive power generated by VSC_3.

4.5.3. System response during large power step

a) Power step due to WT blocking

To test the response of the system during large transients, simulations are carried out when the 500 MW WT (VSC_1) is suddenly blocked at t=1.5 s (e.g. caused by high wind speed), resulting in the reduction of total generated wind power from 1 pu to 0.5 pu. The simulation results are shown in Figure 4.18. Due to the large power change, the offshore AC voltage fluctuates following the blocking of VSC_1 but is quickly recovered to the rated value, shown in Figure 4.18 (b). To further observe the change on the PCC voltage, the RMS (root mean square) value is shown in Figure 4.18 (f). As seen, the PCC voltage drops to around 0.7 pu at the time when VSC_1 is blocked but recovers within around 0.1 s. The DC voltage also fluctuates as shown in Figure 4.18 (a) because of the sudden power imbalance between the onshore and offshore sites, but it is well controlled by the onshore MMC_2. The current flows through the MMC_1 station is well controlled and gradually reduces to 0.5 pu when the power is reduced to 0.5 pu, as seen in Figure 4.18 (c) and (d). Again, the offshore frequency is well controlled even during such a large transient, as illustrated in Figure 4.18 (e).

The responses of each WT cluster are shown in Figure 4.19. VSC_1 is blocked at 1.5s and its output wind power reduces to zero quickly as shown in Figure 4.19 (a) and (d). However, VSC_2 and VSC_3 are still operating as normal and continue transmitting wind power to the onshore site through MMC_1. Because of the constant output wind power, reduced PCC voltage leads to the temporary increase of the WT current as shown in Figure 4.19 (b) and (c). To protect the WT converters, their currents are limited to 1.2 pu which results in a small dip of active power generation for a short period around 1.5 s as seen from Figure 4.19 (e) and (f). After the recovery of voltage on the PCC bus, the output currents return to the pre-fault values.

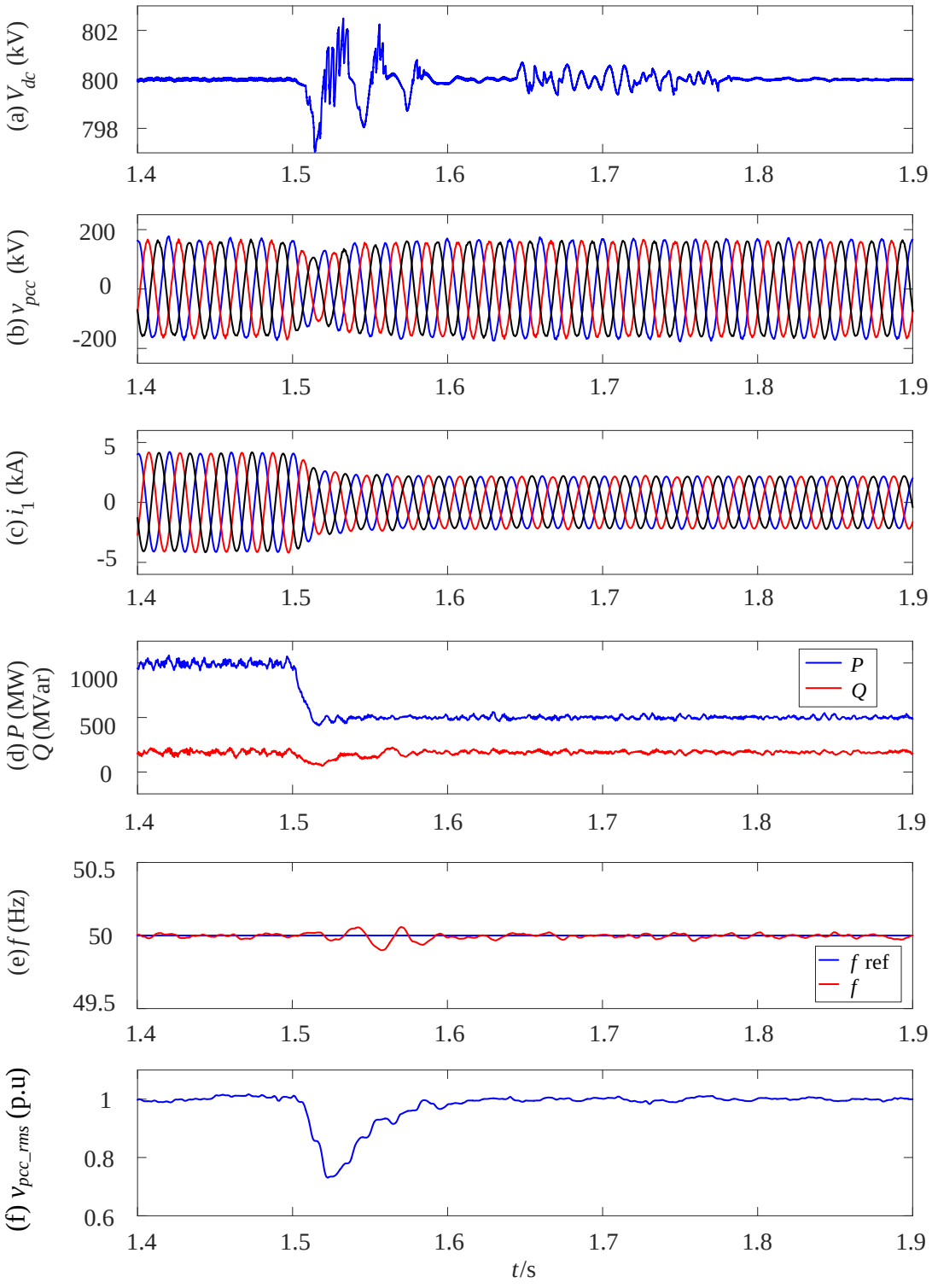

Figure 4.18 Simulation waveforms of offshore station MMC_1 during power step.

(a) DC voltage on HVDC link, (b) three-phase voltage on PCC, (c) three-phase currents i_1, (d). MMC_1 active and reactive power, (e) offshore frequency, (f) PCC RMS voltage.

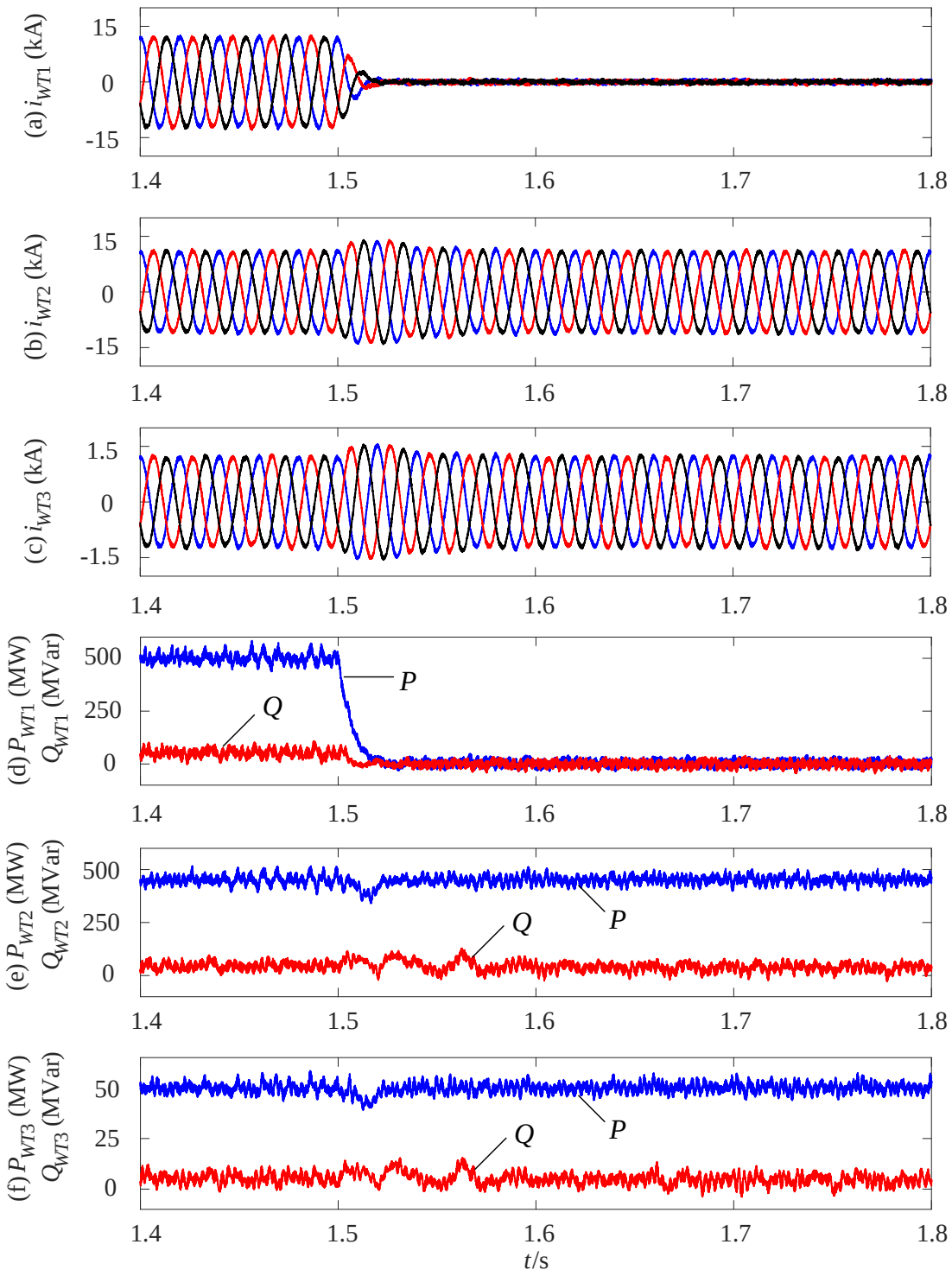

Figure 4.19 AC current and output power on each WT cluster during power step.

(a) Three-phase current of VSC_1, (b) Three-phase current of VSC_2, (c) Three-phase current of VSC_3, (d) active and reactive power generated by VSC_1, (e) active and reactive power generated by VSC_2, (f) active and reactive power generated by VSC_3.

b) Comparisons of the proposed and conventional controls during WT disconnecting

The advantages of the proposed control over conventional method can be further demonstrated by comparing the offshore voltages and currents during a large transient caused by the tripping of a WT cluster. The PCC voltage and the AC current of the offshore MMC are compared in Figure 4.20.

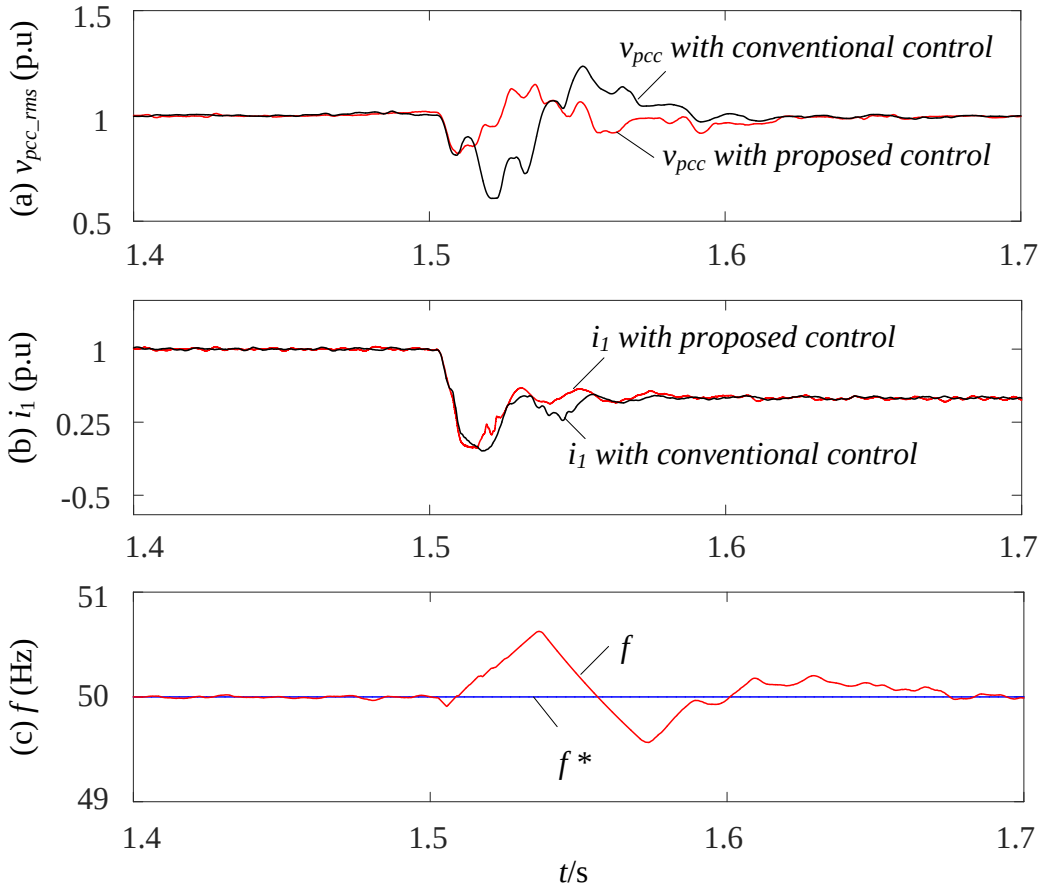

Figure 4.20 Voltage and current comparison during the WT disconnection. (a) PCC RMS voltage, (b) MMC_1 RMS current, (c) Offshore frequency.

At t=1.5 s, WT1 cluster (VSC_1) suddenly disconnects from the PCC bus by opening CB1 (circuit breaker). The total wind power transmitted to offshore MMC station is immediately reduced to 0.5 pu which leads to large transient on the PCC bus voltage. As can be seen, with the proposed control, the offshore voltage is more stable with faster

restoration than that under conventional fixed frequency control, as shown in Figure 4.20 (a). Due to better offshore AC voltage control, the current of the offshore MMC station experiences less disturbance and exhibits better dynamic response with the proposed scheme than the conventional one, as displayed in Figure 4.20 (b). The frequency under the proposed control does have relatively large fluctuations, though the oscillation is still controlled within around ±1% pu.

4.6. Summary

In this chapter, the control and operation of offshore wind farm connected by MMC-HVDC transmission systems are investigated. To analyse the operation process of an offshore wind farm, all the WTs connected in the offshore system are divided into groups and aggregated to WT clusters represented by VSCs.

An enhanced frequency and AC voltage control scheme of the offshore MMC station for wind energy transmission is proposed. An additional frequency loop based on PLL principle is used to set the *q*-axis voltage reference to control the offshore network frequency. With the proposed control, the frequency is tightly regulated through the adjustment of *q*-axis voltage at normal operation and it also allows slightly frequency deviating during transients to improve voltage performance. Simulation studies validated that during start-up and power step, MMC with the proposed enhanced frequency and voltage control presents a faster dynamic response when compared to the conventional method without frequency loop. The effectiveness of the proposed control is further demonstrated during large transients caused by the sudden blocking and tripping of a 0.5 pu WT cluster.

Chapter 5

Small-signal modelling and analysis of offshore AC system

5.1. Introduction

In Chapter 4, an enhanced AC voltage and frequency control method for the offshore MMC was proposed to improve the dynamic response of offshore wind farm. The simulation results in Chapter 4 have shown many advantages of the proposed control method with the additional PLL-based frequency control loop. In this chapter, further studies on the effect of the proposed controller on offshore wind farm system stability are investigated.

Generally, small-signal analysis based on the state space models is utilized to investigate the dynamic response of a system. Thus, in this chapter, the corresponding small-signal state space model of the offshore wind farm system is developed to analyse the system responses and behaviors of the system. The interaction of wind power and offshore voltage is studied using Bode plots and the impacts of control parameters on system stability are examined using pole/zero maps. Moreover, system frequency responses with the proposed and conventional controls are compared.

5.2. Offshore wind farm small-signal modelling

In order to simplify the system structure but keep adequate dynamic response, both the offshore MMC station and VSCs at WT side are modeled as controllable voltage sources. Since the focus of this study is on the offshore AC network, the internal dynamics of the offshore MMC is thus neglected. Transmission cables and transformers are also

represented by equivalent resistors and inductors. The equivalent circuit diagram of the offshore wind farm system is shown in Figure 5.1. To analyse the stability of the offshore wind farm system with enhanced AC voltage control, the system state equations are formed and linearized based on this simplified model.

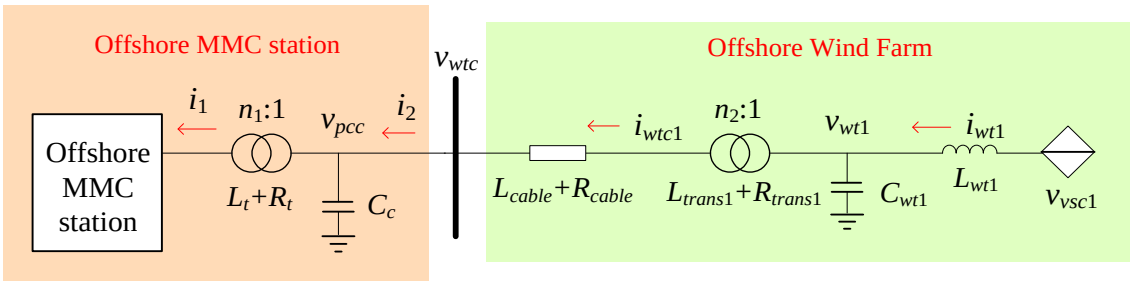

Figure 5.1 Offshore wind farm equivalent circuit.

5.2.1. Offshore MMC small-signal modelling

For system level studies, the average MMC model [116] is usually employed instead of the detailed MMC model. As the focus of this study is the stability of offshore AC system, the DC dynamics of the HVDC system is thus neglected, and the DC voltage is assumed to be controlled to a constant value by the onshore MMC. Besides, as previously described, controllable AC voltage source is used to represent the AC side of the offshore MMC and its internal dynamics, e.g., SM capacitor voltage variation, arm energy balancing, etc., are not considered. Consequently, the small-signal model of the offshore MMC includes the AC side MMC equivalent circuit, the voltage on the PCC bus and the MMC controller.

a) MMC side network system modelling

Using the simplified equivalent MMC circuit, the small-signal model of the MMC and PCC bus can be developed based on the structure shown in Figure 5.2. The transformer is equivalent to a series connected resistance R_t and reactance L_t at the primary side. Dynamic AC voltage which formed by MMC can be calculated using the differential equations on the PCC capacitor and the total inductance L_{total} composed of MMC arm inductance L_{mmc} and transformer inductance L_t.

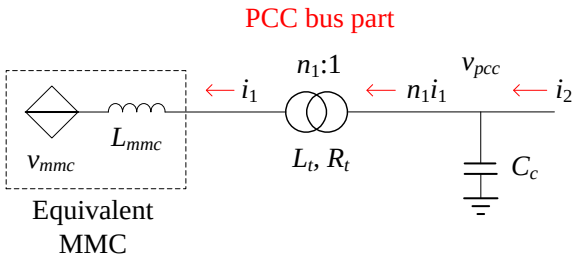

Figure 5.2 The circuit diagram of the PCC side grid connected with equivalent MMC.

The AC voltage on the PCC bus can be defined as:

$$i_2 = n_1 i_1 + C_c \frac{dv_{pcc}}{dt} \tag{5.1}$$

where v_{pcc} is the voltage on PCC bus, i_1 is the MMC current at the primary side of the MMC transformer, i_2 is the current flowing from the offshore WT side, n_1 is the ratio of MMC transformer, C_c represents the cable capacitance at PCC bus or any AC filters installed at the offshore MMC station [117].

Transforming (5.1) into *dq* frame as demonstrated in (4.8) and then expressing the *dq* axis separately:

$$\begin{cases} n_1 i_{1d} = i_{2d} + \omega C_c v_{pccq} - C_c \dfrac{dv_{pccd}}{dt} \\ n_1 i_{1q} = i_{2q} + \omega C_c v_{pccd} - C_c \dfrac{dv_{pccq}}{dt} \end{cases}. \tag{5.2}$$

The equation (5.2) can be linearized at the operating point as:

$$\begin{cases} \Delta \dot{v}_{pccd} = \dfrac{\Delta i_{2d} - n_1 \Delta i_{1d}}{C_c} + \omega_0 \Delta v_{pccq} + \Delta \omega v_{pccq0} \\ \Delta \dot{v}_{pccq} = \dfrac{\Delta i_{2q} - n_1 \Delta i_{1q}}{C_c} - \omega_0 \Delta v_{pccd} - \Delta \omega v_{pccd0} \end{cases}. \tag{5.3}$$

The voltages and currents with Δ denote the terms which are deviated from the operation point, and subscripts *d* and *q* indicate the *d*-axis or *q*-axis components. The equations are linearized at ω_0, v_{pccd0} and v_{pccq0} [118]. By selecting Δv_{pccd} and Δv_{pccq} as the two state

variables, $\Delta\omega$, Δi_{1dq} and Δi_{2dq} as the input signals, the state space matrix can be described as:

$$\begin{bmatrix} \Delta\dot{v}_{pccd} \\ \Delta\dot{v}_{pccq} \end{bmatrix} = \begin{bmatrix} 0 & \omega_0 \\ -\omega_0 & 0 \end{bmatrix} \begin{bmatrix} \Delta v_{pccd} \\ \Delta v_{pccq} \end{bmatrix} + \begin{bmatrix} v_{pccq0} & \dfrac{-n_1}{C_c} & 0 & \dfrac{1}{C_c} & 0 \\ -v_{pccd0} & 0 & \dfrac{-n_1}{C_c} & 0 & \dfrac{1}{C_c} \end{bmatrix} \begin{bmatrix} \Delta\omega \\ \Delta i_{1d} \\ \Delta i_{1q} \\ \Delta i_{2d} \\ \Delta i_{2q} \end{bmatrix}. \quad (5.4)$$

To calculate the MMC current, the differential equation across the impedance between MMC equivalent voltage source and PCC bus on the primary side of the MMC transformer (at MMC side) is given as:

$$n_1 v_{pcc} = v_{mmc} + (L_{mmc} + L_t)\frac{di_1}{dt} + R_t i_1 . \quad (5.5)$$

In (5.5), L_t and R_t are the respective inductance and resistance of the transformer seen at the primary side, v_{mmc} represents MMC equivalent voltage which is obtained from MMC control output. Describe (5.5) under *dq* frame as:

$$\begin{cases} \Delta\dot{i}_{1d} = \dfrac{n_1\Delta v_{pccd} - \Delta v_{mmcd}}{L_{mmc} + L_t} - \dfrac{R_t}{L_{mmc} + L_t}\Delta i_{1d} + \omega_0\Delta i_{1q} + \Delta\omega i_{1q0} \\ \Delta\dot{i}_{1q} = \dfrac{n_1\Delta v_{pccq} - \Delta v_{mmcq}}{L_{mmc} + L_t} - \dfrac{R_t}{L_{mmc} + L_t}\Delta i_{1q} - \omega_0\Delta i_{1d} - \Delta\omega i_{1d0} \end{cases}. \quad (5.6)$$

Linearizing (5.6) at ω_0, i_{1d0} and i_{1q0} and selecting Δi_{1d} and Δi_{1q} as the state variables, the state space equation can be described as:

$$\begin{bmatrix} \Delta\dot{i}_{1d} \\ \Delta\dot{i}_{1q} \end{bmatrix} = \begin{bmatrix} \dfrac{-R_t}{L_{mmc} + L_t} & \omega_0 \\ -\omega_0 & \dfrac{-R_t}{L_{mmc} + L_t} \end{bmatrix} \begin{bmatrix} \Delta i_{1d} \\ \Delta i_{1q} \end{bmatrix} + \begin{bmatrix} i_{1q0} & \dfrac{-1}{L_{mmc} + L_t} & 0 & \dfrac{n_1}{L_{mmc} + L_t} & 0 \\ -i_{1d0} & 0 & \dfrac{-1}{L_{mmc} + L_t} & 0 & \dfrac{n_1}{L_{mmc} + L_t} \end{bmatrix} \begin{bmatrix} \Delta\omega \\ \Delta v_{mmcd} \\ \Delta v_{mmcq} \\ \Delta v_{pccd} \\ \Delta v_{pccq} \end{bmatrix}. \quad (5.7)$$

Combining (5.4) and (5.7), the state space model of the offshore MMC and PCC bus is developed as shown in Figure 5.3.

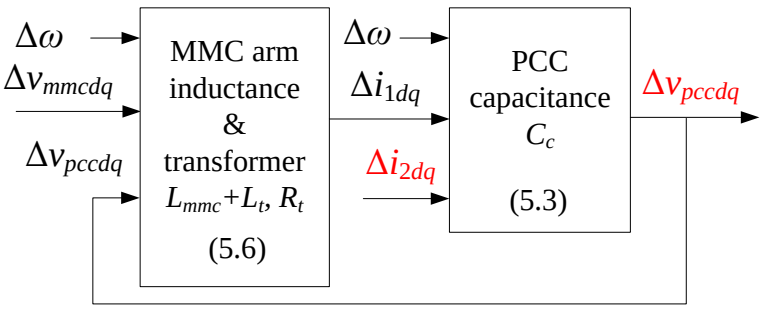

Figure 5.3 State space model of PCC side grid.

b) PLL linearization

A PLL at offshore MMC is employed to track the frequency and phase angle of the offshore network voltage which is used for *dq* transformation and frequency control in the control system. In steady-state condition, the *dq* frame formed by the PLL in the control system is aligned with the plant *dq* frame which defined by the actual grid voltage. However, once a perturbation is added to the grid, an angle difference will arise between the *dq* frame detected by the PLL and the actual plant *dq* frame. Thus, two *dq* frames are required in the model, i.e. the actual plant *dq* frame and the controller *dq* frame [119, 120]. When developing the small-signal model, the angle difference between the two systems needs to be fed into the control loop to represent the effect of the PLL loop dynamics. With the angle difference $\Delta\theta$, as:

$$\Delta\theta = \theta_{plant} - \theta_{pll}\,. \tag{5.8}$$

Signals expressed in the converter control system can be transformed to the actual plant *dq* frame as:

$$x_{plant} = x_{contrl} e^{j\Delta\theta} \tag{5.9}$$

where $x_{control}$ can be the voltage or current signals defined by the PLL with measured phase angle θ_{pll} in the converter control loop, and x_{plant} represents the corresponding voltage or current at the wind farm plant with the actual system angle θ_{plant}. Reformulating this equation by using Euler's formula yields:

$$(x_{cd} + jx_{cq}) = (x_{pd} + jx_{pq})(\cos\Delta\theta - j\sin\Delta\theta) \tag{5.10}$$

where x_{cd} and x_{cq} are the *d*- and *q*-axis components of $x_{control}$. x_{pd} and x_{pq} represent the *d*- and *q*-axis components of x_{plant}. Equation (5.10) can be described in matrix form as:

$$\begin{bmatrix} x_{cd} \\ x_{cq} \end{bmatrix} = \begin{bmatrix} \cos\Delta\theta & \sin\Delta\theta \\ -\sin\Delta\theta & \cos\Delta\theta \end{bmatrix} \begin{bmatrix} x_{pd} \\ x_{pq} \end{bmatrix}. \tag{5.11}$$

For small angle difference $\Delta\theta$ with steady-state operation point θ_{pll0}=0, x_{pd0} and x_{pq0}, (5.11) can be linearized as [118]:

$$\begin{bmatrix} x_{cd} \\ x_{cq} \end{bmatrix} = \begin{bmatrix} x_{pd0} \\ x_{pq0} \end{bmatrix} + \begin{bmatrix} 1 & 0 & x_{pq0} \\ 0 & 1 & -x_{pd0} \end{bmatrix} \begin{bmatrix} \Delta x_{pd} \\ \Delta x_{pq} \\ \Delta\theta \end{bmatrix}. \tag{5.12}$$

This signal transformation needs to be applied before the measured voltage and current signals entering the converter control loop. On the other hand, when the signals are output from the controller, they should also be transformed before being fed to the plant model using the following inverse transformation:

$$\begin{bmatrix} x_{pd} \\ x_{pq} \end{bmatrix} = \begin{bmatrix} x_{cd0} \\ x_{cq0} \end{bmatrix} + \begin{bmatrix} 1 & 0 & -x_{cq0} \\ 0 & 1 & x_{cd0} \end{bmatrix} \begin{bmatrix} \Delta x_{cd} \\ \Delta x_{cq} \\ \Delta\theta \end{bmatrix} \tag{5.13}$$

c) MMC control linearization

The basic MMC control system has been introduced in Chapter 4 and thus will not be repeated here. The MMC control system consists of a frequency control loop, an AC voltage control loop, and a current control loop. The linearized MMC control block diagram which introduced in Chapter 4 is shown in Figure 5.4 at its operation point (variations with subscript 0). The voltages $v_{pccd,control}$ and $v_{pccq,control}$ are the corresponding *d*- and *q*-axis voltage v_{pcc} after doing the PLL angle shift (5.12). The currents $i_{1dq,control}$ and $i_{2dq,control}$ are the currents i_{1dq} and i_{2dq} after the PLL angle shift transforming.

Adding the PLL, the control structure of the MMC system can be demonstrated in Figure 5.5, where the v_{pccdq} and i_{1dq} are the measured network voltage and current, $v_{pccdq,control}$ and $i_{1dq,control}$ are the voltage and current signal at MMC control loop as described in Figure 5.4. Moreover, MMC is assumed to have no control delays, i.e., after

transforming the voltage v_{mmcdq} into three phase form, it is the same with voltage v_{mmc} as shown in Figure 5.2.

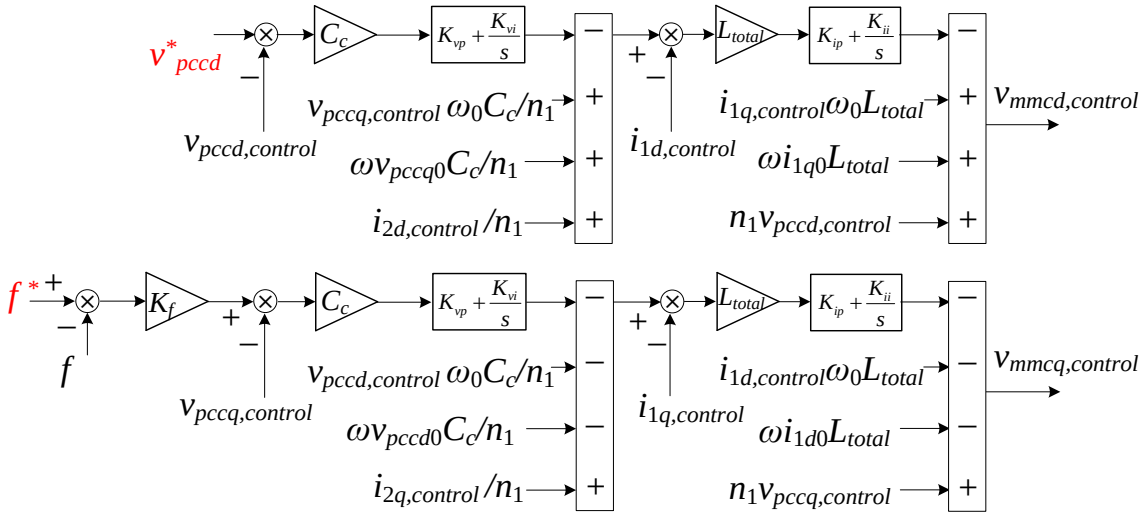

Figure 5.4 Linearized MMC control block diagram.

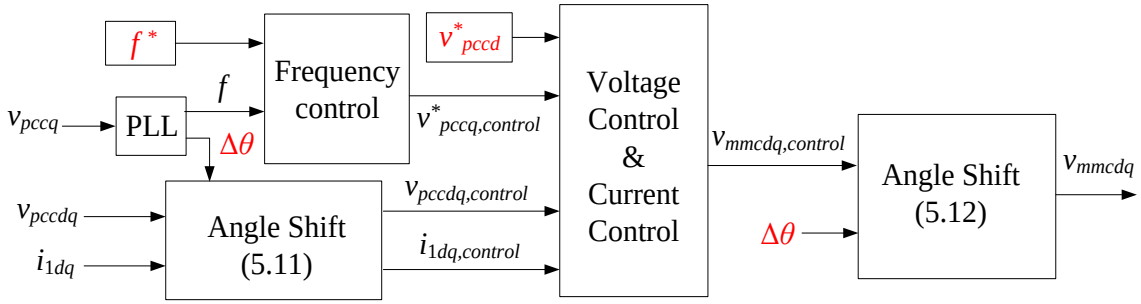

Figure 5.5 Control structure of offshore MMC with PLL angle shift.

d) MMC small-signal model validate

To validate the developed equivalent MMC and PCC side small-signal model, the frequency responses of the linearized MMC state space model are compared to those from the time-domain Simulink model under the same operating condition. The system parameters are listed in Table 5.1.

The Bode plots for the close-loop response (to the reference value) of v_{pccd}, v_{pccq} and f from the two models are compared in Figure 5.6, where the blue curves are from the small-signal model (SS model) with state space equations while the red curves are from

the time-domain non-linear model (TD model). It can be seen from Figure 5.6 that the linearized SS model matches the frequency responses well with the TD model in the frequency range of 0.1 Hz to 1000 Hz. Above 1000 Hz, there are considerable errors between the two models which are primarily caused by the Taylor transformation when applying the SS models. As the main interest of frequency for stability investigation in this thesis is below a few hundred Hertz, the linearized SS model is adequate.

Table 5.1 Parameters on offshore wind farm PCC side.

MMC control parameters		
Frequency loop	K_f	0.5 pu
Voltage loop	$K_{vp}=2\zeta_v(2\pi f_v)$	$K_{vi}=(2\pi f_v)^2$
	f_v	30 Hz
	ζ_v	1.2
Current loop	$K_{ip}=2\zeta_c(2\pi f_c)$	$K_{ii}=(2\pi f_c)^2$
	f_c	50 Hz
	ζ_c	1
MMC grid parameters		
MMC arm inductance L_{mmc}		14 mH (0.1 pu)
Transformer	Ratio n_1	429 kV/200 kV
	Resistance R_t	0.74 Ω (0.004 pu)
	Inductance L_t	64 mH (0.11 pu)
PCC capacitor C_c		7.16 μF

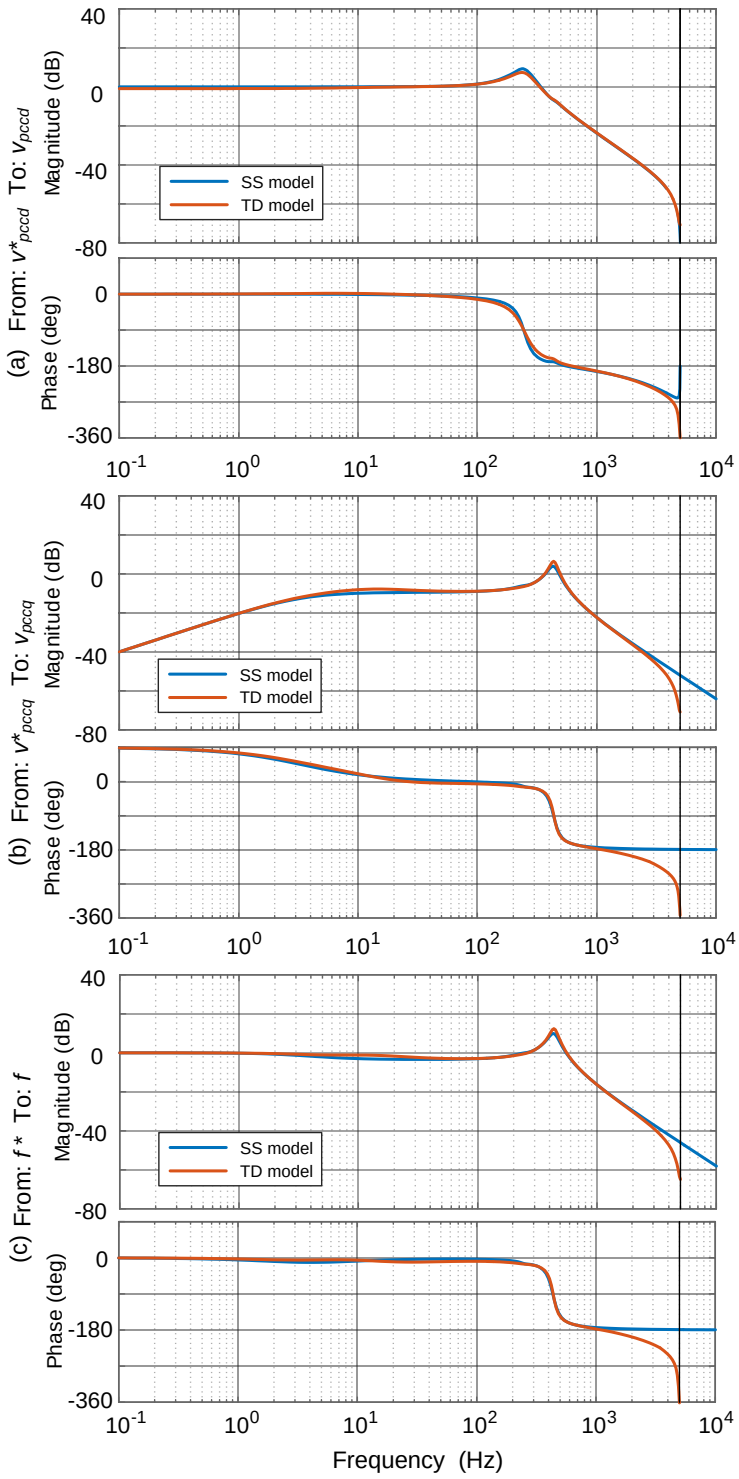

Figure 5.6 Frequency responses comparisons on SS model and TD model at PCC side.

(a) Bode plot of the *d*-axis voltage reference v^*_{pccd} to the *d*-axis voltage v_{pccd}, (b) Bode plot of the *q*-axis voltage reference v^*_{pccq} to the *q*-axis voltage v_{pccq}, (c) Bode plot of frequency reference f^* to frequency *f*.

5.2.2. Offshore wind farm small-signal modelling

In this study, a lumped WT model is considered and is represented by a controllable voltage source as shown in Figure 5.1. The WT transformer and transmission cable are again represented by equivalent inductance and resistance as shown in Figure 5.1. Although only one WT model is considered in the study, the developed model can be extended to multiple WTs by considering the interconnection cables between different WT converters.

a) WT cluster equivalent

As shown in Figure 5.1, to describe the dynamic response at WT cluster side, the relationship between the output current and voltage on WT converter is given as:

$$v_{vsc1} = v_{wt1} + L_{wt1}\frac{di_{wt1}}{dt} \tag{5.14}$$

where v_{vsc1} is the VSC AC output voltage and i_{wt1} is the VSC output current. L_{wt1} is the inductance of the VSC filter while v_{wt1} is the voltage at WT filter side. Transforming (5.14) into *dq* frame yields:

$$\begin{cases} \Delta\dot{i}_{wt1d} = \dfrac{\Delta v_{vsc1d} - \Delta v_{wt1d}}{L_{wt1}} + \omega_0 \Delta i_{wt1q} + \Delta\omega i_{wt1q0} \\ \Delta\dot{i}_{wt1q} = \dfrac{\Delta v_{vsc1q} - \Delta v_{wt1q}}{L_{wt1}} - \omega_0 \Delta i_{wt1d} - \Delta\omega i_{wt1d0} \end{cases}. \tag{5.15}$$

Assuming the steady-state operating point of VSC is ω_0, i_{wt1d0} and i_{wt1q0} and by selecting Δi_{wt1d} and Δi_{wt1q} as the state variables, the state space equation of (5.15) can be described as:

$$\begin{bmatrix} \Delta\dot{i}_{wt1d} \\ \Delta\dot{i}_{wt1d} \end{bmatrix} = \begin{bmatrix} 0 & \omega_0 \\ -\omega_0 & 0 \end{bmatrix} \begin{bmatrix} \Delta i_{wt1d} \\ \Delta i_{wt1q} \end{bmatrix} + \begin{bmatrix} i_{wt1q0} & \dfrac{1}{L_{wt1}} & 0 & \dfrac{-1}{L_{wt1}} & 0 \\ -i_{wt1d0} & 0 & \dfrac{1}{L_{wt1}} & 0 & \dfrac{-1}{L_{wt1}} \end{bmatrix} \begin{bmatrix} \Delta\omega \\ \Delta v_{vsc1d} \\ \Delta v_{vsc1q} \\ \Delta v_{wt1d} \\ \Delta v_{wt1q} \end{bmatrix}. \tag{5.16}$$

The dynamics of the voltage on the capacitor of the WT filter can be defined as:

$$i_{wt1} = n_2 i_{wtc1} + C_{wt1} \frac{dv_{wt1}}{dt} \tag{5.17}$$

where i_{wtc1} is the three-phase currents at WT transmission cable, C_{wt1} is the capacitance of the WT filter and n_2 is the VSC transformer ratio. Transforming (5.17) into *dq* frame and expressing at the operating point yield:

$$\begin{cases} \Delta \dot{v}_{wt1d} = \dfrac{\Delta i_{wt1d} - n_2 \Delta i_{wtc1d}}{C_{wt1}} + \omega_0 \Delta v_{wt1q} + \Delta \omega v_{wt1q0} \\ \Delta \dot{v}_{wt1q} = \dfrac{\Delta i_{wt1q} - n_2 \Delta i_{wtc1q}}{C_{wt1}} - \omega_0 \Delta v_{wt1d} - \Delta \omega v_{wt1d0} \end{cases} \tag{5.18}$$

where v_{wt1d0} and v_{wt1q0} are the voltage operating points. By selecting Δv_{wt1d} and Δv_{wt1q} as the state variables, (5.18) is then expressed in state space format as:

$$\begin{bmatrix} \Delta \dot{v}_{wt1d} \\ \Delta \dot{v}_{wt1q} \end{bmatrix} = \begin{bmatrix} 0 & \omega_0 \\ -\omega_0 & 0 \end{bmatrix} \begin{bmatrix} \Delta v_{wt1d} \\ \Delta v_{wt1q} \end{bmatrix} + \begin{bmatrix} v_{wt1q0} & \dfrac{1}{C_{wt1}} & 0 & \dfrac{-n_2}{C_{wt1}} & 0 \\ -v_{wt1d0} & 0 & \dfrac{1}{C_{wt1}} & 0 & \dfrac{-n_2}{C_{wt1}} \end{bmatrix} \begin{bmatrix} \Delta \omega \\ \Delta i_{wt1d} \\ \Delta i_{wt1q} \\ \Delta i_{wtc1d} \\ \Delta i_{wtc1q} \end{bmatrix}. \tag{5.19}$$

According to Figure 5.1, there are:

$$\begin{aligned} L_{wtc1} &= L_{cable} + L_{trans1} \\ R_{wtc1} &= R_{cable} + R_{trans1} \end{aligned} \tag{5.20}$$

$$n_2 v_{wt1} = v_{wtc} + L_{wtc1} \frac{di_{wtc1}}{dt} + R_{wtc1} i_{wtc1} \tag{5.21}$$

where R_{trans} and R_{cable} are the resistances of WT transformer and transmission cable respectively, L_{trans} and L_{cable} are the inductances of WT transformer and transmission cable respectively. Similarly, linearizing (5.21) in dq frame yields:

$$\begin{cases} \Delta\dot{i}_{wtc1d} = \dfrac{n_2\Delta v_{wt1d} - \Delta v_{wtcd}}{L_{wtc1}} - \dfrac{R_{wtc1}}{L_{wtc1}}\Delta i_{wtc1d} + \omega_0\Delta i_{wtc1q} + \Delta\omega i_{wtc1q0} \\ \Delta\dot{i}_{wtc1q} = \dfrac{n_2\Delta v_{wt1q} - \Delta v_{wtcq}}{L_{wtc1}} - \dfrac{R_{wtc1}}{L_{wtc1}}\Delta i_{wtc1q} - \omega_0\Delta i_{wtc1d} - \Delta\omega i_{wtc1d0} \end{cases} . \quad (5.22)$$

In the equations, i_{wt1d0} and i_{wt1q0} are the steady-state points. Selecting state variables Δi_{wt1d} and Δi_{wt1q}, the state space equation can be described as:

$$\begin{bmatrix} \Delta\dot{i}_{wtc1d} \\ \Delta\dot{i}_{wtc1q} \end{bmatrix} = \begin{bmatrix} -\dfrac{R_{t1}}{L_{t1}} & \omega_0 \\ -\omega_0 & -\dfrac{R_{t1}}{L_{t1}} \end{bmatrix} \begin{bmatrix} \Delta i_{wtc1d} \\ \Delta i_{wtc1q} \end{bmatrix} + \begin{bmatrix} i_{wtc1q0} & \dfrac{n_2}{L_{t1}} & 0 & \dfrac{-1}{L_{t1}} & 0 \\ -i_{wtc1d0} & 0 & \dfrac{n_2}{L_{t1}} & 0 & \dfrac{-1}{L_{t1}} \end{bmatrix} \begin{bmatrix} \Delta\omega \\ \Delta v_{wt1d} \\ \Delta v_{wt1q} \\ \Delta v_{wtcd} \\ \Delta v_{wtcq} \end{bmatrix} . \quad (5.23)$$

As shown in Figure 5.1, the current i_2 injected to the PCC bus is equals to the i_{wtc1}.

b) WT control linearization

As described in Chapter 4, WT side VSC control system includes the PLL control, power control and current control. Linearizing the power control loop and current control loop at its operation point (variations with subscript 0), the WT control diagram can be described as Figure 5.7.

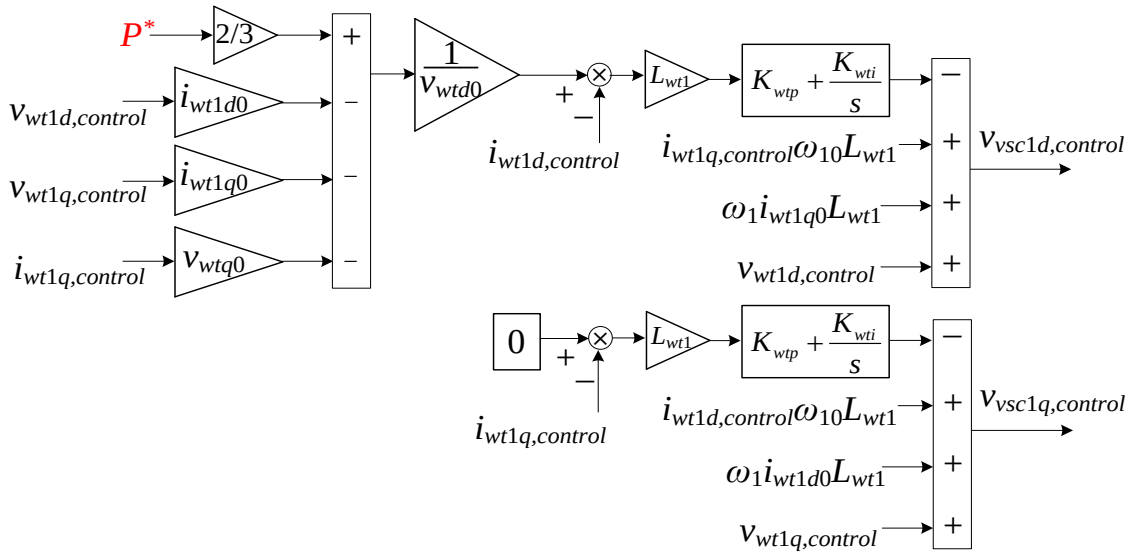

Figure 5.7 Linearized control diagram on WT VSC.

It should be noticed that the voltages and currents with subscript *control* are all the signals applying at control loop, which have been transformed by PLL angle shift.

The small-signal model of the complete WT system is expressed in Figure 5.8. As seen in Figure 5.8, v_{wt1dq} and i_{wt1dq} are the grid measured voltage and current, $v_{wt1dq,control}$ and $i_{wt1dq,control}$ are the control signals which have been corrected by PLL angle difference $\Delta\theta_{wt}$ and are then fed to the control loop as demonstrated in Figure 5.7, $v_{vsc1dq,control}$ is the output voltage of VSC control loop while v_{vsc1dq} is the VSC output voltage after the angle compensation.

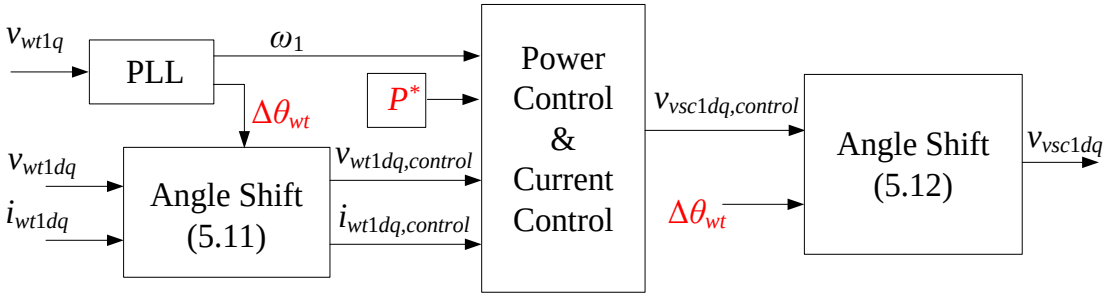

Figure 5.8 The entire control structure of WT with PLL angle shift.

c) WT small-signal model validation

To validate the accuracy of the WT converter side small-signal model, the frequency responses from its corresponding SS model and TD model are compared in Figure 5.9 with the parameters shown in Table 5.2.

From Figure 5.9 (a), active power responses (from power to reference power) of the two models when the WT is connected to a stable AC source match well in the frequency range of 0.1 HZ to 1000 Hz. Similar trends can be observed in the i_{wt1d} and i_{wt1q} responses shown in Figure 5.9 (b) and (c), where the blue curves from the SS model with state space equations perfectly match to the red curves from the TD model. These results indicate that the SS model of WT side can reflect the features of actual WT model within the specific frequency range.

Table 5.2 Parameters at offshore wind farm WT side.

VSC control parameters		
PLL	$K_{PLLp}=2\zeta_{PLL}(2\pi f_{PLL})$	$K_{PLLi}=(2\pi f_{PLL})^2$
	f_{PLL}	10 Hz
	ζ_{PLL}	1
Current loop	$K_{wtp}=2\zeta_{WT}(2\pi f_{wt})$	$K_{wti}=(2\pi f_{wt})^2$
	f_{wt}	50 Hz
	ζ_{wt}	1
VSC grid parameters		
VSC inductance L_{wt1}		1.4 mH (0.2 pu)
VSC capacitor C_{wt1}		219 μF (0.15 pu)
Transformer	Ratio n_2	200 kV/33 kV
	Resistance R_t	0.32 Ω (0.004 pu)
	Inductance L_t	25.5 mH (0.1 pu)
Cable	Resistance R_c	0.15 Ω
	Inductance L_c	3 mH

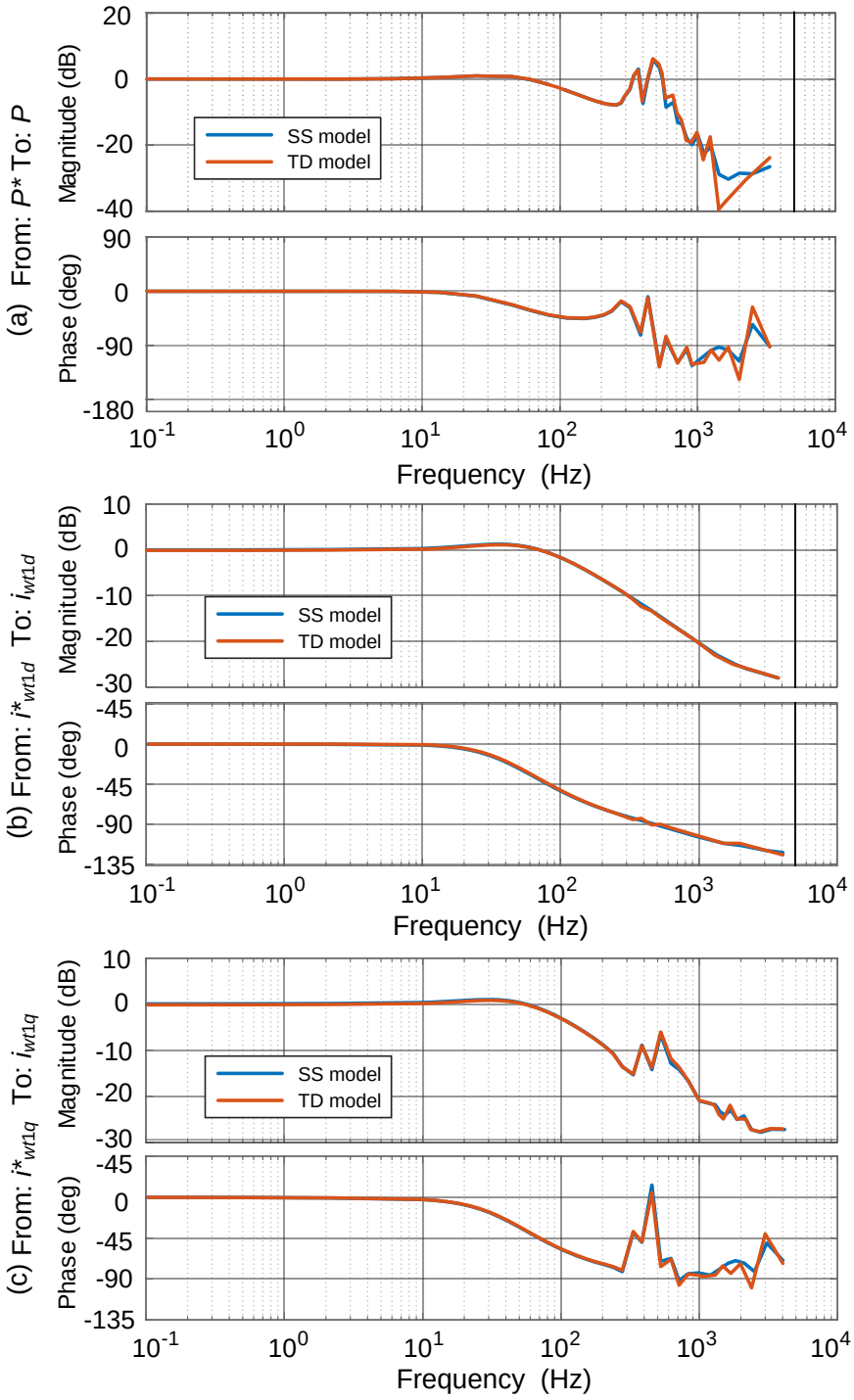

Figure 5.9 Frequency response comparisons between the SS model and TD model at WT side.

(a) Bode plot of the WT power reference P^* to the power P, (b) Bode plot of the WT d-axis current reference i^*_{wt1d} to the d-axis current i_{wt1d}, (c) Bode plot of the WT q-axis current reference i^*_{wt1q} to the q-axis current i_{wt1q}.

5.2.3. Small-signal modelling of the complete offshore system

In the previous small-signal modelling approach, the offshore wind farm system is divided into the PCC MMC part and WT part. Each part is modeled on their own *dq* reference frame defined by their PLL as shown in Figure 5.10.

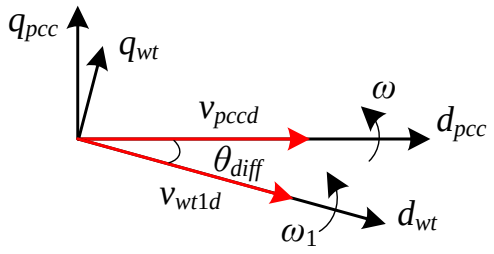

Figure 5.10 Reference frame transformation

To connect the PCC MMC part SS model and WT side SS model, the angle shift between the two *dq* frames should be considered [118]. In Figure 5.10, the angle difference θ_{diff} is calculated as:

$$\theta_{diff} = \theta_{pcc} - \theta_{wt} = (\omega - \omega_1)t \tag{5.24}$$

where the θ_{pcc} and ω are obtained from the PLL at offshore MMC station, and the θ_{wt} and ω_1 are obtained from the PLL of the WT side VSC. To translate the PCC voltage which is formed by the MMC to the WT side *dq* frame, the angle shift matrix should be implemented, and the corresponding voltage can be calculated as:

$$\begin{bmatrix} v_{wtcd} \\ v_{wtcq} \end{bmatrix} = \begin{bmatrix} \cos\theta_{diff} & -\sin\theta_{diff} \\ \sin\theta_{diff} & \cos\theta_{diff} \end{bmatrix} \begin{bmatrix} v_{pccd} \\ v_{pccq} \end{bmatrix}. \tag{5.25}$$

By applying (5.25), the voltage v_{pccdq} under MMC *dq* frame is transferred to WT side *dq* frame expressed as v_{wtcdq}.

To translate the output current from WT side under WT *dq* frame to the PCC side, the inverse transformation is required as:

$$\begin{bmatrix} i_{2d} \\ i_{2q} \end{bmatrix} = \begin{bmatrix} \cos\theta_{diff} & \sin\theta_{diff} \\ -\sin\theta_{diff} & \cos\theta_{diff} \end{bmatrix} \begin{bmatrix} i_{wtc1d} \\ i_{wtc1q} \end{bmatrix} \tag{5.26}$$

where i_{2dq} is the current under MMC dq frame and the current i_{wtc1dq} is the original WT output current under WT side VSC dq frame.

With the angle shift, the PCC side voltage signal which has transformed to WT dq frame can be fed into WT side SS model. This equally applies to the WT side, where WT current after the inverse angle shift can be fed to PCC side SS model. It also need to note the voltages and currents are all measured from the network and thus, before fed into the control loop from plant, they need to apply the angle shift as described in (5.12) and (5.13).

Figure 5.11 shows the SS model of the entire offshore wind farm system corresponding to the TD model shown in Figure 5.1.

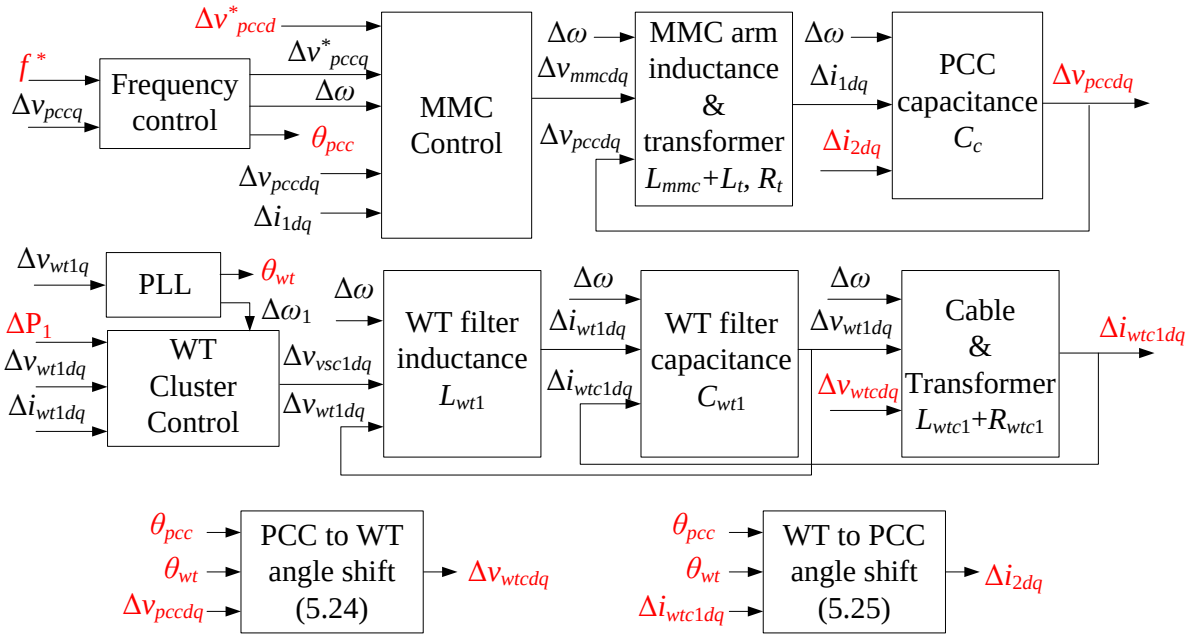

Figure 5.11 SS model of the offshore wind farm system.

5.2.4. Offshore wind farm small-signal model validation

To validate the effectiveness and accuracy of the developed offshore wind farm SS model and investigate the interactions between the WTs output power and AC voltage on PCC bus, power and voltage disturbance are introduced at the SS and TD offshore wind farm system models, and their simulation results are compared.

a) Power disturbance

In this section, a small power disturbance is induced at WT side. At t=2.5 s, the reference output power of VSC_1 (WT) increases by 1%, and as shown in Figure 5.12 (a) and (b), the increased power leads to oscillations at both PCC d-axis and q-axis voltages. The results show a good match between the SS model and the TD model. The power perturbation also leads to the frequency oscillation on PCC bus. As illustrated in Figure 5.12 (c), frequency swing occurs at t=2.5 s but quickly recovers to its rated value.

At the WT side, the 1% increase of wind power results in the increased d-axis output current of VSC_1 as shown in Figure 5.13 (a). The changing on the d-axis current affects the PCC voltage and thus leads to small q-axis current oscillation, as shown in Figure 5.13 (b). The output power of VSC_1 is demonstrated in Figure 5.13 (c), an 1% increase in its value can be seen after t=2.5 s.

From Figure 5.12 and Figure 5.13, the accuracy of the small-signal model can be confirmed during power disturbance on the offshore wind farm system. The waveforms from the SS model are in good agreement with those obtained from the TD model.

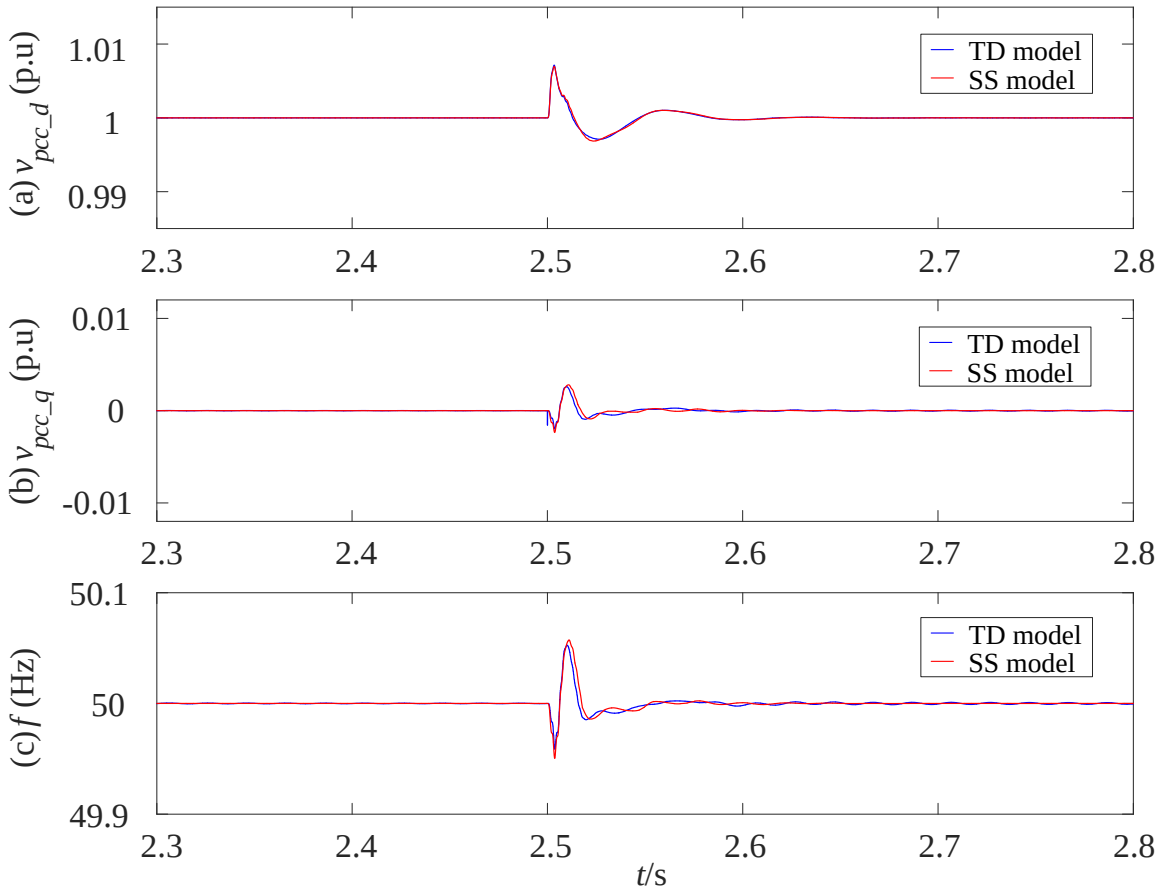

Figure 5.12 Comparisons of PCC voltage and frequency from TD and SS model during the power disturbance.

(a) PCC bus *d*-axis voltage comparison on TD model and SS model, (b) PCC bus *q*-axis voltage comparison on TD model and SS model. (c) frequency of PCC bus comparison on TD model and SS model.

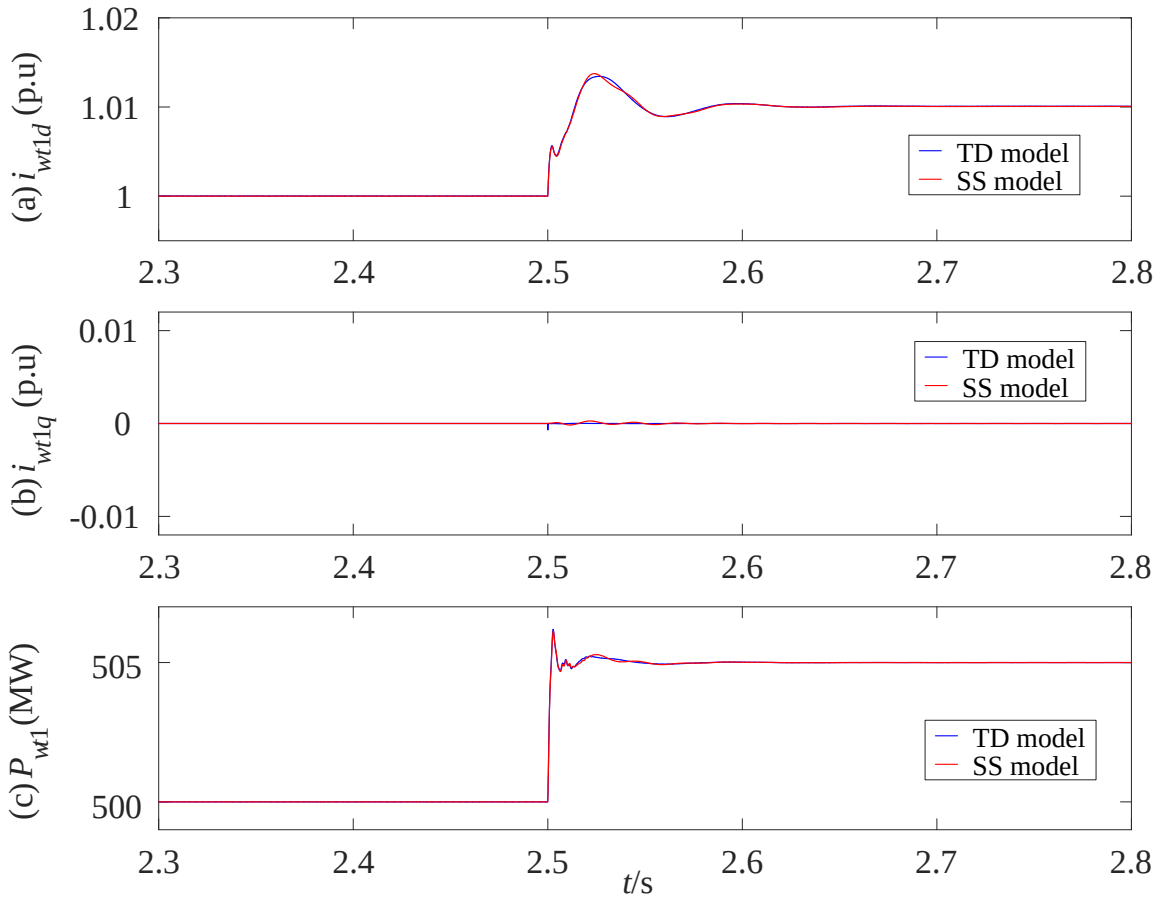

Figure 5.13 VSC_1 current and power responses comparisons during the power disturbance.

(a) VSC_1 *d*-axis current comparison on TD model and SS model, (b) VSC_1 *q*-axis current comparison on TD model and SS model, (c) power comparison on TD model and SS model at VSC_1.

b) Voltage disturbance

To further validate the small-signal model, 1% voltage disturbance is applied at the PCC bus. The reference *d*-axis voltage on the PCC bus which is controlled by the MMC is increased by 1% at t=2.5 s and Figure 5.14 (a) shows the measured PCC *d*-axis voltage from the TD model and SS model. As seen in Figure 5.14 (b) and (c), both the PCC *q*-axis voltage and the frequency are also affected by the voltage disturbance. Good agreements between the waveforms of the SS and TD model are observed.

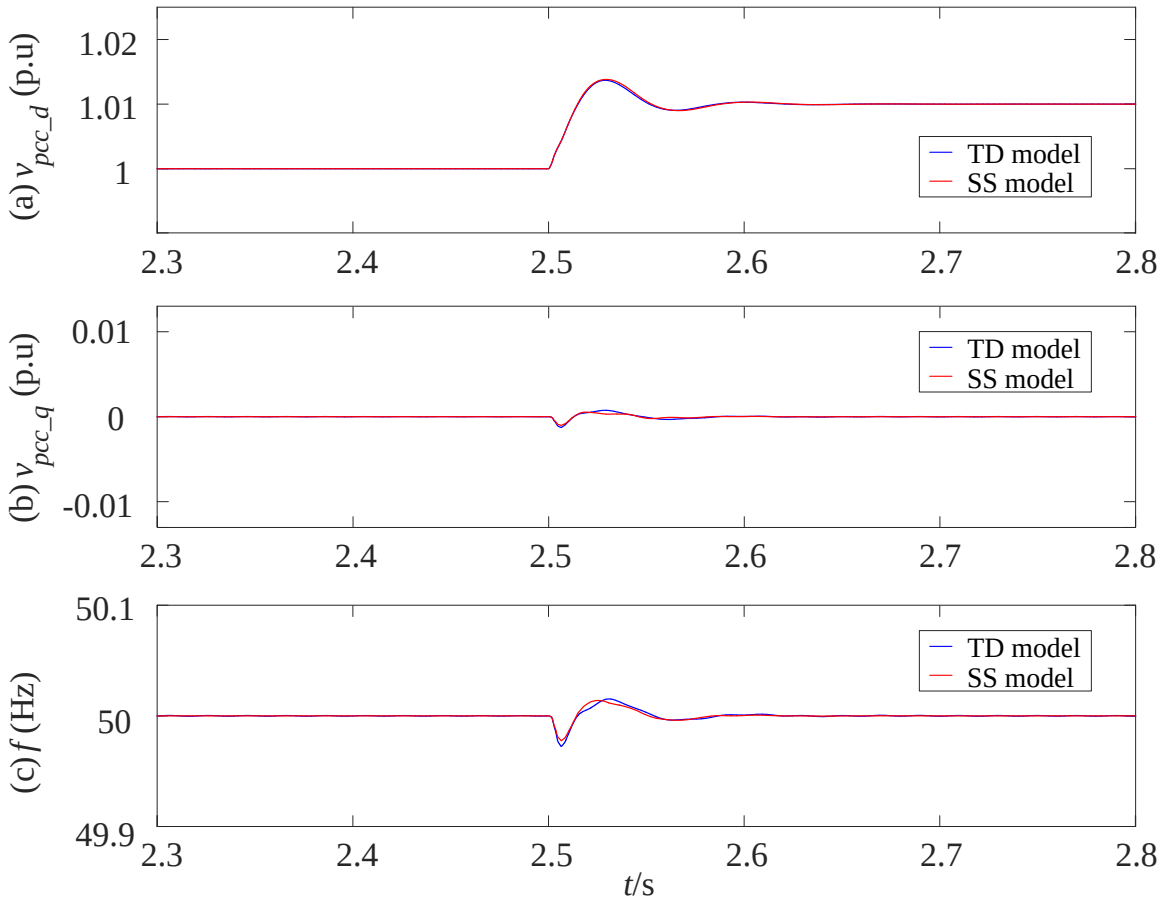

Figure 5.14 PCC voltage and frequency responses comparisons during voltage oscillation.

(a) PCC bus *d*-axis voltage comparison on TD model and SS model, (b) PCC bus *q*-axis voltage comparison on TD model and SS model, (c) frequency of PCC bus comparison on the TD model and SS model.

The increase of voltage on PCC bus leads to the WT side output current reduction due to fixed wind power output, as shown in Figure 5.15 (a) and (c). Small oscillations appear on WT *q*-axis current caused by the PCC bus voltage disturbance, shown in Figure 5.15 (b). Again, the waveforms match well between the two models.

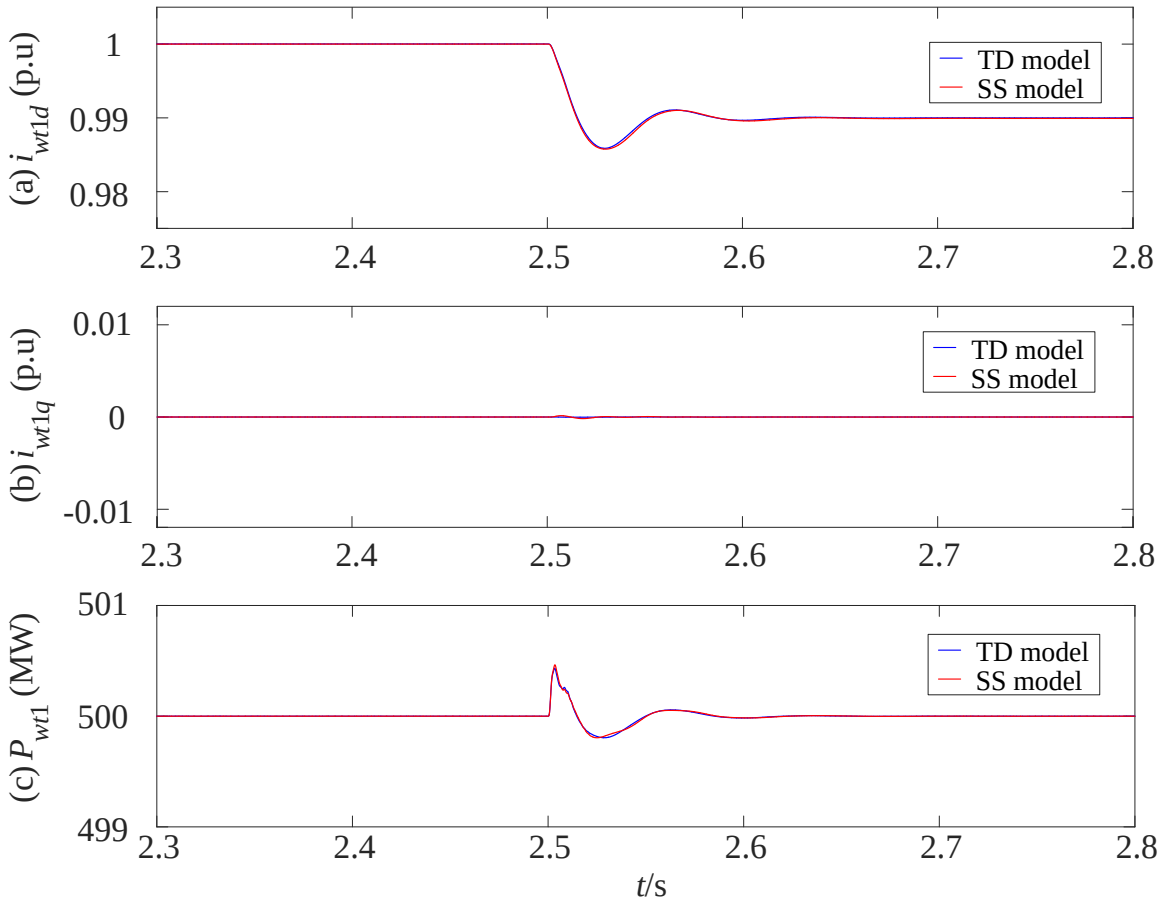

Figure 5.15 VSC_1 current and power responses comparisons during the voltage disturbance.

(a) *d*-axis current comparison on TD model and SS model at VSC_1, (b) *q*-axis current comparison on TD model and SS model at VSC_1, (c) power comparison on TD model and SS model at VSC_1.

5.3. Stability analysis with small-signal model of offshore wind farm

In this section, the Bode plots from the developed small-signal offshore system model are used to analyse system frequency response of the offshore wind farm with the proposed frequency control. By applying the pole/zero map (p/z map), the impacts of different parameters of frequency control and voltage control on system stability are analysed.

5.3.1. Stability analysis of PLL based frequency loop

With the linearized SS model, the performance of PLL based frequency control loop is analysed by considering the transfer functions across the frequency reference f^* to measured frequency f. The corresponding Bode plot is shown in Figure 5.16. As can be seen, the stability of the system with frequency control can be ensured.

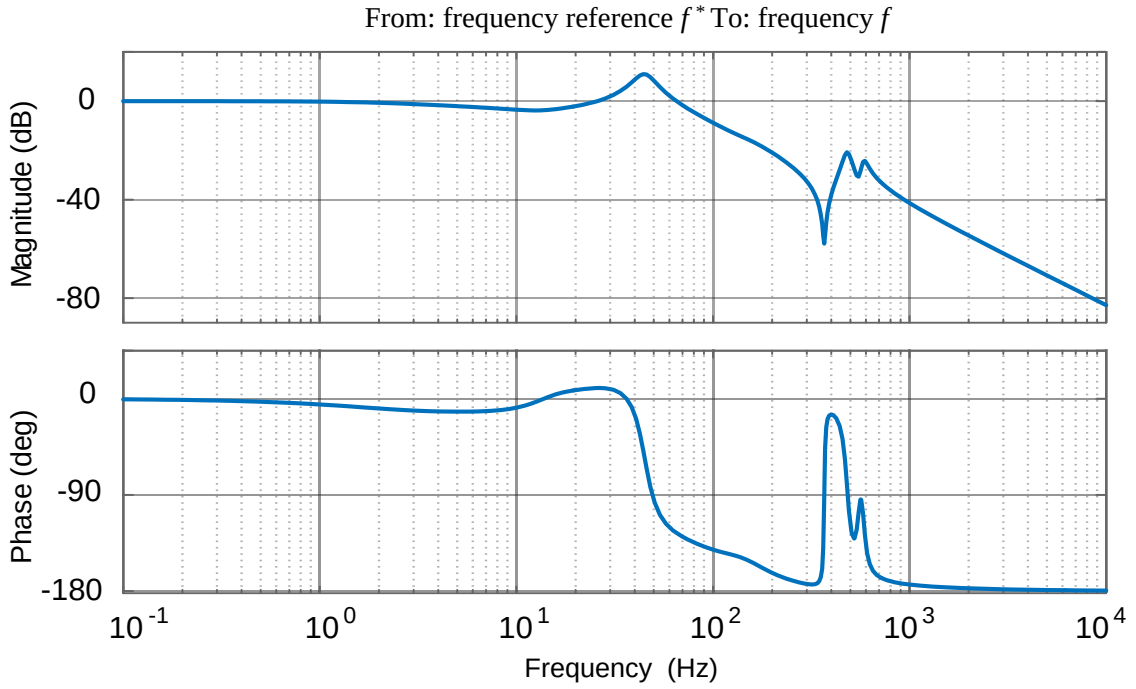

Figure 5.16 Bode plot of the frequency control loop.

To study the impact of the frequency loop parameter K_f (as shown in Figure 4.8 and Table 5.1) on system stability, the p/z map is published with the K_f increasing from 0.05 pu to 15 pu (with f=50 Hz and v_{pccq}=350 kV set as rated values), while the other parameters are set as listed in Table 5.1 and Table 5.2. After the K_f increases from 0.186 pu to 0.2 pu, all the poles are located at the left half plane, and this stipulates that the system is stable.

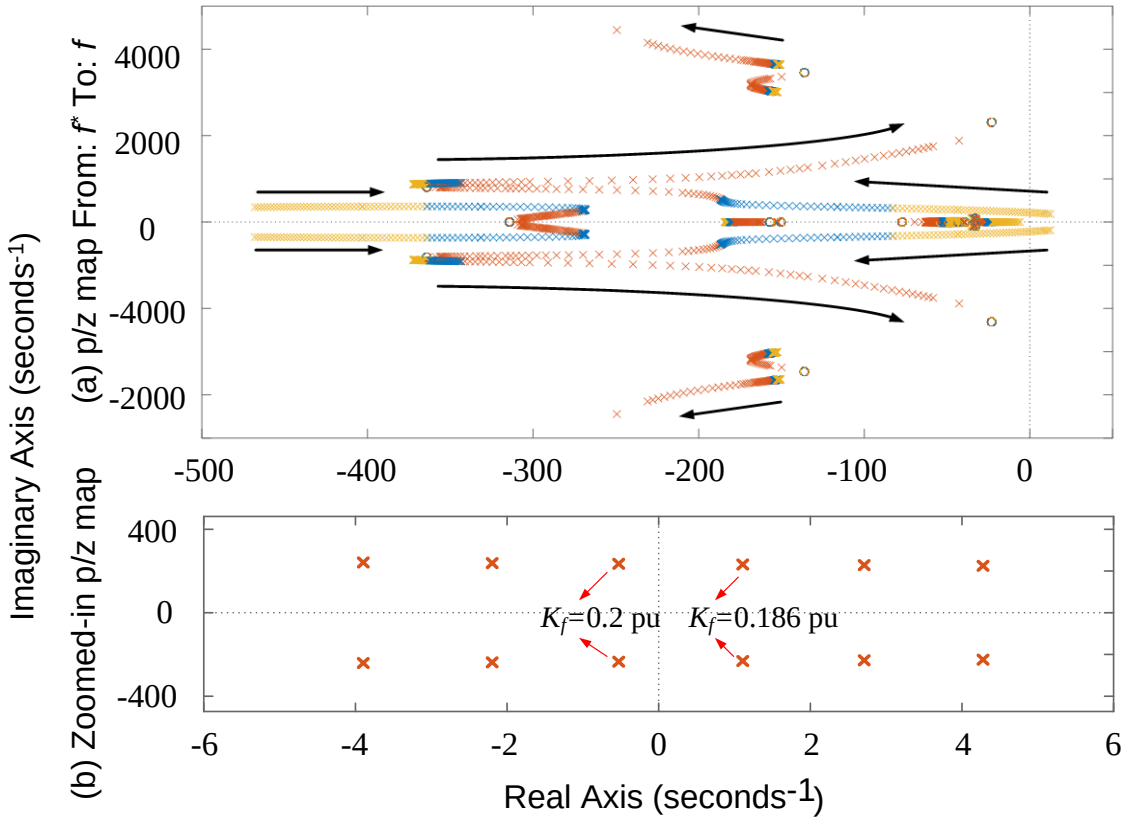

Figure 5.17 The p/z map of PCC voltage with variable K_f.

(a) The p/z map of system frequency when K_f increases from 0.05pu to 30 pu, (b) the zoomed-in p/z map when K_f increases from 0.186 pu to 0.2 pu.

By changing the frequency loop parameter K_f from 0.186 pu to 0.2 pu, the frequency and voltage on the PCC bus from the time-domain model are illustrated in Figure 5.18. Before 0.6 s, K_f=0.186 pu, and as shown in Figure 5.18 (a), (b) and (c), the frequency, *d*-axis PCC voltage and *q*-axis PCC voltage are all diverged, indicating that the system is unstable. After 0.6 s, the K_f changes to 0.2 pu, and the PCC voltages and frequency begin to converge. The time-domain simulation results are in good agreement with the p/z map analysis which derived from the developed small-signal model.

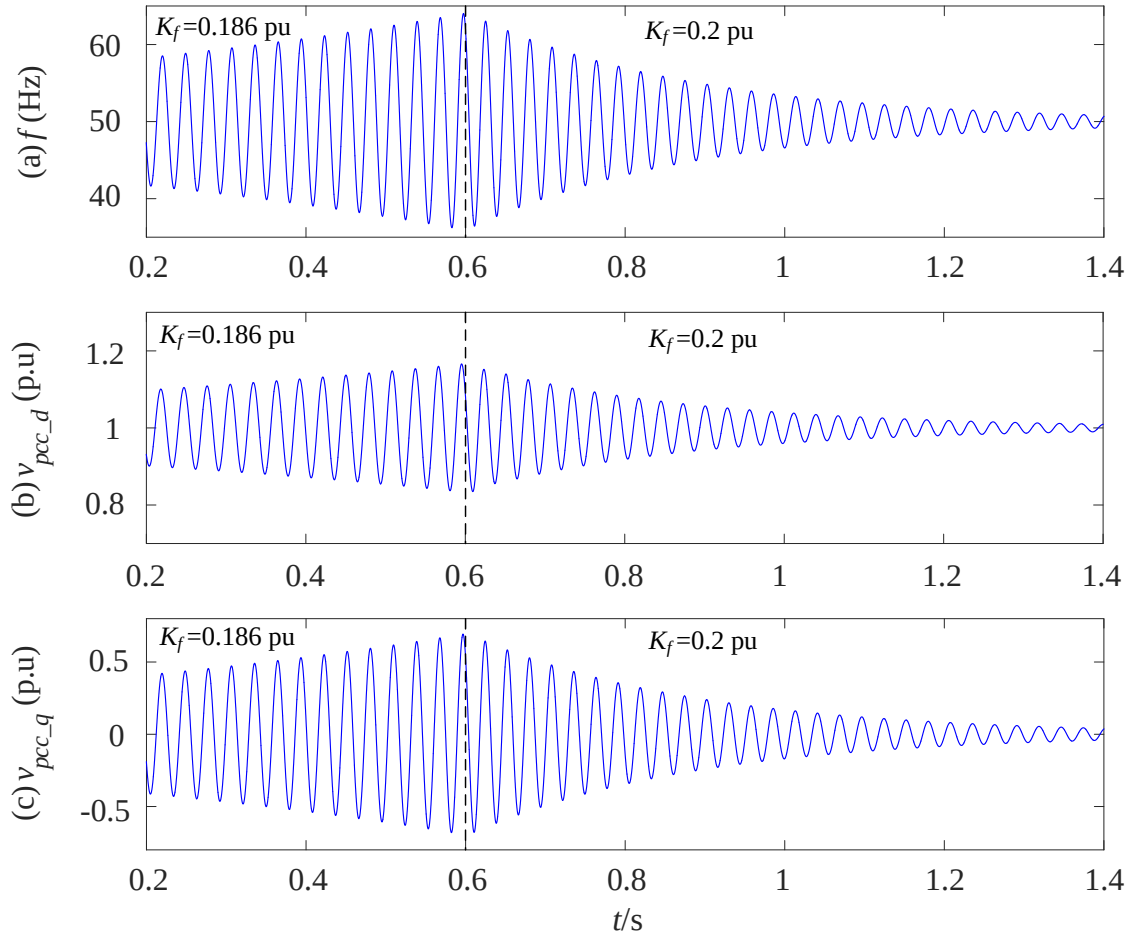

Figure 5.18 Simulation waveforms of PCC frequency and voltage with variable K_f. (a) Frequency on PCC bus, (b) *d*-axis voltage on PCC bus, (c) *q*-axis voltage on PCC bus.

5.3.2. Stability analysis of PCC voltage

To further study the system stability with proposed control, pole/zero map are used to investigate the variation of the parameters in voltage control loop on system stability.

a) Stability analysis of nature frequency f_v at voltage control loop

To study the impact of the natural frequency f_v in MMC voltage control loop as described in Table 5.1 on system stability, poles and zeros of the SS model transfer function with f_v increasing from 1 Hz to 700 Hz are plotted, while the K_f is set at 0.5 pu and damping value ζ_v of voltage control is 1.2. Figure 5.19 (a) and (b) demonstrate the p/z map of *d*-axis voltage reference to measured *d*-axis voltage and *q*-axis reference to

measured q-axis voltage, respectively. When f_v increases from 15 HZ to 20 Hz, all the poles in Figure 5.19 move to the left half plane, and this p/z map stipulates that system is stable when f_v is greater than 15 Hz.

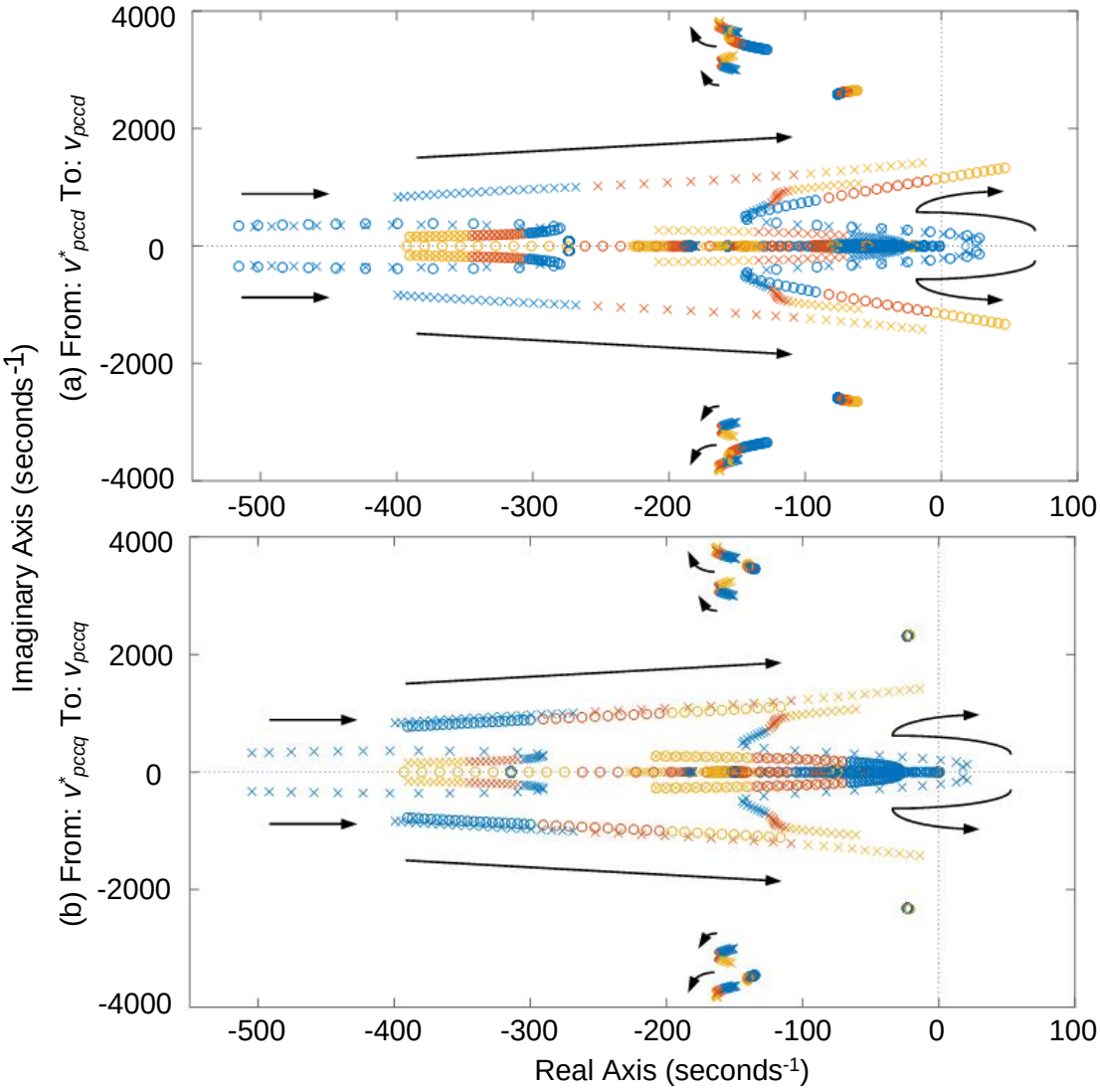

Figure 5.19 The p/z map of PCC voltage with variable f_v.
(a) The p/z map of d-axis PCC voltage, (b) the p/z map of q-axis PCC voltage.

Figure 5.20 shows the simulation results of the PCC frequency and voltage from the time-domain model with different voltage control parameter f_v. As seen, the offshore AC system is unstable before 0.6 s when f_v is 15 Hz but becomes stable after f_v increases to 20

Hz. This shows good agreement with the p/z map analysis using the developed offshore wind farm SS model.

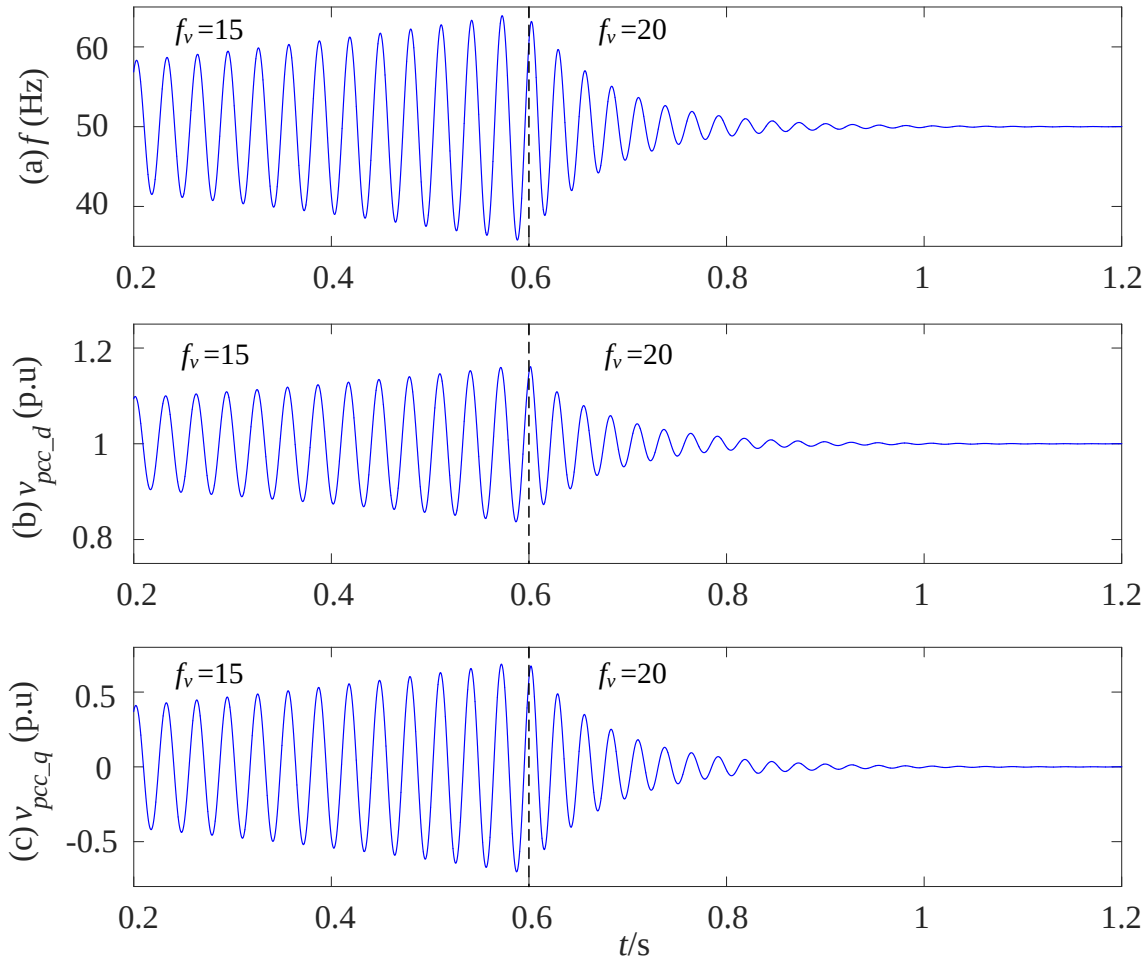

Figure 5.20 Simulation waveforms of PCC frequency and voltage when f_v increase from 15 Hz to 20 Hz.

(a) Frequency on PCC bus, (b) *d*-axis voltage on PCC bus, (c) *q*-axis voltage on PCC bus.

To further investigate the stability, the nature frequency f_v varied from 17 Hz to 18 Hz in the voltage control loop is carried out. The p/z map of PCC voltage is shown in Figure 5.21 and the time-domain simulation waveforms are illustrated in Figure 5.22.

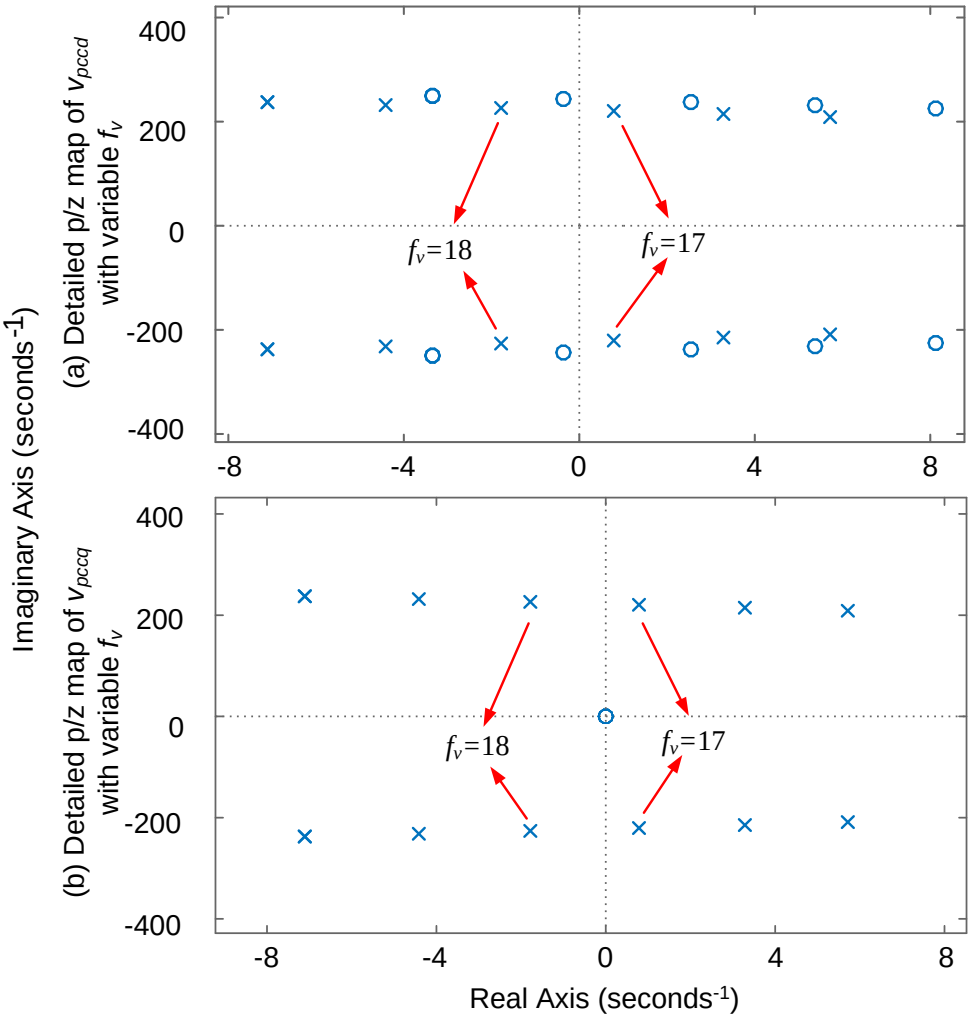

Figure 5.21 Zoomed-in p/z map of PCC voltage when f_v increases from 15 to 20. (a) The p/z map of *d*-axis PCC voltage, (b) the p/z map of *q*-axis PCC voltage.

From Figure 5.21, it shows that the system becomes stable when f_v is increased from 17 Hz to 18 Hz. As demonstrated in Figure 5.22 (a), (b) and (c), before t=0.6 s, f_v is 17 Hz and the frequency and voltage diverged with large oscillations. After t=0.6 s, f_v increases to 18 Hz and the frequency and voltage began to converge slowly. Again, the results from the SS model and those from the TD model match well.

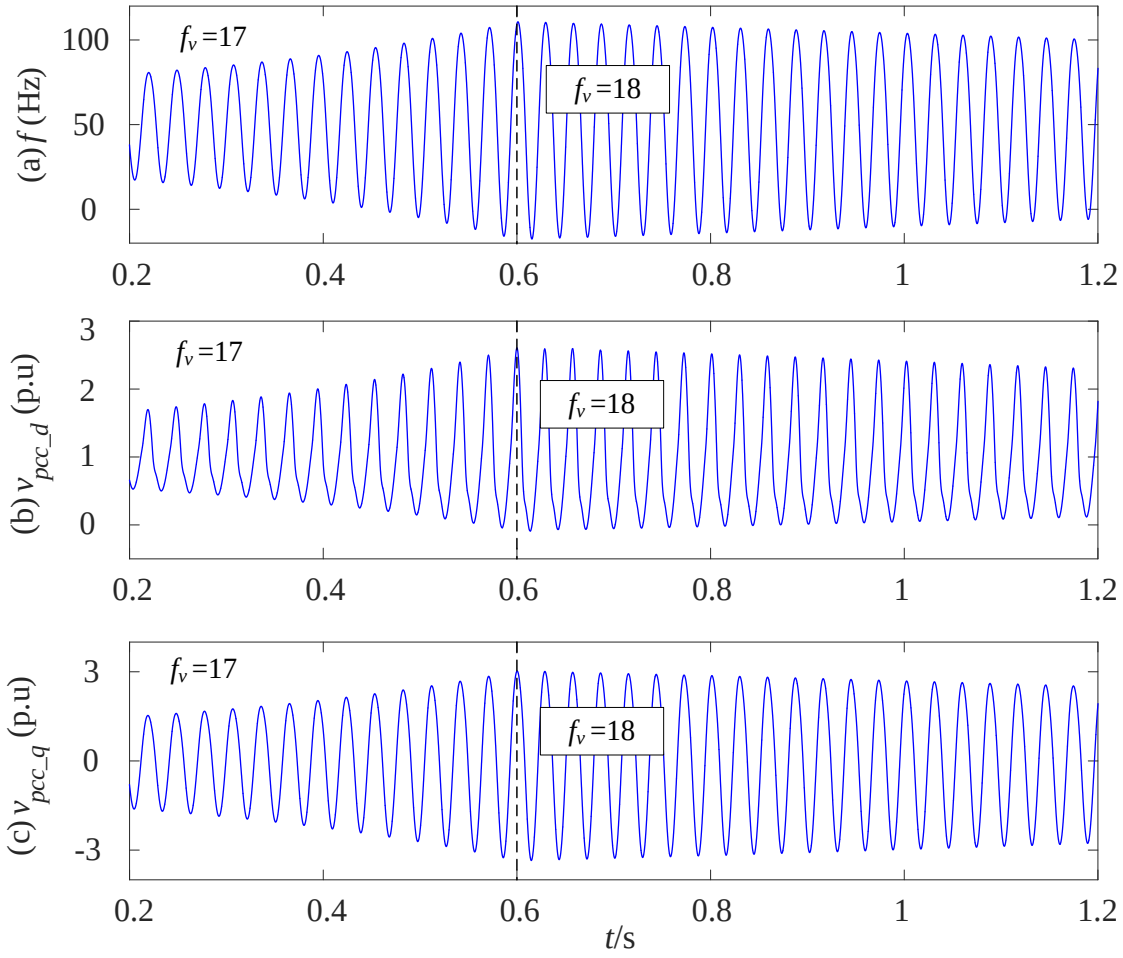

Figure 5.22 Simulation waveforms of PCC frequency and voltage when f_v increase from 17 Hz to 18 Hz.

(a) Frequency on PCC bus, (b) *d*-axis voltage on PCC bus, (c) *q*-axis voltage on PCC bus.

b) Stability analysis of voltage control damping value ζ_v

With the frequency control parameter K_f, control frequency f_v and current control parameters keep at constant as defined in Table 5.1, Figure 5.23 shows the movements of the poles and zeros when the voltage control damping value ζ_v increases from 0.1 to 10, whereas Figure 5.24 shows the zoomed-in poles and zero positions when the ζ_v increases from 0.7 to 1. As can be seen in Figure 5.24 (a) and (b), when ζ_v increases from 0.8 to 0.9, all the poles move to the left half plane, stipulates that the system is stable.

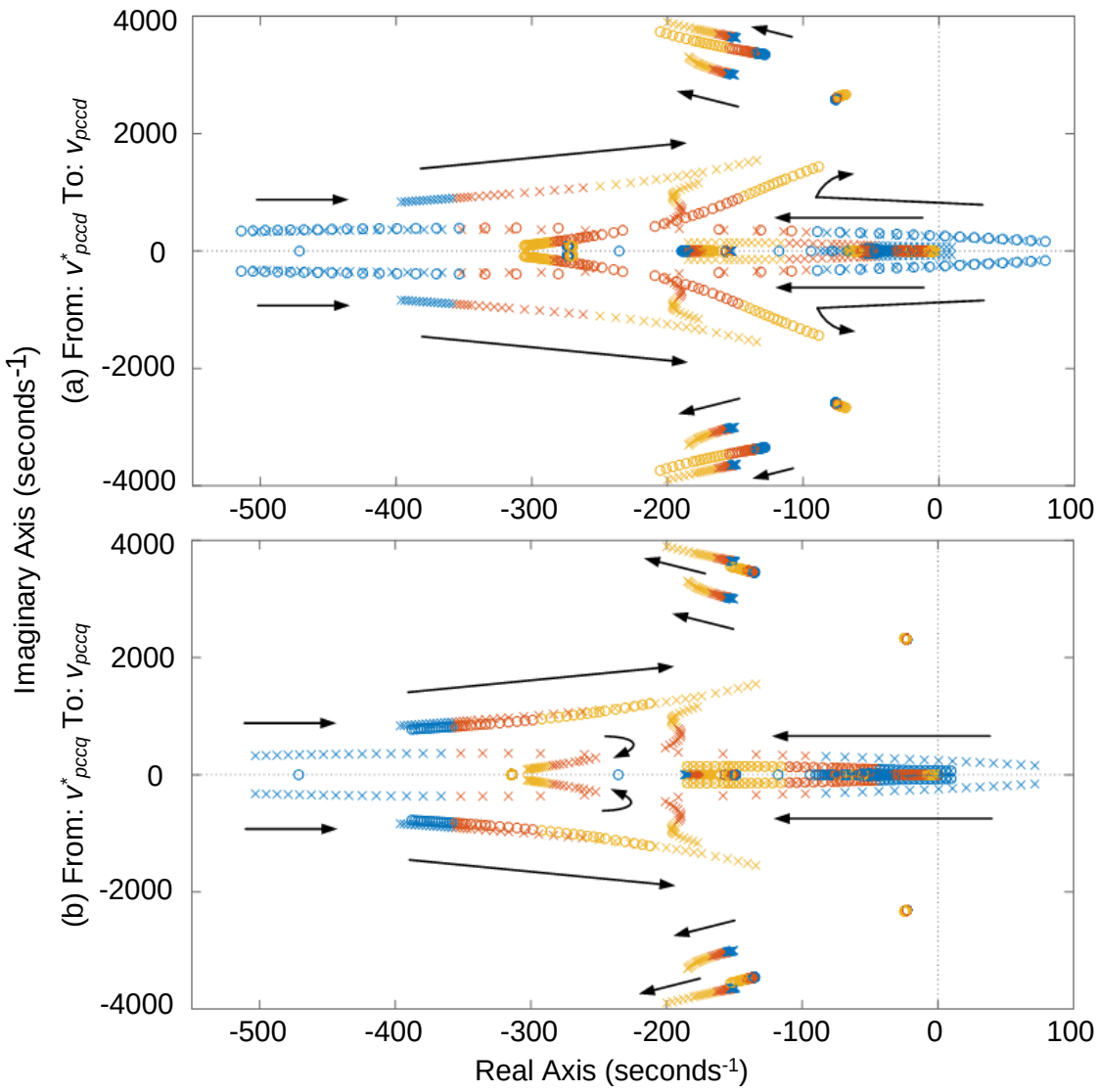

Figure 5.23 The p/z map of PCC voltage with variable ζ_v.

(a) The p/z map of *d*-axis PCC voltage, (b) the p/z map of *q*-axis PCC voltage.

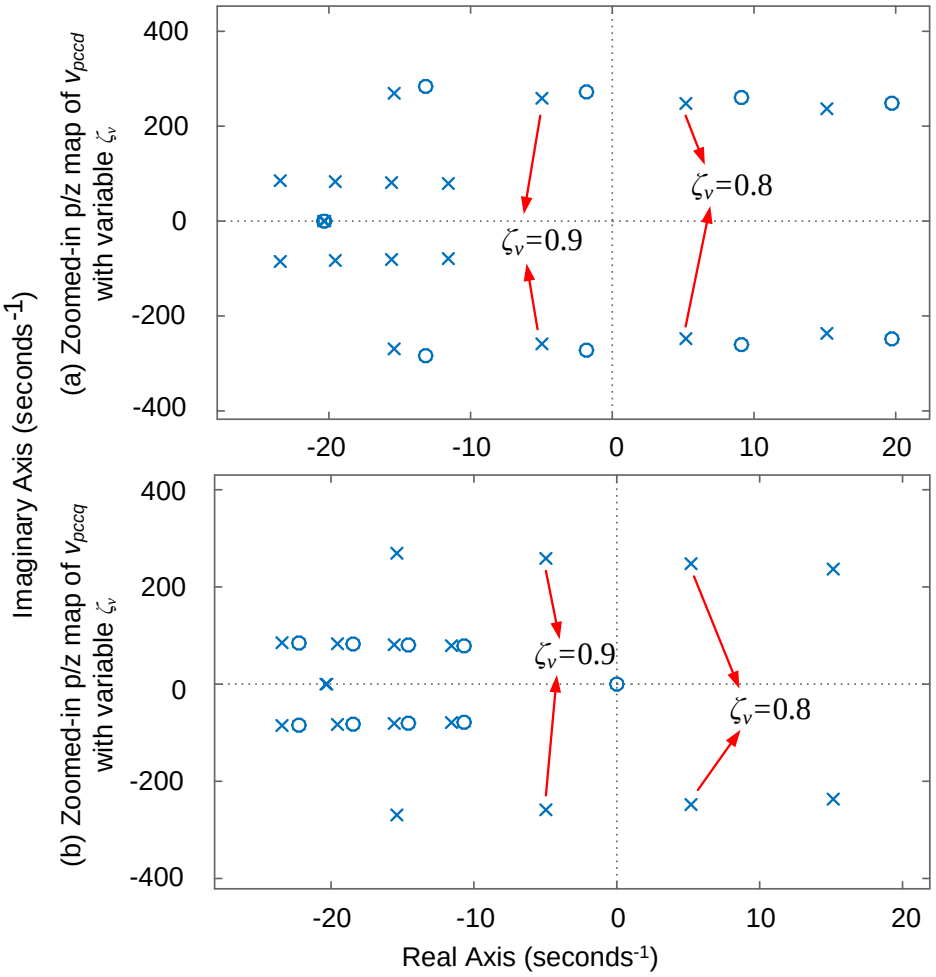

Figure 5.24 The zoomed-in p/z map of voltage on PCC bus with variable ζ_v. (a) The p/z map of *d*-axis PCC voltage, (b) the p/z map of *q*-axis PCC voltage.

Simulation results from the time-domain model with the variable ζ_v values are shown in Figure 5.25. The system is unstable when ζ_v is 0.8 before 0.6 s and after the ζ_v increases to 0.9, the system becomes stable. Again the time-domain simulation results are in the good agreement with the p/z map analysis in Figure 5.23 and Figure 5.24.

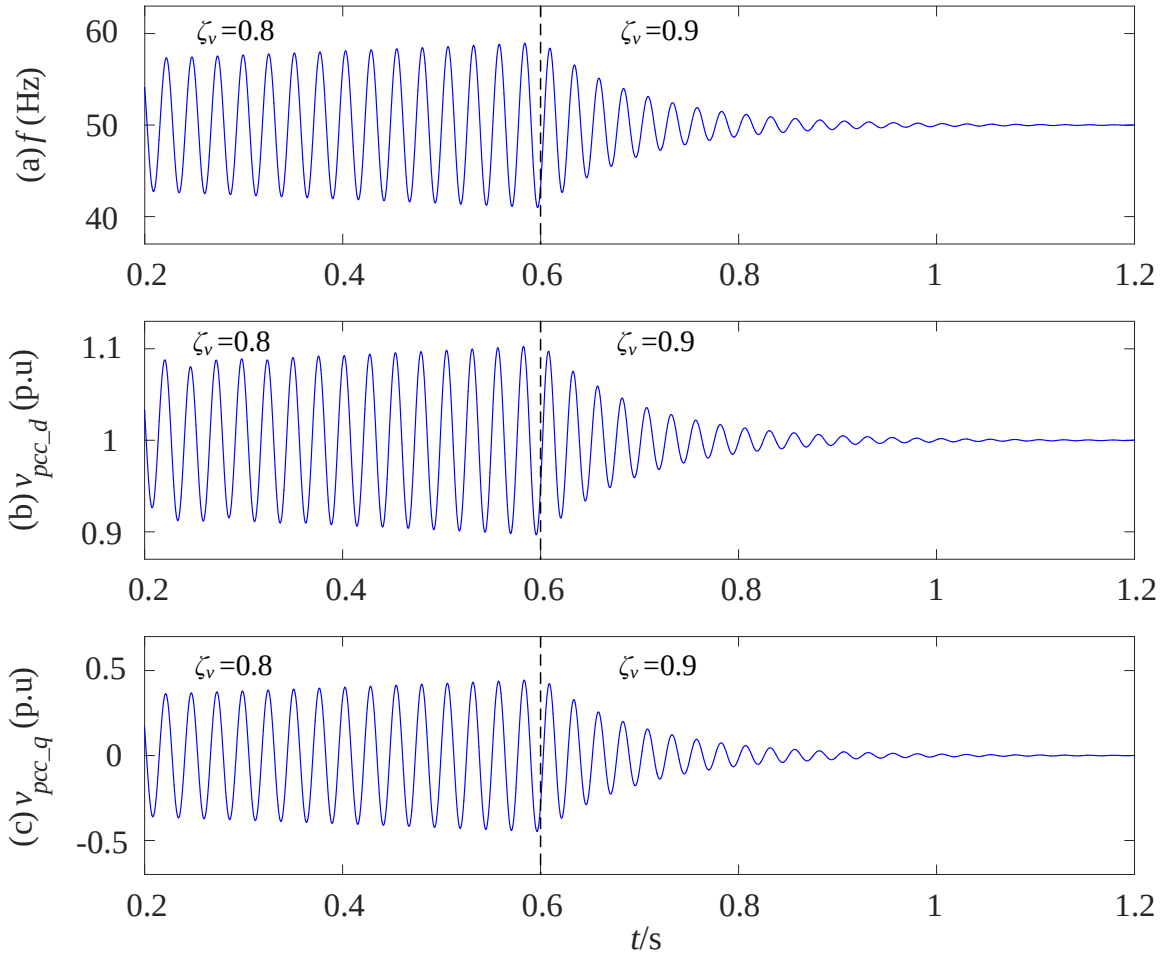

Figure 5.25 Simulation results on PCC frequency and voltage with ζ_v =0.8 and 0.9. (a) Frequency on PCC bus, (b) *d*-axis voltage on PCC bus, (c) *q*-axis voltage on PCC bus.

c) Stability analysis with conventional control without frequency loop

For comparison, system stability with conventional control without frequency loop is studied with variation of the damping ratio ζ_{vs} of the voltage control loop. Under the same offshore wind farm conditions with the same f_v of voltage control and current control parameters, the range of voltage control damping ratio ζ_{vs} is tested and the p/z maps are shown in Figure 5.26. And Figure 5.27 shows the zoomed-in poles and zero positions when the ζ_{vs} increases from 2.6 to 3.2. As illustrated in Figure 5.27 (a) and (b) for the respective *d*-axis and *q*-axis voltage responses, only until ζ_{vs} is increased to 3, all the poles move to the left half plane and the system becomes stable. Compared to the damping ratio

with the proposed frequency control ($\zeta_v \geq 0.9$ can ensure system stability), system with the fixed frequency control presents a higher requirement on the damping ratio (system becoming stable only until $\zeta_{vs} \geq 3$). Requiring a larger damping value indicates that the system is more difficult to be stable. Therefore, the proposed control has better system stability a than the conventional control method.

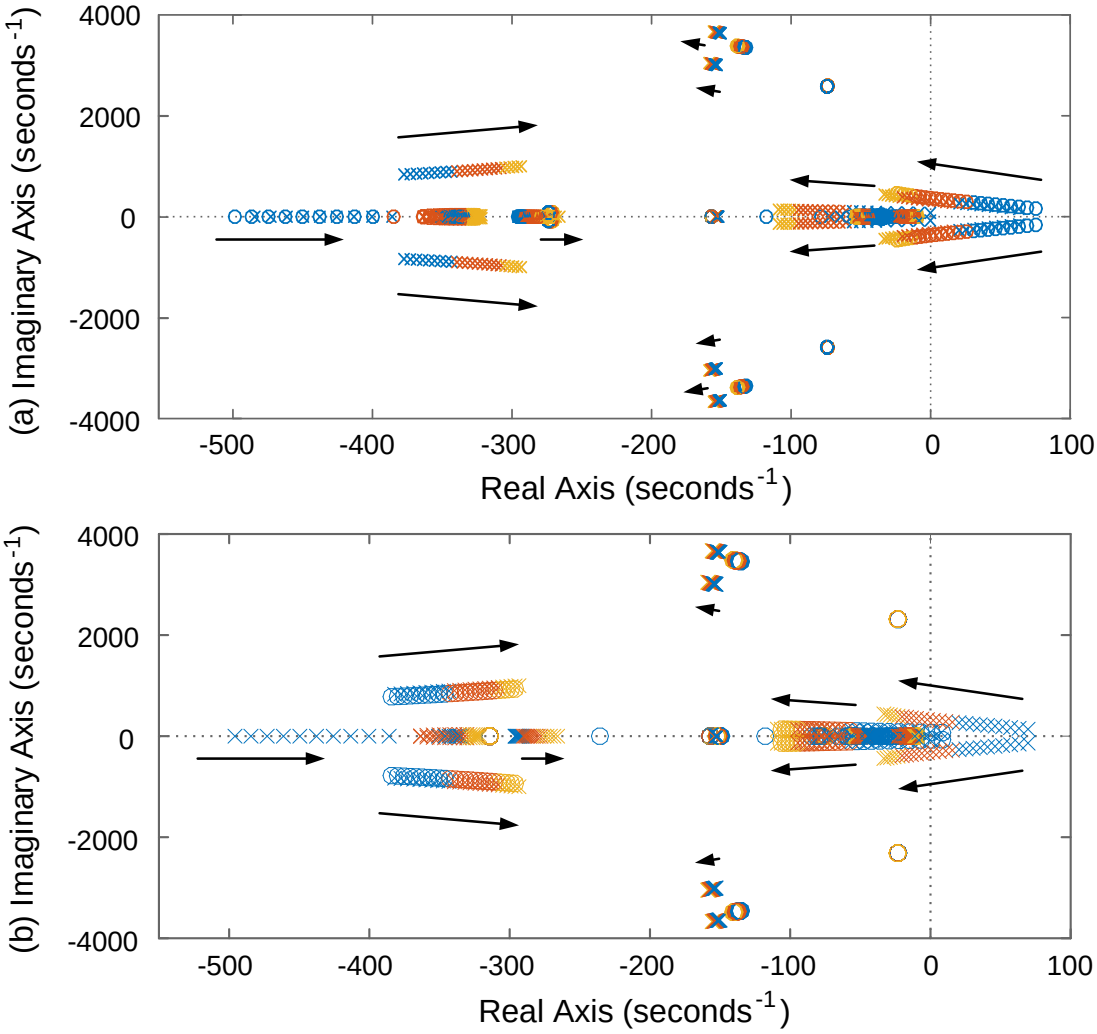

Figure 5.26 P/z map when voltage control parameter ζ_{vs} increases from 0.4 to 5. (a) The p/z map of *d*-axis PCC voltage (b) The p/z map of *q*-axis PCC voltage.

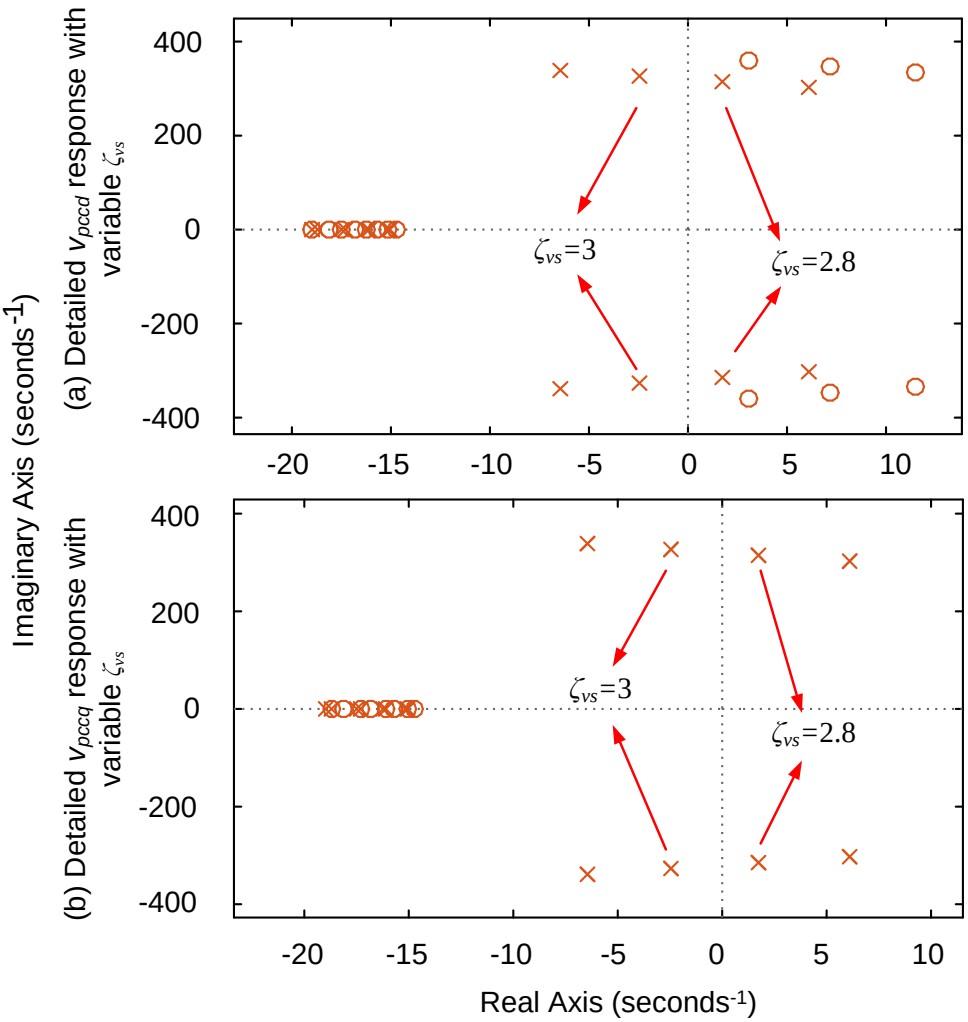

Figure 5.27 The zoomed-in p/z map of voltage on PCC bus with variable ζ_{vs}. (a) The p/z map of *d*-axis PCC voltage, (b) the p/z map of *q*-axis PCC voltage.

5.3.3. Wind power interaction with PCC voltage

The offshore network formed by the offshore MMC is typically weak. Consequently, wind power variation can affect the stability of the offshore wind farm system, especially on the PCC voltage. To study the interactions between the wind power and PCC voltage, the transfer functions are obtained from the developed SS model as illustrated in Figure 5.11. The SS model of conventional control with fixed frequency is also studied for comparison.

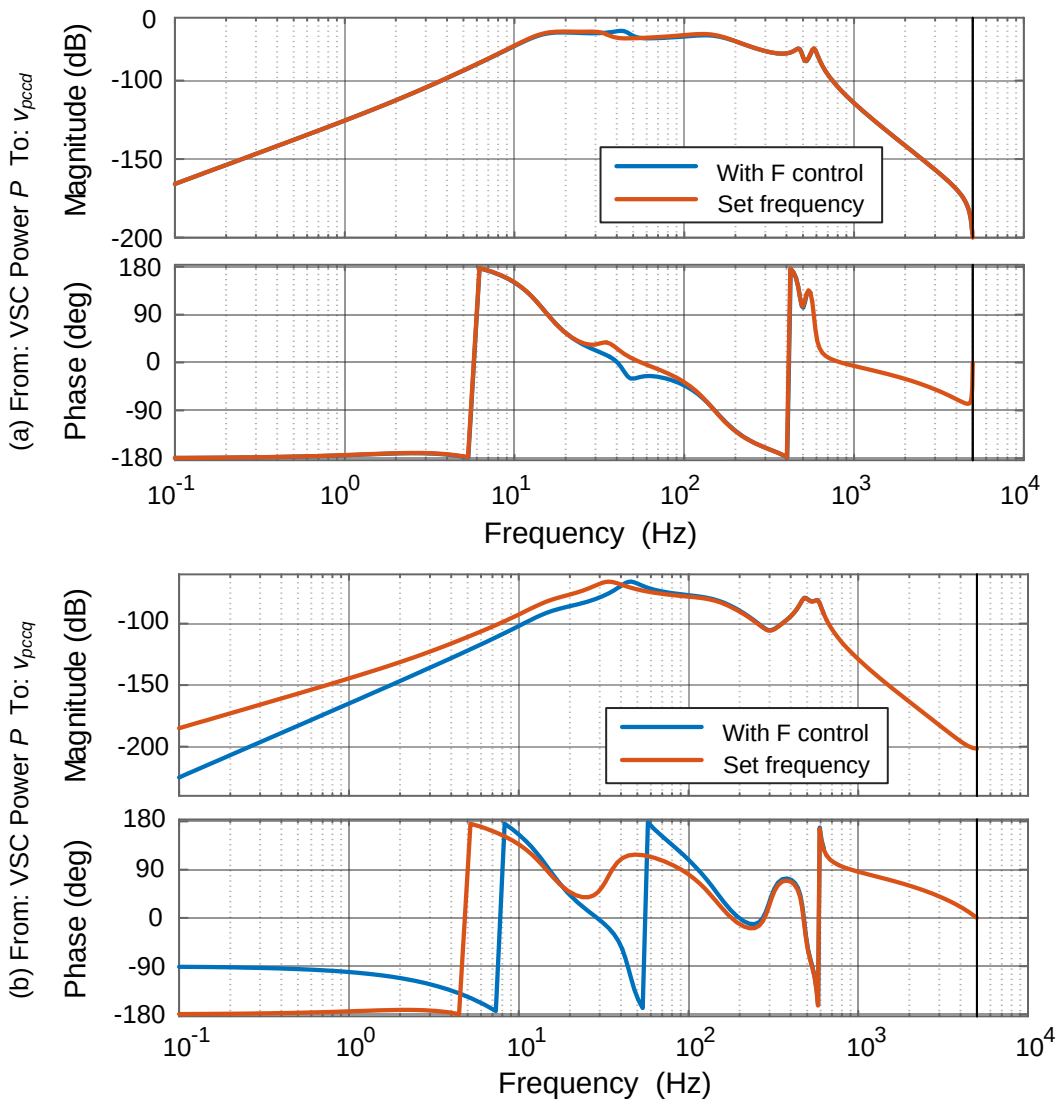

Figure 5.28 Bode plots comparison from power to PCC voltage response in two systems. (a) Response from VSC output power P to *d*-axis PCC voltage, (b) response from VSC output power P to *q*-axis PCC voltage.

Figure 5.28 shows the PCC *d*-axis and *q*-axis voltage responses to the inject power from VSC_1 respectively. Due to the frequency control lies on *q*-axis, PCC *d*-axis voltage with proposed control has a similar response with the system applying conventional control as shown in Figure 5.28 (a), and this characteristic also reflects on its relationship with the power change. The main difference lies on the *q*-axis and the proposed control improves the PCC *q*-axis voltage response as illustrated in Figure 5.28 (b). With the

proposed frequency control, power injected to MMC has a smaller impact on v_{pccq} compared to the traditional control system in the low to medium frequency range. Therefore, the system with frequency control is less affected by the injected wind power variation.

5.4. Summary

This chapter develops small-signal models of the complete offshore system including the MMC model and the WT system model. To validate the developed SS model, frequency responses from the separate MMC and WT SS models are compared to the corresponding TD models. The complete offshore wind farm SS model is then validated using the same approach by using the TD model. Waveforms form SS model and TD model with small power and voltage disturbances further validated the accuracy of the SS model.

With the small-signal state space model, system stability is analysed in frequency domain. The impacts of various control parameters on the system stability are studied using Bode plot and p/z map. Compared to the conventional control, system with the proposed control allows a wider parameter range. The interactions between the PCC voltage and offshore wind power are also investigated. Simulation results show that the voltage on PCC bus is less influenced by the wind power variation while utilizing the enhanced frequency and voltage control than the conventional fixed frequency method.

Chapter 6

Fault analysis of MMC-HVDC system connecting offshore wind farm

6.1. Introduction

With the increasing penetration of wind power and development of large-scale offshore wind farms, it is important to ensure wind farms can remain connected during large transients, e.g., onshore and offshore AC faults. In the events of AC faults at the offshore AC system of HVDC (MMC) connected offshore wind farms, there are a number of challenges that need to be addressed:

- ensuring the currents of the MMC and WT converters are limited within safe ranges;
- adequate fault currents are provided to enable fault detection and proper operation of protection devices;
- fast system recovery after fault clearance.

In the events of onshore AC grid faults, onshore voltage dip during the fault period can result in significant reduction of active power that can be transmitted through the onshore MMC converter, leading to imbalanced power transmission between onshore and offshore sites. This potentially can lead to excessive DC voltage at the HVDC link and the disconnection of the entire offshore system [49].

In this chapter, system control and operation of the HVDC system and WTs are investigated, and different types of protection relay settings are studied for offshore wind farm system application. To enable offshore AC fault protection, a fault current injection

control for offshore MMC and WTs is proposed such that faults at different parts of the offshore AC network, e.g. WT cluster cables, string cables etc. can be adequately protected. To enable the safe operation and satisfactory ride-through during the onshore AC faults, an offshore MMC voltage reduction control strategy based on HVDC system overvoltage is proposed to rapidly balance the generated and transmitted power. The proposed design and control are validated by MATLAB/SIMULINK simulations.

6.2. Control and operation during offshore AC faults

In the event of an offshore AC fault, the offshore voltage drops and the fault currents from the MMC and WT converters can potentially increase rapidly if immediate control actions are not taken. To limit the fault currents and avoid damage to the offshore MMC station, the three-phase currents are measured and if the currents are out of the predefined range, the offshore voltage is reduced accordingly in order to decrease the MMC output currents [121].

To supply adequate fault currents for offshore AC protection purpose while avoiding excessive fault current for protection relays, a fault current providing control is developed in MMC station. Considering the overcurrent protection at WT side during abnormal conditions, the control strategy with a fault current supply at WT side is introduced and applied at WTs to help with the fault recovery.

6.2.1. Fault current providing control

a) Fault current supply of offshore MMC station

After an offshore AC fault occurs at the wind farm network, MMC_1 initially tries to restore the AC voltage by increasing the reversed current (from receiving current to generating current). However, when the offshore AC voltage is significantly reduced, e.g. around to zero, no active power can be generated and transmitted, i_{1d} in Figure 6.1 is thus limited at around zero (i.e., no current reversal). To provide sufficient fault current for the

protection relays connected to the offshore AC system, the *q*-axis current reference of the offshore MMC station i^*_{1q} is modified accordingly as shown in Figure 6.1 (a).

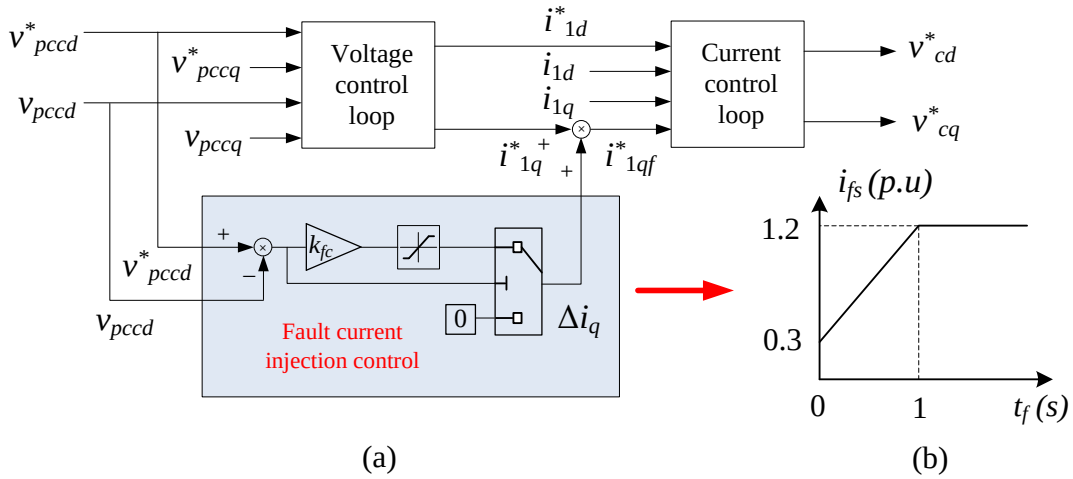

Figure 6.1 Fault current injection control of offshore MMC station.
(a) Fault current injection control, (b) Fault current injection curve.

As shown, the difference between the measured PCC voltage magnitude v_{pccd} and its reference v^*_{pccd} (v^*_{pccd} -v_{pccd}) is calculated and compared to the pre-set threshold, e.g. 0.4 pu. During normal operation, v^*_{pccd} - v_{pccd} is less than the threshold and i^*_{1q} is set by the *q*-axis voltage control loop. However, during an offshore AC fault, v_{pccd} is significantly reduced and the *d*-axis voltage error will be over the threshold. Thus, an additional component Δi_q is added to the reference to inject *q*-axis fault current to the offshore network. The fault current profile is illustrated in Figure 6.1 (b) and as seen, the fault current i_{fs} provided by the offshore MMC in this example is gradually ramped up from 0.3 pu with the rate of 0.9 pu/s, up to a maximum current of 1.2 pu. As the fault current i_{fs} supplied by MMC_1 flows to the offshore system, it is negative to i_1 (i_1 is positive when the current flows from WF to MMC) as:

$$\begin{aligned} i_{fs} &= -i^*_{1qf} = -i^*_{1q} - \Delta i_q \\ &= 0.3 + 0.9 \times t_f \ \text{(pu)} \end{aligned} \quad . \tag{6.1}$$

where the t_f is the time after fault occurs. As will be shown in the following sections, considering the relay's time-current characteristic profile, offshore circuit can operate by

overcurrent protection while potential excessive fault current of the circuit breakers is avoided.

b) Fault current supply of WTs

When the fault occurs at the offshore side, AC voltage on the PCC bus drops to around zero and MMC station starts to increase *q*-axis current to provide fault current. At WT sides, in order to output the generated power, the currents of the WTs initially increase rapidly because of the voltage drop but are quickly limited to their maximum values. Meanwhile, the PLLs at WT sides are unlikely to be able to track the phase angle and the offshore network frequency if the AC voltage is reduced to around zero (e.g. during a severe 3-phase fault). To stay connected and contribute to system recovery, WTs are controlled such that their *q*-axis (reactive) currents are used to assists relay tripping and the frequency of the WT converters (i.e., frequency output from the WT PLLs) are set to fixed value during the fault conditions.

On the other hand, if an AC fault occurs at a WT string, the currents generated by the other healthy WTs as well as the MMC directly feed to the fault point, and lead to excessive fault current flowing through the faulty WT string. The fault current could potentially reach tens of times of their rated capacities and might overstretch the capability of the protection equipment/relay at the faulty WTs string.

To reduce the capacity and size of relays at WT strings and contribute to the overcurrent protection of offshore wind farm systems, a similar method of fault current supply as for offshore MMC converter is implemented at WTs side as shown in Figure 6.2. The current i_{rated} is from the power control loop of WTs, v^*_{wt} and v_{wt} are the respective rated and measured WT voltages, i^*_{wtd} and i^*_{wtq} are the *d*- and *q*-axis current references which feed to the WT current control loop. As shown in Figure 6.2, *d*-axis current reference i^*_{wtd} is equal to the nominal value and *q*-axis current reference i^*_{wtq} is zero (or at any other values as required) while the WT working at normal mode. When the fault occurs, and the detected voltage drop is more than the pre-set threshold (e.g 0.4 pu), the current i_{wtd} generated by WTs follows the new reference and quickly drops to zero. Fault

current is presented in i_{wtq} which increases from 0 to the upper current limit (e.g 1.2 pu) as:

$$i_{wtq}^{*} = k_{iq} \times t_f \,. \tag{6.2}$$

The increasing rate k_{iq} is set as 4 pu/s in this thesis which means after 0.3 s the fault current supplied by the WT reaches to the maximum value of 1.2 pu. Once the fault is clear, i_{wtq} backs to 0 while i_{wtd} recovers to the initial value. With this proposed fault current supply, the fault current injected to the fault point only increases gradually after fault occurrence and thus, the capacity of WT string protection relays can be reduced.

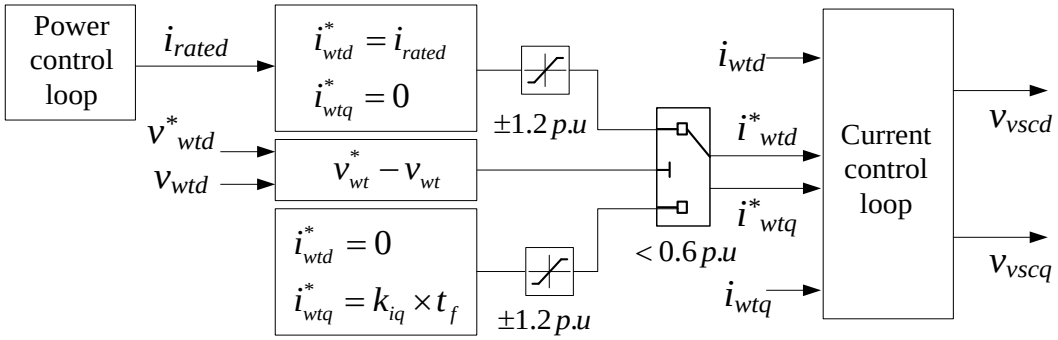

Figure 6.2 Fault current supply by WTs.

With the fault current providing controls implemented at offshore MMC and WTs, and proper setting of the different relay parameters, offshore AC fault can be accurately located, and the corresponding circuit breaker can be opened to isolate the fault. Although MMC and WT converters have limited fault current capability, during an offshore fault, substantial overcurrent can still be present as all the converters will feed fault current to the fault point as will be analysed in more details in the following sections.

6.2.2. Wind farm relay design

Overcurrent relaying protection is the most economical and simplest way to protect the facilities and transmission lines. The speed of an overcurrent protection relay e.g. inverse definite minimum time relay (IDMT), is dependent on the magnitude of the overcurrent. By applying IDMT relay, the operating time will be shorter with a higher overcurrent magnitude and the selective protection is easy to be implemented.

a) IDMT relay

For IDMT relay, its operating time is inversely proportional to the fault current above the inverse time pick-up current value and becomes constant when the fault current is over the definite time pick-up current threshold. The time-current characteristic is shown in Figure 6.3, and usually, the definite time pick up value is set as *n* times to inverse time pick up value.

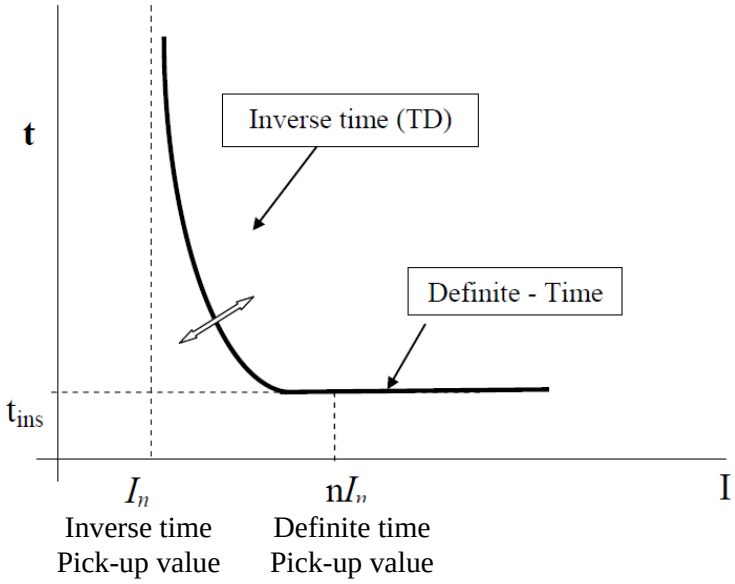

Figure 6.3 Mixed curves IDMT characteristic [122].

For inverse-time characteristic area of IDMT relay, the operation time is inversely proportional to the fault current and the operation time can be expressed by the fault current as:

$$t_{CB} = \frac{k \times TMS}{(\frac{i_F}{CTR \times PS})^{\alpha} - 1} \tag{6.3}$$

where α and k are the curve set-related parameters which are decided by the different types of time-current characteristic, i_F is the measured phase current, *CTR* is transformer ratio of the relay, *PS* is the relay rated operating current, and time multiple setting (*TMS*) is an adjustable time multiplier. With the increase of *TMS*, the tripping time becomes longer

with the same phase current. The *PS* is usually set at 100% or 125% of detect phase current i_F. When 100% is chosen as *PS* value (equals to 1), the rated current value of the relay follows the test phase current rated value in per unit. With normal inverse curve parameters, α=0.14 and k=0.02, and *PS* is chosen as 100%, (6.3) can be simplified as:

$$t_{CB} = \frac{0.14 \times TMS}{MPS^{0.02} - 1} \tag{6.4}$$

where the *MPS*, multiples of plug settings, equals to $i_F/(CTR \times PS)$. By selecting the proper *TMS* and *MPS*, the different protection requirements of system can be actualized by relays with variable settings.

b) Offshore wind farm relay setting

In this study, IDMT relays are applied at the offshore wind farm system for overcurrent protection. They are installed at the end of the WTs clusters and terminal of WTs strings as shown in Figure 6.4 (a). As shown in Figure 6.4 (a), the considered offshore wind farm contains two WT clusters and each WT cluster consists of five WT strings with the same capacity. Each WT string is made up of ten 10 MW fully rated converter WTs. Different *TMS* characteristics lead to various tripping times to meet the requirement for different fault current levels.

System protections under two different AC fault positions are investigated with this model as shown in Figure 6.4 (a). AC fault F_1 occurs on WT cluster and F_2 occurs on WT string.

The parameters of the offshore system are given in Table 6.1. As previously described, string CBs (circuit breaker) are placed at every end of WT strings, whereas WT cluster CBs are installed at every terminal of WT clusters as illustrated in Figure 6.4 (a).

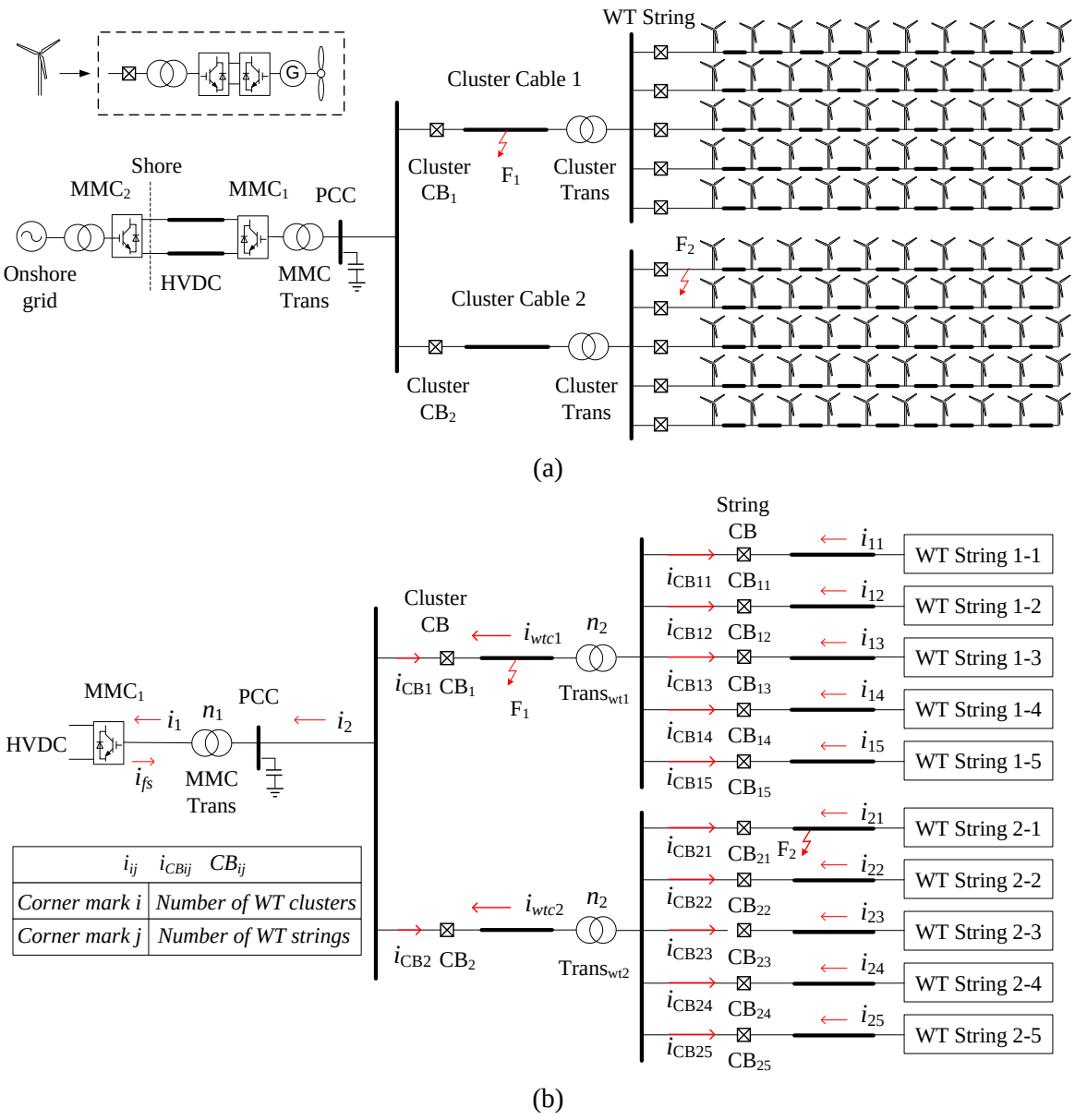

Figure 6.4 Offshore wind farm structure with defined current and relays.
(a) System structure, (b) System with defined current and relays.

Table 6.1 Offshore wind farm system parameters and relay setting.

AC voltage on PCC		429 kV	
MMC power rating		1000 MW	
MMC transformer ratio		429/200	
WT side	WT power rating	10 MW	
	WT string power rating	100 MW	
	WT cluster power rating	500 MW	
	WT cluster transformer ratio	200 kV/33 kV	
WT string CB (IDMT relay)	Inverse part setting	*MPS* 2 pu	0.04 *TMS*
	Definite part setting	*MPS* 3 pu	0.04 s
WT cluster CB (IDMT relay)	Inverse part setting	*MPS* 2 pu	0.04 *TMS*
	Definite part setting	*MPS* 3 pu	0.25 s

As shown in Figure 6.4 (b), once the fault F_1 occurs at WT cluster, fault currents from the other healthy WT cluster i_{wtc2} and offshore MMC station i_{fs} both flow to the fault point through CB_1. When CB_1 detects the current on the cluster is over 2 pu, the time-current characteristic of the IDMT relay comes into the inverse-time part setting as indicated in Table 6.1. If the fault current which flows through the CB_1 reaches the definite time area of 3 pu, CB_1 enters the definite time part and trip after 0.25 s (according to the general operation time settings introduced in [122]). CBs on WT strings experience 1.2 pu (output current limit of WTs) of their own rated value at this time and thus, they will not trip. After the fault is cleared by CB_1, the offshore voltage recovers, the healthy WT strings back to normal operation. The cluster relay CB_1 can be described as:

$$t_{CB} = \begin{cases} \infty & MPS < 2 \\ \dfrac{0.14 \times 0.04}{MPS^{0.02} - 1} & 2 \le MPS < 3 \\ 0.25 & MPS \ge 3 \end{cases}. \tag{6.5}$$

For fault F_2 occurring at a WT string connected to CB_{21} as illustrated in Figure 6.4, the currents of other healthy WT strings as well MMC_1 all flow into the fault point through CB_{21} and therefore, the fault current is likely to be far larger than 3 pu. In order to protect the faulty WT string, CBs on WT string are designed to trip as soon as possible. Therefore, the definite operating time of string CB is set at 0.04 s which means once the detected current is above 3 pu, WT string CB will take 0.04 s to disconnect the fault WT string (the fastest operation time of overcurrent relay is about 4 milliseconds). The relay set on WT strings can be described as:

$$t_{CB} = \begin{cases} \infty & MPS < 2 \\ \dfrac{0.14 \times 0.04}{MPS^{0.02} - 1} & 2 \le MPS < 3 \\ 0.04 & MPS \ge 3 \end{cases}. \tag{6.6}$$

The characteristics of these two kinds of relays with different settings are illustrated in Table 6.1. The characteristic curves of operation time-overcurrent for these relays are demonstrated in Figure 6.5, where the currents are expressed using actual phase current values.

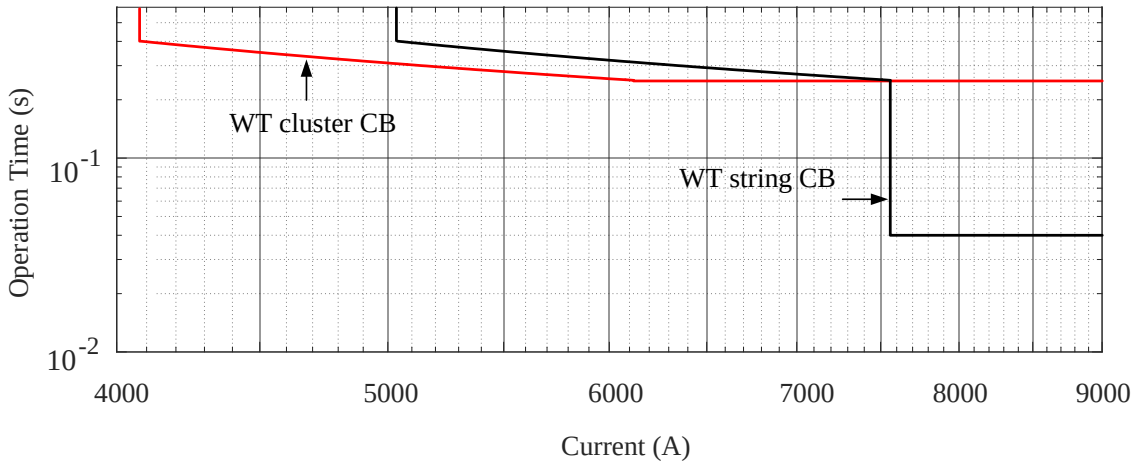

Figure 6.5 System relay characteristics.
(Note: WT cluster is 200 kV and WT string is 33 kV)

The time-current curve indicates the relationship between the operation time of a relay and the fault current flowing through it. However, the total tripping time of a relay

includes the safety margin duration t_s which is defined by the period of a fault has been detected but has not led to the relay's immediate action. Therefore, the relay's tripping time is given as:

$$t_{trip} = t_s + t_{CB}\,. \tag{6.7}$$

6.2.3. Overcurrent detection of offshore AC faults

To further analyse the fault conditions and operation characteristics of relays, the system structure with defined current and relays as displayed in Figure 6.4 (b) is described in more details. As shown in Figure 6.4 (b), i_{ij} (i=1, 2, and j = 1,…5) are the currents on the WT strings, i_{CBij} are the currents flow through the relatively WT string CBs.

a) Fault on WT cluster F_1

Considering that the fault occurs on a WT cluster, F_1 in Figure 6.4, the fault currents flowing through the CB_1 come from MMC_1 and WTs connected at clusters 2, as:

$$i_{CB1} = i_{fs} + i_{wtc2}. \tag{6.8}$$

With the increasing fault current as defined in (6.1) and (6.2), the current flowing through CB_1 gradually increases. The breakers on the healthy cable CB_2 experiences maximum overcurrent of 1.2 pu and thus the relay remains closed during the cluster fault F1. Fault current through CB_2 can be express as:

$$i_{CB2} = -i_{wtc2} = -\sum_{j=1}^{5} i_{2j}\,. \tag{6.9}$$

As the fault current flows through CB_1 is not a constant during the cluster fault F_1, as i_{fs} and i_{wtc2} in (6.8) are not constant. Thus, formula (6.5) cannot be used in this condition to calculate the tripping time of the cluster relay. To model the relay tripping time more accuracy with dynamic fault current, it is assumed that the integration of fault current i_{CB1} during faulty time t_f determines relay tripping time which is described as:

$$\Delta Q = \int_{t_s}^{t_{trip}} i_{CB1} dt_f \tag{6.10}$$

where i_{CB1} dependent on the time is the fault current flows through CB_1, t_s is the time when fault current reaches to the pick-up value of CB_1 (2 pu in the previous setting) and t_{trip} is the time when the relay is tripping. Considering the inverse part setting of relays, ΔQ can set at 0.8 (when the fault current is 2 pu, CB trips after 0.4 s). Thus, the ramped-up fault current leads to a shorter relay tripping time.

The current flows through CB_1 during the fault F_1 is the sum of fault currents supplied by MMC_1 and the healthy WT cluster. According to the fault current profiles of MMC_1 and WTs as previously described, as the capacity of MMC_1 is twice of the WT cluster, the fault current supplied by MMC_1 should be doubled with the WT cluster reference in per-unit terms. Thus, the increasing rate of fault current from MMC_1 becomes 1.8 pu/s, and the starting current is 0.6 pu for CB_1. Current flows from the other WT cluster increases with the rate of 4 pu/s from 0 pu. According to (6.1) and (6.2), the variation of fault current flowing through CB_1 can be expressed as:

$$\begin{aligned} i_{CB1} &= i_{fs} + i_{wtc2} \\ &= 2\times(0.3+0.9\times t_f)+4\times t_f \end{aligned}. \tag{6.11}$$

The time t_s when the fault current hit the CB pick-up value 2 pu can be calculated with (6.11), and then the fault current starts to be integrated on the time to calculate the tripping time of CB_1. The constant integration ΔQ (integration of fault current which is dependent on the time) can be calculated as:

$$\Delta Q = \int_{t_s}^{t_{trip}} 2\times(0.3+0.9\times t_f)+4\times t_f dt_f \,. \tag{6.12}$$

Therefore, the tripping time according to (6.12) can be calculated as:

$$\begin{aligned} 0.8 &= (0.6t+2.9t^2)\Big|_{(2-0.6)/5.8}^{t_{trip}} \\ t_{trip} &\approx 0.52 \end{aligned}. \tag{6.13}$$

Consequently, the tripping time t_{trip} of CB_1 is 0.52s while the fault current flows through CB_1 is 2.74 pu. This means the relay trips before it goes into the definite time characteristic area of its time-current curve. The status of the relays at the offshore wind farm and the currents flow through different CBs are shown in Table 6.2.

Table 6.2 Relay tripping time with the WT cluster fault.

		max CB current	t_s	t_{CB}	t_{trip}	CB status
WT cluster relay	**CB_1**	2.74 pu	0.24 s	0.28 s	0.52 s	Open
	CB_2	1.2 pu	0.52 s	∞	∞	Closed
WT string relay	**CB_{1j}**	1.2 pu	0.52 s	∞	∞	Closed
	CB_{2j}	1.2 pu	0.52 s	∞	∞	Closed

As described in Table 6.2, once the fault occurs at WT cluster 1, CB_1 on WT cluster 1 trips after 0.52 s and the voltage on the PCC is quickly controlled back to the rated value by MMC_1. The CBs connected to other healthy WT clusters will not trip because the fault current has not reached the pick-up value 2 pu during the fault event. The current flows through the AC cable at MMC_1 side even has not reached 1 pu before the fault is cleared. Thus, by appropriately setting the relays parameters, the protection of cluster cable fault can be implemented using the reliable and straightforward overcurrent protection approach. If faster relay tripping is required, the fault currents from MMC and WTs can be modified accordingly.

b) Fault on WT string F_2

If a fault occurs on the WT string i.e. F_2 as shown in Figure 6.4, all fault currents will flow into the fault point at the faulty WT string. The currents through WT cluster 1 CB_1 and WT cluster 2 CB_2, and the current through WT string CB_{21} can be expressed as

$$\begin{aligned} i_{CB1} &= -i_{wtc1} = -\sum_{j=1}^{5} i_{1j} \\ i_{CB2} &= i_{fs} + i_{wtc1} \end{aligned} \tag{6.14}$$

$$i_{CB21} = \sum_{j=2}^{5} i_{2j} + i_{CB2} = \sum_{j=2}^{5} i_{2j} + i_{fs} + i_{wtc1}. \tag{6.15}$$

Considering the capacity of MMC_1 is 10 times of that of the WT string, fault current i_{fs} supplied by MMC_1 starts to increase from 3 pu with a rate of 9 pu/s in WT string per-unit terms, and the other healthy WTs (total 9 strings) begin to generate fault current from 0 with a rate of equivalent 36 pu/s (4 pu/s respectively). According to the fault current supplied as shown in (6.1), once the fault occurs at WT string, CB_{21} detects 3 pu phase current from MMC_1 station immediately and the relay time-current curve comes into the definite time characteristic directly. CB_{21} trips after 0.04s according to the relay setting in Table 6.1. When the faulty WT string is disconnected by CB_{21}, the currents flowing through the CBs connected to the WT cluster relays and other healthy WT strings have not reached their pick-up values. The maximum currents at the fault clear and tripping time of the relays are shown in Table 6.3.

Table 6.3 Relay tripping time with the WT string fault.

		max CB current	t_s	t_{CB}	t_{trip}	**CB status**
WT cluster relay	**CB1**	0.16 pu	0.04 s	∞	∞	Closed
	CB2	0.83 pu	0.04 s	∞	∞	Closed
WT string relay	**CB1j**	0.16 pu	0.04 s	∞	∞	Closed
	CB21	4.8 pu	0 s	0.04 s	0.04 s	Open
	CB2j (j)≠1	0.16 pu	0.04 s	∞	∞	Closed

From Table 6.3, relays on WT strings with the smallest capacities are the most sensitive equipment. Once the fault occurs, it could potentially experience excessively large fault current from other healthy parts of the wind farm and offshore MMC converter. The fault current profiles of the MMC and WT converters proposed in this study where the fault currents increase gradually avoid such a problem whilst also ensuring correct protection actions.

6.2.4. SM capacitance requirements

Compared to normal operation, the fault current providing capability of the offshore MMC station might require relatively larger SM capacitance, which will be described in this subsection.

The arm voltage v_{arm} of the MMC station is given as [107]

$$v_{arm}(\omega t)=\sqrt{\frac{2N\times\Delta E_{arm}(\omega t)}{C_{SM}}+{V_{dc}}^{2}} \tag{6.16}$$

where N is the SM number per arm; C_{SM} is the SM capacitance; ΔE_{arm} is the arm energy variation; V_{dc} is the DC voltage. With third harmonic injection in the arm voltage as commonly used, ΔE_{arm} is expressed as (6.17) [123]:

$$\begin{aligned}\Delta E_{arm}(\omega t)&=\frac{1}{\omega}\int_0^{\omega t}v_{arm}i_{arm}d(\omega t)=\frac{V_{dc}I_m}{4\omega}\left[\cos\varphi-\cos\left(\omega t-\varphi\right)\right]\\&-\frac{V_mI_{dc}}{3\omega}\left[1-\cos\left(\omega t\right)\right]+\frac{V_mI_m}{8\omega}\left[\sin\left(2\omega t-\varphi\right)+\sin\varphi\right]\\&\underbrace{-\frac{V_{3m}I_m}{4\omega}\left\{\frac{1}{2}\sin\left(2\omega t+\varphi\right)-\frac{1}{4}\sin\left(4\omega t-\varphi\right)-\frac{1}{4}\sin\varphi+\frac{4I_{DC}}{9I_m}\left[1-\cos\left(3\omega t\right)\right]\right\}}_{\text{third harmonic influence}}\end{aligned} \tag{6.17}$$

where i_{arm} is the arm current; V_m and I_m are the phase voltage and current amplitudes respectively; V_{3m} is the amplitude of the third harmonic voltage; I_{dc} is the DC current; and φ is the phase angle difference between the voltage and current on the MMC AC side.

From (6.16) and (6.17), the arm voltage is illustrated in Figure 6.6. With the equivalent capacitor discharging time constant set at 30 ms (30 kJ/MVA) [124], the arm voltage is well regulated in the range of ±10%. After a solid offshore AC fault at t=0.1 s, the offshore voltage drops to zero and the MMC station starts to provide q-axis reactive current to enable fault detection. The arm voltage variation then increases to 1.44 times that of normal operation. Thus, to provide the fault current, relatively large SM capacitance is required, which can be designed according to (6.16) and (6.17). Alternatively, the maximum fault current might have to be limited to be less than 1.2 pu.

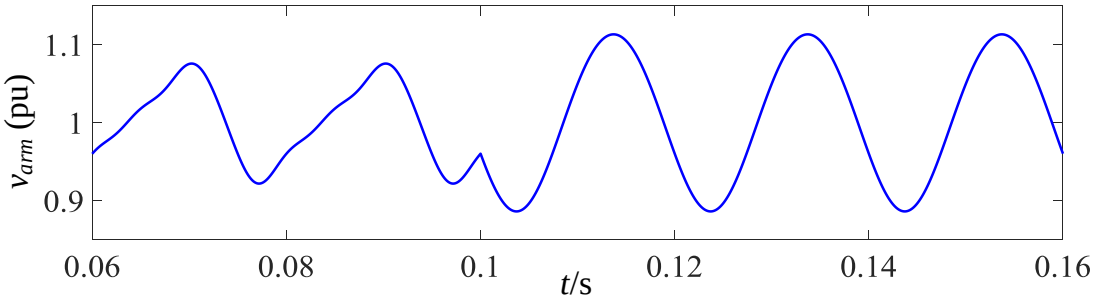

Figure 6.6 Arm voltage of MMC, where the offshore station provides q-axis current to enable fault detection after an offshore AC fault at t=0.1 s.

6.3. Control and operation during onshore AC Faults

Apart from offshore faults, MMC-HVDC connected offshore wind farm systems should also be able to ride-through faults at the onshore networks. In this section, to ride-through onshore AC faults, a DC voltage-dependent AC voltage controller is introduced to the offshore MMC station to actively reduce the offshore AC voltage to alleviate potential DC overvoltage of the HVDC system.

After a solid onshore three-phase fault, the onshore grid voltage drops and thus the active power that can be transmitted by the onshore MMC station is significantly reduced. Meanwhile, the WTs still try to transmit power to the HVDC-link and the resultant power surplus leads to the increase of the HVDC link voltage. To alleviate the DC overvoltage, the offshore MMC station needs to reduce power absorption from the offshore network immediately, and the power generation from the WTs also needs to be rapidly reduced.

To achieve this, the offshore grid voltage is reduced immediately by the offshore MMC after detecting DC overvoltage using an HVDC voltage-dependent offshore AC voltage controller which is introduced to actively regulate the offshore voltage, as shown in Figure 6.7. The DC voltage V_{dc} at the HVDC link and offshore AC voltage v^*_{pccd} are controlled at the rated value $V_{dcrated}$ and $V_{acrated}$ respectively during normal operation. Once V_{dc} is over the lower threshold V_{thl} after an onshore fault, the offshore voltage v^*_{pccd} starts to reduce according to the solid curves defined in Figure 6.7 and (6.18) as:

$$v^*_{pccd} = \begin{cases} V_{acrated}, & V_{dc} \le V_{thl} \\ \dfrac{V_{acrated}}{V_{thl} - V_{thu}}\left(V_{dc} - V_{thu}\right), & V_{thl} < V_{dc} \le V_{thu} \\ 0, & V_{thu} < V_{dc} \end{cases}. \quad (6.18)$$

The offshore AC voltage v^*_{pccd} is decreased to zero when the DC voltage reaches the upper threshold V_{thu}. Due to the reduced offshore AC voltage, the power generated by WTs is reduced, and so does the power inject to the HVDC-link. This ensures power flows in and out of the HVDC link is rebalanced and excessive DC overvoltage thus is avoided.

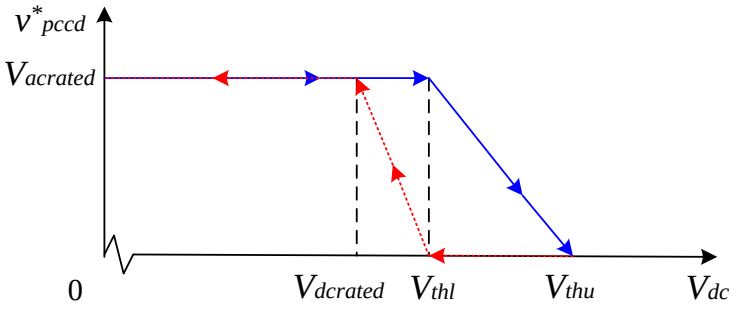

Figure 6.7 Characteristics of the HVDC voltage dependent offshore AC voltage.

After onshore fault clearance (typically several tens milliseconds), the onshore MMC station resumes DC voltage control capability and the HVDC-link overvoltage starts to reduce. When the DC voltage reaches the lower threshold V_{thl}, the offshore voltage v^*_{pccd} is gradual restores according to the dashed curve in Figure 6.7 and (6.19) as

$$v^*_{pccd} = \begin{cases} 0, & V_{thl} < V_{dc} \\ \dfrac{V_{acrated}}{V_{dcrated} - V_{thl}}\left(V_{dc} - V_{thl}\right), & V_{dcrated} < V_{dc} \le V_{thl} \\ V_{acrated}, & V_{dc} \le V_{dcrated} \end{cases}. \quad (6.19)$$

If during an onshore AC fault (e.g. remote fault or high impedance fault), relatively high AC voltage is retained at the onshore converter terminal. In such a situation, the onshore MMC can still transmit part of wind power and consequently, the voltage at offshore network will remain at a certain level with reduced wind power generation.

During the period with reduced offshore AC voltage, WTs operate in current limitation mode and the system can be recovered quickly after the onshore fault clearance.

6.4. Simulation results

By simplifying the offshore wind farm system and aggregating WTs as described in Chapter 4, the complete offshore grid shown in Figure 6.4 is simplified as the model displayed in Figure 6.8. The parameters of MMC-HVDC connected offshore wind farm model are listed in Table 6.4.

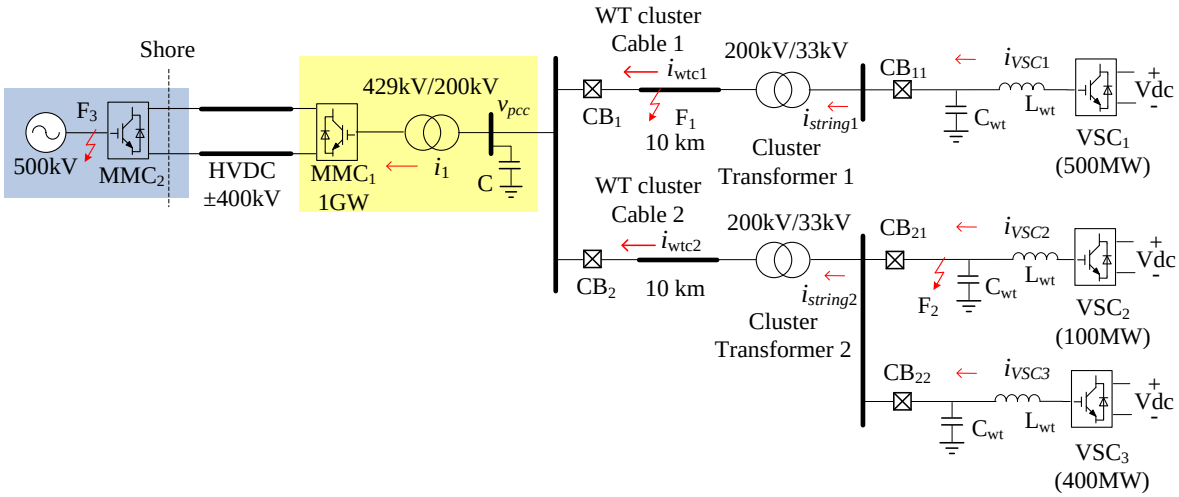

Figure 6.8 Offshore wind farm connected with MMC-HVDC model.

The proposed AC fault control strategies are tested using the model in Figure 6.8 in Matlab/Simulink. In this model, the same five WT strings connected to cluster 1 are aggregated as a large lumped WT model represented by a single VSC rated at 500 MW and connected to the collector bus through a 10 km cable. In order to simulate the fault occurring on WT string, WT strings connected to cluster 2 are divided into two parts: VSC_2 rated at 100 MW which is employed to represent a single WT string and an aggregated VSC_3 rated at 400 MW representing the other four strings. WT cluster 2 includes VSC_2 and VSC_3 and is connected to the collector bus through another 10 km cable in the same way as cluster 1.

Table 6.4 Parameters of the MMC-HVDC system.

MMC-HVDC system		
AC grid voltage		429 kV
HVDC voltage		800 kV
Rated power		1000 MW
MMC transformer	Voltage ratio	429 kV/200 kV
	MVA rating	1000 MVA
	Reactance	0.2 pu
	Resistance	0.004452 pu
MMC side AC capacitance		0.01 pu
PCC voltage		200 kV
Lumped wind turbine models		
DC voltage of WT converter		65 kV
WT power rating	VSC_1	500 MW
	VSC_2	100 MW
	VSC_3	400 MW
Cluster transformer	Voltage ratio	200 kV/33 kV
	MVA rating	500 MVA
	Reactance	0.1 pu
	Resistance	0.004 pu
WT side capacitor		0.15 pu
WT side inductor		0.2 pu
***R, L,* and *C* of cluster Cable (10 km)**		15 mΩ/km, 0.3 mH/km, 0.12 μF/km

With the parameters listed in Table 6.4, simulations studies during offshore AC fault at cluster and string cables are carried out whereas for onshore AC faults, three different voltage drop conditions are considered.

6.4.1. Offshore AC faults on WT cluster cable

Figure 6.9 shows the simulation results when a symmetrical offshore AC fault F_1 is applied at Cable 1 as shown in Figure 6.8 at t=1.1 s. As shown in Figure 6.9 (a), the offshore AC voltage rapidly drops to around zero. As the voltage on PCC cannot follow the reference, the AC voltage controller in MMC_1 tends to reduce the active power intake from the offshore wind farm and thus its *d*-axis current is rapidly reduced as shown in Figure 6.9 (e). This leads to the saturation of the voltage loop and the lower *d*-axis current is limited to zero set by the controller (to ensure no power reversal in this design). The offshore MMC_1 then provides fault currents by increasing its *q*-axis current which is gradually ramped from -0.3 pu with the rate of -0.9 pu/s (negative values represent capacitive reactive power) which can be used for fault detection, as shown in Figure 6.9 (b) and (f). Because of the large fault current injected to cluster 1, CB_1 trips at around 1.62s according to the presented overcurrent fault detection to isolate the fault. After the fault isolation, the AC voltage of the offshore network gradually restores to the rated value by MMC_1 as shown in Figure 6.9 (a). The offshore frequency is also restored to the reference value after the fault isolation, Figure 6.9 (d). The generated and transmitted power recover to half of the previous rated value as only one healthy cluster is connected, as shown in Figure 6.9 (c).

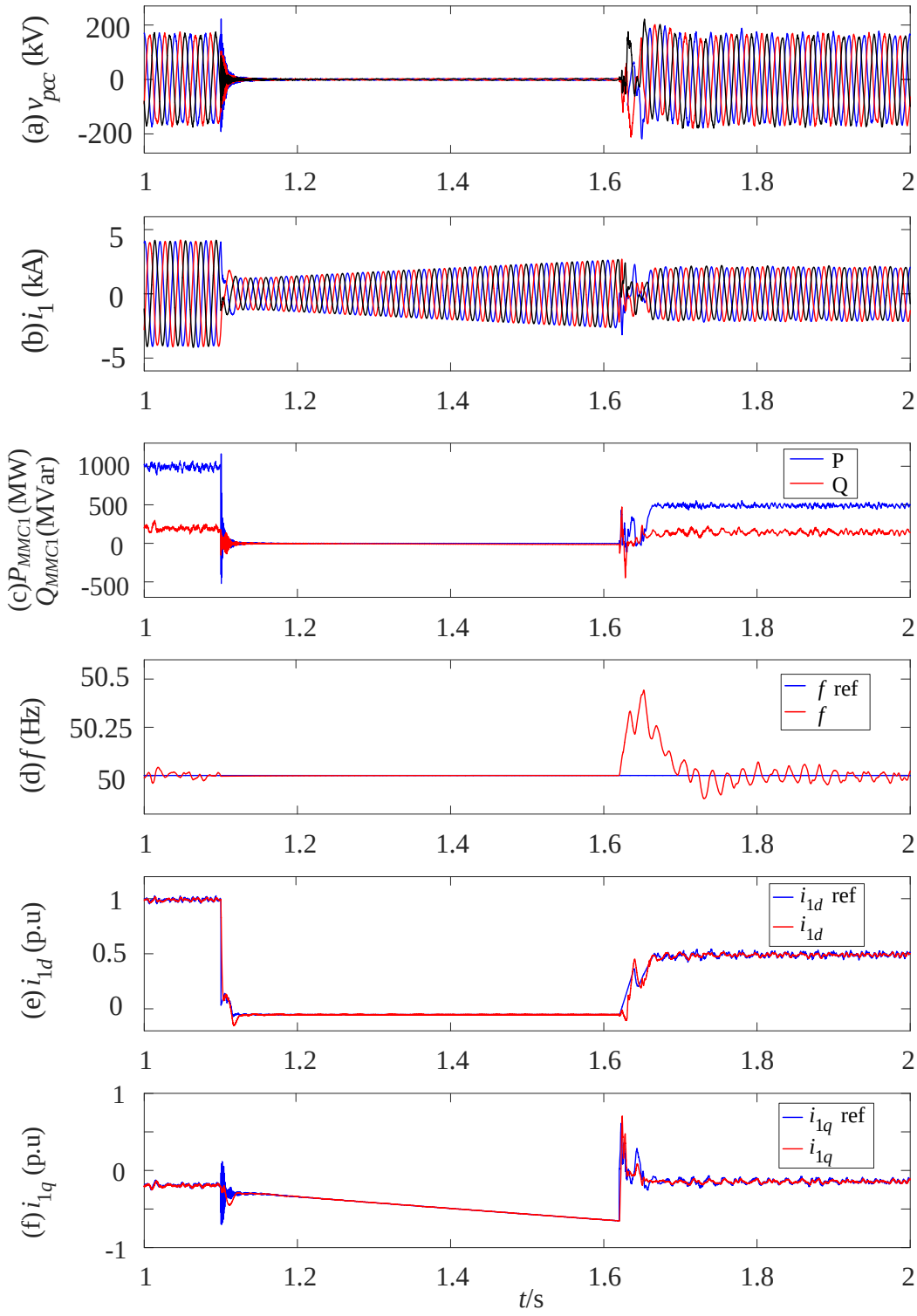

Figure 6.9 Simulation waveforms of offshore MMC_1 during WT cluster fault.

(a) PCC three-phase voltage, (b) MMC_1 three-phase current, (c) MMC_1 real and reactive power, (d) offshore grid frequency, (e) MMC_1 *d*-axis current, (f) MMC_1 *q*-axis current.

Figure 6.10 (a) to (e) display the currents at WT clusters and strings during the offshore AC fault at cluster cable 1. After fault occurrence at t=1.1 s, the output currents of wind turbines initially drop rapidly. This is due to the limit of the active current when the lower AC voltage is detected by the WT converters. The currents then increase gradually according to the reactive/fault current provision as indicated in (6.2), from 0 pu to 1.2 pu with a rate of 4 pu/s. Thus, as can be seen in Figure 6.10, within 0.3 s, the currents all hit the maximum WT output limit of 1.2 pu. As previously shown in Figure 6.9 (b), the fault current provided by MMC_1 is also gradually ramped up and flows through the circuit breaker on the faulty branch (CB_1, Figure 6.8) together with the fault current supplied by the healthy WT strings. The total current at CB_1 then reaches to the protection threshold (the rated current of CB_1 is calculated as 2.04 kA) as shown in Figure 6.10 (f), and CB_1 now is commanded to open to isolate the faulty branch. According to the relay setting and tripping period calculated in Table 6.2, CB_1 trips at t=1.62 s. Once the fault at Cable 1 is cleared by CB_1, currents on Cables 2 and WT strings of cluster 2 are quickly recovered to their pre-fault values, shown in Figure 6.10 (b), (d) and (e). In the simulation and for illustration purpose, cluster 1 (VSC_1) remains operational (operating at current upper limit) after being isolated from the rest of the offshore AC network though in reality, it is likely to be shut down after fault isolation.

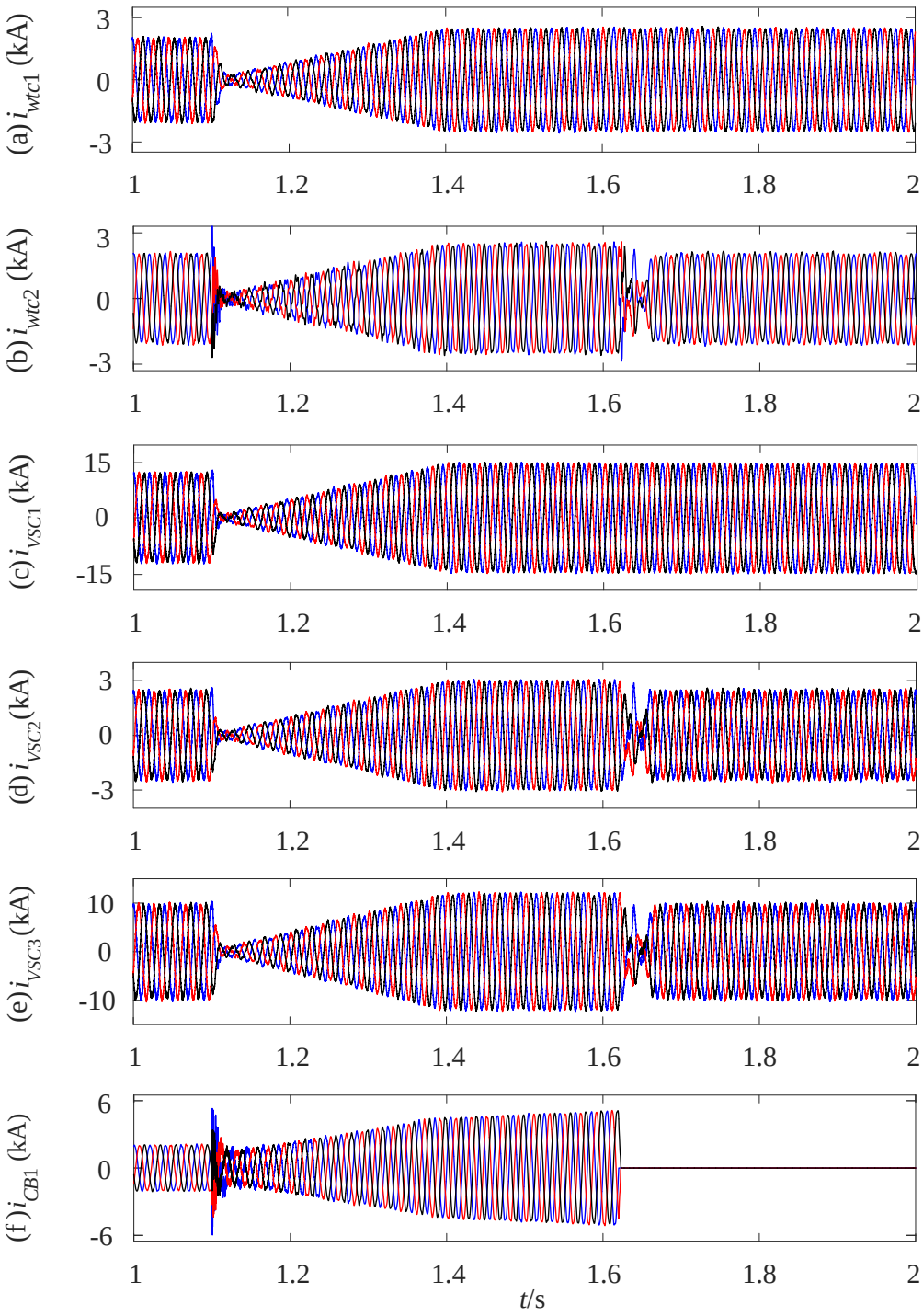

Figure 6.10 Simulation waveforms of offshore WT cluster and string during WT cluster fault.

(a) WT cluster 1 current, (b) WT cluster 2 current, (c) sum current of WT strings at cluster 1 (VSC_1 current), (d) current of signal WT string at WT cluster 2 (VSC_2 current), (e) sum current of four WT strings on cluster 2 (VSC_3 current), (f) current through CB_1.

During the fault on offshore AC system, MMC_1 stops power transmission and this leads to power imbalance on the HVDC link. Figure 6.11 (a) and (b) shows the DC voltage and power flow at onshore MMC_2 during the offshore AC fault. When the fault occurs at t=1.1 s, MMC_2 initially keeps absorbing power from the HVDC system, leading to DC voltage drop as shown in Figure 6.11 (a). MMC_2 then controls the DC voltage after the initial transient, whilst no power transmission at HVDC system. With the clearance of offshore AC fault, MMC_1 rebalances the power transmission and regulates DC voltage with small oscillation at t=1.62 s, as seen in Figure 6.11 (a) and (b).

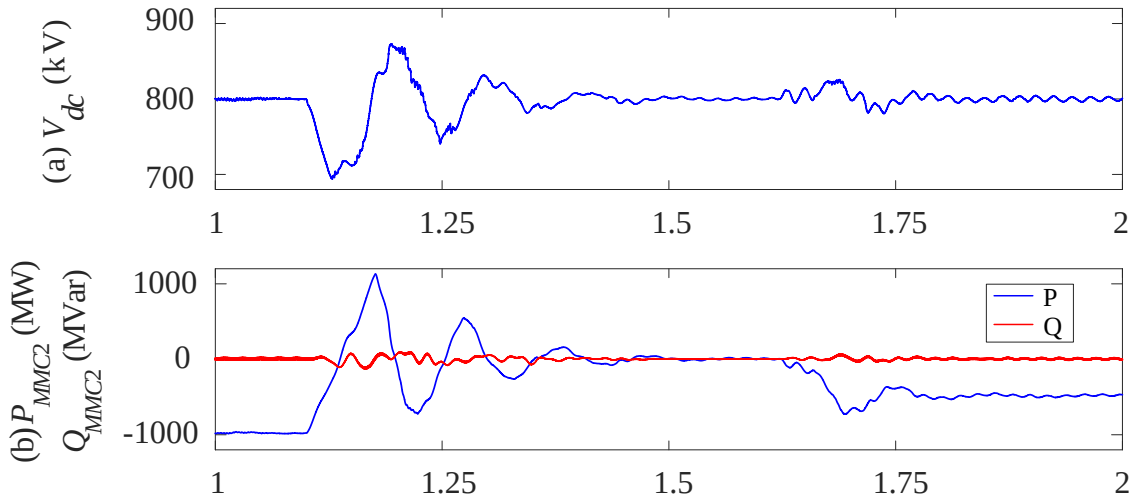

Figure 6.11 Simulation waveforms of HVDC link during WT cluster fault.
(a) DC voltage on HVDC link, (b) MMC_2 real and reactive power.

With the proposed fault current provision, the whole offshore system is well controlled during such serious offshore AC faults and can restore normal operation automatically.

6.4.2. Offshore AC faults on WT string

A symmetrical three-phase fault F_2 is applied at WT string 2-1 (VSC_2) at 1.1 s and the simulation results are shown in Figure 6.12 and Figure 6.13. Once the fault is applied, the PCC voltage drops immediately. For the offshore MMC_1, i_{1d} is limited and i_{1q} increases from -0.3 pu according to (6.1), shown in Figure 6.12 (e) and (f). The currents of MMC_1 as illustrated in Figure 6.12 (b) also shows a similar trend. In the meantime, WT converters detect the voltage drop and switch to fault current supplying mode. As demonstrated at Figure 6.13 (c), (d) and (e), currents of VSC_1, VSC_2 and VSC_3 all drop to around zero at 1.1 s and then increase with the rate of 4 pu/s. Currents flowing through cluster 1 and cluster 2 are shown in Figure 6.13 (a) and (b) respectively. Due to the long cluster cable and cluster transformer, current on cluster 1 is slightly different from that of VSC_1. Current at CB_{21} of the faulty WT string 2-1 contains the fault current flowing from MMC_1, WT cluster 1 and VSC_3 (the healthy part of cluster 2), and therefore is very high, as shown in Figure 6.13 (f). According to Table 6.3, fault current at CB_{21} during the fault period quickly reaches 4.8 pu and thus lead to the fast trip of WT string relay after 0.04 s. in the simulation, in the first few milliseconds after the fault occurrence, the current of each WT does not drop to zero immediately and with additional discharging current of the transmission cables, the initial fault current flowing through CB_{21} is about 6 pu.

After isolating the faulty WT string, the voltage on PCC and the current gradually recovers under the control of MMC_1 shown in Figure 6.12 (a) and (b). The power transmission after the fault clearance with the loss of one WT string is 0.9 pu, as shown in Figure 6.12 (c). The offshore frequency has small oscillation after system recovery but is quickly controlled to the rated value as shown in Figure 6.12 (d).

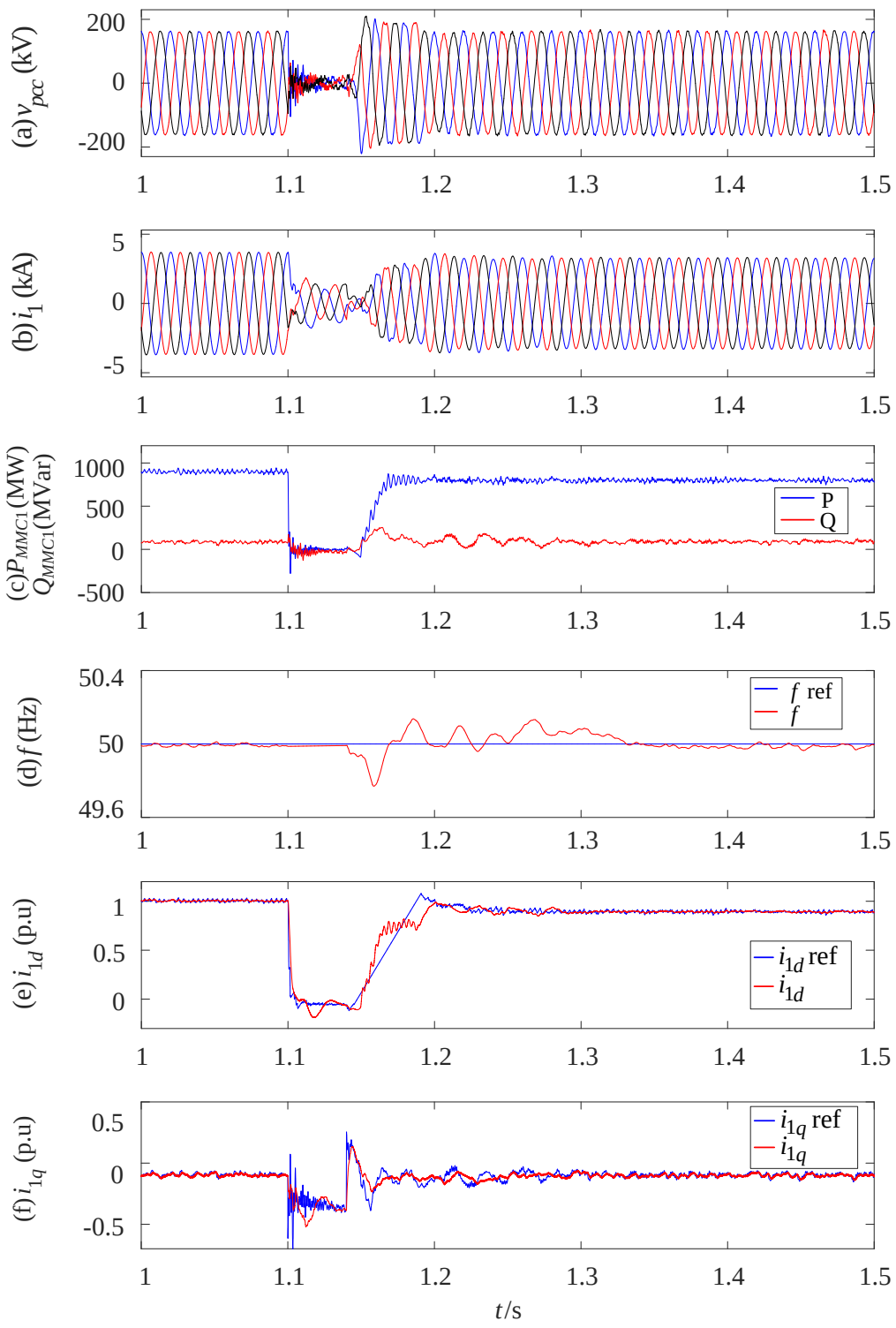

Figure 6.12 Simulation waveforms of offshore MMC_1 during WT string fault.

(a) PCC three-phase voltage, (b) MMC_1 three-phase current, (c) MMC_1 real and reactive power, (d) offshore frequency, (e) MMC_1 d-axis current, (f) MMC_1 q-axis current.

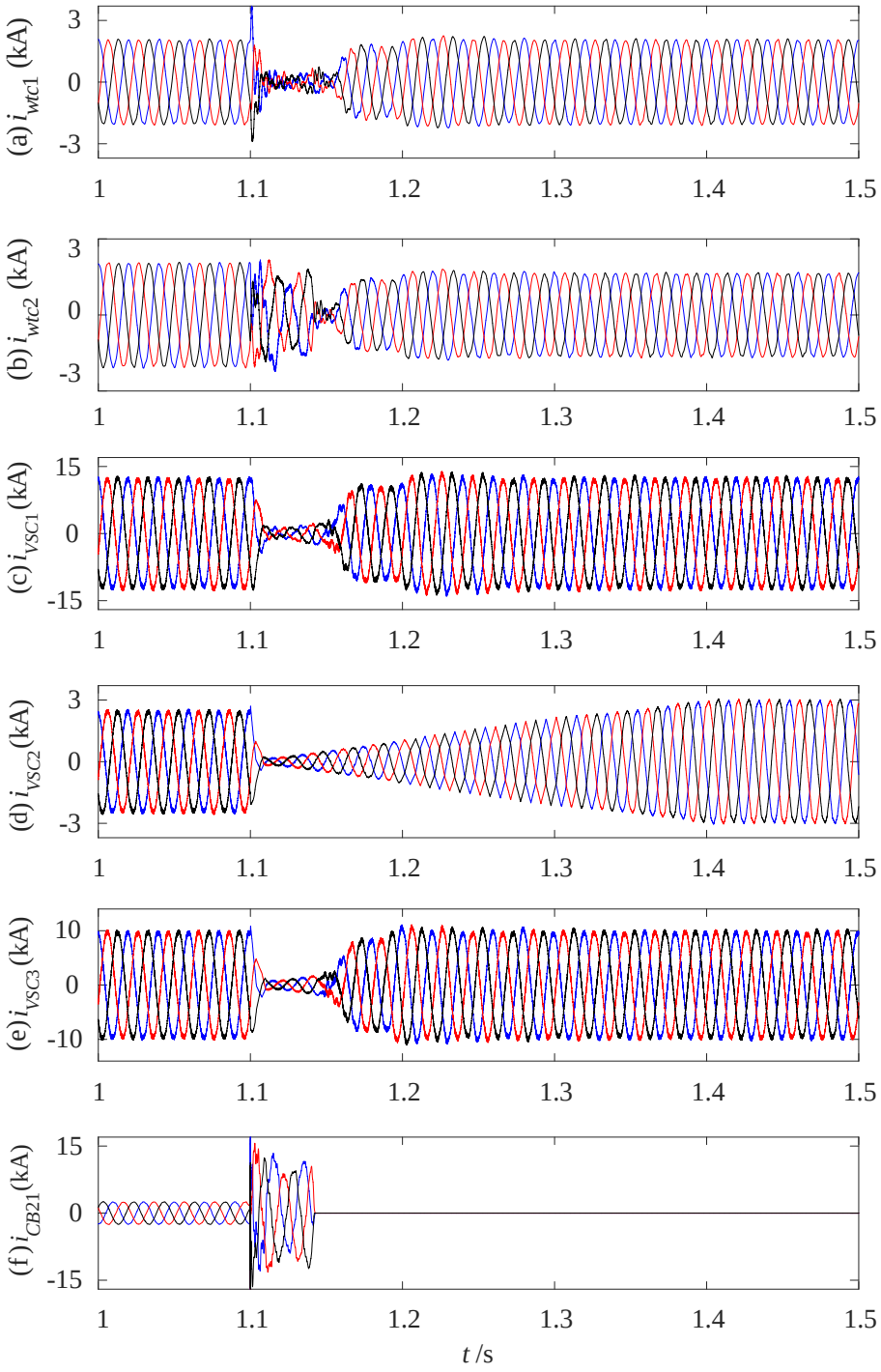

Figure 6.13 Simulation waveforms of offshore WT cluster and string during the fault occurs on the string cable.

(a) WT cluster 1 current, (b) WT cluster 2 current, (c) WT strings 1 (VSC_1) current, (d) WT strings 2-1 (VSC_2) current, (e) Sum of current of WT string 2-2 to WT string 2-5 (VSC_3), (f) Current through CB_{21}.

Although the overcurrent experienced by the CBs at WT string is still high, it is far smaller when compared to that without the proposed fault current ramping control strategy. If no fault current supply control strategy applies at WT side (output current directly increasing to 1.2 pu) and MMC_1 current is simply limited at around zero when AC fault occurs, the total current flows through the CB will be huge. As demonstrated in Figure 6.14, the fault current flows through CB reaches 12 pu without the WTs fault current supply control.

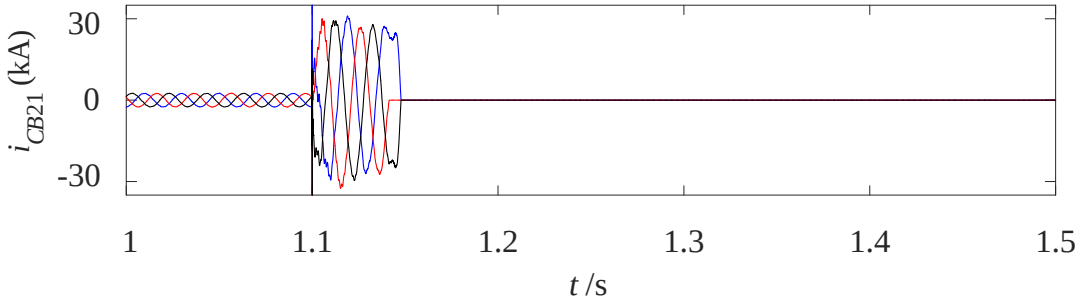

Figure 6.14 Current through CB_{21} while WTs without fault current control.

6.4.3. Onshore AC faults

To test the proposed control in the events of onshore AC faults, a symmetrical solid fault F_3 is applied at the AC side of the onshore station MMC_2 as illustrated in Figure 6.8. Fault applies at t=1.2 s and is cleared after 0.3 s (at t=1.5 s). Three fault conditions resulting in different voltage drops of 100% and 50% and 20%, respectively, are tested in Simulink/MATLAB. The lower and upper DC voltage thresholds of onshore AC fault ride-through control V_{thl} and V_{thu} are set at 1.05 pu and 1.15 pu in this simulation work.

a) Onshore AC fault with 100% voltage drop at MMC_2

In this scenario, a solid fault F_3 is applied at the AC terminals of the onshore station MMC_2 at t=1.2 s and the simulation results are shown in Figure 6.15 - Figure 6.17. As shown in Figure 6.15 (a), the onshore voltage drops to zero after the fault and onshore MMC_2 operates on current limiting mode with its current limited to 1.4 pu as shown in Figure 6.15 (c). As the power transmission capacity of MMC_2 is reduced to zero because of the drop of AC voltage, whereas the offshore wind energy is still imported to the HVDC

link, the DC voltage rapidly increases, as displayed in Figure 6.15 (b). The increased DC voltage hits the lower voltage threshold and triggers the offshore fault protection control. Consequently, the offshore AC voltage as shown in Figure 6.16 (a) is actively decreased to zero according to the profile defined in Figure 6.7. This reduces WT generated power and the imported power to the HVDC link to zero as shown in Figure 6.17 (d) - (f) and Figure 6.16 (c). Thus, the DC voltage of the HVDC link is limited to be less than 1.2 pu, seen in Figure 6.15 (b). It is clear that during the fault condition, no power is able to be delivered to the onshore grid.

During the fault condition, the voltage on PCC is controlled at zero and current i_1 of offshore station MMC_1 balances the overall current from the WTs, whose value is around 1.2 pu, as illustrated in Figure 6.16 (b). The measured offshore frequency is temporary increased as shown in Figure 6.16 (d) though the AC voltage now is zero (so frequency is not a valid parameter). After fault clearance at onshore site and the power transmission of the onshore MMC_2 restores, the offshore AC voltage increases, and the system autonomously restores normal operation without any communication.

WTs all operate in current limitation mode (1.2 pu) because of the offshore voltage drops to zero, as illustrated in Figure 6.17 (a), (b) and (c). The wind power cannot be exported and has to be consumed at WT level or de-loading using proper FRT method employed at WTs. Thus, the output power of VSCs are zero as shown in Figure 6.17 (d), (e) and (f). After the onshore fault clear, all WTs recover to normal operation mode.

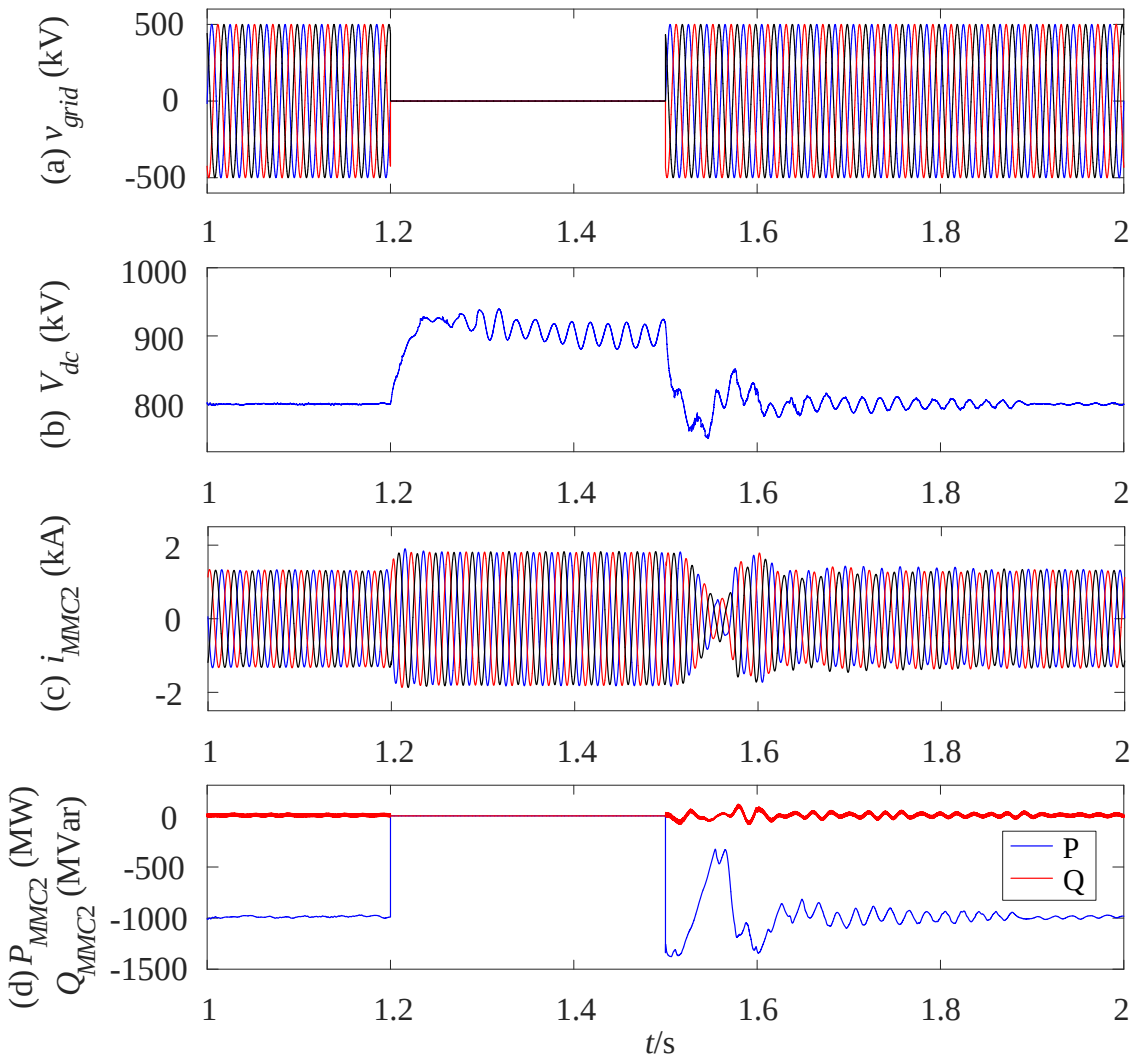

Figure 6.15 Simulation waveforms of onshore MMC_2 during 100% voltage drop at onshore site.

(a) Onshore grid voltages, (b) three-phase currents of MMC_2, (c) DC voltage of HVDC transmission line, (d) real and reactive power of onshore MMC station.

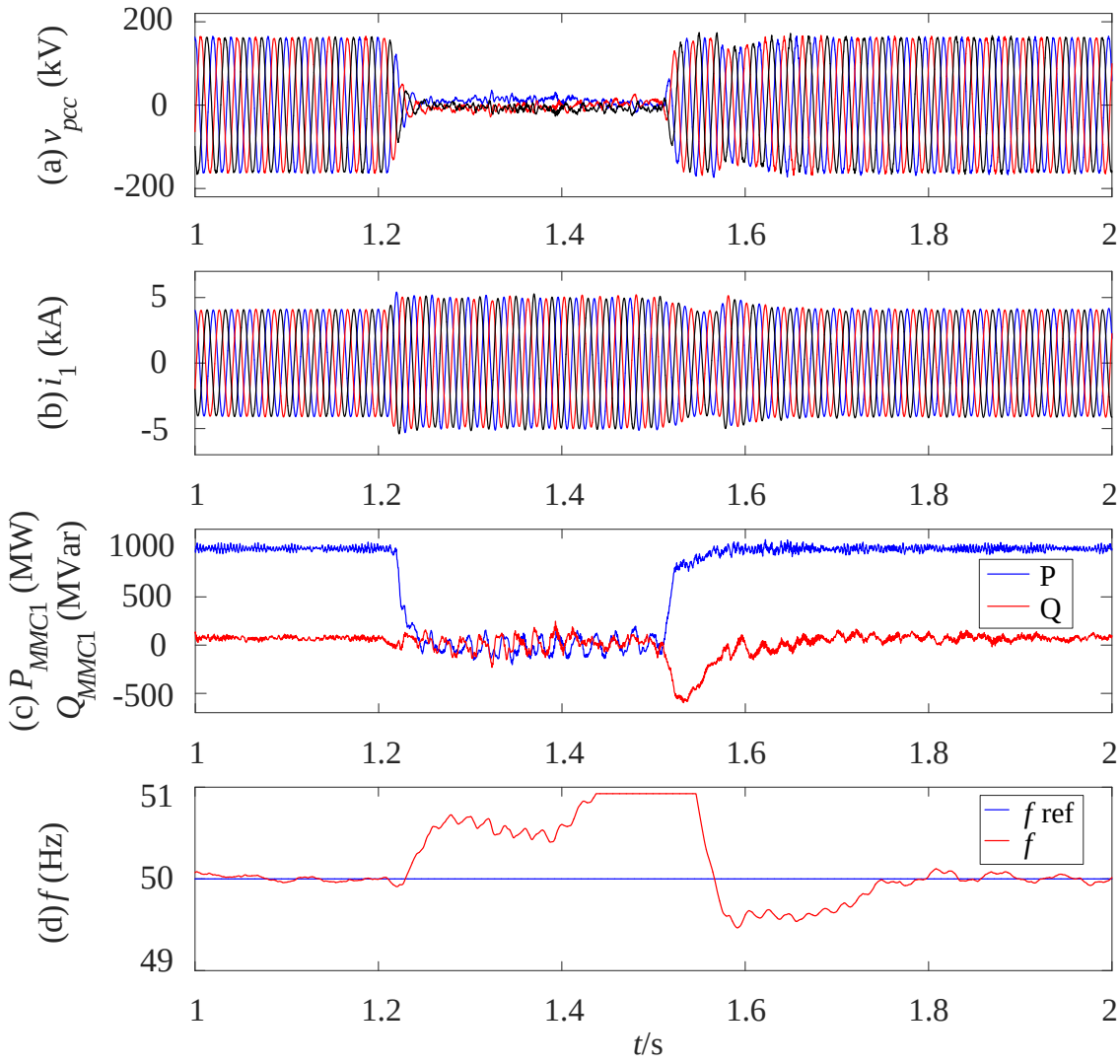

Figure 6.16 Simulation waveforms of offshore MMC_1 during 100% voltage drop at onshore site.

(a) Voltages on offshore PCC bus, (b) currents of MMC_1, (c) active and reactive power of MMC_1, (d) offshore frequency.

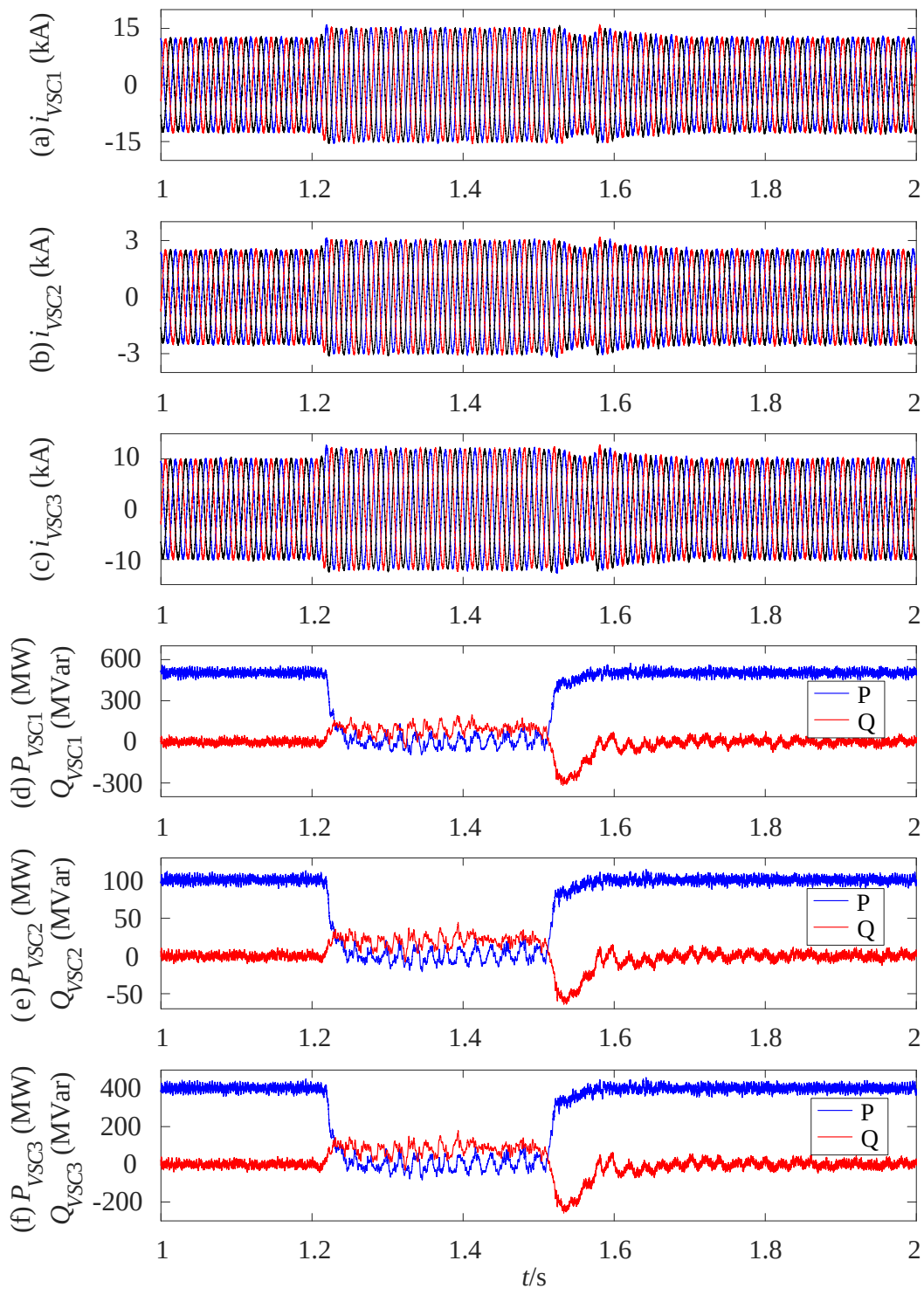

Figure 6.17 Simulation waveforms of WT side during 100% voltage drop at onshore site.

(a) Current of VSC_1, (b) current of VSC_2, (c) current of VSC_3, (d) real and reactive power of VSC_1, (e) real and reactive power of VSC_2, (f) real and reactive power of VSC_3.

b) Onshore AC fault with 50% voltage drop at MMC_2

In this condition, onshore AC fault F_3 occurs at t=1.2 s and results in a 50% AC voltage drop at the onshore grid, shown in Figure 6.18 (a). This results in MMC_2 operating at current limit of 1.4 pu and the power transmission from DC to onshore AC to around 700 MW, 70% of rated power as shown in Figure 6.18 (c) and (d). Because the wind power delivered from offshore wind farm remains at rated value and continues being imported to the HVDC link, DC voltage increases because of the power imbalance, shown in Figure 6.18 (b). The rising DC voltage activates the offshore AC voltage control at MMC_1 and the offshore PCC bus voltage is reduced accordingly, illustrated in Figure 6.19 (a). Currents on every WTs are limited to 1.2 pu, seen in Figure 6.20 (a), (b) and (c) and the output power then reduced consequently to around 0.7 pu, illustrated in Figure 6.20 (d), (e) and (f). Thus, HVDC link power balance is reestablished and the DC overvoltage is limited to around 5%. Offshore frequency is controlled at around 50 Hz with small fluctuation which results in some oscillation on reactive power, seen Figure 6.19 (d) and (c). At t=1.5 s, the onshore fault is cleared, and the DC voltage is restored gradually. Consequently, the voltage on the PCC bus is also recovered back to its rated value according to (6.19), and normal system operation resumes.

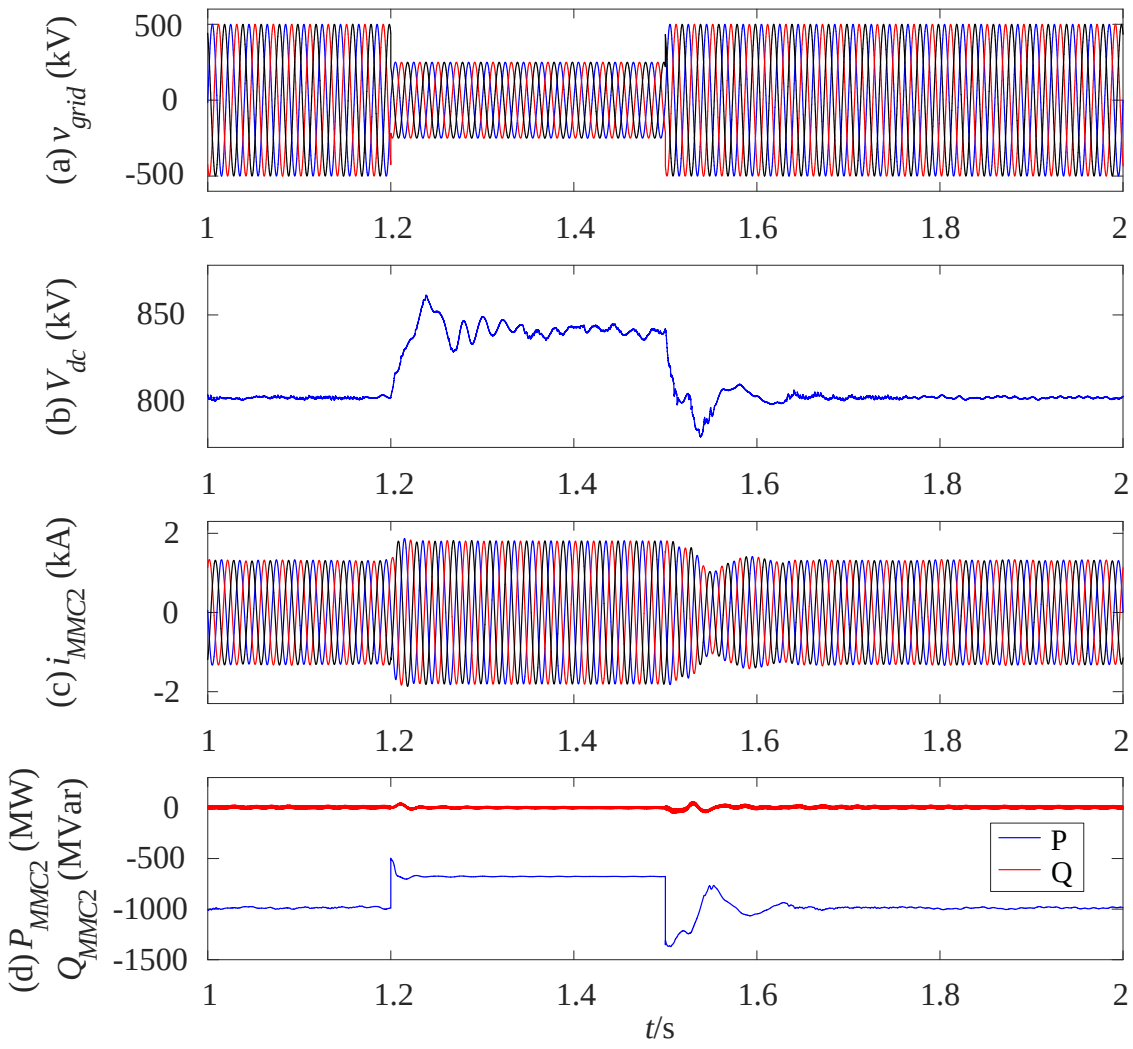

Figure 6.18 Simulation waveforms of onshore MMC_2 during 50% voltage drop at onshore site.

(a) Onshore grid voltages, (b) three-phase currents of MMC_2, (c) DC voltage of HVDC transmission line, (d) real and reactive power of onshore MMC station.

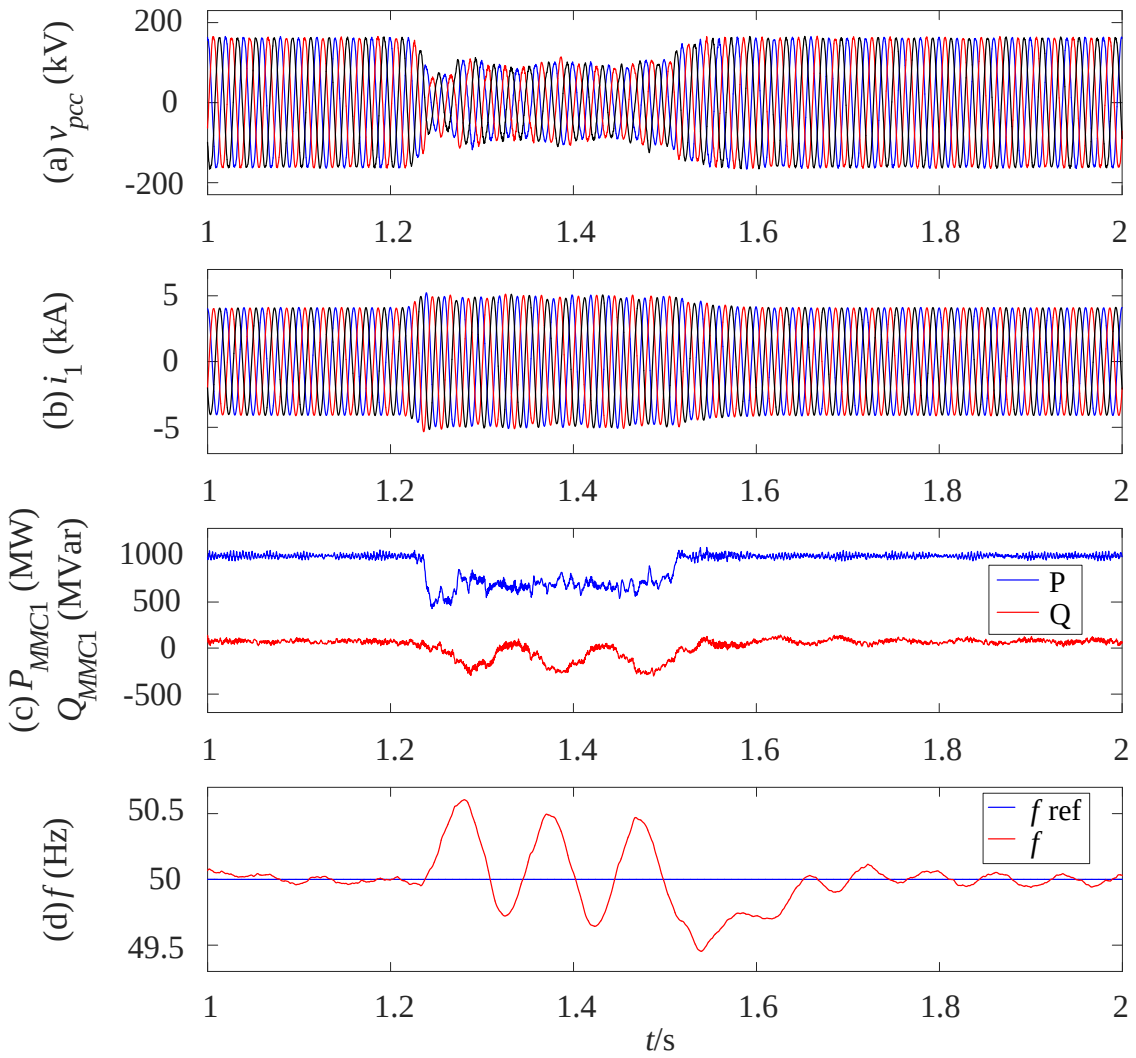

Figure 6.19 Simulation waveforms of offshore MMC_1 during 50% voltage drop at onshore site.

(a) Voltage on offshore PCC bus, (b) three-phase currents of MMC_1, (c) real and reactive power of MMC_1, (d) offshore frequency.

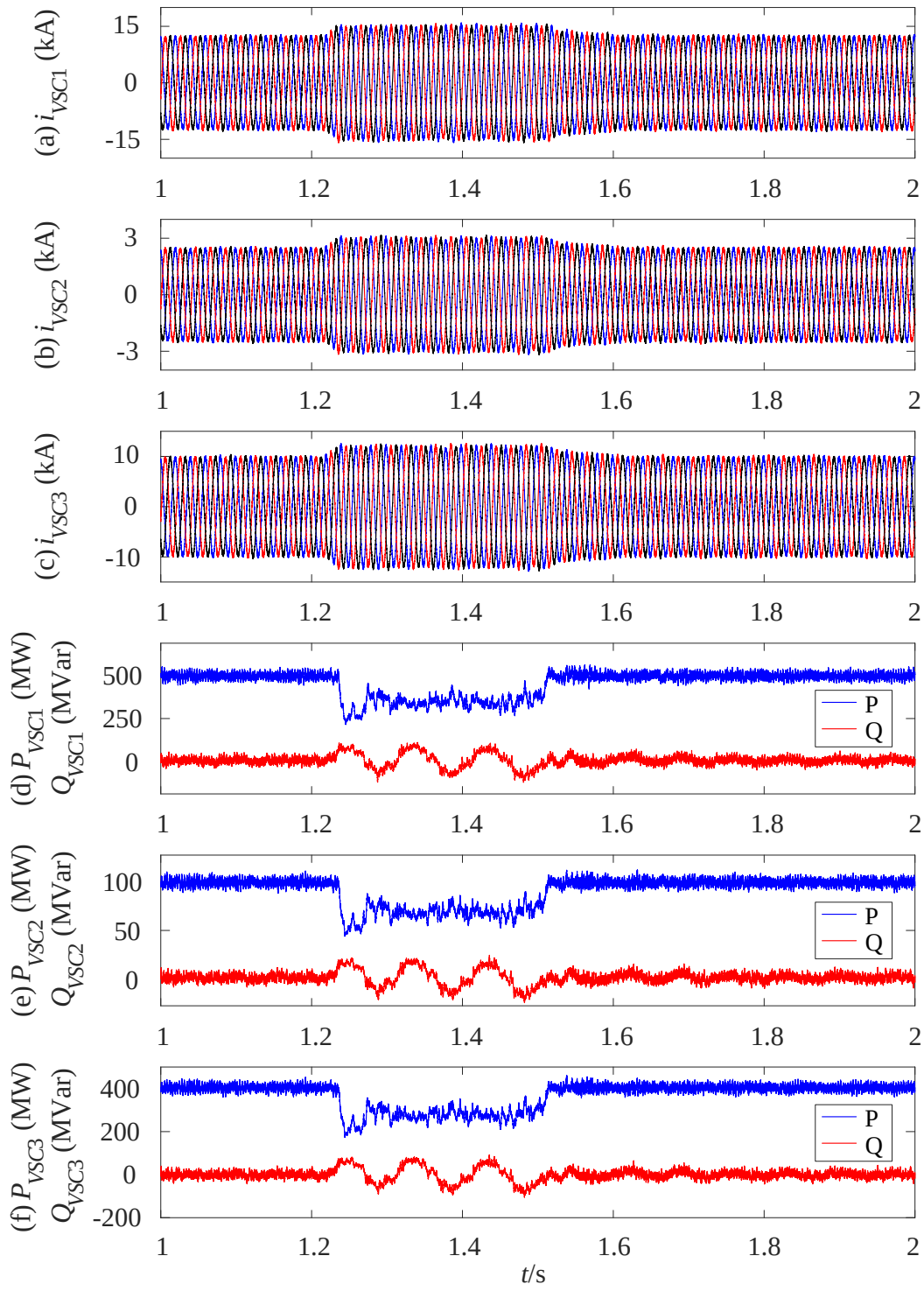

Figure 6.20 Simulation waveforms of WT side during 50% voltage drop at onshore site.

(a) Output current of VSC_1, (b) output current of VSC_2, (c) output current of VSC_3, (d) real and reactive power of VSC_1, (e) real and reactive power of VSC_2, (f) real and reactive power of VSC_3.

c) Onshore AC fault with 20% voltage drop at MMC_2

The simulation results during an AC fault at onshore site leading to a small 20% voltage drop are shown in Figure 6.21 and Figure 6.22. As can be seen, during the fault, due to the overcurrent capability of the onshore MMC_2 station, DC voltage can still be regulated and thus the offshore AC voltage control is not activated by MMC_1. The offshore system operates as normal as shown in Figure 6.22.

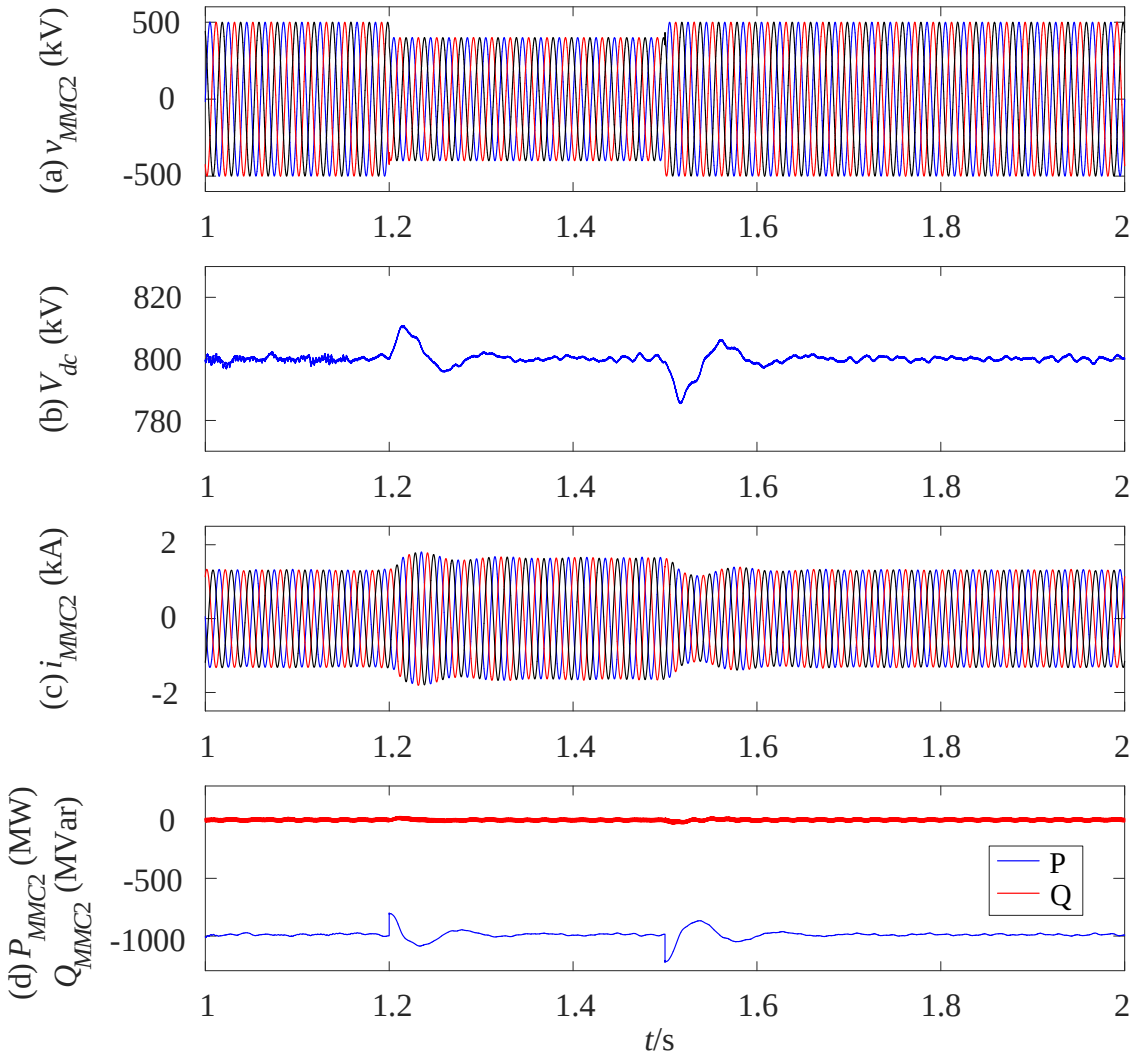

Figure 6.21 Simulation waveforms of onshore MMC_2 during 20% voltage drop at onshore site.

(a) Onshore grid voltages, (b) three-phase currents of MMC_2, (c) DC voltage of HVDC transmission line, (d) real and reactive power of onshore MMC station.

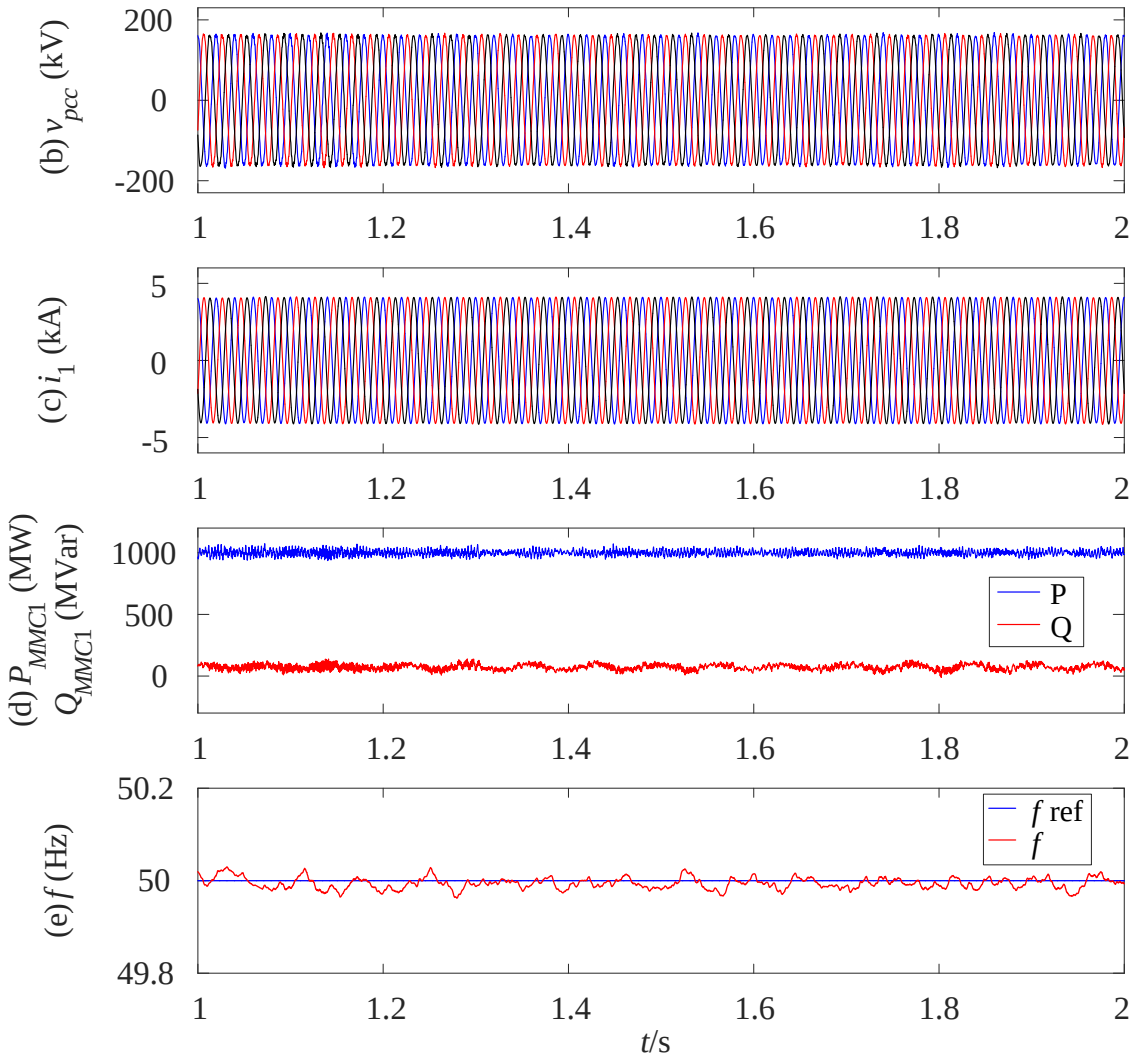

Figure 6.22 Simulation waveforms of offshore MMC_1 during 20% voltage drop at onshore site.

(a) Voltage on offshore PCC bus, (b) three-phase currents of MMC_1, (c) real and reactive power of MMC_1, (d) offshore frequency.

6.5. Summary

Aiming at supplying sufficient fault current to enable overcurrent protection during offshore AC faults, coordinated control methods of fault current injection at offshore MMC station and WT VSC are proposed. With the offshore MMC station actively provides fault currents under fault occasion, overcurrent protection of offshore network can be achieved with AC faults occur at WT cluster or WT string. With coordination of relay characteristics setting and fault current injection control, the proposed fault control strategy can well tackle the challenge of different AC faults, locations and fault current requirements. The proposed method ensures sufficient fault current during wind farm cluster faults whilst preventing excessive fault current during wind farm string faults.

System control and operation during AC faults at onshore network of MMC-HVDC connected offshore wind farm system are studied. Due to the reduced power exported from the DC side of the HVDC network to onshore AC system during such AC faults, excessive DC overvoltage could occur which can potentially cause damage to the HVDC system and/or system disconnection. To ride through such onshore AC faults, a DC voltage dependent AC voltage profile is introduced to the offshore MMC converter to actively reduce the offshore AC voltage when DC overvoltage is detected. This indeed reduces the power generated by the offshore WTs and thus, power import and export to the HVDC system can be rebalanced. Offshore system responses under three different voltage drops at onshore grid are investigated by simulation. The results show that with the proposed onshore AC fault ride-through control, the DC voltage at HVDC link can be limited to a safe range and offshore wind farm can remain connected and operational.

Chapter 7

Conclusion and Future Work

7.1. General conclusion

This thesis focuses on the control and operation of MMC based HVDC systems for offshore wind farm connection. A comprehensive overview has been carried out to review the recently developed HVDC system controls and operation performances when used for large offshore wind farm integration. From the assessment of the literature, HVDC connected offshore wind farms are still facing many challenges that need further investigation. An enhanced offshore AC voltage and frequency control strategy has been proposed and the system stability with this proposed control is analysed. A fault current providing control was developed for offshore MMC and WTs to ensure adequate control and protection during offshore AC faults. To solve potential overvoltage on HVDC link during onshore voltage dip, a DC voltage dependent offshore AC voltage control was developed. Extensive simulations by using the MATLAB/Simulink have been presented to test and verify the proposed controls.

The offshore AC power system of large offshore wind farms formed by the offshore MMC station is significantly different to conventional power networks and can exhibit voltage oscillation or harmonic resonance in the event of faults. Stable AC voltage and frequency control is a prerequisite for the transmission of offshore wind energy. The fixed frequency with vector-current control for the offshore MMC is the most common approach to regulate the AC voltage of an offshore network. However, such method reduces the controllability of the offshore AC voltage and leads to slower dynamic response, especially during large transients. To improve the voltage controllability and system dynamic response during disturbances, an enhanced voltage and frequency control

based on the PLL operating principle was proposed. A *q*-axis voltage reference is generated by frequency loop and fed to the *q*-axis voltage controller of the MMC. With the additional frequency control added in the MMC, the frequency can be tightly regulated but is also allowed to vary slightly during transients to improve system dynamic response. This proposed enhanced voltage and frequency control was tested under several offshore operation conditions including system start-up, WT connection process, wind power ramping-up and normal system operation in the simulations. The advantages of the proposed control when compared to the fixed frequency control were demonstrated during MMC start-up and WT disconnecting conditions, including faster and better voltage reference tracking during start-up and more stable offshore AC voltage in the event of suddenly disconnecting of WTs.

To further study the effects of the proposed control on the stability of the MMC-HVDC connected offshore wind farm system, a small-signal model of the simplified offshore system, including the MMC and WF grid side converter have been developed. Frequency responses from the small-signal model and its corresponding time-domain model were compared to verify the accuracy of the developed small-signal model. Using the small-signal state space model, system stability was analysed in frequency domain using Bode plots and pole/zero maps (p/z maps). With the p/z maps, the control requirements of the offshore wind farm system were investigated, and the impact of control parameters on system stability were studied. Comparing to the conventional control, the proposed control allows wider parameter ranges that can be used whilst maintain system stability. The interaction between offshore wind power and AC voltage were also investigated with Bode plots and results demonstrated that the voltage was less influenced by wind power variation while using the enhanced AC and frequency control.

For large-scale offshore wind farms, ensuring stable operation during large transients, e.g. AC faults, is critically important and many operation challenges under AC fault conditions need to be addressed, such as the potential large fault currents through MMC and WT converters, offshore protection and fast post-fault recovery. Some researches proposed to directly limit the fault current to protect the offshore equipment. However,

directly limiting fault current results in difficulties in fault detection and operation of protection devices. On the other hand, fast fault current provision from MMC and WT converters could potentially lead to very high overcurrent for circuit breakers connected to some parts of the offshore network, e.g. WT strings, in the event of faults at string cables. This thesis thus proposed a new fault current providing control for both the offshore MMC and WT converters. Once an offshore AC fault is detected (by detecting the dropped AC voltage), the reactive current from the offshore MMC is quickly ramped up from 0.3 pu to 1.2 pu at a rate of 0.9 pu/s whilst for the WT grid side converters, the reactive current also increases from zero at the rate of 4 pu/s. By carefully considering the different circuit breaker parameters at different locations in the offshore wind farm, e.g. difference in WT cluster relays and WT string relays, and the fault current provision of the MMC and WT converters, adequate protection can be realized whilst ensuring maximum currents of the circuit breakers are not exceeded. Typical overcurrent relay characteristics were considering during fault current variation in determining the tripping time. Simulation results verified the effectiveness of the proposed fault current providing control during different offshore fault locations.

Onshore AC voltage drop caused by onshore AC faults leads to significant reduction of power that can be exported from DC to offshore AC network and potentially results in DC overvoltage. To ensure continuous operation of the HVDC link and offshore wind power generation, the excess power from the WF has to be dissipated, or the power generated by the wind turbines be reduced. This thesis proposed a DC voltage dependent offshore AC voltage control method to ensure active power balancing during onshore AC faults. Once a DC overvoltage is detected by the offshore MMC station, the offshore grid voltage controlled by the offshore MMC is quickly reduced according to a predefined characteristic. The reduction of the offshore AC voltage limits the maximum power that can be generated by the offshore wind farm and active power balancing between imported to and exported from the HVDC link can thus be re-established. Consequently, severe DC link overvoltage is avoided. Once the onshore AC voltage restores and DC voltage reduces, the offshore grid voltage is then restored by the offshore MMC. Three different onshore

fault conditions with voltage drops of 100%, 50% and 20% were tested respectively. The results showed that by adequately setting the DC voltage dependent offshore AC voltage limiter, HVDC power rebalancing can be achieved and DC overvoltage avoided whilst the system continued transmitting maximum active power that can be handled by the onshore AC network during onshore AC faults. The proposed method reduces the requirements on additional hardware, e.g. DC damping resistor on HVDC link, with no need for fast communication either.

7.2. Author's contribution

The contributions of this thesis can be summarized as follows:

- Proposing an enhanced AC voltage and frequency control of offshore MMC station for wind farm connection. By employing an additional frequency control loop designed on the basis of PLL operation principle, the voltage controllability of offshore PCC bus is improved. The proposed control creates a closer relationship between offshore frequency and voltage and enables a better dynamic response of offshore wind farm system.
- To ensure adequate fault detection and system protection during offshore AC faults, a fault current injection control is proposed. Considering the different characteristics of relays at different locations, e.g. WT strings and WT clusters, the reactive fault currents of the MMC and WTs are increased gradually so as not to over stress the circuit breakers connected at low power cables, e.g. WT strings, whilst still ensuring sufficient overcurrent for protection.
- A DC voltage dependent offshore AC voltage control method is proposed to ride-through onshore AC faults. By reducing the offshore AC voltage upon the detection of DC overvoltage of the HVDC link by the offshore MMC, active power balancing of the HVDC link can be re-established whilst continuing transmitting certain power from the wind farm to the onshore AC grid.

7.3. Further work

Based on the studies carried out in this thesis, further studies can be carried out in the following areas:

- In this thesis, all the wind turbines are aggregated and presented by grid side VSCs. Because the detailed WT models are not used, the detailed interactions among the different WTs and the offshore MMC are not considered in this research. To further study the proposed control, the aggregated VSCs can be replaced by detailed WT strings and clusters including the interconnection cables to investigate potential interaction within the offshore system.
- For offshore AC faults, this thesis only considers the WT cluster fault and WT string fault with one specific wind farm layout. For different wind farm layouts, e.g. meshed network, the studies on AC fault and offshore system protection require further investigation.
- Fault studies in this thesis only considered three-phase symmetrical faults. System response and converter controls during asymmetric faults at both onshore and offshore networks need to be further studied.
- Point-to-point HVDC configuration is studied in this thesis with one offshore MMC station connected to the wind farm. For large offshore wind farms, multiple offshore MMC stations might be required which requires further investigation into their control, e.g. synchronization control and power-sharing control.

References

[1] "REN21, 2019. Renewables 2019 Global Status Report," REN21 Community, https://www.ren21.net/reports/global-status-report/2019. Accessed: 18-07-2019.

[2] IRENA, "Renewable Power Generation Costs in 2017," http://irena.org/-/media/Files/IRENA/Agency/Publication/2018/Jan/IRENA_2017_Power_Costs_2018.pdf.2018. Accessed: 16-06-2019.

[3] P. ReleasesStatistics, "WIND POWER CAPACITY REACHES 546 GW, 60 GW ADDED IN 2017," World Wind Energy Association, https://wwindea.org/blog/2018/02/12/2017-statistics/2019 February 12, 2018. Acessed: 16-06-2019.

[4] "Installed Capacity by the end of 2018 (MW)," WWEA LIBRARY, https://library.wwindea.org/global-statistics-2018-preliminary/November 2018. Accessed: 18-07-2019.

[5] E. Trend, "GWEC Reports Global Cumulative Capacity of Offshore Wind Generation Reached 23GW in 2018," https://m.energytrend.com/news/view/13466.html2019-03-11. Accessed: 18-07-2019.

[6] A. Dhabi, "RENEWABLE CAPACITY STATISTICS 2019," International Renewable Energy Agency (IRENA), www.irena.org/Publications2019. Accessed: 20-06-2019.

[7] Y. Zhang, J. Ravishankar, J. Fletcher, R. Li, and M. Han, "Review of modular multilevel converter based multi-terminal HVDC systems for offshore wind power transmission," *Renewable and Sustainable Energy Reviews*, vol. 61, pp. 572-586, 2016/08/01/ 2016.

[8] X. Xiang, M. M. C. Merlin, and T. C. Green, "Cost analysis and comparison of HVAC, LFAC and HVDC for offshore wind power connection," in *12th IET International Conference on AC and DC Power Transmission (ACDC 2016)*, 2016, pp. 1-6.

[9] ADMIN, "Difference between HVDC and HVAC Transmission," Power Electronics A to Z, http://www.completepowerelectronics.com/difference-between-hvdc-and-hvac-transmission/JUNE 19, 2018.

[10] S. Sharma, "COMPARISON BETWEEN LCC AND VSC," *International Journal of Scientific Research Engineering & Technology (IJSRET)*, vol. 2, pp. 445-449, October 2013 2013.

[11] J. He, M. Li, J. Yi, Q. Chang, T. Xu, and Y. Zhao, "Research on dynamic characteristics and countermeasures of AC-DC hybrid power system with large scale HVDC transmission," in *2014 International Conference on Power System Technology*, 2014, pp. 799-805.

[12] S. Bozhko, G. Asher, R. Li, J. Clare, and L. Yao, "Large Offshore DFIG-Based Wind Farm With Line-Commutated HVDC Connection to the Main Grid:

Engineering Studies," *IEEE Transactions on Energy Conversion*, vol. 23, pp. 119-127, 2008.

[13] P. Cartwright, L. Xu, and J. Ekanayake, "The Integration of Large Scale Wind Power Generation into Transmission Networks using Power Electronics," 01/01 2004.

[14] J.-H. Ying, H. Duchen, M. Karlsson, L. Ronstrom, and B. Abrahamsson, "HVDC with voltage source converters - a powerful standby black start facility," in *2008 IEEE/PES Transmission and Distribution Conference and Exposition*, 2008, pp. 1-9.

[15] N. T. N. Barberis, T.Ackermannc, "Loss evaluation of HVAC and HVDC transmission solutions for large offshore wind farms," *Electric Power Systems Research*, vol. 76, pp. 916-927, July 2006.

[16] U. G. Knight, *Power Systems in Emergencies: From Contingency Planning to Crisis Management*, 2001.

[17] E. A. A. Coelho, P. C. Cortizo, and P. F. D. Garcia, "Small signal stability for parallel connected inverters in stand-alone AC supply systems," in *Conference Record of the 2000 IEEE Industry Applications Conference. Thirty-Fifth IAS Annual Meeting and World Conference on Industrial Applications of Electrical Energy (Cat. No.00CH37129)*, 2000, pp. 2345-2352 vol.4.

[18] L. Zhang, L. Harnefors, and H. P. Nee, "Interconnection of Two Very Weak AC Systems by VSC-HVDC Links Using Power-Synchronization Control," *IEEE Transactions on Power Systems*, vol. 26, pp. 344-355, 2011.

[19] G. Ö, N. A. Cutululis, P. S∅rensen, and L. Zeni, "Asymmetrical fault analysis at the offshore network of HVDC connected wind power plants," in *2017 IEEE Manchester PowerTech*, 2017, pp. 1-5.

[20] A. Bangar and V. Hamidi, "Control strategy requirements for connection of offshore windfarms using VSC-HVDC for frequency control," in *10th IET International Conference on AC and DC Power Transmission (ACDC 2012)*, 2012, pp. 1-6.

[21] H. Ergun, D. Van Hertem, and R. Belmans, "Transmission System Topology Optimization for Large-Scale Offshore Wind Integration," *Sustainable Energy, IEEE Transactions on*, vol. 3, pp. 908-917, 10/01 2012.

[22] A. Madariaga, J. L. Martín, I. Zamora, I. Martínez de Alegría, and S. Ceballos, "Technological trends in electric topologies for offshore wind power plants," *Renewable and Sustainable Energy Reviews*, vol. 24, pp. 32-44, 2013/08/01/ 2013.

[23] P. H. V. F. Lescale, R. Ottersten, Y. J Häfner, "Parallelling offshore wind farm HVDC ties on offshore side," Cigré Session, Paris2012.

[24] J. Reeve, "Multiterminal HVDC Power Systems," *IEEE Transactions on Power Apparatus and Systems*, vol. PAS-99, pp. 729-737, 1980.

[25] M. Zhang, J. Ding, Y. Cai, and H. Wang, "Research on Control Strategy of MMC-MTDC System based on Improved Droop Control," *Journal of Physics: Conference Series*, vol. 1176, p. 062011, 2019/03 2019.

[26] B. Chang, O. Cwikowski, M. Barnes, and R. Shuttleworth, "Multi-terminal VSC-HVDC Pole-to-pole Fault Analysis and Fault Recovery Study," in *11th IET International Conference on AC and DC Power Transmission*, 2015, pp. 1-8.

[27] A. Garcés, S. Sanchez, G. Bergna, and E. Tedeschi, "HVDC meshed multi-terminal networks for offshore wind farms: Dynamic model, load flow and equilibrium," in *2017 IEEE 18th Workshop on Control and Modeling for Power Electronics (COMPEL)*, 2017, pp. 1-6.

[28] D. Van Hertem and M. Ghandhari, "Multi-terminal VSC HVDC for the European supergrid: Obstacles," *Renewable and Sustainable Energy Reviews*, vol. 14, pp. 3156-3163, 2010/12/01/ 2010.

[29] S. Gang, P. Simin, C. Xu, C. Zhe, and H. Wei, "Grid integration of offshore wind farms and offshore oil/gas platforms," in *Proceedings of The 7th International Power Electronics and Motion Control Conference*, 2012, pp. 1301-1305.

[30] S. Sanchez, A. Garcés, G. Bergna-Diaz, and E. Tedeschi, "Dynamics and Stability of Meshed Multiterminal HVDC Networks," *IEEE Transactions on Power Systems*, vol. 34, pp. 1824-1833, 2019.

[31] E. Prieto-Araujo, A. Egea-Alvarez, S. Fekriasl, and O. Gomis-Bellmunt, "DC Voltage Droop Control Design for Multiterminal HVDC Systems Considering AC and DC Grid Dynamics," *IEEE Transactions on Power Delivery*, vol. 31, pp. 575-585, 2016.

[32] F. Yan, G. Tang, Z. He, and M. Kong, "An improved droop control strategy for MMC-based VSC-MTDC systems," *Zhongguo Dianji Gongcheng Xuebao/Proceedings of the Chinese Society of Electrical Engineering*, vol. 34, pp. 397-404, 01/25 2014.

[33] P. Mitra and L. Zhang, "Real-time simulation of a wind connected HVDC grid," in *10th IET International Conference on AC and DC Power Transmission (ACDC 2012)*, 2012, pp. 1-6.

[34] D. Jovcic, D. v. Hertem, K. Linden, J. Taisne, and W. Grieshaber, "Feasibility of DC transmission networks," in *2011 2nd IEEE PES International Conference and Exhibition on Innovative Smart Grid Technologies*, 2011, pp. 1-8.

[35] M. Abedrabbo, C. Petino, and A. Schnettler, "Analysis of the behavior of HVDC converter based on full-bridge submodules during DC fault conditions," in *2016 IEEE International Energy Conference (ENERGYCON)*, 2016, pp. 1-6.

[36] R. Sharma, M. Andersen, V. Akhmatov, K. Jensen, and T. Wederberg Rasmussen, *Electrical Structure of Future Off-shore Wind Power Plant with a High Voltage Direct Current Power Transmission*, 2012.

[37] M. Amin, A. Rygg, and M. Molinas, "Self-Synchronization of Wind Farm in an MMC-Based HVDC System: A Stability Investigation," *IEEE Transactions on Energy Conversion*, vol. 32, pp. 458-470, 2017.

[38] L. Xu, L. Yao, and C. Sasse, "Grid Integration of Large DFIG-Based Wind Farms Using VSC Transmission," *IEEE Transactions on Power Systems*, vol. 22, pp. 976-984, 2007.

[39] H. Terry Chi Young, R. Li, A. García-Cerrada, J. L. Zamora-Macho, and P. Brogan, "Voltage source converter AC voltage controller design and dynamic response for a large offshore wind farm network," in *2013 International Conference on Renewable Energy Research and Applications (ICRERA)*, 2013, pp. 470-475.

[40] H. Liu and J. Sun, "Voltage Stability and Control of Offshore Wind Farms With AC Collection and HVDC Transmission," *IEEE Journal of Emerging and Selected Topics in Power Electronics,* vol. 2, pp. 1181-1189, 2014.

[41] Z. Wang, D. Luo, R. Li, L. Zhang, C. Liu, X. Tian, *et al.*, "Research on the active power coordination control system for wind/photovoltaic/energy storage," in *2017 IEEE Conference on Energy Internet and Energy System Integration (EI2)*, 2017, pp. 1-5.

[42] S. Cao, W. Xiang, L. Yao, B. Yang, and J. Wen, "AC and DC fault ride through hybrid MMC integrating wind power," *The Journal of Engineering,* vol. 2017, pp. 828-833, 2017.

[43] L. Holdsworth, N. Jenkins, and G. Strbac, "Electrical stability of large, offshore wind farms," in *Seventh International Conference on AC-DC Power Transmission*, 2001, pp. 156-161.

[44] M. Raza and O. Gomis-Bellmunt, "Control System of Voltage Source Converter to Interconnect Offshore AC Hub with Multiple Onshore Grids," in *2015 International Conference on Renewable Energy Research and Applications (ICRERA)*, 2015, pp. 677-682.

[45] L. Zhang, L. Harnefors, and H. Nee, "Modeling and Control of VSC-HVDC Links Connected to Island Systems," *IEEE Transactions on Power Systems,* vol. 26, pp. 783-793, 2011.

[46] J. Beerten, S. Cole, and R. Belmans, "Implementation aspects of a sequential AC/DC power flow computation algorithm for Multi-terminal VSC HVDC systems," in *9th IET International Conference on AC and DC Power Transmission (ACDC 2010)*, 2010, pp. 1-6.

[47] M. Nazari and M. Ghandhari, "Application of multi-agent control to multi-terminal HVDC systems," in *2013 IEEE Electrical Power & Energy Conference*, 2013, pp. 1-6.

[48] C. Dierckxsens, K. Srivastava, M. Reza, S. Cole, J. Beerten, and R. Belmans, "A distributed DC voltage control method for VSC MTDC systems," *Electric Power Systems Research,* vol. 82, pp. 54-58, 2012/01/01/ 2012.

[49] M. E. Elshiekh, D. A. Mansour, and A. M. Azmy, "Improving Fault Ride-Through Capability of DFIG-Based Wind Turbine Using Superconducting Fault Current Limiter," *IEEE Transactions on Applied Superconductivity,* vol. 23, pp. 5601204-5601204, 2013.

[50] B. Liu, J. Xu, R. E. Torres-Olguin, and T. Undeland, "Faults mitigation control design for grid integration of offshore wind farms and oil & gas installations using VSC HVDC," in *SPEEDAM 2010*, 2010, pp. 792-797.

[51] U. Karaagac, J. Mahseredjian, L. Cai, and H. Saad, "Offshore Wind Farm Modeling Accuracy and Efficiency in MMC-Based Multiterminal HVDC Connection," *IEEE Transactions on Power Delivery,* vol. 32, pp. 617-627, 2017.

[52] J. N. Sakamuri, Z. H. Rather, J. Rimez, M. Altin, G. Ö, and N. A. Cutululis, "Coordinated Voltage Control in Offshore HVDC Connected Cluster of Wind Power Plants," *IEEE Transactions on Sustainable Energy,* vol. 7, pp. 1592-1601, 2016.

[53] L. Zhang, L. Harnefors, and H. P. Nee, "Power-Synchronization Control of Grid-Connected Voltage-Source Converters," *IEEE Transactions on Power Systems,* vol. 25, pp. 809-820, 2010.

[54] L. Zhang, L. Harnefors, and H. P. Nee, "Modeling and Control of VSC-HVDC Links Connected to Island Systems," *IEEE Transactions on Power Systems,* vol. 26, pp. 783-793, 2011.

[55] J. Svensson, "Synchronisation methods for grid-connected voltage source converters," *IEE Proceedings - Generation, Transmission and Distribution,* vol. 148, pp. 229-235, 2001.

[56] H. Zhang, D. Flórez, C. Saudemont, and F. Gruson, "Improved overvoltage limitation control approach of a DC series offshore wind farm based on MMC," in *2016 18th Mediterranean Electrotechnical Conference (MELECON)*, 2016, pp. 1-6.

[57] J. Maneiro, S. Tennakoon, C. Barker, and F. Hassan, "Energy diverting converter topologies for HVDC transmission systems," in *2013 15th European Conference on Power Electronics and Applications (EPE)*, 2013, pp. 1-10.

[58] S. K. Chaudhary, R. Teodorescu, P. Rodriguez, and P. C. Kjær, "Chopper controlled resistors in VSC-HVDC transmission for WPP with full-scale converters," in *2009 IEEE PES/IAS Conference on Sustainable Alternative Energy (SAE)*, 2009, pp. 1-8.

[59] S. Nanou and S. Papathanassiou, "Evaluation of a communication-based fault ride-through scheme for offshore wind farms connected through high-voltage DC links based on voltage source converter," *IET Renewable Power Generation,* vol. 9, pp. 882-891, 2015.

[60] M. A. Ahmed and Y. C. Kim, "Hierarchical Communication Network Architectures for Offshore Wind Power Farms," in *2014 International Symposium on Computer, Consumer and Control*, 2014, pp. 299-303.

[61] G. Ramtharan, A. Arulampalam, J. B. Ekanayake, F. M. Hughes, and N. Jenkins, "Fault ride through of fully rated converter wind turbines with AC and DC transmission," *IET Renewable Power Generation,* vol. 3, pp. 426-438, 2009.

[62] Y. Yu, Z. Xu, and T. An, "Fault ride-through strategy for fully rated converter wind turbines connected to the grid via MMC-HVDC transmission," in *12th IET International Conference on AC and DC Power Transmission (ACDC 2016)*, 2016, pp. 1-5.

[63] B. LI, J. HE, J. TIAN, Y. FENG, and Y. DONG, "DC fault analysis for modular multilevel converter-based system," *Journal of Modern Power Systems and Clean Energy,* vol. 5, pp. 275-282, March 01 2017.

[64] R. Zeng, L. Xu, L. Yao, and D. J. Morrow, "Precharging and DC Fault Ride-Through of Hybrid MMC-Based HVDC Systems," *IEEE Transactions on Power Delivery,* vol. 30, pp. 1298-1306, 2015.

[65] C. M. Franck, "HVDC Circuit Breakers: A Review Identifying Future Research Needs," *IEEE Transactions on Power Delivery,* vol. 26, pp. 998-1007, 2011.

[66] K. Sano and M. Takasaki, "A Surgeless Solid-State DC Circuit Breaker for Voltage-Source-Converter-Based HVDC Systems," *IEEE Transactions on Industry Applications,* vol. 50, pp. 2690-2699, 2014.

[67] R. Hasegawa, K. Kanaya, Y. Koyama, T. Matsumoto, and T. Ishiguro, "Principle Experiment of Current Commutated Hybrid DCCB for HVDC Transmission Systems," in *2018 International Power Electronics Conference (IPEC-Niigata 2018 -ECCE Asia)*, 2018, pp. 2011-2015.

[68] A. Daibo, Y. Niwa, N. Asari, W. Sakaguchi, K. Takimoto, K. Kanaya, *et al.*, "High-speed current interruption performance of hybrid DCCB for HVDC transmission system," in *2017 4th International Conference on Electric Power Equipment - Switching Technology (ICEPE-ST)*, 2017, pp. 329-332.

[69] C. Lv and N. Tai, "Control for offshore wind power integration based on modular multilevel converter," *The Journal of Engineering*, vol. 2017, pp. 1885-1889, 2017.

[70] M. Zhu, H. Nian, Y. Xu, and L. Chen, "Impedance-Based Stability Analysis of MMC-HVDC for Offshore DFIG-Based Wind Farms," in *2018 21st International Conference on Electrical Machines and Systems (ICEMS)*, 2018, pp. 1139-1144.

[71] L. Cai, U. Karaagac, and J. Mahseredjian, "Simulation of Startup Sequence of an Offshore Wind Farm With MMC-HVDC Grid Connection," *IEEE Transactions on Power Delivery*, vol. 32, pp. 638-646, 2017.

[72] R. Vidal-Albalate, H. Beltran, A. Rolán, E. Belenguer, R. Peña, and R. Blasco-Gimenez, "Analysis of the Performance of MMC Under Fault Conditions in HVDC-Based Offshore Wind Farms," *IEEE Transactions on Power Delivery*, vol. 31, pp. 839-847, 2016.

[73] I. Colak, R. Bayindir, and E. Kabalci, "A modified harmonic mitigation analysis using Third Harmonic Injection PWM in a multilevel inverter control," in *Proceedings of 14th International Power Electronics and Motion Control Conference EPE-PEMC 2010*, 2010, pp. T2-215-T2-220.

[74] K. Ogata, *Modern Control Engineering*: Prentice Hall PTR, 2001.

[75] H. Alyami and Y. Mohamed, "Review and development of MMC employed in VSC-HVDC systems," in *2017 IEEE 30th Canadian Conference on Electrical and Computer Engineering (CCECE)*, 2017, pp. 1-6.

[76] H. Lang, Y. Xu, X. Peng, Z. Fan, M. Xin, L. Tao, *et al.*, "The evolution and variation of sub-module topologies with DC-fault current clearing capability in MMC-HVDC," in *2017 IEEE 3rd International Future Energy Electronics Conference and ECCE Asia (IFEEC 2017 - ECCE Asia)*, 2017, pp. 1938-1943.

[77] B. J. Pawar and V. J. Gond, "Modular multilevel converters: A review on topologies, modulation, modeling and control schemes," in *2017 International conference of Electronics, Communication and Aerospace Technology (ICECA)*, 2017, pp. 431-440.

[78] L. Zhang, Y. Zou, J. Yu, J. Qin, V. Vittal, G. G. Karady, *et al.*, "Modeling, control, and protection of modular multilevel converter-based multi-terminal HVDC systems: A review," *CSEE Journal of Power and Energy Systems*, vol. 3, pp. 340-352, 2017.

[79] Y. Gao, M. Bazargan, L. Xu, and W. Liang, "DC fault analysis of MMC based HVDC system for large offshore wind farm integration," in *2nd IET Renewable Power Generation Conference (RPG 2013)*, 2013, pp. 1-4.

[80] S. H. A. Niaki, S. A. N. Niaki, and A. A. Abdoos, "Fault detection of HVDC cable in multi-terminal offshore wind farms using transient sheath voltage," *IET Renewable Power Generation*, vol. 11, pp. 1707-1713, 2017.

[81] H. Akagi, "Classification, Terminology, and Application of the Modular Multilevel Cascade Converter (MMCC)," *IEEE Transactions on Power Electronics*, vol. 26, pp. 3119-3130, 2011.

[82] R. Marquardt, "Modular Multilevel Converter: An universal concept for HVDC-Networks and extended DC-Bus-applications," in *The 2010 International Power Electronics Conference - ECCE ASIA -*, 2010, pp. 502-507.

[83] A. Dekka, B. Wu, and N. R. Zargari, "Start-Up Operation of a Modular Multilevel Converter With Flying Capacitor Submodules," *IEEE Transactions on Power Electronics*, vol. 32, pp. 5873-5877, 2017.

[84] A. Nami, J. Liang, F. Dijkhuizen, and G. D. Demetriades, "Modular Multilevel Converters for HVDC Applications: Review on Converter Cells and Functionalities," *IEEE Transactions on Power Electronics*, vol. 30, pp. 18-36, 2015.

[85] M. Hagiwara and H. Akagi, "Control and Experiment of Pulsewidth-Modulated Modular Multilevel Converters," *IEEE Transactions on Power Electronics*, vol. 24, pp. 1737-1746, 2009.

[86] S. Rohner, S. Bernet, M. Hiller, and R. Sommer, "Modulation, Losses, and Semiconductor Requirements of Modular Multilevel Converters," *IEEE Transactions on Industrial Electronics*, vol. 57, pp. 2633-2642, 2010.

[87] P. Hu and D. Jiang, "A Level-Increased Nearest Level Modulation Method for Modular Multilevel Converters," *IEEE Transactions on Power Electronics*, vol. 30, pp. 1836-1842, 2015.

[88] Q. Tu and Z. Xu, "Power losses evaluation for modular multilevel converter with junction temperature feedback," in *2011 IEEE Power and Energy Society General Meeting*, 2011, pp. 1-7.

[89] R. Zhang, D. Boroyevich, V. H. Prasad, H. Mao, F. C. Lee, and S. Dubovsky, "A three-phase inverter with a neutral leg with space vector modulation," in *Proceedings of APEC 97 - Applied Power Electronics Conference*, 1997, pp. 857-863 vol.2.

[90] B. Gemmell, J. Dorn, D. Retzmann, and D. Soerangr, "Prospects of multilevel VSC technologies for power transmission," in *2008 IEEE/PES Transmission and Distribution Conference and Exposition*, 2008, pp. 1-16.

[91] Q. Tu, Z. Xu, and L. Xu, "Reduced Switching-Frequency Modulation and Circulating Current Suppression for Modular Multilevel Converters," *IEEE Transactions on Power Delivery*, vol. 26, pp. 2009-2017, 2011.

[92] J. Qin and M. Saeedifard, "Reduced Switching-Frequency Voltage-Balancing Strategies for Modular Multilevel HVDC Converters," *IEEE Transactions on Power Delivery*, vol. 28, pp. 2403-2410, 2013.

[93] H. Zhang, D. Jovcic, W. Lin, and A. J. Far, "Average value MMC model with accurate blocked state and cell charging/discharging dynamics," in *2016 4th International Symposium on Environmental Friendly Energies and Applications (EFEA)*, 2016, pp. 1-6.

[94] H. Saad, J. Peralta, S. Dennetière, J. Mahseredjian, J. Jatskevich, J. A. Martinez, *et al.*, "Dynamic Averaged and Simplified Models for MMC-Based HVDC Transmission Systems," *IEEE Transactions on Power Delivery,* vol. 28, pp. 1723-1730, 2013.

[95] S. Wang, G. P. Adam, A. M. Massoud, D. Holliday, and B. W. Williams, "Analysis and Assessment of Modular Multilevel Converter Internal Control Schemes," *IEEE Journal of Emerging and Selected Topics in Power Electronics,* pp. 1-1, 2019.

[96] R. Zeng, L. Xu, L. Yao, and S. J. Finney, "Analysis and Control of Modular Multilevel Converters under Asymmetric Arm Impedance Conditions," *IEEE Transactions on Industrial Electronics,* vol. 63, pp. 71-81, 2016.

[97] R. Picas, S. Ceballos, J. Pou, J. Zaragoza, G. Konstantinou, and V. G. Agelidis, "Closed-Loop Discontinuous Modulation Technique for Capacitor Voltage Ripples and Switching Losses Reduction in Modular Multilevel Converters," *IEEE Transactions on Power Electronics,* vol. 30, pp. 4714-4725, 2015.

[98] X. Li, Q. Song, W. Liu, S. Xu, Z. Zhu, and X. Li, "Performance Analysis and Optimization of Circulating Current Control for Modular Multilevel Converter," *IEEE Transactions on Industrial Electronics,* vol. 63, pp. 716-727, 2016.

[99] K. Ilves, A. Antonopoulos, S. Norrga, and H. Nee, "Steady-State Analysis of Interaction Between Harmonic Components of Arm and Line Quantities of Modular Multilevel Converters," *IEEE Transactions on Power Electronics,* vol. 27, pp. 57-68, 2012.

[100] S. Li, X. Wang, Z. Yao, T. Li, and Z. Peng, "Circulating Current Suppressing Strategy for MMC-HVDC Based on Nonideal Proportional Resonant Controllers Under Unbalanced Grid Conditions," *IEEE Transactions on Power Electronics,* vol. 30, pp. 387-397, 2015.

[101] R. Picas, J. Pou, S. Ceballos, V. G. Agelidis, and M. Saeedifard, "Minimization of the capacitor voltage fluctuations of a modular multilevel converter by circulating current control," in *IECON 2012 - 38th Annual Conference on IEEE Industrial Electronics Society*, 2012, pp. 4985-4991.

[102] J. Pou, S. Ceballos, G. Konstantinou, V. G. Agelidis, R. Picas, and J. Zaragoza, "Circulating Current Injection Methods Based on Instantaneous Information for the Modular Multilevel Converter," *IEEE Transactions on Industrial Electronics,* vol. 62, pp. 777-788, 2015.

[103] O. G. B. M. Raza, "Multi-Infeed Control of VSC-HVDC Transmission System for Offshore Wind Power Plant Integration," presented at the 13th Wind Integration Workshop, Berlin Germany, 2014.

[104] M. Saeedifard and R. Iravani, "Dynamic performance of a modular multilevel back-to-back HVDC system," in *2011 IEEE Power and Energy Society General Meeting*, 2011, pp. 1-1.

[105] N. Ahmed, A. Haider, D. V. Hertem, L. Zhang, and H. P. Nee, "Prospects and challenges of future HVDC SuperGrids with modular multilevel converters," in *Proceedings of the 2011 14th European Conference on Power Electronics and Applications*, 2011, pp. 1-10.

[106] P. Wang, X. P. Zhang, P. F. Coventry, and R. Zhang, "Start-Up Control of an Offshore Integrated MMC Multi-Terminal HVDC System With Reduced DC Voltage," *IEEE Transactions on Power Systems,* vol. 31, pp. 2740-2751, 2016.
[107] R. Zeng, L. Xu, L. Yao, and B. W. Williams, "Design and Operation of a Hybrid Modular Multilevel Converter," *IEEE Transactions on Power Electronics,* vol. 30, pp. 1137-1146, 2015.
[108] S. Debnath and M. Chinthavali, "Control of MMC-HVDC in low-inertia weak grids," in *2017 IEEE 12th International Conference on Power Electronics and Drive Systems (PEDS)*, 2017, pp. 435-441.
[109] U. Karaagac, L. Cai, and J. Mahseredjian, "Simulation of startup sequence of an offshore wind farm with MMC-HVDC grid connection," in *2017 IEEE Power & Energy Society General Meeting*, 2017, pp. 1-1.
[110] J. Lyu, X. Cai, and M. Molinas, "Frequency Domain Stability Analysis of MMC-Based HVdc for Wind Farm Integration," *IEEE Journal of Emerging and Selected Topics in Power Electronics,* vol. 4, pp. 141-151, 2016.
[111] X. Cheng, W. Lee, M. Sahni, Y. Cheng, and L. K. Lee, "Dynamic Equivalent Model Development to Improve the Operation Efficiency of Wind Farm," *IEEE Transactions on Industry Applications,* vol. 52, pp. 2759-2767, 2016.
[112] P. Wang, Z. Zhang, Q. Huang, N. Wang, X. Zhang, and W. Lee, "Improved Wind Farm Aggregated Modeling Method for Large-Scale Power System Stability Studies," *IEEE Transactions on Power Systems,* vol. 33, pp. 6332-6342, 2018.
[113] J. Zou, C. Peng, H. Xu, and Y. Yan, "A Fuzzy Clustering Algorithm-Based Dynamic Equivalent Modeling Method for Wind Farm With DFIG," *IEEE Transactions on Energy Conversion,* vol. 30, pp. 1329-1337, 2015.
[114] Y. Li, Z. Xu, J. Østergaard, and D. J. Hill, "Coordinated Control Strategies for Offshore Wind Farm Integration via VSC-HVDC for System Frequency Support," *IEEE Transactions on Energy Conversion,* vol. 32, pp. 843-856, 2017.
[115] F. B. Ajaei and R. Iravani, "Enhanced Equivalent Model of the Modular Multilevel Converter," *Power Delivery, IEEE Transactions on,* vol. 30, pp. 666-673, 2015.
[116] J. Freytes, S. Akkari, J. Dai, F. Gruson, P. Rault, and X. Guillaud, "Small-signal state-space modeling of an HVDC link with modular multilevel converters," in *2016 IEEE 17th Workshop on Control and Modeling for Power Electronics (COMPEL)*, 2016, pp. 1-8.
[117] M. Sztykiel, R. d. Silva, R. Teodorescu, L. Zeni, L. Helle, and P. C. Kjaer, "Modular multilevel converter modelling, control and analysis under grid frequency deviations," in *2013 15th European Conference on Power Electronics and Applications (EPE)*, 2013, pp. 1-11.
[118] N. Pogaku, M. Prodanovic, and T. C. Green, "Modeling, Analysis and Testing of Autonomous Operation of an Inverter-Based Microgrid," *IEEE Transactions on Power Electronics,* vol. 22, pp. 613-625, 2007.
[119] L. Harnefors, M. Bongiorno, and S. Lundberg, "Input-Admittance Calculation and Shaping for Controlled Voltage-Source Converters," *IEEE Transactions on Industrial Electronics,* vol. 54, pp. 3323-3334, 2007.

[120] B. Wen, D. Boroyevich, R. Burgos, P. Mattavelli, and Z. Shen, "Analysis of D-Q Small-Signal Impedance of Grid-Tied Inverters," *IEEE Transactions on Power Electronics*, vol. 31, pp. 675-687, 2016.
[121] U. Karaagac, J. Mahseredjian, L. Cai, and H. Saad, "Offshore wind farm modeling accuracy and efficiency in MMC-based multi-terminal HVDC connection," in *2017 IEEE Power & Energy Society General Meeting*, 2017, pp. 1-1.
[122] D. P. M. Tawfeeq, "Overcurrent Protective Relays," in *Power System Protection*, ed. Philadelphia University.
[123] R. Li, J. E. Fletcher, L. Xu, and B. W. Williams, "Enhanced Flat-Topped Modulation for MMC Control in HVDC Transmission Systems," *IEEE Transactions on Power Delivery*, vol. 32, pp. 152-161, 2017.
[124] R. Li, L. Xu, L. Yao, and B. W. Williams, "Active Control of DC Fault Currents in DC Solid-State Transformers During Ride-Through Operation of Multi-Terminal HVDC Systems," *IEEE Transactions on Energy Conversion*, vol. 31, pp. 1336-1346, 2016.

Author's Publications

1. Y. Jing, R. Li, L. Xu, and Y. Wang, "Enhanced AC voltage and frequency control of offshore MMC station for wind farm connection," *IET Renewable Power Generation*, vol. 12, pp. 1771-1777, 2018

Abstract: Connecting large offshore wind farms using high-voltage direct current (HVDC) transmission systems based on the modular multilevel converter (MMC), the offshore alternating current (AC) voltage and frequency are regulated by the offshore MMC station and are important for the stable wind power generation and transmission. This study proposes an enhanced AC voltage and frequency control strategy of the offshore MMC for wind farm integration, where an additional frequency loop is used to improve its AC voltage and frequency controllability. A fault current injection control is also proposed, where the offshore MMC station actively provides fault currents during an offshore AC fault to enable overcurrent protection for the network. To ride-through onshore AC faults, a direct current (DC) voltage-dependent AC voltage controller is introduced to actively reduce the offshore AC voltage during an onshore AC fault to alleviate the DC overvoltage of the HVDC system. Simulation results in normal operation and during offshore and onshore faults confirm the feasibility of the proposed control scheme.

2. Y. Jing, R. Li, L. Xu, and Y. Wang, "Enhanced AC voltage and frequency control on offshore MMC station for wind farm," *The Journal of Engineering*, vol. 2017, pp. 1264-1268, 2017.

Abstract: For high voltage direct current transmission systems based on a modular multilevel converter (MMC) for connecting large offshore wind farms, the offshore alternating current (AC) voltage is regulated by the offshore MMC station and stable offshore AC voltage and frequency are important for the stable wind power generation and transmission. This study proposes an enhanced AC voltage and frequency control strategy of the offshore MMC for wind farm integration, where an additional frequency

loop is used to improve its AC voltage and frequency controllability. The proposed scheme considers the working principle of the phase locked loop where the measured q -axis voltage drives the frequency output for the generated AC voltage. Thus, the output of the proposed frequency loop sets the q -axis voltage reference and feeds to the AC voltage loop to regulate the offshore AC frequency. Compared with conventional approach where no frequency loop is used and the converter simply produces the output as per the offline phase information, the proposed strategy can tightly control the AC voltage of the offshore network, which contributes to a stable transmission of the offshore wind energy. Simulation results in normal operation and during symmetrical fault confirm the feasibility of the proposed control scheme.